Micromechanical modeling of size-dependent crystal plasticity and deformation twinning

Vom Promotionsausschuss der
Technischen Universität Hamburg

zur Erlangung des akademischen Grades

Doktor-Ingenieur (Dr.-Ing.)

genehmigte Dissertation

von
Edgar Husser

aus
Tschkalowsk

2019

DOI: https://doi.org/10.15480/882.2370

Gutachter der Dissertation:
Prof. Dr.-Ing. Swantje Bargmann, Bergische Universität Wuppertal
Prof. Dr.techn. Christian Frithiof Niordson, Technical University of Denmark
Prof. Dr.-Ing. Christian Johannes Cyron, Technische Universität Hamburg

Vorsitzender des Prüfungsausschusses:
Prof. Dr.-Ing. Norbert Hoffmann, Technische Universität Hamburg
Datum der Disputation: 13. Dezember 2018

Acknowledgments

First of all, I would like to thank my supervisor, Prof. Swantje Bargmann, for giving me the opportunity to work on such an exciting topic as part of a great team consisting of creative and committed scientists from the department of Simulation of Solids and Structures at the Helmholtz-Zentrum Geesthacht and the Institute of Continuum Mechanics and Material Mechanics at the Hamburg University of Technology. It was an exceptional time for me and I am very grateful for all the kind advice and guidance I received form you during that time. The discussions with you whether related to scientific topics or to issues of more general nature gave me always motivation and kept me on track. Thank you for all the encouragement and support which helped me to become a more independent researcher.

I also want to express my gratitude to Prof. Christian Niordson and Prof. Christian Cyron for acting as reviewers of this thesis and for all the effort and work which is linked to it. Many thanks also to Prof. Norbert Hoffmann for acting as the chairman of the examination committee.

A big thank you goes to all the colleagues who had accompanied me during my time as PhD student. You all created a pleasant and interesting working environment to me for which I am very grateful. I would like to make special mention of the extremely helpful support of Ingo und Dirk who always shared their knowledge with me and from whose experience I have learned a lot. Special thanks is also due to Erika for intense discussions on dislocation mechanics and deformation twinning but also for the pleasant and enjoyable cooperation. Moreover, many thanks to Celal for the great and professional cooperation as well as the inspiring discussions on surface effects in small-scaled materials. Particular thanks also to Markus and Erika for the adventure at the ESRF in Grenoble. I gained a lot from this extraordinarily experience with you in the lab. I would also like to thank Prof. Daya Reddy and his students Emma and Ritesh for a very pleasant stay at the University of Cape Town.

I am very grateful indeed to all colleagues from the departments at the HZG and the TUHH. Jan, Jana, Baran, Benedikt, Benjamin, Birthe, Celal, Charlotte, Dirk, Erika, Henry, Ingo, Lidiia, Lukas, Julia, Julian, Jürgen, Kaixiong, Kathrin, Konrad, Manuel, Markus, Mamun, Nadiia, Nam, Paula, Songyun, Tobias, Xiaowei, you all contributed to this thesis in one way or another. It was a great time with all of you and I appreciate all the climbing hours, the basketball training sessions and games, the Feuervogel evenings, the "Kicker" tournaments and all the other meet-ups with you. Thank you very much.

Micromechanical modeling of size-dependent crystal plasticity and deformation twinning

Edgar Husser

Abstract

The computational modeling and simulation of the deformation behavior of crystalline materials at the micron scale is the objective of this thesis. Numerous experimental studies have proven that small-scaled metallic probes behave mechanically different from their bulk counterparts, in particular, the yield strength and work hardening behavior is affected in the way that smaller single crystals behave stronger. This characteristic behavior opens up new design possibilities for further improvement of mechanical properties of engineering material systems. In view of high expenses for advanced and complex experimental work along with the inherent testing limitations, numerical methods offer a great option to validate experimental findings, support the development of suitable theories, and extend scientific investigations on a computer-aided basis.

A gradient crystal plasticity model is presented in this thesis and applied to selected scientific problems including the mechanical testing of single crystals via simulation of microcompression and microbending using a three-dimensional finite element framework. The model is implemented on an element basis and linked to the commercial finite element software Abaqus via the user subroutine UEL. Two major deformation mechanism are considered by the underlying model. Deformation via crystallographic slip is modeled in a non-local fashion allowing to account for gradient effects. Geometrically necessary dislocation (GND) densities associated with plastic slip gradients are introduced as additional nodal degrees of freedom while the actual plastic slip variables are handled as internal variables. Deformation twinning is accounted for in terms of a simple shear deformation associated with shear and shuffling of atoms. In addition, the twinning-induced reorientation of the crystal lattice is fully considered along with subsequent activation of slip modes within the twinned region. In accordance to the non-local crystal plasticity framework, the gradient of the twin volume fraction is introduced at the nodal level. The actual twin volume fraction is treated as an extended internal variable yielding a coupled system of highly non-linear equations at the local level. The competitive nature between slip deformation and deformation by twinning is addressed by physically motivated interaction relations. The characteristic features of the model are portrayed for a variety of micromechanical problems and in relation to experimental results.

Mikromechanische Modellierung größenabhängiger Kristallplastizität und Zwillingsbildung

Kurzfassung

Gegenstand dieser Arbeit ist die Modellierung und Simulation des Deformationsverhaltens von kristallinen Werkstoffen auf der Mikroskala. Diverse experimentelle Studien haben bewiesen, dass sich das mechanische Materialverhalten von kleinskaligen Metallproben gegenüber großskaligen Proben unterscheidet, insbesondere hinsichtlich der Fließgrenze und des Verfestigungsverhaltens. Dabei verhalten sich kleinere Einkristalle fester und zäher als größere. Dieses charakteristische Verhalten eröffnet neue Gestaltungsmöglichkeiten zur weiteren Verbesserung von mechanischen Eigenschaften technischer Materialsysteme.

Ein Gradienten-basiertes Kristallplastizitätsmodell wird im Rahmen dieser Arbeit präsentiert und basierend auf einer dreidimensionalen Finite-Elemente Implementierung auf ausgewählte wissenschaftliche Problemstellungen angewendet. Die Implementierung des Modells erfolgt hierbei mittels einer Benutzerroutine welche auf Element-Ebene in die kommerzielle Finite-Elemente Software Abaqus integriert wird. Schwerpunkt dieser Arbeit ist die numerische Simulation von mechanischen Prüfverfahren, darunter die Mikrokompression und Mikrobiegung von einkristallinen metallischen Werkstoffen. Die Modellierung von Versetzungsgleitung erfolgt durch einen nichtlokalen Ansatz, wodurch die Abbildung von Gradienteneffekten ermöglicht wird. Geometrisch notwendige Versetzungsdichten, assoziiert mit Gradienten der plastischen Gleitung, werden hierbei als zusätzliche Knoten-Freiheitsgrade eingeführt wohingegen die Gleitsystem-bezogenen plastischen Scherungen interne Variablen darstellen. Verformungszwillingsbildung beschreibt die Scherung und Umsortierung von Atomen und wird in Form einer einfachen Scherdeformation abgebildet. Darüber hinaus wird die dabei induzierte Reorientierung des Kristallgitters vollständig berücksichtigt und eine anschließende Aktivierung von Gleitmoden innerhalb verzwillingter Regionen zugelassen. In Anlehnung an die nichtlokale Kristallplastizität wird der Gradient der Zwillingsvolumenfraktion auf der Knotenebene eingeführt. Die Zwillingsvolumenfraktion selbst stellt eine zusätzliche interne Variable dar. Auf der lokalen Ebene ergibt sich somit ein gekoppeltes System von stark nichtlinearen Gleichungen. Deformationsvorgänge im Sinne von Versetzungsgleitung und Zwillingsbildungen stehen auf natürlicher Weise in Konkurrenz. Die hierbei auftretenden Interaktionsvorgänge werden durch physikalisch motivierte Zusammenhänge beschrieben. Die wesentlichen Charakteristika des Modells werden für eine Vielzahl von mikromechanischen Problemen und mit Bezug auf experimentelle Ergebnisse dargestellt.

Contents

List of Figures

List of Tables

General Notation

In the general notation, non-bold letters (e.g. a, B, λ) are used to indicate scalars, bold lowercase letters (e.g. $\boldsymbol{a}, \boldsymbol{b}, \boldsymbol{\xi}$) are used for vectors, and bold uppercase letters (e.g. $\boldsymbol{A}, \boldsymbol{B}$) are used for the representation of second order tensors. Some deviations apply depending on the context. In the following, some standard operations are reviewed with respect to the three-dimensional Euclidean space using the standard (orthonormal) basis $\{\boldsymbol{e}_1, \boldsymbol{e}_2, \boldsymbol{e}_3\}$.

Einstein summation convention	$\boldsymbol{a} = \sum_i^3 a_i \boldsymbol{e}_i = a_1\boldsymbol{e}_1 + a_2\boldsymbol{e}_2 + a_3\boldsymbol{e}_3$ $\boldsymbol{A} = \sum_i^3 \sum_j^3 A_{ij}\boldsymbol{e}_i \otimes \boldsymbol{e}_j$ $= A_{11}\boldsymbol{e}_1 \otimes \boldsymbol{e}_1 + A_{12}\boldsymbol{e}_1 \otimes \boldsymbol{e}_2 + A_{13}\boldsymbol{e}_1 \otimes \boldsymbol{e}_3 + \ldots$
scalar (or inner) product	$\boldsymbol{a} \cdot \boldsymbol{b} = a_i b_j \delta_{ij} = a_i b_i$ where δ_{ij} denotes the Kronecker Delta with $\delta_{ij} = 1$ if $i = j$ and $\delta_{ij} = 0$ if $i \neq j$
vector (or cross) product	$\boldsymbol{a} \times \boldsymbol{b} = \epsilon_{ijk} a_i b_j \boldsymbol{e}_k$ where ϵ_{ijk} denotes the Levi-Civita (or permutation) tensor with $\epsilon_{123} = \epsilon_{231} = \epsilon_{312} = 1$, $\epsilon_{321} = \epsilon_{213} = \epsilon_{132} = -1$, and $\epsilon_{ijk} = 0$ for all other cases
dyadic (or outer) product	$\boldsymbol{a} \otimes \boldsymbol{b} = a_i b_j \boldsymbol{e}_i \otimes \boldsymbol{e}_j$
contraction product	$\boldsymbol{A} \cdot \boldsymbol{b} = A_{ij} b_j \boldsymbol{e}_i$
transpose of a tensor	$\boldsymbol{A}^{\mathrm{T}} = [A_{ij}\boldsymbol{e}_i \otimes \boldsymbol{e}_j]^{\mathrm{T}} = A_{ij}\boldsymbol{e}_j \otimes \boldsymbol{e}_i$
determinant	$\det(\boldsymbol{A}) = \epsilon_{ijk} A_{i1} A_{j2} A_{k3} = \frac{1}{6}\epsilon_{ijk}\epsilon_{lmn} A_{il} A_{jm} A_{kn}$
inverse of a tensor	$\boldsymbol{A}^{-1} = \frac{1}{2\det(\boldsymbol{A})}\epsilon_{imn}\epsilon_{jkl} A_{km} A_{ln} \boldsymbol{e}_i \otimes \boldsymbol{e}_j$ and $\boldsymbol{A} \cdot \boldsymbol{A}^{-1} = \boldsymbol{A}^{-1} \cdot \boldsymbol{A} = \boldsymbol{I}$ with $\boldsymbol{I} = \delta_{ij}\boldsymbol{e}_i \otimes \boldsymbol{e}_j$ being the identity tensor
vector norm	$\lvert\boldsymbol{a}\rvert^2 = \boldsymbol{a} \cdot \boldsymbol{a} = a_i a_i$
tensor norm	$\lVert\boldsymbol{A}\rVert^2 = \boldsymbol{A} : \boldsymbol{A} = A_{ij} A_{ij}$
inner tensor product	$\boldsymbol{A} \cdot \boldsymbol{B} = A_{ij} B_{jk} \boldsymbol{e}_i \otimes \boldsymbol{e}_k$
double contraction product	$\boldsymbol{A} : \boldsymbol{B} = A_{ij} B_{ij}$
outer tensor product	$\boldsymbol{A} \otimes \boldsymbol{B} = A_{ij} B_{kl} \boldsymbol{e}_i \otimes \boldsymbol{e}_j \otimes \boldsymbol{e}_k \otimes \boldsymbol{e}_l$

Let the spatial position of a material point be defined by the triplet (X_1, X_2, X_3). Furthermore, let $\lambda(X_1, X_2, X_3)$ be a scalar field, $\boldsymbol{v}(X_1, X_2, X_3)$ a vector field, and $\boldsymbol{T}(X_1, X_2, X_3)$ a tensor field with respect to the three-dimensional Cartesian coordinate system. Then, the here relevant differential operators acting on these fields are defined below.

gradient of a scalar field	$\nabla a = \dfrac{\partial a}{\partial X_i}\boldsymbol{e}_i = a_{,i}\boldsymbol{e}_i$
gradient of a vector field	$\nabla \boldsymbol{v} = \dfrac{\partial v_i}{\partial X_j}\boldsymbol{e}_i \otimes \boldsymbol{e}_j = v_{i,j}\boldsymbol{e}_i \otimes \boldsymbol{e}_j$
divergence of a vector field	$\mathrm{div}(\boldsymbol{v}) = \dfrac{\partial v_i}{\partial X_i} = v_{i,i}$
divergence of a tensor field	$\mathrm{div}(\boldsymbol{T}) = \dfrac{\partial T_{ij}}{\partial X_j}\boldsymbol{e}_i = T_{ij,j}\boldsymbol{e}_i$
rotation of a vector field	$\mathrm{curl}(\boldsymbol{v}) = \epsilon_{ijk}\dfrac{\partial v_i}{\partial X_j}\boldsymbol{e}_k = \epsilon_{ijk}v_{i,j}\boldsymbol{e}_k$

Nomenclature

General

$\mathcal{E}$	elastic domain
$\mathbb{E}^3$,$\mathbb{E}^3_{\mathrm{r}}$,$\mathbb{E}^3_{\mathrm{c}}$	three-dimensional Euclidean space
$\mathcal{G}_{\mathrm{iso}}$	symmetry group of isotropic materials
$\mathcal{G}_{\mathrm{tri}}$	symmetry group of transversely isotropic materials
$\mathcal{O}$	higher-order terms
$\mathbb{R}$	set of real numbers
$\mathbb{R}^3$	set of real triplets
$\mathcal{SO}(3)$	full special orthogonal group
$\mathcal{TB}_{\mathrm{r}}$,$\mathcal{TB}_{\mathrm{i}}$,$\mathcal{TB}_{\mathrm{c}}$	tangent space
$\mathcal{TB}^*_{\mathrm{r}}$,$\mathcal{TB}^*_{\mathrm{i}}$,$\mathcal{TB}^*_{\mathrm{c}}$	cotangent space
$\mathbb{V}^3_{\mathrm{r}}$,$\mathbb{V}^3_{\mathrm{c}}$	three-dimensional vector space
∇_{r},∇_{i},∇_{c}	gradient operator
Θ^A,θ^A	curvilinear coordinates
$\boldsymbol{E}_a$,$\boldsymbol{e}_a$	standard basis vector
$\boldsymbol{G}_A$,$\overline{\boldsymbol{G}}_\alpha$,$\boldsymbol{g}_a$	covariant basis vector
$\boldsymbol{G}^A$,$\overline{\boldsymbol{G}}^\alpha$,$\boldsymbol{g}^a$	contravariant basis vector
$\boldsymbol{Q}$,$\boldsymbol{Q}_{\mathrm{iso}}$,$\boldsymbol{Q}_{\mathrm{bas}}$,$\boldsymbol{Q}_{<c>}$	transformation matrix
t	time
t_0	initial time
Δt	time increment
X^A,x^a	cartesian coordinates

Continuum mechanics

$\mathcal{B}$	material body
$\mathcal{B}_{\mathrm{r}}$	reference or material configuration
$\partial\mathcal{B}_{\mathrm{r}}$	boundary of reference configuration
$\mathcal{B}_{\mathrm{i}}$	intermediate configuration
$\partial\mathcal{B}_{\mathrm{i}}$	boundary of intermediate configuration
$\partial\mathcal{B}^F_{\mathrm{i}}$	Dirichlet boundary portion (traction)
$\partial\mathcal{B}^u_{\mathrm{i}}$	Neumann boundary portion (displacement)

$\partial\mathcal{B}_{\mathrm{i}}^{\mathrm{g}}$	Dirichlet boundary portion (microfree)
$\partial\mathcal{B}_{\mathrm{i}}^{\nu}$	Neumann boundary portion (microhard)
$\partial\mathcal{B}_{\mathrm{i,crystal}}$	entire intermediate crystal boundary
$\mathcal{B}_{\mathrm{i}}^{\mathrm{p}}$	parent portion of the intermediate configuration
$\partial\mathcal{B}_{\mathrm{i}}^{\mathrm{p}}$	parent portion of the intermediate boundary
$\mathcal{B}_{\mathrm{i}}^{\mathrm{tw}}$	twin portion of the intermediate configuration
$\partial\mathcal{B}_{\mathrm{i}}^{\mathrm{tw}}$	twin portion of the intermediate boundary
$\mathcal{B}_{\mathrm{c}}$	current or spatial configuration
$\partial\mathcal{B}_{\mathrm{c}}$	boundary of current configuration
$\mathbb{C}_{\mathrm{E}}$	elastic stiffness tensor
$\mathcal{C}_{\mathrm{E}}$	forth order tensor
$\mathcal{D}$	dissipation
$\mathcal{D}_{\mathrm{red}}$	reduced dissipation
$\mathcal{D}_{\mathrm{red}}^{\mathrm{L}}$	local bulk dissipation
$\mathcal{D}_{\mathrm{red}}^{\mathrm{L(b)}}$	local boundary dissipation
$\mathcal{I}$	forth order identity tensor
$\mathcal{P}$	specific stress power
$\mathcal{P}_{\mathrm{E}}$	specific elastic stress power
$\mathcal{P}_{\mathrm{P}}$	specific plastic stress power
$\boldsymbol{\chi}$	one-to-one mapping
$\boldsymbol{\chi}_{\mathrm{r}}$	placement into reference configuration
$\boldsymbol{\chi}_{\mathrm{c}}$	placement into current configuration
δ_{AB}	Kronecker delta
$\varepsilon_{\mathrm{ben}}$	bending strain
$\varepsilon_{\mathrm{eng}}$	engineering strain
ϵ_{ijk}	permutation tensor
$\boldsymbol{\epsilon}$	infinitesimal strain tensor
φ	deformation map
Φ_{r},Φ_{c}	surface of the material body
ρ_{r},ρ_{i}	density
σ_{ben}	bending stress
σ_{eng}	engineering stress
σ	unidirectional true stress
$\boldsymbol{\sigma}$	Cauchy stress tensor
$\overline{\boldsymbol{\sigma}}$	volume averaged Cauchy stress tensor
Ξ_{α},$\tilde{\Xi}_{\alpha}$,Ξ_{η}	microscopic surface traction
a,A,A_{r},A_{i}	area
$\boldsymbol{a}$,$\boldsymbol{A}_{\mathrm{r}}$,$\boldsymbol{A}_{\mathrm{i}}$	axis of transverse isotropy
$\boldsymbol{b}$,$\boldsymbol{b}_{\mathrm{E}}$	left Cauchy-Green stretch tensor

$\boldsymbol{C}$,$\boldsymbol{C}_{\mathrm{E}}$	right Cauchy-Green stretch tensor
$\delta\boldsymbol{C}_{\mathrm{E}}$	variation of the right Cauchy-Green stretch tensor
$\boldsymbol{d}$	deformation-rate tensor
$\boldsymbol{d}_{\mathrm{E}}$	elastic deformation-rate tensor
$\boldsymbol{d}_{\mathrm{P}}$	plastic deformation-rate tensor
$\boldsymbol{e}$	Almansi strain tensor
$\boldsymbol{E}$,$\boldsymbol{E}_{\mathrm{E}}$	Green-Lagrange strain tensor
$\mathrm{d}\boldsymbol{f}$	differential surface force
$\boldsymbol{F}$	deformation gradient
$\boldsymbol{F}_{\mathrm{E}}$	elastic deformation part
$\boldsymbol{F}_{\mathrm{I}}$	inelastic deformation part
$\boldsymbol{L}_{\mathrm{I}}$,$\boldsymbol{l}_{\mathrm{I}}$	inelastic velocity gradient part
$\boldsymbol{F}_{\mathrm{P}}$	plastic deformation part
$\boldsymbol{F}_{\mathrm{T}}$	twinning shear deformation part
$\boldsymbol{g}$,$\overline{\boldsymbol{G}}$,$\boldsymbol{G}$	metric tensor
I_1,I_2,I_3	principal invariants
I_4,I_5	(pseudo) invariants
$\boldsymbol{I}$,$\boldsymbol{i}$	identity tensor
J	Jacobian determinant
J_{E}	elastic Jacobian determinant
J_{E}	plastic Jacobian determinant
$\boldsymbol{l}$	spatial velocity gradient
$\boldsymbol{l}_{\mathrm{E}}$	elastic velocity gradient part
$\boldsymbol{L}_{\mathrm{P}}$,$\widetilde{\boldsymbol{L}}_{\mathrm{P}}$,$\boldsymbol{l}_{\mathrm{P}}$	plastic velocity gradient part
$\boldsymbol{M}_{\mathrm{E}}$	Mandel stress tensor
$\boldsymbol{N}$,$\boldsymbol{N}_{\mathrm{r}}$,$\boldsymbol{N}_{\mathrm{i}}$,$\boldsymbol{n}$	normal vector
P,q,Q	material point
$\boldsymbol{P}$	first Piola-Kirchhoff stress tensor
$\boldsymbol{R}$	rotation tensor
$\boldsymbol{s}$	offset vector
$\boldsymbol{S}$,$\boldsymbol{S}_{\mathrm{E}}$	second Piola-Kirchhoff stress tensor
$\boldsymbol{S}_{\mathrm{E}}^{\mathrm{iso}}$	isotropic second Piola-Kirchhoff stress tensor
$\boldsymbol{S}_{\mathrm{E}}^{\mathrm{aniso}}$	anisotropic second Piola-Kirchhoff stress tensor
$\boldsymbol{T}$,$\boldsymbol{T}_{\mathrm{r}}$,$\boldsymbol{T}_{\mathrm{i}}$,$\boldsymbol{t}$,$\check{\boldsymbol{t}}$	surface traction vector
$\boldsymbol{u}$	displacement vector
$\bar{\boldsymbol{u}}$	prescribed displacement vector
$\boldsymbol{U}$	stretch tensor
$\overline{\boldsymbol{U}}$	volume averaged logarithmic stretch tensor
v,V,V_{r},V_{i}	volume
$\boldsymbol{v}$	velocity vector
$\delta\boldsymbol{v}$	variation of the velocity vector
$\boldsymbol{V}$	stretch tensor

$\boldsymbol{w}$	spin tensor
$\boldsymbol{w}_{\mathrm{E}}$	elastic spin tensor
$\boldsymbol{w}_{\mathrm{P}}$	plastic spin tensor
$\boldsymbol{X}$,$\overline{\boldsymbol{X}}$,$\boldsymbol{x}$	position vector
$\mathrm{d}\boldsymbol{X}$,$\mathrm{d}\boldsymbol{Y}$,$\mathrm{d}\boldsymbol{Z}$,$\mathrm{d}\overline{\boldsymbol{X}}$,$\mathrm{d}\boldsymbol{x}$,$\mathrm{d}\boldsymbol{y}$,$\mathrm{d}\boldsymbol{z}$	line element

Crystallography

$\mathfrak{b}$,$\mathfrak{b}_\alpha$	net sum of Burgers vectors
$\mathcal{C}$	Burgers circuit
α,β	slip system index
$\upalpha$,$\upbeta$,$\upgamma$	angles between lattice constants
η	twin variant index
η_0	twinning shear magnitude
$\boldsymbol{\eta}_1$,$\boldsymbol{\eta}_2$	twin direction elements
ϕ	angle between loading direction and basal plane normal
ϕ_n	angle between loading direction and slip plane normal
ϕ_s	angle between loading direction and slip direction
$\varphi_\alpha^{\mathrm{e}}$	misorientation angle for edge dislocations
$\varphi_\alpha^{\mathrm{s}}$	misorientation angle for screw dislocations
a,b,c	general lattice constants
a,c	lattice constants
$\mathbf{a}, \mathbf{b}, \mathbf{c}$	general lattice basis vectors
$\boldsymbol{a}_1$,$\boldsymbol{a}_2$,$\boldsymbol{a}_3$,$\boldsymbol{c}$	lattice basis vectors (primitive hexagonal lattice)
$\boldsymbol{a}_1^*$,$\boldsymbol{a}_2^*$,$\boldsymbol{c}^*$	reciprocal lattice basis vectors (primitive hexagonal lattice)
$\boldsymbol{a}_1$,$\boldsymbol{a}_2$,$\boldsymbol{a}_3$,$\boldsymbol{c}$	lattice basis vectors (full hexagonal lattice)
$\boldsymbol{A}_1^*$,$\boldsymbol{A}_2^*$,$\boldsymbol{A}_3^*$,$\boldsymbol{C}^*$	reciprocal lattice basis vectors (full hexagonal lattice)
$\boldsymbol{A}$	coordinate transformation matrix
b,b_α,b_η	magnitude of Burgers vector
$\boldsymbol{b}_\alpha$	Burgers vector
$\boldsymbol{B}$	coordinate transformation matrix
$d_{\{10\bar{1}2\}}$	distance between two adjacent planes
f_α,f_{basal},$\tilde{f}_{\mathrm{basal}}$,$f_{\mathrm{pris}}$,$f_{\pi 2}$,$f_{\text{t-tw}}$	Schmid factor
$\boldsymbol{f}_\alpha^{\mathrm{e}+}$,$\boldsymbol{f}_\alpha^{\mathrm{e}-}$	flow direction of edge dislocation
$\boldsymbol{f}_\alpha^{\mathrm{s}+}$,$\boldsymbol{f}_\alpha^{\mathrm{s}-}$	flow direction of screw dislocation
$\boldsymbol{K}_1$,$\boldsymbol{K}_2$	twin plane elements
$\boldsymbol{l}_\alpha^{\mathrm{e}+}$,$\boldsymbol{l}_\alpha^{\mathrm{e}-}$	line direction (edge dislocation)
$\boldsymbol{l}_\alpha^{\mathrm{s}+}$,$\boldsymbol{l}_\alpha^{\mathrm{s}-}$	line direction (screw dislocation)
$\boldsymbol{n}_{(h,k,l)}$,$\boldsymbol{n}_{(h',k',i',l')}$	crystallographic plane normal vector

$\boldsymbol{p}_\alpha$	line direction vector
$\boldsymbol{s}_{[u,v,w]}$,$\boldsymbol{s}_{[u',v',t',w']}$	crystallographic direction vector

Crystal plasticity

$\mathbb{S}_\alpha$,$\widehat{\mathbb{S}}_\alpha$	Schmid tensor
$\mathcal{V}$	set of kinematic variables
χ_i	dissipation potential
ϕ_α	yield function
γ_α	accumulated plastic slip
$\Delta\gamma_\alpha$	plastic slip increment
γ^eff	effective accumulated plastic slip
κ	micro-hardening stress
$\kappa_\alpha^\mathrm{(b)}$	micro-boundary stress
$\boldsymbol{\kappa}$	micro-hardening stress vector
ν_α,$\widetilde{\nu}_\alpha$	plastic slip rate
$\delta\nu_\alpha$,$\delta\widetilde{\nu}_\alpha$	variation of the plastic slip rate
π_α,$\tilde{\pi}_\alpha$,π_η	microforce
ψ_i	free energy density
$\psi_\mathrm{i}^\mathrm{el}$,$\tilde{\psi}_\mathrm{i}^\mathrm{el}$,$\hat{\psi}_\mathrm{i}^\mathrm{el}$	elastic free energy
$\psi_\mathrm{i}^\mathrm{el,iso}$	isotropic elastic free energy
$\psi_\mathrm{i}^\mathrm{el,aniso}$	anisotropic elastic free energy
$\psi_\mathrm{lin}^\mathrm{el,aniso}$	anisotropic elastic free energy (linear theory)
ψ^l	local energy
$\psi_\mathrm{i}^\mathrm{g}$	defect energy
$\psi_\mathrm{i}^\mathrm{tb}$	twin boundary energy
ρ_α	total dislocation density
$\rho_{\alpha 0}$	initial dislocation density
τ_α,$\widetilde{\tau}_\alpha$,τ_η	resolved shear stress (Schmid stress)
τ_α^eff	effective shear stress
τ_α^h,$\tilde{\tau}_\alpha^\mathrm{h}$	slip system hardening
$\tau_{\alpha,\mathrm{basal}}^\mathrm{h}$,$\tilde{\tau}_{\alpha,\mathrm{basal}}^\mathrm{h}$	basal slip hardening
$\tau_{\alpha,\mathrm{pris}/\pi 2}^\mathrm{h}$,$\tilde{\tau}_{\alpha,\mathrm{pris}/\pi 2}^\mathrm{h}$	prismatic/sec. order pyramidal slip hardening
τ_α^y	size-dependent yield stress
$\tau_\alpha^{\mathrm{tw}\to\mathrm{sl}}$	twin-slip interaction resistance
τ_η^int	friction stress
τ_η^y	energetic stress barrier
$\tau_\eta^{\mathrm{sl}\to\mathrm{tw}}$	slip-twin interaction resistance
$\tau_\mathrm{i}^\mathrm{b}$	backstress
$\tau_\mathrm{b}^\mathrm{eff}$	effective backstress

Υ_{i}	energy storage rate density
$\boldsymbol{\xi}_\alpha$,$\tilde{\boldsymbol{\xi}}_\alpha$,$\boldsymbol{\xi}_\eta$	microstress vector
ζ_α	SSD density
$\zeta_{\alpha 0}$	initial SSD density
ζ^{eff}	effective SSD density
ζ_0^{eff}	initial effective SSD density
d_{tw}	twin thickness
f_η	twin volume fraction
δf_η	variation of the twin volume fraction
F	step function
$g_{\mathrm{i}\alpha}$	total GND density
$g_{\mathrm{i}\alpha}^{\mathrm{e}}$	edge GND density
$g_{\mathrm{i}\alpha 0}^{\mathrm{e}}$	initial edge GND density
$\Delta g_{\mathrm{i}\alpha}^{\mathrm{e}}$	edge GND density increment
$g_{\mathrm{i}\alpha}^{\mathrm{s}}$	screw GND density
$g_{\mathrm{i}\alpha 0}^{\mathrm{s}}$	initial screw GND density
$\Delta g_{\mathrm{i}\alpha}^{\mathrm{s}}$	screw GND density increment
$g_{\mathrm{i}\alpha}^{\mathrm{e}\perp}$	edge GND density normal to slip plane
$g_{\mathrm{i}}^{\mathrm{eff}}$	effective GND density
$\boldsymbol{g}_{\mathrm{r}\alpha}$,$\boldsymbol{g}_{\mathrm{i}\alpha}$	GND density vector
$\boldsymbol{G}_{\mathrm{r}}$,$\boldsymbol{G}_{\mathrm{i}}$	dislocation tensor
$\boldsymbol{N}_\alpha$,$\boldsymbol{n}_\alpha$,$\widehat{\boldsymbol{n}}_\alpha$	slip plane normal
$\tilde{\boldsymbol{n}}_\alpha$	reoriented slip plane normal
$\boldsymbol{n}_\eta$	twin plane normal
r_α,$\tilde{r}_\alpha$,R_α	slip system resistance
r_η	twinning shear resistance
r_{i}	rate potential
$\boldsymbol{S}_\alpha$,$\boldsymbol{s}_\alpha$,$\boldsymbol{s}_\alpha^+$,$\boldsymbol{s}_\alpha^-$,$\widehat{\boldsymbol{s}}_\alpha$	slip direction
$\tilde{\boldsymbol{s}}_\alpha$	reoriented slip direction
$\boldsymbol{s}_\eta$	twinning shear direction
$\boldsymbol{T}_\alpha$,$\boldsymbol{t}_\alpha$,$\widehat{\boldsymbol{t}}_\alpha$	transverse slip direction
$\tilde{\boldsymbol{t}}_\alpha$	reoriented transverse slip direction
$\bar{v}_\alpha$	average line velocity

Material/model parameters

α,β,δ	anisotropic elastic model parameters
$\chi_{\alpha\beta}$	slip coplanarity moduli
Γ	twin boundary energy
$\iota_{\alpha\beta}^{\mathrm{ee}}$	edge-edge interaction moduli
$\iota_{\alpha\beta}^{\mathrm{es}}$	edge-screw interaction moduli

$\iota^{\mathrm{se}}_{\alpha\beta}$	screw-edge interaction moduli
$\iota^{\mathrm{ss}}_{\alpha\beta}$	screw-screw interaction moduli
λ,$\lambda^{\perp}$	Lamé parameter
Λ	twinning shear magnitude on each layer
μ,$\mu^{\perp}$	Lamé parameter
ν,$\nu^{\perp}$	Poisson's ratio
ν_0	reference shear rate
$c_{\alpha,\mathrm{sat}}$,c_{sat}	saturation rate
C_{Γ}	boundary coefficient
$\overline{C}_{\Gamma}$	cut-off value for the boundary coefficient
C_0	reference drag stress
C_{11}, C_{12}, C_{13}, C_{33}, C_{44}, C_{66}	elastic constants (Voigt notation)
D_0	characteristic crystal size
E	(isotropic) Young's modulus
E^{ϕ}	directional-dependent Young's modulus
E^{e}	elastic energy of edge dislocation
E^{s}	elastic energy of screw dislocation
g^{c}	critical dislocation density
$g^{\max}_{\mathrm{i}\alpha}$	maximum permissible GND density
h^{∞}_{α}	ultimate stress
$H^{\mathrm{l}}_{\alpha\beta}$	local hardening matrix
$H^{\mathrm{e}}_{\alpha\beta}$,$H^{\mathrm{s}}_{\alpha\beta}$	gradient hardening matrix
$H^{\mathrm{l}}_{\alpha 0}$	local hardening modulus
$\Delta H^{\mathrm{l}}_{\alpha}$	saturation stress
H^{g}_0	gradient hardening modulus
H^{e}_0	edge GND gradient hardening modulus
H^{s}_0	screw GND gradient hardening modulus
$\boldsymbol{H}^{\mathrm{tb}}$	interfacial hardening matrix
$k_{\alpha\beta}$	mutual immobilization coefficients
K	coefficient
l,l_{α}	intrinsic length scale, radius of GND interactions
l_{η}	twin boundary thickness
$\tilde{l}$	mean spacing between forest dislocations
L_{α}	mean free path
L_{SSD}	mean spacing between SSDs
m	rate sensitivity exponent
n	number of twin layers
n_{α}	number of admissible slip systems
n_{η}	number of admissible twin variants
$q_{\alpha\beta}$	hardening interaction coefficients

$q^{\xi}_{\alpha\beta}$	gradient hardening interaction coefficients
s_{Γ}	rate of dislocation absorption/transmission
y, k, z	power fit parameters
y_{c}	dislocation capture radius
$Y_{\alpha 0}$	microscopic initial yield limit
Y_{bas}	initial yield limit of basal slip modes
Y_{pri}	initial yield limit of prismatic slip modes
$Y_{\pi 2}$	initial yield limit of sec. order pyramidal slip modes
$\overline{Y}_{\alpha 0}$	yield strength pre-factor
$\overline{Y}$	macroscopic initial yield limit

Others

φ	loading angle
D_0	initial specimen/ligament diameter
D_1	grip diameter
D_{m}	nominal pillar diameter
F_{R}	reaction force
$\delta g^{\mathrm{e}}_{\alpha}$,$\delta g^{\mathrm{s}}_{\alpha}$	test function of GND density fields
h	cantilever beam thickness
K_{lat}	lateral spring stiffness
l_{b}	momentum arm along cantilever beam length
L_0	initial specimen length
L_1,L_2,L_3	parallel, grip, and total length of tensile specimen
$M^{\mathrm{p}}_{\mathrm{b}}$	plastic bending moment
R	fillet radius
S^{p}	plastic section modulus
$\delta \boldsymbol{u}$	test function of displacement field
w	cantilever beam width

1 Introduction

Length scale effects and their impact on the plastic behavior of crystalline materials were analyzed comprehensively in the recent years. Decisive for the emergence of this research area was the development of miniaturized sample preparation technologies and sophisticated testing methods along with significant advances in microstructural characterization techniques. The expansion of nanotechnology applications and the associated ever-growing demand for nano-structured functional materials with tailor-made properties place more and more importance on fundamental research in material science. A large number of experimental studies have validated that the mechanical response of small-scale crystalline samples is characterized by the so called 'smaller is stronger' phenomena. Especially the examination of single crystalline samples experienced a boom in the recent past. Such small volumes establish an environment in which unwanted mechanisms can be excluded easier from the deformation process and, at the same time, experimental boundary conditions can be set up in a desired and controlled way. A major challenge in this respect lies in the accurate prediction of size-affected mechanical properties in order to meet technical requirements already at an early stage of the product design process without time-consuming and cost-intensive experimental examinations.

Continuum strain gradient theories began to be extensively employed for explaining size-dependent plasticity. Supported by experimental evidence, these theories state that strain gradients scale inversely proportional to the material length scale over which plastic deformation takes place. Moreover, the appearance of pronounced plastic strain gradients is correlated with microstructural changes in terms of additional dislocation storage which, in turn, enhance the flow strength of materials. Non-local crystal plasticity models are able to account for such gradient effects and can be effectively used to study the micromechanics of small-sized metallic systems. In contrast to other modeling approaches such as molecular dynamics, dislocation dynamics, or discrete dislocation dynamics, theories based on continuum mechanics enable a numerical investigation of comparatively large volume sizes and under real-time conditions. This is of particular advantage if the deformation behavior of, e.g., an entire specimen has to be taking into account in order to derive quantitative conclusions. Other modeling approaches may be limited in their applicability due to non-feasible computational times if the considered volume becomes too large or the structure too complex. Some commonly used small-scale mechanical testing methods for single crystals are reviewed in the following with particular focus on the role of plastic strain gradients in such experiments.

1.1 Size-dependent phenomena in single crystals

The investigation of small, single crystalline volumes has become a main focus in material science. Many experimental studies have shown that the mechanical response of materials changes drastically if the sample size approaches the sub-micrometer regime (typically 10 - 20 μm and below) compared to that typically observed in corresponding bulk material. This phenomenon is usually termed as 'mechanical size effect' whereby this terminology does not indicate any causality of its appearance. In fact, different types of size effects have been reported in the literature as observed from a variety of micromechanical experiments. Worth mentioning in particular are microtorsion [80], microindentation [26, 163, 231], microcompression [67, 157, 245], and microbending [66, 130, 179, 233] tests. A classification of size effects as intrinsic and extrinsic size effects was introduced by Sevillano and co-workers [221, 222]. By definition, intrinsic size effects are driven by a microstructural length that is characteristic for the actual physical process. The length acts, so to say, as a microstructural constraint (Arzt [6]). This effect may also be associated with characteristic sample dimensions such as the distance between free surfaces in a single crystal as is, e.g., the case for microcompression experiments where geometric confinements by free surfaces induce a strong intrinsic size effect, see [146]. Extrinsic size effects, in contrast, are associated with strain gradients which are macroscopically imposed by non-homogeneous loading conditions. In other words, plastic strain gradients are induced by the geometry of strain (deformation field). Typical examples in this respect are twisting of microwires or bending of microbeams. A classification of well-studied size effects in the aforementioned categories is given, for instance, in the textbooks of Kubin [146] and Budiman [38]. Note that there is not always consistency in the literature. However, this might be due to the fact that size effects are often caused by intrinsic and extrinsic phenomena at the same time, i.e., one effect becomes superimposed on the other. A typical example for that is the size effect observed during thin film testing where a geometrical constraint is given in thickness direction and a microstructural constraint results from, e.g., the average grain size or the average particle spacing, cf. [6].

1.2 Microstructural length

A meaningful consideration of length-scale effects requires a detailed understanding about when plastic strain gradients significantly affect the stress-strain relation. Therefore, the identification and quantification of the material intrinsic length l is of crucial importance for strain gradient plasticity models. As an example, a variation of the mean spacing d ($\approx 1-40$ μm) between hard, non-deforming particles in a crystalline material affects the extent to which plastic strain gradients evolve and, in turn, determines the extent of size-dependent hardening arising from the geometrical necessity of dislocation storage, cf. for instance Lloyd [159], Kouzeli and Mortensen [140]. Dislocations which accumulate for compatibility reasons along strain gradients are termed geometrically necessary dislocations (GNDs), see Ashby [9]. With respect to pure single crystals, i.e., without any particle inclusions, a material intrinsic length is not directly evident. Nevertheless, an intrinsic length can be established based on other internal irregularities such as the mean spacing $\tilde{l}$ between forest dislocations which is at moderate deformations in the order of 1 μm.

With the advent of continuum-based gradient theories in which constitutive length-scale parameters have been incorporated in order to scale hardening effects arising from plastic strain gradients, a considerable number of studies have been elaborated on determining accurate

values. Nix and Gao [183] defined $l = 4L_{\mathrm{SSD}}/3b$ where L_{SSD} is the mean spacing of statistically stored dislocations (SSDs) which accumulate randomly due to plastic deformation and b denotes the magnitude of the Burgers vector. Based on microindentation experiments, it was found that $l = 12$ μm for the investigated case of annealed single crystal copper. Begley and Hutchinson [26] fitted indentation hardness data of Atkinson [10] for a wide range of metals. The results showed that $l = 1.6$ μm for soft metals (annealed) and $0.5\ \mu\mathrm{m} \leq l \leq 1.0\ \mu\mathrm{m}$ for hard metals (cold-worked) represent a good fit of the experimental data, i.e., the smallest length-scale parameter is associated with the hardest material and vice versa. Stölken and Evans [233] determined values of $l = 4$ μm for copper and $l = 5$ μm for nickel via microbending tests of thin foils. These results appear in accordance to previously determined values for Cu using microtorsion tests, cf. [80].

1.3 Plastic strain gradients in micromechanical experiments

Plastic strain gradients can play an important role in the deformation behavior of materials tested at small scales. As mentioned above, their appearance is associated with different deformation confinements for the volume under investigation including microstructural, geometrical, or even combined limitations to deform plastically. In the following, the impact of plastic strain gradients is discussed with respect to size effects observed in microindentation, microcompression, and microbending experiments, see Fig. 1.1 for a graphical description of each testing method.

One widely studied mechanical testing method at small scales is the instrumental indentation test, see, e.g., [174, 231]. In this, it was found that crystals exhibit a so-called indentation size effect (ISE) which is characterized by a depth dependence of the hardness, i.e., the hardness increases with decreasing penetration (indentation) depth for self-similar indenter tips like pyramids and cones as the angle of indented surface remains the same in these cases. A less obvious correlation between hardness and indentation depth is found for spherical indenter tips due to the missing self-similarity, cf. for instance Nix and Gao [183], Swadener et al. [239]. Nix and Gao developed a model which describes the ISE (for conical indenters) in terms of a gradient-induced storage of GNDs which evolve inversely proportional to the penetration depth and becomes stored underneath the indenter tip. The model is based on the assumption that the radius of the hemispheric plastic zone is equal to the radius of the contact zone. However, the first assumption is somewhat unrealistic as it overestimates the GND density

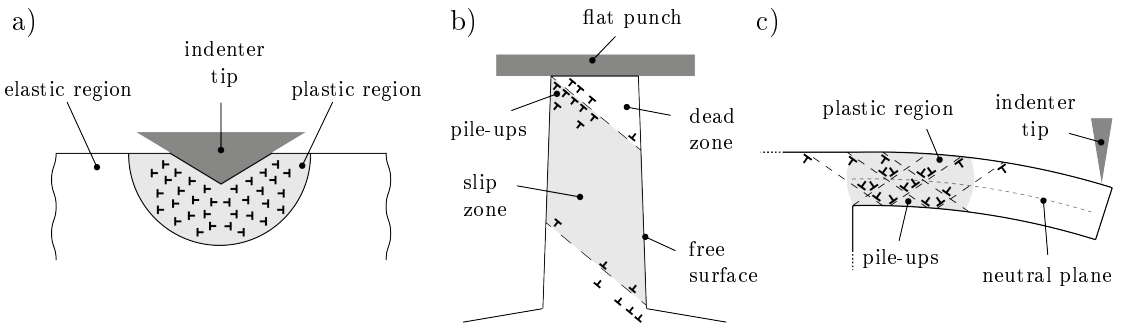

Figure 1.1: Plastic strain gradients and typical arrangements of dislocations during micromechanical testing of single crystals: a) microindentation, b) microcompression, c) microbending.

at very small contact sizes and, hence, the predicted hardness becomes too high compared to certain experiments, see Pharr et al. [204] for more details. Nevertheless, it is experimentally observed that the extra storage of dislocations results in a lattice rotation within the plastic process zone, cf. Fig. 1.1 a). This was proven via electron backscatter diffraction (EBSD), e.g., by Kiener et al. [128] for W and Cu single grains and by Zaafarani et al. [263] for Cu single crystals. In the latter study, results have been additionally supported by finite element simulations. The combination of experimental techniques for microstructure analysis such as EBSD and the usage of crystal plasticity simulations became a promising approach to gain more details about the ongoing processes within the plastified zone.

In contrast to indentation tests, the stress state induced during microcompression is less complex and allows therefore more focused investigations on particular deformation modes in single crystals. In general, pillar-shaped samples loaded by a flat punch are exposed to nominally uniaxial stress conditions, see Fig. 1.1 b). But with advancing load, such samples typically experience an intense localized shear deformation. According to Dimiduk et al. [67], the deformation process takes place in a confined slip zone which is primarily defined by the distance set by the free surfaces. Localized slip traces or even large slip bands are accompanied by unslipped, so-called dead zones. In-situ Laue diffraction and EBSD of Au pillars (Maaß et al. [165]) and Cu pillars (Maaß et al. [164]) revealed that the crystals undergo lattice rotation during deformation. In the study of Kiener et al. [124], localized lattice rotation was attributed to the fact that dislocations are prevented from leaving the sample through the top surface since the sample is in contact with the loading device. It was found that dislocation pile-ups are present in the corners of the sample/punch interface where local lattice rotations up to $\sim 10^\circ$ can be expected, dependent on the average pile-up length. However, due to relaxation and annihilation effects upon unloading, misorientation angles determined by post measurements must be expected to be smaller. Similar conclusions were made after in-situ micro-Laue diffraction in the study of Kirchlechner et al. [131]. Shade et al. [223] examined lateral constraint effects during microcompression and found that the conditions at the sample/punch interface for the extreme cases of zero friction and extensive friction (almost no relative motion) lead to strong changes in the mechanical response, the intermittency of strain bursts, the spatial distribution of slip bands, and the development of internal lattice rotations. Some crucial aspects regarding the accurate design of microcompression experiments are discussed by Zhang et al. [265].

Single crystals are further tested via microbending experiments which are outstandingly suitable to investigate the material behavior, in particular, during cyclic loading. With focus on cantilever beam bending tests, cf. Fig. 1.1 c), the non-homogeneously imposed deformation gives rise for additional storage of GNDs in order to accommodate the resulting lattice curvature (Fleck and Hutchinson [79]). Motz et al. [179] found that the flow stress measured for such geometries shows a strong dependence on the beam thickness. It was further argued that stresses resulting from dislocation pile-ups around the neutral plane are capable to explain the observed strengthening effect. The accumulation of GNDs has two major impacts on the micromechanics. Firstly, they act as additional obstacles to mobile dislocations. In contrast to the case of plane strain bending with single slip where a simple configuration of GNDs can be expected (see, for instance, Gao et al. [82]), when multi slip systems are active, the evolution of the dislocation structure and related hardening behavior is drastically affected, cf. Cleveringa et al. [58]. On the other hand, the stress field of accumulating GNDs is opposed to the macroscopically applied load. As a result, back stresses are manifested, resulting in a strong Bauschinger effect (Kiener et al. [125]) and support reversal load (Demir and Raabe [65]). Kirchlechner et al. [130] investigated the extent of reversible plasticity during bending

of Cu single crystals using in-situ micro-Laue diffraction. Beside a direct observation of the Bauschinger effect, it was noted that dislocation pile-ups dissolve upon load reversal which is caused by the back stress effect.

1.4 Outline of the thesis

Chapter 2 outlines the continuum mechanical framework in the context of finite crystal plasticity theory which serves as the basis for the constitutive modeling. All relevant tensorial quantities are introduced using a general coordinate representation which allows for a more intuitive geometrical interpretation which is further highlighted by means of commutative diagrams.

In view of modeling the deformation behavior of crystalline materials, Chapter 3 provides the required preliminaries including a brief introduction into the crystallographic description of crystals. Furthermore, some constitutive aspects of crystal elasticity and crystal plasticity are discussed. Of particular relevance is the constitutive description of anisotropic hyperelasticity and the thermodynamic framework of gradient crystal plasticity.

In Chapter 4, the gradient crystal plasticity model is applied to microcompression testing of Mg single crystals. Since microcompression of free standing pillars is a relatively new technique which allows to investigate the micromechanics of materials at the sub-micron regime, it serves as a practical application in order to quantify the performance of the model. This is done by direct comparison of numerical results with experimental data. In addition, an extensive comparison between conventional and gradient-enhanced crystal plasticity is provided.

Another prominent application is studied in Chapter 5. Here, the gradient crystal plasticity model is applied to microbending testing of cantilever beams fabricated from Cu single crystals. The role of GND densities is investigated during the imposed bending deformation with focus on the back stress effect. The numerically determined relation between the flow stress and the beam thickness appears reasonable with regard to experimental data, at least for a particular range of beam thicknesses. Other size-dependent phenomena are discussed in this context.

Chapter 6 deals with the modeling of advanced higher-order boundary conditions for gradient crystal plasticity. A geometrically and physically motivated relation for the plastic slip at the surface is established within the surface term of the variational form. In contrast to idealized boundary conditions which do not require the implementation of the surface term, the proposed approach allows to consider more realistic surface (or grain boundary) conditions including a size-dependent surface yielding behavior. As a case study, the influence of advanced higher-order boundary conditions is investigated for an exemplary microstructure representing ultra-fine nanoporous gold.

In Chapter 7, the general framework is extended towards the incorporation of deformation twinning. The process of twinning is accounted for in terms of a shear deformation associated with the motion of twin partials. In this respect, the sudden change of the crystal lattice orientation at the very final stage of the twinning shear process is considered explicitly in the modeling approach. This allows to describe dislocation glide deformation with respect to the new lattice orientation, i.e., within twinned regions of the crystal. Illustrative examples are presented in which different local stress distributions are used to mimic situations as they occur in different regions within a single crystal or grain, e.g., close to a boundary and far off. A demonstrative microcompression example is further presented by which the growth behavior of a single twin is analyzed.

2 Continuum mechanical framework

This chapter deals with some selected aspects of the continuum theory of solids which allows the reader to understand and interpret the underlying continuum mechanical framework in which the constitutive material model is formulated. Particular attention is laid on the kinematic description of deformation in which the deformation gradient is of major significance as it represents a central tensor from which the definition of strain emerges. The content is given in a very general format using curvilinear coordinates. This requires the definition of metric tensors together with associated transformation rules for coordinates and basis vectors. Based on this general treatment, a more intuitive interpretation, e.g., of strain tensors is given. Furthermore, commutative diagrams are consistently used to highlight the relationships between introduced tensor quantities and to enable a geometrical interpretation of the mapping relations.

At the end of this chapter, the continuum mechanical framework is extended with regard to crystal plasticity, considering a multiplicative decomposition of the deformation gradient. On this basis, an intermediate, in general not coherent configuration is introduced which implies a split of the total deformation map into two partial mappings. Although these mappings are generally no gradients of a vector field, they do represent the elastic and plastic deformation parts within an infinitesimal neighborhood. Extended commutative diagrams summarize all relevant mapping relations which involve intermediate strain and stress measures. As a last aspect, a brief overview of relevant deformation-rate measures is given which form together with suitable stress measures energetically conjugate pairs. Of particular interest is the elasto-plastic split of the rate of internal work (stress power) with respect to the intermediate configuration which is applied later within the thermodynamic framework of gradient crystal plasticity.

2.1 Material body

In classical continuum mechanics, a material body $\mathcal{B} \subset \mathbb{R}^3$ represents a physical system which fills a part of the three-dimensional space with continuously distributed matter. This matter carries the actual physical process and can be understood as a continuous composition of particles or material points $P \in \mathcal{B}$. At different moments of time $t \in \mathbb{R}$, the totality of particles $\mathcal{B} = \{P\}$, is occupying different parts of the space. There is a set of one-to-one mappings $\mathcal{K} = \{\boldsymbol{\chi}, t\}$ where each $\boldsymbol{\chi} \in \mathcal{K}$ defines a snapshot of the occupied region (subset of $\mathbb{R}^3$) called configuration or image of the material body. Each configuration establishes a one-to-one correspondence between a material point P and a triple of real numbers denoting the coordinates. For a well-defined reference time $t = t_0$ (usually $t_0 = 0$), a fixed configuration is defined for which all material points P are referred to an initially known and typically undeformed configuration $\mathcal{B}_\mathrm{r} = \boldsymbol{\chi}_\mathrm{r}[\mathcal{B}]$:

$$\boldsymbol{\chi}_\mathrm{r} : \begin{cases} \mathcal{B} & \to & \mathcal{B}_\mathrm{r} \subset \mathbb{R}^3 \\ P & \mapsto & \boldsymbol{\chi}_\mathrm{r}(P) = (\Theta^1, \Theta^2, \Theta^3) \Leftrightarrow P = \boldsymbol{\chi}_\mathrm{r}^{-1}(\Theta^1, \Theta^2, \Theta^3). \end{cases} \tag{2.1}$$

$\mathcal{B}_\mathrm{r}$ refers to the (time-independent) reference configuration of the material body, indicated by the index '$_\mathrm{r}$', and $\Theta^A = (\Theta^1, \Theta^2, \Theta^3)$ are the curvilinear material coordinates of P which are associated with curved and non-orthogonal coordinate lines. For other moments of time $t > 0$, a family of configurations $\mathcal{B}_\mathrm{c} = \boldsymbol{\chi}_\mathrm{c}[\mathcal{B}, t]$ is defined and parametrized by time:

$$\boldsymbol{\chi}_\mathrm{c} : \begin{cases} \mathcal{B} \times \mathbb{R} & \to & \mathcal{B}_\mathrm{c} \subset \mathbb{R}^3 \\ (P, t) & \mapsto & \boldsymbol{\chi}_\mathrm{c}(P, t) = (\theta^1(t), \theta^2(t), \theta^3(t)) \Leftrightarrow P = \boldsymbol{\chi}_\mathrm{c}^{-1}(\theta^1(t), \theta^2(t), \theta^3(t)). \end{cases} \tag{2.2}$$

The time-dependent configuration $\mathcal{B}_\mathrm{c}$ refers to the current (or deformed) configuration of the material body, indicated by the index '$_\mathrm{c}$', and $\theta^a = (\theta^1, \theta^2, \theta^3)$ are the curvilinear spatial coordinates of P. According to Fig. 2.1, the time-dependent change of configurations can be understood as an undergoing motion of the material body. Its coordinate transformation from material to spatial description is archived by the composition of both mappings, i.e.,

$$\boldsymbol{\chi}_\mathrm{c} \circ \boldsymbol{\chi}_\mathrm{r}^{-1} : \begin{cases} \mathcal{B}_\mathrm{r} \times \mathbb{R} & \to & \mathcal{B}_\mathrm{c} \\ (\Theta^1, \Theta^2, \Theta^3, t) & \mapsto & \theta^a = \varphi(\Theta^B, t) = \boldsymbol{\chi}_\mathrm{c}(\boldsymbol{\chi}_\mathrm{r}^{-1}(\Theta^B), t). \end{cases} \tag{2.3}$$

Every configuration $\boldsymbol{\chi}_\mathrm{c}$ and consequently every composition $\boldsymbol{\chi}_\mathrm{c} \circ \boldsymbol{\chi}_\mathrm{r}^{-1}$ of the set $\mathcal{K}$ is required to be invertible and sufficiently differentiable, i.e., every configuration is understood as a smooth homeomorphism (one-to-one relation and invertible) onto a region of the three-dimensional space. Under these conditions, the material body $\mathcal{B}$ is a (three-dimensional) differentiable manifold. This mathematical concept was adopted from differential geometry and employed in the context of continuum mechanics, among others, by Noll [185].

2.2 Geometric structure of configurations

At this point, no statement is given about the geometric structure of configurations. To do so, it is necessary to impute geometric measures to each material point. In classical mechanics, the three-dimensional Euclidean space $\mathbb{E}^3$ is the common choice as a domain of physical observation for the material body. Consequently, the material body is embedded in the Euclidean structure such that the position of each material point $Q \in \mathbb{E}^3_\mathrm{r}$ with respect to the reference configuration

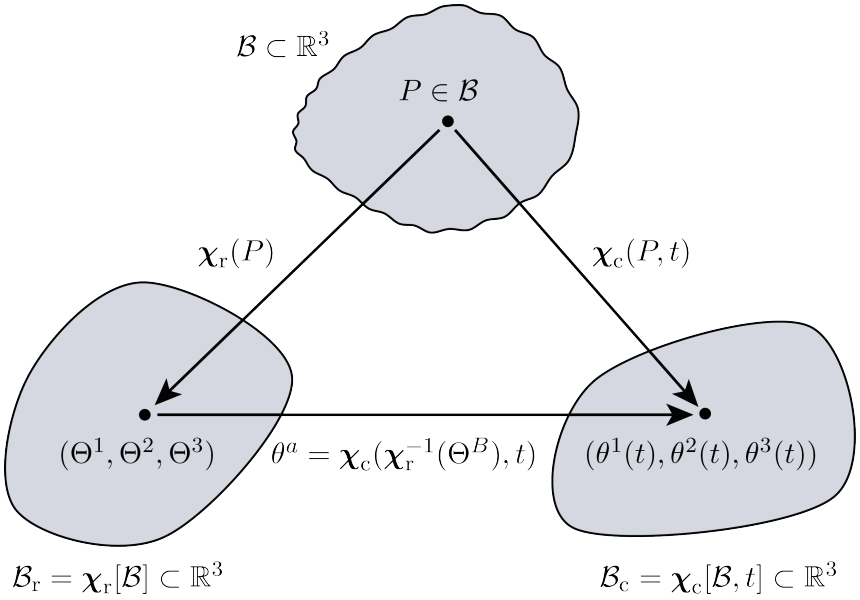

Figure 2.1: Reference and current configuration.

can be identified by Cartesian coordinates $X^A = (X^1, X^2, X^3)$ which are functions of the corresponding curvilinear coordinates, i.e.,

$$X^A = \hat{X}^A(\Theta^B) \Leftrightarrow \Theta^A = \hat{\Theta}^A(X^B). \tag{2.4}$$

Here, the Cartesian frame of reference[1] consists of three orthogonal unit vectors $\{\boldsymbol{E}_1, \boldsymbol{E}_2, \boldsymbol{E}_3\}$ which obey the relation $\boldsymbol{E}_A \cdot \boldsymbol{E}_B = \delta_{AB}$ ($\delta_{AB} = 1$ for $A = B$ and $\delta_{AB} = 0$ for $A \neq B$). Then the position in the three-dimensional Euclidean vector space $\mathbb{V}_\mathrm{r}^3$ is identified by the material position vector $\boldsymbol{X} \in \mathbb{V}_\mathrm{r}^3$. Its component representation is given as

$$\boldsymbol{X} = \hat{X}^A(\Theta^B)\boldsymbol{E}_A = X^A\boldsymbol{E}_A. \tag{2.5}$$

Accordingly, point $q \in \mathbb{E}_\mathrm{c}^3$ is identified by Cartesian coordinates $x^a = (x^1, x^2, x^3)$ for which

$$x^a = \hat{x}^a(\theta^b) \Leftrightarrow \theta^a = \hat{\theta}^a(x^b), \tag{2.6}$$

holds. The spatial position vector $\boldsymbol{x} \in \mathbb{V}_\mathrm{c}^3$ is written in terms of the orthonormal basis $\{\boldsymbol{e}_1, \boldsymbol{e}_2, \boldsymbol{e}_3\}$ with $\boldsymbol{e}_a \cdot \boldsymbol{e}_b = \delta_{ab}$ ($\delta_{ab} = 1$ for $a = b$ and $\delta_{ab} = 0$ for $a \neq b$) as

$$\boldsymbol{x} = \hat{x}^a(\theta^b)\boldsymbol{e}_a = x^a\boldsymbol{e}_a. \tag{2.7}$$

Likewise to the coordinate representation of the motion shown in Eq. (2.3), the motion can be described in terms of the position vectors. In this case, the deformation map φ transforms position vectors from the reference configuration to the current configuration as follows:

$$\varphi : \begin{cases} \mathbb{V}_\mathrm{r}^3 \times \mathbb{R} & \to & \mathbb{V}_\mathrm{c}^3 \\ (\boldsymbol{X}, t) & \mapsto & \boldsymbol{x} = \boldsymbol{\chi}_\mathrm{c}(\boldsymbol{\chi}_\mathrm{r}^{-1}(\boldsymbol{X}), t) = \varphi(\boldsymbol{X}, t) \Leftrightarrow \boldsymbol{X} = \varphi^{-1}(\boldsymbol{x}, t). \end{cases} \tag{2.8}$$

[1] If not otherwise stated, basis vectors denoted by capital letters are related to the reference configuration and, accordingly, basis vectors denoted by small letters are related to the current configuration.

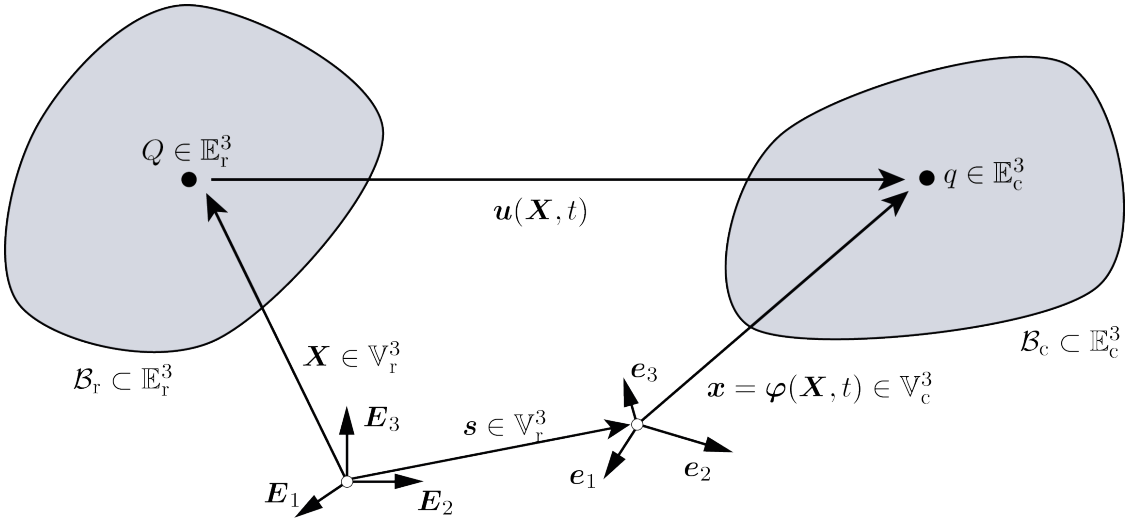

Figure 2.2: Illustration of motion.

At the reference time ($t = 0$), the identity $\varphi(\boldsymbol{X}) = \boldsymbol{X}$, $\forall \boldsymbol{X} \in \mathcal{B}_{\mathrm{r}}$ is obtained. In addition to this, the displacement vector $\boldsymbol{u} = \boldsymbol{x} + \boldsymbol{s} - \boldsymbol{X}$ is of great interest in solid mechanics as it describes the motion without scrutinizing its cause. In general, the vector $\boldsymbol{s}$ describes the position of the current coordinate system relative to the reference coordinate system, see Fig. 2.2. In most cases it is useful to choose $\boldsymbol{s} = \boldsymbol{0}$ and let both systems coincide, i.e., $\boldsymbol{E}_A = \boldsymbol{e}_a$. Based on the above defined relations between Cartesian and curvilinear coordinates, two reciprocal (or dual) base systems can be defined. The first base system consists of tangent vectors $\boldsymbol{G}_A$, locally defined along each coordinate line as

$$\boldsymbol{G}_A = \frac{\partial \boldsymbol{X}}{\partial \Theta^A} = \frac{\partial \hat{X}^B(\Theta^1, \Theta^2, \Theta^3)}{\partial \Theta^A} \boldsymbol{E}_B. \tag{2.9}$$

The three vectors $\{\boldsymbol{G}_1, \boldsymbol{G}_2, \boldsymbol{G}_3\}$ form the covariant basis with respect to the reference configuration. A second basis can be constructed in the way such that each of the new basis vectors $\boldsymbol{G}^A$ is orthogonal to two basis vectors of the covariant basis. This gives

$$\boldsymbol{G}^A = \nabla_{\mathrm{r}}(\Theta^A(\boldsymbol{X})) = \frac{\partial \hat{\Theta}^A(X^1, X^2, X^3)}{\partial X^B} \boldsymbol{E}_B, \tag{2.10}$$

cf. the geometrical illustration given in Fig. 2.3. In this case, each basis vector represents a gradient vector, lying normal to an infinitesimal area element formed by the respectively other two coordinate lines. Finally, the set $\{\boldsymbol{G}^1, \boldsymbol{G}^2, \boldsymbol{G}^3\}$ of new basis vectors form the contravariant basis. Since the co- and contravariant basis pairs are reciprocal to each another, it results that $\boldsymbol{G}_A \cdot \boldsymbol{G}^B = \delta_A^{\cdot B}$, with $\delta_A^{\cdot B} = 1$ for $A = B$ and $\delta_A^{\cdot B} = 0$ for $A \neq B$.

Analogically, the spatial tangent basis vectors $\boldsymbol{g}_a$ and spatial gradient basis vectors $\boldsymbol{g}^a$ define respectively the co- and contravariant basis in the current configuration, i.e.,

$$\boldsymbol{g}_a = \frac{\partial \boldsymbol{x}}{\partial \theta^a} = \frac{\partial \hat{x}^b(\theta^1, \theta^2, \theta^3)}{\partial \theta^a} \boldsymbol{e}_b, \quad \boldsymbol{g}^a = \nabla_{\mathrm{c}}(\theta^a(\boldsymbol{x})) = \frac{\partial \hat{\theta}^a(x^1, x^2, x^3)}{\partial x^b} \boldsymbol{e}_b, \tag{2.11}$$

with $\boldsymbol{g}_a \cdot \boldsymbol{g}^b = \delta_a^{\cdot b}$ ($\delta_a^{\cdot b} = 1$ for $a = b$ and $\delta_a^{\cdot b} = 0$ for $a \neq b$). It is noted that in contrast to Cartesian coordinate systems, curvilinear coordinate systems are defined locally and their orientation changes from point to point, hence, they are space-dependent.

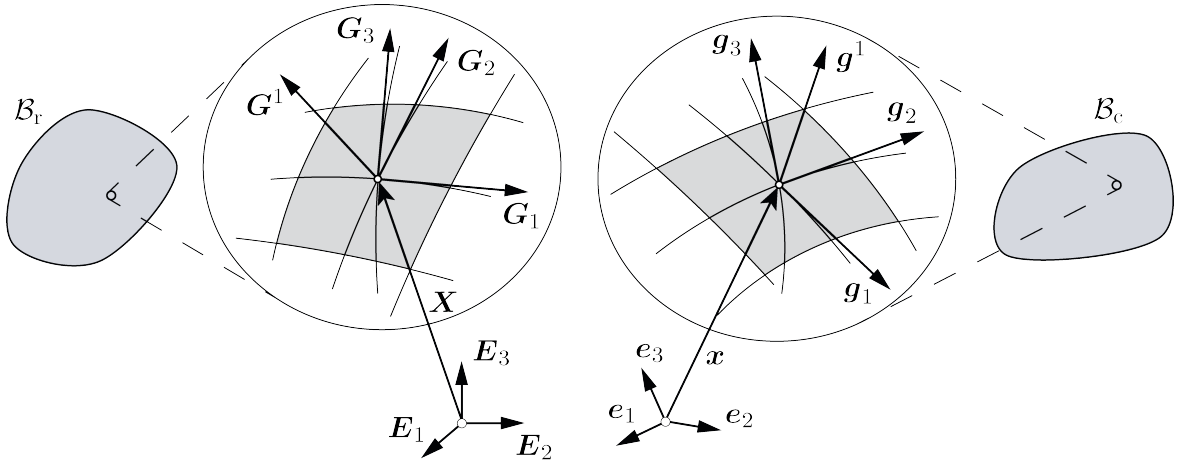

Figure 2.3: Reciprocal (or dual) basis vectors in $\mathbb{E}^3$.

2.3 Metric tensors

In context of locally defined coordinate systems, the metric coefficients play an substantial role in the representation of geometric measurements as they deliver information about lengths and angles. In the following, only so-called Riemannian metric tensors, i.e., symmetric and positive definite metric tensors, are under consideration.

Covariant and contravariant metric coefficients are defined in analogy to the basis vectors as

$$\begin{aligned} G_{AB} &= \boldsymbol{G}_A \cdot \boldsymbol{G}_B; \quad G^{AB} = [G_{AB}]^{-1} = \boldsymbol{G}^A \cdot \boldsymbol{G}^B; \\ g_{ab} &= \boldsymbol{g}_a \cdot \boldsymbol{g}_b; \qquad g^{ab} = [g_{ab}]^{-1} = \boldsymbol{g}^a \cdot \boldsymbol{g}^b, \end{aligned} \tag{2.12}$$

see, for instance, Ogden [188]. Without proof, Eq. (2.12) stats that the inverse of the matrix of covariant metric coefficients is identical to the matrix of contravariant metric coefficients. Furhtermore, metric coefficients allow to switch between tangent to the co-tangent space by means of raising or lowering of indices (index shifting). This yields the transformation relation between respective dual basis vectors (Green and Zerna [86]), i.e.,

$$\boldsymbol{G}_A = G_{AB}\boldsymbol{G}^B; \quad \boldsymbol{G}^A = G^{AB}\boldsymbol{G}_B; \quad \boldsymbol{g}_a = g_{ab}\boldsymbol{g}^b; \quad \boldsymbol{g}^a = g^{ab}\boldsymbol{g}_b. \tag{2.13}$$

Furthermore, the components of a vector must contra-vary with a change of basis to maintain the physical meaning (e.g. velocity). Same holds for a dual vectors (e.g. gradient) which must co-vary to be coordinate system invariant. Therefore, the components must vary in either case by the same transformation as the change of its basis. With $\boldsymbol{V} = V^A\boldsymbol{G}_A$ being the contravariant component representation and $\boldsymbol{V}_\# = V_A\boldsymbol{G}^A$ the covariant component representation, the corresponding transformation relations are defined as

$$V_A\boldsymbol{G}^A = V_A G^{AB}\boldsymbol{G}_B = V^B\boldsymbol{G}_B \tag{2.14}$$

and

$$V^A\boldsymbol{G}_A = V^A\left[G^{AB}\right]^{-1}\boldsymbol{G}^B = V^A G_{AB}\boldsymbol{G}^B = V_B\boldsymbol{G}^B, \tag{2.15}$$

respectively. Same transformation relations are defined with respect to the current configura-

tion, i.e.,

$$v_a \boldsymbol{g}^a = v_a g^{ab} \boldsymbol{g}_b = v^b \boldsymbol{g}_b \tag{2.16}$$

as well as

$$v^a \boldsymbol{g}_a = v^a \left[g^{ab} \right]^{-1} \boldsymbol{g}^b = v^a g_{ab} \boldsymbol{g}^b = v_b \boldsymbol{g}^b. \tag{2.17}$$

These lead to the following relationships, namely

$$V^B = V_A G^{AB}; \quad V_B = V^A G_{AB}; \quad v^b = v_a g^{ab}; \quad v_b = v^a g_{ab}. \tag{2.18}$$

By making use of the definition of metric tensors given as

$$\boldsymbol{G} = G_{AB} \boldsymbol{G}^A \otimes \boldsymbol{G}^B; \quad \boldsymbol{G}^{-1} = G^{AB} \boldsymbol{G}_A \otimes \boldsymbol{G}_B; \quad \boldsymbol{g} = g_{ab} \boldsymbol{g}^a \otimes \boldsymbol{g}^b; \quad \boldsymbol{g}^{-1} = g^{ab} \boldsymbol{g}_a \otimes \boldsymbol{g}_b, \tag{2.19}$$

Eq. (2.14)-2.18 can be rewritten in terms of an absolute representation. The corresponding mapping relations can be summarized as

$$\boldsymbol{G} : \begin{cases} \mathcal{TB}_\mathrm{r} & \rightarrow & \mathcal{TB}_\mathrm{r}^* \\ \boldsymbol{V} & \mapsto & \boldsymbol{V}_\# = \boldsymbol{G} \cdot \boldsymbol{V} \Leftrightarrow \boldsymbol{V} = \boldsymbol{G}^{-1} \cdot \boldsymbol{V}_\# \end{cases} \tag{2.20}$$

and

$$\boldsymbol{g} : \begin{cases} \mathcal{TB}_\mathrm{c} & \rightarrow & \mathcal{TB}_\mathrm{c}^* \\ \boldsymbol{v} & \mapsto & \boldsymbol{v}_\# = \boldsymbol{g} \cdot \boldsymbol{v} \Leftrightarrow \boldsymbol{v} = \boldsymbol{g}^{-1} \cdot \boldsymbol{v}_\#, \end{cases} \tag{2.21}$$

respectively. As already mentioned, the metric tensors act as a correspondence between the tangent and the cotangent space of the corresponding configuration. An illustrative interpretation of these vector spaces appears below in the context of the deformation gradient and in relation to associated stretch tensors.

2.4 Deformation gradient

Consider a material point with position vector $\boldsymbol{X}$ and any other material point nearby. Their distance to each other is quantified by a material line element or material tangent vector $\mathrm{d}\boldsymbol{X} \in \mathcal{TB}_\mathrm{r}(\boldsymbol{X})$. The totality of material line elements passing the point $\boldsymbol{X}$ form the tangent space $\mathcal{TB}_\mathrm{r}(\boldsymbol{X})$. After applied deformation, the same bundle of line elements pass through the considered material point but in the deformed configuration, i.e., through $\boldsymbol{x}$. Hence, the totality of spatial line elements $\mathrm{d}\boldsymbol{x} \in \mathcal{TB}_\mathrm{c}(\boldsymbol{x})$ form the tangent space $\mathcal{TB}_\mathrm{c}(\boldsymbol{x})$, see Fig. 2.4. The relation between these line elements is characterized by the deformation gradient tensor $\boldsymbol{F}$. Recalling that the deformation map given by Eq. (2.8) is continuously differentiable, the motion of the vector $\boldsymbol{X} + \mathrm{d}\boldsymbol{X}$ can be approximated by the Taylor expansion

$$\varphi(\boldsymbol{X} + \mathrm{d}\boldsymbol{X}, t) = \varphi(\boldsymbol{X}, t) + \nabla_\mathrm{r}(\varphi(\boldsymbol{X}, t)) \cdot \mathrm{d}\boldsymbol{X} + \boldsymbol{\mathcal{O}}(\boldsymbol{X}, \mathrm{d}\boldsymbol{X}, t), \tag{2.22}$$

where higher order terms $\boldsymbol{\mathcal{O}}(\boldsymbol{X}, \mathrm{d}\boldsymbol{X}, t) \approx \boldsymbol{0}$ can be neglected due to

$$\lim_{\mathrm{d}\boldsymbol{X} \rightarrow \boldsymbol{0}} \boldsymbol{\mathcal{O}}(\boldsymbol{X}, \mathrm{d}\boldsymbol{X}, t) = \boldsymbol{0}. \tag{2.23}$$

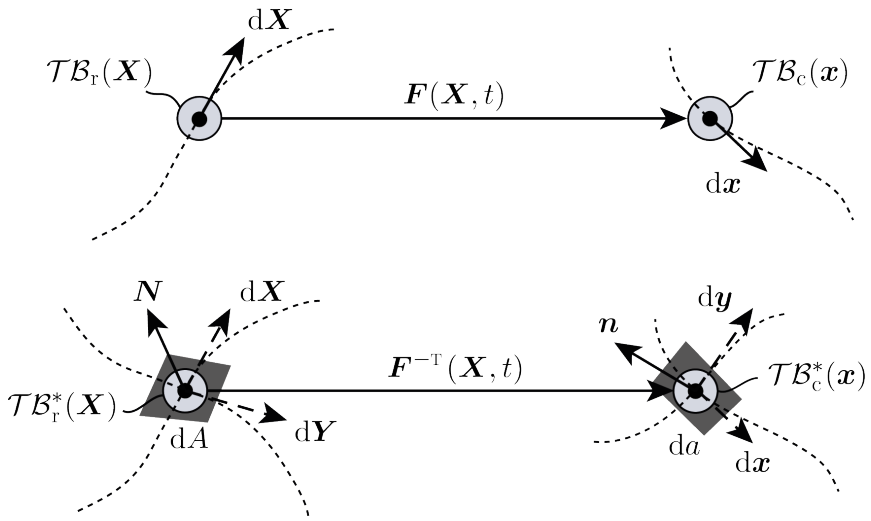

Figure 2.4: Deformation mapping of tangent and normal vectors.

From Eq. (2.22), the definition of the deformation gradient arises as

$$\boldsymbol{F} = \nabla_\mathrm{r}(\varphi(\boldsymbol{X},t)) = \frac{\partial \boldsymbol{x}}{\partial \boldsymbol{X}}. \tag{2.24}$$

Its inverse is accordingly defined as

$$\boldsymbol{F}^{-1} = \nabla_\mathrm{c}(\varphi^{-1}(\boldsymbol{x})) = \frac{\partial \boldsymbol{X}}{\partial \boldsymbol{x}}. \tag{2.25}$$

As is shown in the upper illustration of Fig. 2.4, the deformation gradient $\boldsymbol{F}$ characterizes the change in shape of infinitesimal line elements by mapping material tangent vectors $\mathrm{d}\boldsymbol{X}$ into spatial tangent vectors $\mathrm{d}\boldsymbol{x}$. This is expressed by the following linear transformation relation

$$\boldsymbol{F}: \begin{cases} \mathcal{TB}_\mathrm{r} & \rightarrow & \mathcal{TB}_\mathrm{c} \\ \mathrm{d}\boldsymbol{X} & \mapsto & \mathrm{d}\boldsymbol{x} = \boldsymbol{F}(\boldsymbol{X},t)\cdot\mathrm{d}\boldsymbol{X} \Leftrightarrow \mathrm{d}\boldsymbol{X} = \boldsymbol{F}^{-1}(\boldsymbol{x})\cdot\mathrm{d}\boldsymbol{x}. \end{cases} \tag{2.26}$$

Because $\boldsymbol{F}$ corresponds between reference and current configuration, the deformation gradient is referred to as two-point or two-state tensor. This is further evident from its component representation which is related to the mixed basis of tensors denoted as $\boldsymbol{g}_a \otimes \boldsymbol{G}^A$, i.e.,

$$\boldsymbol{F} = \frac{\partial \boldsymbol{x}}{\partial \boldsymbol{X}} = \frac{\partial \boldsymbol{x}}{\partial \Theta^A} \otimes \frac{\partial \Theta^A}{\partial \boldsymbol{X}} = \frac{\partial \boldsymbol{x}}{\partial \theta^a}\frac{\partial \theta^a}{\partial \Theta^A} \otimes \frac{\partial \Theta^A}{\partial \boldsymbol{X}} = \frac{\partial \theta^a}{\partial \Theta^A}\boldsymbol{g}_a \otimes \boldsymbol{G}^A = F^a_{\cdot A}\boldsymbol{g}_a \otimes \boldsymbol{G}^A. \tag{2.27}$$

Accordingly, the inverse $\boldsymbol{F}^{-1}$ is related to the mixed basis $\boldsymbol{G}_A \otimes \boldsymbol{g}^a$ which yields the following component representation

$$\boldsymbol{F}^{-1} = \frac{\partial \boldsymbol{X}}{\partial \boldsymbol{x}} = [F^{-1}]^A_{\cdot a}\boldsymbol{G}_A \otimes \boldsymbol{g}^a. \tag{2.28}$$

With the above definitions, the component representation of the mapping relations shown in Eq. (2.26) becomes

$$\mathrm{d}\boldsymbol{x} = F^a_{\cdot A}\mathrm{d}X^B[\boldsymbol{g}_a \otimes \boldsymbol{G}^A]\cdot\boldsymbol{G}_B = F^a_{\cdot B}\mathrm{d}X^B\boldsymbol{g}_a = \mathrm{d}x^a\boldsymbol{g}_a, \tag{2.29}$$

and

$$\mathrm{d}\boldsymbol{X} = [F^{-1}]^{A}_{.a}\mathrm{d}x^{b}[\boldsymbol{G}_A \otimes \boldsymbol{g}^{a}] \cdot \boldsymbol{g}_b = [F^{-1}]^{A}_{.b}\mathrm{d}x^{b}\boldsymbol{G}_A = \mathrm{d}X^{A}\boldsymbol{G}_A, \tag{2.30}$$

respectively. The existence of the inverse relation is guaranteed by the condition of a non-vanishing Jacobian determinant, i.e., $J = \det(\partial\theta^a/\partial\Theta^A) \neq 0$. Moreover $J > 0$ is required to ensure that positive volume remain positive during deformation. Provided that $\boldsymbol{F}$ is non-singular, the material and spatial identity tensors are obtained by the inner tensor product between $\boldsymbol{F}$ and its inverse. The material identity tensor is obtained as

$$\begin{aligned}\boldsymbol{I} = \boldsymbol{F}^{-1} \cdot \boldsymbol{F} &= [F^{-1}]^{A}_{.a}F^{b}_{.B}[\boldsymbol{G}_A \otimes \boldsymbol{g}^{a}] \cdot [\boldsymbol{g}_b \otimes \boldsymbol{G}^{B}] \\ &= [F^{-1}]^{A}_{.a}F^{b}_{.B}\delta^{a}_{.b}\boldsymbol{G}_A \otimes \boldsymbol{G}^{B} \\ &= \delta^{A}_{.B}\boldsymbol{G}_A \otimes \boldsymbol{G}^{B},\end{aligned} \tag{2.31}$$

whereas the inverse relation yields the spatial identity tensor, i.e.,

$$\begin{aligned}\boldsymbol{i} = \boldsymbol{F} \cdot \boldsymbol{F}^{-1} &= F^{a}_{.A}[F^{-1}]^{B}_{.b}[\boldsymbol{g}_a \otimes \boldsymbol{G}^{A}] \cdot [\boldsymbol{G}_B \otimes \boldsymbol{g}^{b}] \\ &= F^{a}_{.A}[F^{-1}]^{B}_{.b}\delta^{A}_{.B}\boldsymbol{g}_a \otimes \boldsymbol{g}^{b} \\ &= \delta^{a}_{.b}\boldsymbol{g}_a \otimes \boldsymbol{g}^{b}.\end{aligned} \tag{2.32}$$

In analogy to the transformation of infinitesimal line elements, the cofactor of the deformation gradient, $\mathrm{cof}(\boldsymbol{F}) = J\boldsymbol{F}^{-\mathrm{T}}$, acts as a linear transformation between infinitesimal area elements $\mathrm{d}\boldsymbol{a} = \boldsymbol{n}\ \mathrm{d}a$ and $\mathrm{d}\boldsymbol{A} = \boldsymbol{N}\ \mathrm{d}A$ in the following way

$$\boldsymbol{n}\mathrm{d}a = \mathrm{cof}(\boldsymbol{F}) \cdot \boldsymbol{N}\mathrm{d}A, \tag{2.33}$$

with $\boldsymbol{N}$ and $\boldsymbol{n}$ being normal vectors perpendicular to the corresponding area element. The transformation of areas via Eq. (2.33) is also known as Nanson's formula or as Piola transformation. It is of primary importance in the definition of stresses in terms of force per area as is shown later.

The transformation relation between the normal vectors is considered next. For that reason, the surface of a material body is introduced with respect to its different configurations as $\Phi_{\mathrm{r}}(\boldsymbol{X}) \in \partial\mathcal{B}_{\mathrm{r}}$ and $\Phi_{\mathrm{c}}(\boldsymbol{x}) \in \partial\mathcal{B}_{\mathrm{c}}$ respectively. By differentiating the identity $\Phi_{\mathrm{r}}(\boldsymbol{X}) = \Phi_{\mathrm{c}}(\varphi(\boldsymbol{X}, t))$ and in consideration of the chain rule follows

$$\nabla_{\mathrm{r}}(\Phi_{\mathrm{r}}(\boldsymbol{X})) = \frac{\mathrm{d}\Phi_{\mathrm{r}}(X^A)}{\mathrm{d}X^B}\boldsymbol{G}^B = \frac{\mathrm{d}\Phi_{\mathrm{c}}(x^a)}{\mathrm{d}x^b}\frac{\mathrm{d}x^b}{\mathrm{d}X^B}\boldsymbol{G}^B = \boldsymbol{F}^{\mathrm{T}} \cdot \nabla_{\mathrm{c}}(\Phi_{\mathrm{c}}(\boldsymbol{x})). \tag{2.34}$$

Both gradient vectors lie orthogonal to the corresponding surface plane, i.e., $\boldsymbol{N} = \nabla_{\mathrm{r}}(\Phi_{\mathrm{r}}(\boldsymbol{X}))$ and $\boldsymbol{n} = \nabla_{\mathrm{c}}(\Phi_{\mathrm{c}}(\boldsymbol{x}))$, whereas generally $\mid \boldsymbol{N} \mid \neq 1$ and $\mid \boldsymbol{n} \mid \neq 1$. Based on this, the mapping relation between the material normal vector $\boldsymbol{N} \in \mathcal{TB}^{*}_{\mathrm{r}}(\boldsymbol{X})$ and the spatial normal vector $\boldsymbol{n} \in \mathcal{TB}^{*}_{\mathrm{c}}(\boldsymbol{x})$ is given by the transpose of the inverse of the deformation gradient tensor, i.e.,

$$\boldsymbol{F}^{-\mathrm{T}} : \begin{cases}\mathcal{TB}^{*}_{\mathrm{r}} & \rightarrow & \mathcal{TB}^{*}_{\mathrm{c}} \\ \boldsymbol{N} & \mapsto & \boldsymbol{n} = \boldsymbol{F}^{-\mathrm{T}}(\boldsymbol{X}, t) \cdot \boldsymbol{N} \Leftrightarrow \boldsymbol{N} = \boldsymbol{F}^{\mathrm{T}}(\boldsymbol{x}) \cdot \boldsymbol{n},\end{cases} \tag{2.35}$$

cf. the lower illustration in Fig. 2.4. The cotangent space $\mathcal{TB}^{*}_{\mathrm{r}}(\boldsymbol{X}) = \mathcal{B}_{\mathrm{r}} \times \mathbb{R}^3$ and respectively $\mathcal{TB}^{*}_{\mathrm{c}}(\boldsymbol{x}) = \mathcal{B}_{\mathrm{c}} \times \mathbb{R}^3$ are dual vector spaces to $\mathcal{TB}_{\mathrm{r}}(\boldsymbol{X})$ and respectively $\mathcal{TB}_{\mathrm{c}}(\boldsymbol{x})$. Moreover, $\boldsymbol{F}^{-\mathrm{T}} = [\boldsymbol{F}^{\mathrm{T}}]^{-1} = [\boldsymbol{F}^{-1}]^{\mathrm{T}}$. The component representation of the transpose of $\boldsymbol{F}$ and the

transpose of $\boldsymbol{F}^{-1}$ read

$$\begin{aligned}\boldsymbol{F}^{\mathrm{T}} &= [F^{\mathrm{T}}]^{A}_{.a}[\boldsymbol{G}_A \otimes \boldsymbol{g}^a] \\ &= G^{AB}F^{b}_{.B}g_{ba}[\boldsymbol{G}_A \otimes \boldsymbol{g}^a]\end{aligned} \tag{2.36}$$

and

$$\begin{aligned}\boldsymbol{F}^{-\mathrm{T}} &= [F^{-\mathrm{T}}]^{a}_{.A}[\boldsymbol{g}_a \otimes \boldsymbol{G}^A] \\ &= g^{ab}F^{B}_{.b}G_{BA}[\boldsymbol{g}_a \otimes \boldsymbol{G}^A],\end{aligned} \tag{2.37}$$

respectively, see also Clayton [54] and Dorfmann and Ogden [68]. With that, the component representation of the regular and inverse mapping relation given by Eq. (2.35) becomes

$$\boldsymbol{n} = [F^{-\mathrm{T}}]^{a}_{.A}N_B[\boldsymbol{g}_a \otimes \boldsymbol{G}^A] \cdot \boldsymbol{G}^B = g^{ab}[F^{-1}]^{C}_{.b}G_{CA}N_BG^{AB}\boldsymbol{g}_a = [F^{-1}]^{C}_{.b}N_C\boldsymbol{g}^b = n_b\boldsymbol{g}^b \tag{2.38}$$

and

$$\boldsymbol{N} = [F^{\mathrm{T}}]^{A}_{.a}n_b[\boldsymbol{G}_A \otimes \boldsymbol{g}^a] \cdot \boldsymbol{g}^b = G^{AB}F^{c}_{.B}g_{ca}n_bg^{ab}\boldsymbol{G}_A = F^{c}_{.B}n_c\boldsymbol{G}^B = N_B\boldsymbol{G}^B, \tag{2.39}$$

respectively. Finally, by considering the line elements $\{\mathrm{d}\boldsymbol{X}, \mathrm{d}\boldsymbol{Y}, \mathrm{d}\boldsymbol{Z}\}$ and $\{\mathrm{d}\boldsymbol{x}, \mathrm{d}\boldsymbol{y}, \mathrm{d}\boldsymbol{z}\}$, the resulting triple products $\mathrm{d}V = [\mathrm{d}\boldsymbol{X} \times \mathrm{d}\boldsymbol{Y}] \cdot \mathrm{d}\boldsymbol{Z} = \mathrm{d}\boldsymbol{A} \cdot \mathrm{d}\boldsymbol{Z}$ and $\mathrm{d}v = [\mathrm{d}\boldsymbol{x} \times \mathrm{d}\boldsymbol{y}] \cdot \mathrm{d}\boldsymbol{z} = \mathrm{d}\boldsymbol{a} \cdot \mathrm{d}\boldsymbol{z}$ form a material volume element in the reference and current configuration, respectively where two line elements respectively form an area element. With the transformation relation for line elements via Eq. (2.26) and for area elements via Eq. (2.33), it follows that

$$\mathrm{d}v = [\boldsymbol{F} \cdot \mathrm{d}\boldsymbol{X} \times \boldsymbol{F} \cdot \mathrm{d}\boldsymbol{Y}] \cdot \boldsymbol{F} \cdot \mathrm{d}\boldsymbol{Z} = J\,[\mathrm{d}\boldsymbol{X} \times \mathrm{d}\boldsymbol{Y}] \cdot \mathrm{d}\boldsymbol{Z} = J\mathrm{d}V. \tag{2.40}$$

Similar to the mapping of line elements via $\boldsymbol{F}$ and the mapping of area elements via $\mathrm{cof}(\boldsymbol{F})$, the Jacobian J maps volume elements from the reference configuration into the current configuration. The Jacobian determinant is further given as $J = \sqrt{\det(g_{ab})/\det(G_{AB})}\det(F^{a}_{.A})$. Hence, $\det(\boldsymbol{F}) > 0$ is required to ensure $J > 0$.

2.5 Measures of deformation and strain

The deformation gradient contains information about the local rotation and shape change of a material point with respect to the infinitesimal neighborhood of $\boldsymbol{X}$. The latter is associated with the actual deformation in terms of stretching and shearing. If $J > 0$, then the deformation gradient can be (uniquely) decomposed as

$$\boldsymbol{F} = \boldsymbol{R} \cdot \boldsymbol{U} = \boldsymbol{V} \cdot \boldsymbol{R}. \tag{2.41}$$

In this, $\boldsymbol{U}$ and $\boldsymbol{V}$ are symmetric and positive definite material and spatial stretch tensors whereas $\boldsymbol{R}$ represents a two-point, orthogonal rotation tensor obeying $\boldsymbol{R}^{\mathrm{T}} \cdot \boldsymbol{R} = \boldsymbol{I}$. The component representation of Eq. (2.41) reads

$$\begin{aligned}F^{a}_{.C}[\boldsymbol{g}_a \otimes \boldsymbol{G}^C] &= R^{a}_{.A}U^{B}_{.C}[\boldsymbol{g}_a \otimes \boldsymbol{G}^A] \cdot [\boldsymbol{G}_B \otimes \boldsymbol{G}^C] \\ &= R^{a}_{.B}U^{B}_{.C}[\boldsymbol{g}_a \otimes \boldsymbol{G}^C] \\ &= V^{a}_{.b}R^{c}_{.C}[\boldsymbol{g}_a \otimes \boldsymbol{g}^b] \cdot [\boldsymbol{g}_c \otimes \boldsymbol{G}^C] \\ &= V^{a}_{.c}R^{c}_{.C}[\boldsymbol{g}_a \otimes \boldsymbol{G}^C].\end{aligned} \tag{2.42}$$

The first relation in Eq. (2.41) defines the right polar decomposition whereas the second relation defines the left polar decomposition. Since the deformation gradient contains contributions from rigid body rotations, $\boldsymbol{F}$ cannot be used as a meaningful strain measure. In fact, strain measures are always based on either $\boldsymbol{U}$ or $\boldsymbol{V}$ as these tensors are completely free of rotation. This is evident from their definition

$$\boldsymbol{U} = \sqrt{\boldsymbol{F}^{\mathrm{T}} \cdot \boldsymbol{F}} = \sqrt{\boldsymbol{U}^{\mathrm{T}} \cdot \boldsymbol{R}^{\mathrm{T}} \cdot \boldsymbol{R} \cdot \boldsymbol{U}} = \sqrt{\boldsymbol{U} \cdot \boldsymbol{U}} \tag{2.43}$$

and

$$\boldsymbol{V} = \sqrt{\boldsymbol{F} \cdot \boldsymbol{F}^{\mathrm{T}}} = \sqrt{\boldsymbol{V} \cdot \boldsymbol{R} \cdot \boldsymbol{R}^{\mathrm{T}} \cdot \boldsymbol{V}^{\mathrm{T}}} = \sqrt{\boldsymbol{V} \cdot \boldsymbol{V}}. \tag{2.44}$$

The right Cauchy-Green stretch tensor $\boldsymbol{C}$ and the left Cauchy-Green stretch tensor $\boldsymbol{b}$ are defined in consideration of theses tensors as

$$\boldsymbol{C} = \boldsymbol{U}^2 = \boldsymbol{F}^{\mathrm{T}} \cdot \boldsymbol{F}, \tag{2.45}$$

and

$$\boldsymbol{b} = \boldsymbol{V}^2 = \boldsymbol{F} \cdot \boldsymbol{F}^{\mathrm{T}}, \tag{2.46}$$

respectively. Their component representations are

$$\begin{aligned} \boldsymbol{C} &= [F^{\mathrm{T}}]^{A}_{.a} F^{b}_{.B} [\boldsymbol{G}_A \otimes \boldsymbol{g}^a] \cdot [\boldsymbol{g}_b \otimes \boldsymbol{G}^B] \\ &= G^{AC} F^{c}_{.C} g_{ca} F^{b}_{.B} \delta^{a}_{.b} \boldsymbol{G}_A \otimes \boldsymbol{G}^B \\ &= F^{c}_{.C} g_{cb} F^{b}_{.B} \boldsymbol{G}^C \otimes \boldsymbol{G}^B \\ &= C_{CB} \boldsymbol{G}^C \otimes \boldsymbol{G}^B \end{aligned} \tag{2.47}$$

and

$$\begin{aligned} \boldsymbol{b} &= F^{a}_{.A} [F^{\mathrm{T}}]^{B}_{.b} [\boldsymbol{g}_a \otimes \boldsymbol{G}^A] \cdot [\boldsymbol{G}_B \otimes \boldsymbol{g}^b] \\ &= F^{a}_{.A} G^{BC} F^{c}_{C} g_{cb} \delta^{A}_{.B} \boldsymbol{g}_a \otimes \boldsymbol{g}^b \\ &= F^{a}_{.A} G^{AC} F^{c}_{.C} \boldsymbol{g}_a \otimes \boldsymbol{g}_c \\ &= b^{ac} \boldsymbol{g}_a \otimes \boldsymbol{g}_c, \end{aligned} \tag{2.48}$$

respectively, see, for instance Clayton [54]. In the literature, equivalent definitions[2] for $\boldsymbol{C}$ and $\boldsymbol{b}$ are often given in the form $\boldsymbol{C} = \boldsymbol{F}^{\mathrm{T}} \cdot \boldsymbol{g} \cdot \boldsymbol{F}$ and $\boldsymbol{b} = \boldsymbol{F} \cdot \boldsymbol{G}^{-1} \cdot \boldsymbol{F}^{\mathrm{T}}$. This format indicates the commutative nature of these tensors as illustrated in Fig. 2.5. As can be seen, $\boldsymbol{C}$ establishes a correspondence between tangent to the cotangent space while $\boldsymbol{b}$ act in the inverse way, i.e., $\boldsymbol{C} : \mathcal{TB}_{\mathrm{r}} \rightarrow \mathcal{TB}^{*}_{\mathrm{r}}$ and $\boldsymbol{b} : \mathcal{TB}^{*}_{\mathrm{c}} \rightarrow \mathcal{TB}_{\mathrm{c}}$. Moreover, $\boldsymbol{C}$ can be interpreted as the pull-back of the spatial metric tensor $\boldsymbol{g}$ whereas the inverse left Cauchy-Green tensor (or finger deformation tensor) $\boldsymbol{b}^{-1} : \mathcal{TB}_{\mathrm{c}} \rightarrow \mathcal{TB}^{*}_{\mathrm{c}}$ can be interpreted as the push-forward of the material metric tensor $\boldsymbol{G}$. For furhter details, see, e.g., Epstein [73].

Both tensors, $\boldsymbol{C}$ and $\boldsymbol{b}^{-1}$, define in consideration of the corresponding metric how lengths of line elements and angles between line elements change with respect to the configuration they are defined in. This is reflected in the following calculation of deformed and undeformed

[2] E.g., the expression $\boldsymbol{F}^{\mathrm{T}} \cdot \boldsymbol{g} \cdot \boldsymbol{F} = [F^{\mathrm{T}}]^{A}_{.a} g_{bc} F^{d}_{.B} [\boldsymbol{G}_A \otimes \boldsymbol{g}^a] \cdot [\boldsymbol{g}^b \otimes \boldsymbol{g}^c] \cdot [\boldsymbol{g}_d \otimes \boldsymbol{G}^B]$ $= G^{AC} F^{e}_{.C} g_{ea} g_{bc} F^{d}_{.B} g^{ab} \delta^{c}_{.d} [\boldsymbol{G}_A \otimes \boldsymbol{G}^B] = F^{e}_{.C} g_{ed} F^{d}_{.B} [\boldsymbol{G}^C \otimes \boldsymbol{G}^B]$ is equivalent to the one given by Eq. (2.47). Same can be shown for Eq. (2.48) considering the expression $\boldsymbol{b} = \boldsymbol{F} \cdot \boldsymbol{G}^{-1} \cdot \boldsymbol{F}^{\mathrm{T}}$.

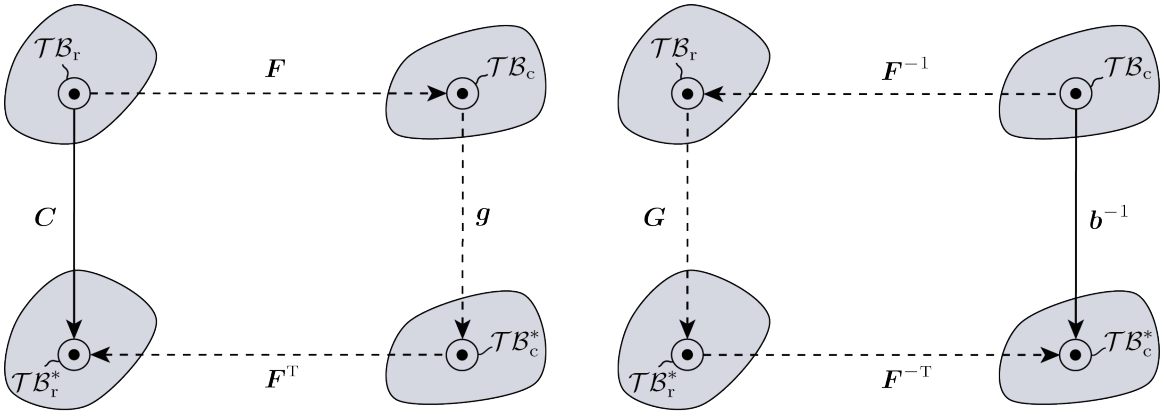

Figure 2.5: Commutative diagrams of stretch tensors. The right Cauchy-Green tensor $\boldsymbol{C}$ can be interpreted as the pull-back of the spatial metric tensor $\boldsymbol{g}$ whereas the inverse left Cauchy-Green $\boldsymbol{b}^{-1}$ can be interpreted as the push-forward of the material metric tensor $\boldsymbol{G}$. In both diagrams, the actual geometrical mapping (bold line) can be obtained in terms of a composition of commutative mappings (dashed lines).

squared lengths, i.e.,

$$\begin{aligned} |\,\mathrm{d}\boldsymbol{x}\,|^2 &= \mathrm{d}\boldsymbol{x}\cdot\mathrm{d}\boldsymbol{x} = \mathrm{d}\boldsymbol{X}\cdot\boldsymbol{F}^\mathrm{T}\cdot\boldsymbol{F}\cdot\mathrm{d}\boldsymbol{X} = \mathrm{d}\boldsymbol{X}\cdot\boldsymbol{C}\cdot\mathrm{d}\boldsymbol{X},\\ |\,\mathrm{d}\boldsymbol{X}\,|^2 &= \mathrm{d}\boldsymbol{X}\cdot\mathrm{d}\boldsymbol{X} = \mathrm{d}\boldsymbol{x}\cdot\boldsymbol{F}^{-\mathrm{T}}\cdot\boldsymbol{F}^{-1}\cdot\mathrm{d}\boldsymbol{x} = \mathrm{d}\boldsymbol{x}\cdot\boldsymbol{b}^{-1}\cdot\mathrm{d}\boldsymbol{x}. \end{aligned} \tag{2.49}$$

Although $\boldsymbol{C}$ and $\boldsymbol{b}^{-1}$ represent objective measures they are not qualified to be used as strain measures. Strain measures are required to vanish not only for any pure rigid body motion but also for any undeformed configuration including the initial undeformed state of the body. Therefore, absolute strain measures are introduced based on the difference in the squared lengths of deformed and undeformed line elements. This leads to

$$|\,\mathrm{d}\boldsymbol{x}\,|^2 - |\,\mathrm{d}\boldsymbol{X}\,|^2 = \mathrm{d}\boldsymbol{X}\cdot\boldsymbol{C}\cdot\mathrm{d}\boldsymbol{X} - \mathrm{d}\boldsymbol{X}\cdot\mathrm{d}\boldsymbol{X} = \mathrm{d}\boldsymbol{X}\cdot[\boldsymbol{C}-\boldsymbol{G}]\cdot\mathrm{d}\boldsymbol{X} = \mathrm{d}\boldsymbol{X}\cdot 2\boldsymbol{E}\cdot\mathrm{d}\boldsymbol{X}, \tag{2.50}$$

where

$$\boldsymbol{E} = \frac{1}{2}[\boldsymbol{C}-\boldsymbol{G}] \tag{2.51}$$

represents the Green-Lagrange strain tensor, a material strain measure. The above relation becomes more clear in the component representation

$$\begin{aligned} |\,\mathrm{d}\boldsymbol{x}\,|^2 - |\,\mathrm{d}\boldsymbol{X}\,|^2 &= \mathrm{d}x^a\mathrm{d}x^b\boldsymbol{g}_a\cdot\boldsymbol{g}_b - \mathrm{d}X^A\mathrm{d}X^B\boldsymbol{G}_A\cdot\boldsymbol{G}_B\\ &= F^a_{\cdot A}\mathrm{d}X^A F^b_{\cdot B}\mathrm{d}X^B g_{ab} - \mathrm{d}X^A\mathrm{d}X^B G_{AB}\\ &= \mathrm{d}X^A[F^a_{\cdot A}g_{ab}F^b_{\cdot B} - G_{AB}]\mathrm{d}X^B\\ &= \mathrm{d}X^A[C_{AB} - G_{AB}]\mathrm{d}X^B\\ &= \mathrm{d}X^A 2E_{AB}\mathrm{d}X^B, \end{aligned} \tag{2.52}$$

from which follows that

$$\boldsymbol{E} = \frac{1}{2}\left[C_{AB} - G_{AB}\right]\boldsymbol{G}^A\otimes\boldsymbol{G}^B = \frac{1}{2}\left[F^a_{\cdot A}g_{ab}F^b_{\cdot B} - G_{AB}\right]\boldsymbol{G}^A\otimes\boldsymbol{G}^B. \tag{2.53}$$

An equivalent strain measure in the current configuration results from the same measurement but related to the deformed configuration, i.e.,

$$| \mathrm{d}\boldsymbol{x} |^2 - | \mathrm{d}\boldsymbol{X} |^2 = \mathrm{d}\boldsymbol{x} \cdot \mathrm{d}\boldsymbol{x} - \mathrm{d}\boldsymbol{x} \cdot \boldsymbol{b}^{-1} \cdot \mathrm{d}\boldsymbol{x} = \mathrm{d}\boldsymbol{x} \cdot [\boldsymbol{g} - \boldsymbol{b}^{-1}] \cdot \mathrm{d}\boldsymbol{x} = \mathrm{d}\boldsymbol{x} \cdot 2\boldsymbol{e} \cdot \mathrm{d}\boldsymbol{x}, \tag{2.54}$$

which gives rise to introduce the Almansi strain tensor as

$$\boldsymbol{e} = \frac{1}{2} \left[\boldsymbol{g} - \boldsymbol{b}^{-1} \right]. \tag{2.55}$$

In analogy to the previous case, the component representation can be written as

$$\begin{aligned} | \mathrm{d}\boldsymbol{x} |^2 - | \mathrm{d}\boldsymbol{X} |^2 &= \mathrm{d}x^a \mathrm{d}x^b \boldsymbol{g}_a \cdot \boldsymbol{g}_b - \mathrm{d}X^A \mathrm{d}X^B \boldsymbol{G}_A \cdot \boldsymbol{G}_B \\ &= \mathrm{d}x^a \mathrm{d}x^b g_{ab} - [F^{-1}]^A_{.a} \mathrm{d}x^a [F^{-1}]^B_{.b} \mathrm{d}x^b G_{AB} \\ &= \mathrm{d}x^a \left[g_{ab} - [F^{-1}]^A_{.a} G_{AB} [F^{-1}]^B_{.b} \right] \mathrm{d}x^b \\ &= \mathrm{d}x^a 2 e_{ab} \mathrm{d}x^b, \end{aligned} \tag{2.56}$$

from which follows that

$$\boldsymbol{e} = \frac{1}{2} \left[g_{ab} - [b^{-1}]_{ab} \right] \boldsymbol{g}^a \otimes \boldsymbol{g}^b = \frac{1}{2} \left[g_{ab} - [F^{-1}]^A_{.a} G_{AB} [F^{-1}]^B_{.b} \right] \boldsymbol{g}^a \otimes \boldsymbol{g}^b. \tag{2.57}$$

As a result of the definitions shown in Eqs. (2.53) and (2.57), it can be seen that the introduced strain tensors are measuring the strain in terms of the difference between two metric tensors. Hence, strain can be understood as the time-dependent change of one metric with respect another metric where either the pull-back of the spatial metric or respectively the push-forward of the material metric is involved. In the end, both strain tensors are related to each other via

$$\boldsymbol{E} = \boldsymbol{F}^{\mathrm{T}} \cdot \boldsymbol{e} \cdot \boldsymbol{F}, \quad \boldsymbol{e} = \boldsymbol{F}^{-\mathrm{T}} \cdot \boldsymbol{E} \cdot \boldsymbol{F}^{-1}. \tag{2.58}$$

2.6 Measures of stress

During motion $\varphi(\boldsymbol{X}, t)$, let $\mathcal{B}_\mathrm{c}$ be subjected to loading conditions which may be described in terms of externally applied surface forces (per unit area) and/or body forces (per unit mass). In response to these loads, the body experiences reaction forces or surface tractions $\boldsymbol{t}(\boldsymbol{x}, t, \boldsymbol{n}) \in \mathcal{TB}_\mathrm{c}$ whose surface element orientation is indicated by the spatial normal vector $\boldsymbol{n} \in \mathcal{TB}^*_\mathrm{c}$. According to Cauchy's stress theorem, there exists an integrable field of traction vectors $\boldsymbol{t}$ upon any smooth, closed, orientable surface which is either the bounding surface $\partial\mathcal{B}_\mathrm{c}$ of the body itself or any (imagined) bounding surface $\partial\Omega_\mathrm{c}$ of a subbody (part) $\Omega_\mathrm{c} \in \mathcal{B}_\mathrm{c}$ (Truesdell [244]). Then $\boldsymbol{t}$ is a linear function of the normal vector $\boldsymbol{n}$ such that there is a tensor $\boldsymbol{\sigma}$ - the Cauchy (true) stress tensor - which describes the transformation

$$\boldsymbol{\sigma} : \begin{cases} \mathcal{TB}^*_\mathrm{c} & \to \quad \mathcal{TB}_\mathrm{c} \\ \boldsymbol{n} & \mapsto \quad \boldsymbol{t} = \boldsymbol{\sigma}(\boldsymbol{x}, t) \cdot \boldsymbol{n}, \end{cases} \tag{2.59}$$

cf. the illustration in Fig. 2.6. With that, the differential force acting on the area element $\mathrm{d}a$ can be written as $\mathrm{d}\boldsymbol{f} = \boldsymbol{t}(\boldsymbol{n})\mathrm{d}a = \boldsymbol{\sigma} \cdot \boldsymbol{n}\mathrm{d}a = \boldsymbol{\sigma} \cdot \mathrm{d}\boldsymbol{a}$. Furthermore, $\boldsymbol{\sigma}$ conserves the balance of linear momentum as well as the balance of angular momentum. The latter results in the property $\boldsymbol{\sigma} = \boldsymbol{\sigma}^{\mathrm{T}}$, i.e., $\boldsymbol{\sigma}$ is symmetric. For a detailed and comprehensive treatment of balance laws see, for instance, Chadwick [44].

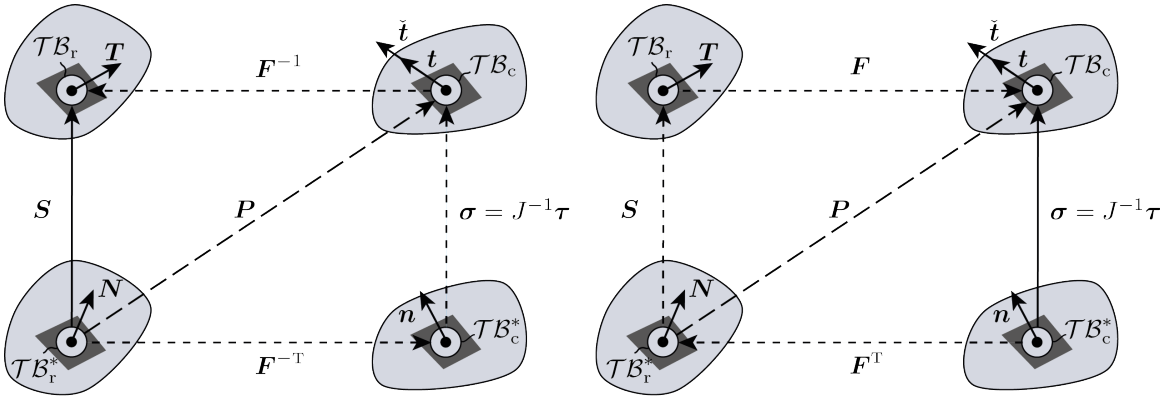

Figure 2.6: Commutative diagrams of stress tensors. The graphical illustration indicates pull-back and push-forward relations between material $\boldsymbol{S}$, spatial $\boldsymbol{\sigma}$, and mixed $\boldsymbol{P}$ stress tensors. In both diagrams, the actual geometrical mapping (bold line) can be obtained in terms of a composition of commutative mappings (dashed lines).

By referring the force, which is obviously a physical process in the current configuration, to a material surface element, gives rise to define an alternative stress tensor. Recalling Nanson's formula from Eq. (2.33), the differential surface force per unit material area can be rewritten as $\mathrm{d}\boldsymbol{f} = \boldsymbol{\sigma} \cdot \boldsymbol{n}\mathrm{d}a = \boldsymbol{P} \cdot \boldsymbol{N}\mathrm{d}A = \check{\boldsymbol{t}}(\boldsymbol{N})\mathrm{d}A$, where $\boldsymbol{N} \in \mathcal{TB}^*_\mathrm{r}$ is the normal vector with respect to the reference configuration, $\check{\boldsymbol{t}} \in \mathcal{TB}_\mathrm{c}$ is a modified (spatial) surface traction vector, and $\boldsymbol{P}$ is the first Piola-Kirchhoff stress tensor. As a result, $\boldsymbol{P}$ is a two-point tensor which can be related to the Cauchy stress via

$$\boldsymbol{P} = J\boldsymbol{\sigma} \cdot \boldsymbol{F}^{-\mathrm{T}} = \boldsymbol{\tau} \cdot \boldsymbol{F}^{-\mathrm{T}}, \tag{2.60}$$

where $\boldsymbol{\tau} = J\boldsymbol{\sigma}$ denotes the weighed Cauchy stress tensor or the Kirchhoff stress tensor. In addition, $\boldsymbol{P} \cdot \boldsymbol{F}^{\mathrm{T}} = \boldsymbol{F} \cdot \boldsymbol{P}^{\mathrm{T}}$ follows from the balance of angular momentum, i.e., $\boldsymbol{P} \neq \boldsymbol{P}^{\mathrm{T}}$ holds in general. In analogy to Eq. (2.59), $\boldsymbol{P}$ describes the following transformation

$$\boldsymbol{P} : \begin{cases} \mathcal{TB}^*_\mathrm{r} & \rightarrow & \mathcal{TB}_\mathrm{c} \\ \boldsymbol{N} & \mapsto & \check{\boldsymbol{t}} = \boldsymbol{P}(\boldsymbol{X}, t) \cdot \boldsymbol{N}. \end{cases} \tag{2.61}$$

A pure material stress measure is obtained from the pull-back of the Kirchhoff stresses $\boldsymbol{\tau}$ or, equivalently, of $\boldsymbol{P}$, yielding the definition of the second Piola-Kirchhoff stress tensor

$$\boldsymbol{S} = \boldsymbol{F}^{-1} \cdot \boldsymbol{\tau} \cdot \boldsymbol{F}^{-\mathrm{T}} = \boldsymbol{F}^{-1} \cdot \boldsymbol{P}, \tag{2.62}$$

where $\boldsymbol{S} = \boldsymbol{S}^{\mathrm{T}}$. see also Fig. 2.6 for a graphical interpretation of pull-back and push-forward relations between the introduced stress tensors. With respect to the reference configuration, the following mapping relation can be established

$$\boldsymbol{S} : \begin{cases} \mathcal{TB}^*_\mathrm{r} & \rightarrow & \mathcal{TB}_\mathrm{r} \\ \boldsymbol{N} & \mapsto & \boldsymbol{T} = \boldsymbol{S}(\boldsymbol{X}, t) \cdot \boldsymbol{N}. \end{cases} \tag{2.63}$$

This leads finally to $\mathrm{d}\boldsymbol{f} = \boldsymbol{P} \cdot \boldsymbol{N}\mathrm{d}A = \boldsymbol{F} \cdot \boldsymbol{S} \cdot \boldsymbol{N}\mathrm{d}A = \boldsymbol{F} \cdot \boldsymbol{T}(\boldsymbol{N})\mathrm{d}A$, where $\boldsymbol{T} \in \mathcal{TB}_\mathrm{r}$ is the material surface traction. In contrast to the previous quantities, $\boldsymbol{T}$ and $\boldsymbol{S}$ are rather fictitious as they do not bear any physical meaning.

2.7 Elasto-plastic decomposition of deformation

The idea of the multiplicative decomposition of the deformation gradient $\boldsymbol{F}$ has its origin in the works of Bilby et al. [32] and Kröner and Seeger [145], and was formulated in the way

$$\boldsymbol{F} = \boldsymbol{F}_{\mathrm{E}} \cdot \boldsymbol{F}_{\mathrm{P}}, \tag{2.64}$$

where $\boldsymbol{F}_{\mathrm{E}}$ is the elastic and $\boldsymbol{F}_{\mathrm{P}}$ the plastic part of the total deformation gradient, cf. also Kröner [142], Lee and Liu [155], and Lee [154]. In fact, the decomposition in the given form has a physical motivation as the deformation of crystals can be idealized in terms of pure plastic deformation associated with dislocation slip, superimposed by pure elastic lattice distortion (stretch and rotation) as is illustrated in Fig. 2.7.

In order to describe plastic deformation in terms of crystallographic slip, the material body is assigned with a crystal lattice which is described (with respect to the reference configuration) in terms of slip direction $\boldsymbol{S}_\alpha$, slip plane normal $\boldsymbol{N}_\alpha$, and transverse slip direction $\boldsymbol{T}_\alpha = \boldsymbol{N}_\alpha \times \boldsymbol{S}_\alpha$. Furthermore, plastic deformation is assumed to be lattice-preserving, i.e., lattice invariant (Bilby et al. [32]), such that material and intermediate lattice directions coincide[3], i.e.,

$$\boldsymbol{s}_\alpha = \boldsymbol{S}_\alpha, \quad \boldsymbol{t}_\alpha = \boldsymbol{T}_\alpha, \quad \boldsymbol{n}_\alpha = \boldsymbol{N}_\alpha. \tag{2.65}$$

From a differential-geometric point of view, the decomposition implies a conceptual relaxation of the material body in a stress-free intermediate[4] configuration $\mathcal{B}_{\mathrm{i}}$ which, in general, is only locally coherent, i.e. simply connected or holonomic (Kondo [139], Clayton et al. [55]). Hence, fictive unloading of a body with a heterogeneous internal stress field distribution leads to an incompatible or anholonomic configuration, cf. for instance Clayton et al. [55]. As a result, neither of the following tangent mappings is generally a continuous one-to-one mapping, i.e., nor the mapping from the reference into the intermediate configuration

$$\boldsymbol{F}_{\mathrm{P}} : \begin{cases} \mathcal{T}\mathcal{B}_{\mathrm{r}} & \rightarrow \quad \mathcal{T}\mathcal{B}_{\mathrm{i}} \\ \mathrm{d}\boldsymbol{X} & \mapsto \quad \mathrm{d}\overline{\boldsymbol{X}} = \boldsymbol{F}_{\mathrm{P}}(\boldsymbol{X}, t) \cdot \mathrm{d}\boldsymbol{X} \Leftrightarrow \mathrm{d}\boldsymbol{X} = \boldsymbol{F}_{\mathrm{P}}^{-1}(\overline{\boldsymbol{X}}) \cdot \mathrm{d}\overline{\boldsymbol{X}} \end{cases} \tag{2.66}$$

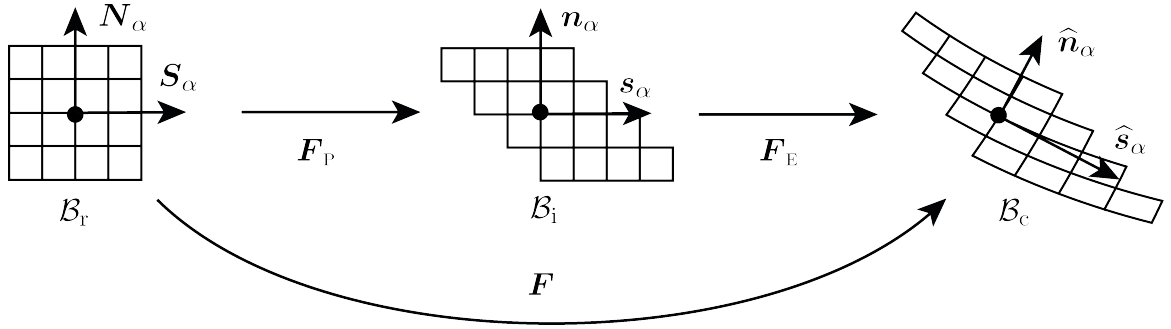

Figure 2.7: Multiplicative decomposition of the deformation gradient. Here, $\boldsymbol{F}_{\mathrm{E}}$ as well as $\boldsymbol{F}_{\mathrm{P}}$ are locally defined mappings. Moreover, plastic deformation is lattice preserving, i.e., $\boldsymbol{s}_\alpha = \boldsymbol{S}_\alpha$ and $\boldsymbol{n}_\alpha = \boldsymbol{N}_\alpha$.

[3] The concept of an isoclinic intermediate configuration goes back to Mandel [168].

[4] As a result of the multiplicative decomposition, certain quantities must be distinguished between reference, intermediate, and current configuration. Henceforth, the indices '$_{\mathrm{r}}$', '$_{\mathrm{i}}$', and '$_{\mathrm{c}}$' are used for that reason.

nor the mapping from the intermediate into the current configuration

$$\boldsymbol{F}_{\mathrm{E}} : \begin{cases} \mathcal{TB}_{\mathrm{i}} & \rightarrow & \mathcal{TB}_{\mathrm{c}} \\ \mathrm{d}\overline{\boldsymbol{X}} & \mapsto & \mathrm{d}\boldsymbol{x} = \boldsymbol{F}_{\mathrm{E}}(\overline{\boldsymbol{X}}) \cdot \mathrm{d}\overline{\boldsymbol{X}} \Leftrightarrow \mathrm{d}\overline{\boldsymbol{X}} = \boldsymbol{F}_{\mathrm{E}}^{-1}(\boldsymbol{x}) \cdot \mathrm{d}\boldsymbol{x}. \end{cases} \tag{2.67}$$

Same holds for the cotangent mappings

$$\boldsymbol{F}_{\mathrm{P}}^{-\mathrm{T}} : \begin{cases} \mathcal{TB}_{\mathrm{r}}^{*} & \rightarrow & \mathcal{TB}_{\mathrm{i}}^{*} \\ \boldsymbol{N} & \mapsto & \boldsymbol{N}_{\mathrm{i}} = \boldsymbol{F}_{\mathrm{P}}^{-\mathrm{T}}(\boldsymbol{X}, t) \cdot \boldsymbol{N} \Leftrightarrow \boldsymbol{N} = \boldsymbol{F}_{\mathrm{P}}^{\mathrm{T}}(\overline{\boldsymbol{X}}) \cdot \boldsymbol{N}_{\mathrm{i}} \end{cases} \tag{2.68}$$

and

$$\boldsymbol{F}_{\mathrm{E}}^{-\mathrm{T}} : \begin{cases} \mathcal{TB}_{\mathrm{i}}^{*} & \rightarrow & \mathcal{TB}_{\mathrm{c}}^{*} \\ \boldsymbol{N}_{\mathrm{i}} & \mapsto & \boldsymbol{n} = \boldsymbol{F}_{\mathrm{E}}^{-\mathrm{T}}(\overline{\boldsymbol{X}}) \cdot \boldsymbol{N}_{\mathrm{i}} \Leftrightarrow \boldsymbol{N}_{\mathrm{i}} = \boldsymbol{F}_{\mathrm{E}}^{\mathrm{T}}(\boldsymbol{x}) \cdot \overline{\boldsymbol{n}}, \end{cases} \tag{2.69}$$

respectively. Hence, neither $\boldsymbol{F}_{\mathrm{E}}$ nor $\boldsymbol{F}_{\mathrm{P}}$ (or their inverse counterparts) are true gradients of vector fields. Nevertheless, the above introduced mappings can be interpreted as pointwise linear transformations in accordance to the concept of infinitesimal neighborhoods. With that in mind, the intermediate (or anholonomic) metric tensors

$$\overline{\boldsymbol{G}} = \overline{G}_{\alpha\beta}\overline{\boldsymbol{G}}^{\alpha} \otimes \overline{\boldsymbol{G}}^{\beta}, \quad \overline{\boldsymbol{G}}^{-1} = \overline{G}^{\alpha\beta}\overline{\boldsymbol{G}}_{\alpha} \otimes \overline{\boldsymbol{G}}_{\beta}, \tag{2.70}$$

are introduced with basis vectors $\overline{\boldsymbol{G}}_{\alpha}$ and their reciprocals $\overline{\boldsymbol{G}}^{\alpha}$ where $\overline{\boldsymbol{G}}_{\alpha} \cdot \overline{\boldsymbol{G}}^{\beta} = \delta_{\alpha}^{\ \beta}$. Notice that Greek letters are used for indices associated with the intermediate configuration. Then, the component representation of the deformation gradient can be formulated in terms of the multiplicative split given by Eq. (2.64) as

$$\boldsymbol{F} = [F_{\mathrm{E}}]_{.\alpha}^{a}[F_{\mathrm{P}}]_{.A}^{\beta}\left[\boldsymbol{g}_a \otimes \overline{\boldsymbol{G}}^{\alpha}\right] \cdot \left[\overline{\boldsymbol{G}}_{\beta} \otimes \boldsymbol{G}^{A}\right] = [F_{\mathrm{E}}]_{.\alpha}^{a}[F_{\mathrm{P}}]_{.A}^{\alpha}\left[\boldsymbol{g}_a \otimes \boldsymbol{G}^{A}\right]. \tag{2.71}$$

Furthermore, the multiplicative split of deformation gives rise to define additional stretch and strain tensors, see also the left illustration in Fig. 2.8. Of particular relevance is the intermediate or elastic[5] right Cauchy-Green tensor which is defined as

$$\boldsymbol{C}_{\mathrm{E}} = \boldsymbol{F}_{\mathrm{E}}^{\mathrm{T}} \cdot \boldsymbol{F}_{\mathrm{E}}, \tag{2.72}$$

with its component representation

$$\begin{aligned} \boldsymbol{C}_{\mathrm{E}} &= [F_{\mathrm{E}}^{\mathrm{T}}]_{.a}^{\alpha}[F_{\mathrm{E}}]_{.\beta}^{b}[\overline{\boldsymbol{G}}_{\alpha} \otimes \boldsymbol{g}^{a}] \cdot [\boldsymbol{g}_b \otimes \overline{\boldsymbol{G}}^{\beta}] \\ &= \overline{G}^{\alpha\beta}[F_{\mathrm{E}}]_{.\gamma}^{c} g_{cb}[F_{\mathrm{E}}]_{.\beta}^{b}\delta_{.b}^{a}\overline{\boldsymbol{G}}_{\alpha} \otimes \overline{\boldsymbol{G}}^{\beta} \\ &= [F_{\mathrm{E}}]_{.\gamma}^{c} g_{cb}[F_{\mathrm{E}}]_{.\beta}^{b}\overline{\boldsymbol{G}}^{\gamma} \otimes \overline{\boldsymbol{G}}^{\beta} \\ &= [C_{\mathrm{E}}]_{\gamma\beta}\overline{\boldsymbol{G}}^{\gamma} \otimes \overline{\boldsymbol{G}}^{\beta}. \end{aligned} \tag{2.73}$$

The spatial or elastic left Cauchy-Green tensor is introduced as

$$\boldsymbol{b}_{\mathrm{E}} = \boldsymbol{F}_{\mathrm{E}} \cdot \boldsymbol{F}_{\mathrm{E}}^{\mathrm{T}}, \tag{2.74}$$

[5] Tensor quantities with index '$_{\mathrm{E}}$' are defined in terms of $\boldsymbol{F}_{\mathrm{E}}$ (e.g. $\boldsymbol{C}_{\mathrm{E}}$) but are not necessarily associated with the intermediate configuration. This is for instance the case for $\boldsymbol{b}_{\mathrm{E}}$, cf. Eq. (2.75).

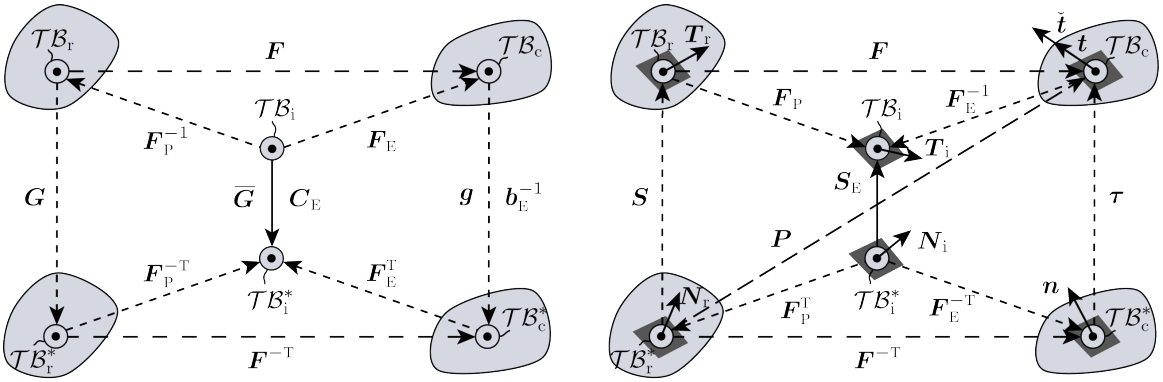

Figure 2.8: Commutative diagrams in the context of finite elastoplasticity. The intermediate configuration results from the multiplicative decomposition $\boldsymbol{F} = \boldsymbol{F}_\mathrm{E} \cdot \boldsymbol{F}_\mathrm{P}$. In both diagrams, the actual geometrical mapping (bold line) can be obtained in terms of a composition of commutative mappings (dashed lines).

with its component representation

$$\begin{aligned}
\boldsymbol{b}_\mathrm{E} &= [F_\mathrm{E}]^a_{.\alpha}[F_\mathrm{E}^{\mathrm{T}}]^{\beta}_{.b}[\boldsymbol{g}_a \otimes \overline{\boldsymbol{G}}^{\alpha}] \cdot [\overline{\boldsymbol{G}}_\beta \otimes \boldsymbol{g}^b] \\
&= [F_\mathrm{E}]^a_{.\alpha}\overline{G}^{\beta\gamma}[F_\mathrm{E}]^c_{.\gamma}g_{cb}\delta^{\alpha}_{.\beta}\boldsymbol{g}_a \otimes \boldsymbol{g}^b \\
&= [F_\mathrm{E}]^a_{.\alpha}\overline{G}^{\alpha\gamma}[F_\mathrm{E}]^c_{.\gamma}\boldsymbol{g}_a \otimes \boldsymbol{g}_c \\
&= [b_\mathrm{E}]^{ac}\boldsymbol{g}_a \otimes \boldsymbol{g}_c.
\end{aligned} \tag{2.75}$$

Moreover, the intermediate version of the Green-Lagrange strain tensor is defined as

$$\boldsymbol{E}_\mathrm{E} = \frac{1}{2}\left[\boldsymbol{C}_\mathrm{E} - \overline{\boldsymbol{G}}\right], \tag{2.76}$$

where the component representation reads

$$\boldsymbol{E}_\mathrm{E} = \frac{1}{2}\left[[C_\mathrm{E}]_{\alpha\beta} - \overline{G}_{\alpha\beta}\right]\overline{\boldsymbol{G}}^{\alpha} \otimes \overline{\boldsymbol{G}}^{\beta} = \frac{1}{2}\left[[F_\mathrm{E}]^a{}_{\alpha}g_{ab}[F_\mathrm{E}]^b{}_{\beta} - \overline{G}_{\alpha\beta}\right]\overline{\boldsymbol{G}}^{\alpha} \otimes \overline{\boldsymbol{G}}^{\beta}. \tag{2.77}$$

Similar to the aforementioned interpretations, $\boldsymbol{C}_\mathrm{E}$ can be seen as the pull-back of the spatial metric tensor $\boldsymbol{g}$. Accordingly, $\boldsymbol{E}_\mathrm{E}$ measures strain in terms of a metric change between the current and intermediate configuration.

Last but not least, a pure intermediate stress measure can be defined similar to the pull-back relation shown in Eq. (2.62). Here, an intermediate version of the second Piola-Kirchhoff stress tensor $\boldsymbol{S}$ is obtained in the form

$$\boldsymbol{S}_\mathrm{E} = \boldsymbol{F}_\mathrm{E}^{-1} \cdot \boldsymbol{\tau} \cdot \boldsymbol{F}_\mathrm{E}^{-\mathrm{T}} = \boldsymbol{F}_\mathrm{E}^{-1} \cdot \boldsymbol{P} \cdot \boldsymbol{F}_\mathrm{P}^{\mathrm{T}}, \tag{2.78}$$

cf. the right illustration in Fig. 2.8. One might also interpret $\boldsymbol{S}_\mathrm{E} = \boldsymbol{F}_\mathrm{P} \cdot \boldsymbol{S} \cdot \boldsymbol{F}_\mathrm{P}^{\mathrm{T}}$ as a push-forward of its material counterpart. In this respect, let $\boldsymbol{T}_\mathrm{i} \in \mathcal{TB}_\mathrm{i}$ and $\boldsymbol{N}_\mathrm{i} \in \mathcal{TB}_\mathrm{i}^*$ be the intermediate surface traction and normal vector respectively. Then, $\boldsymbol{S}_\mathrm{E}$ obeys the following transformation relation with respect to the intermediate configuration

$$\boldsymbol{S}_\mathrm{E} : \begin{cases} \mathcal{TB}_\mathrm{i}^* & \rightarrow \quad \mathcal{TB}_\mathrm{i} \\ \boldsymbol{N}_\mathrm{i} & \mapsto \quad \boldsymbol{T}_\mathrm{i} = \boldsymbol{S}_\mathrm{E}(\overline{\boldsymbol{X}}, t) \cdot \boldsymbol{N}_\mathrm{i}. \end{cases} \tag{2.79}$$

In analogy to Eq. (2.33), the relation between infinitesimal material and intermediate area elements is obtained as

$$\boldsymbol{N}_{\mathrm{i}}\mathrm{d}A_{\mathrm{i}} = \mathrm{cof}(\boldsymbol{F}_{\mathrm{P}}) \cdot \boldsymbol{N}_{\mathrm{r}}\mathrm{d}A_{\mathrm{r}} = \boldsymbol{F}_{\mathrm{P}}^{-\mathrm{T}} \cdot \boldsymbol{N}_{\mathrm{r}}\mathrm{d}A_{\mathrm{r}}. \tag{2.80}$$

With that, the differential surface force becomes $\mathrm{d}\boldsymbol{f} = \boldsymbol{F} \cdot \boldsymbol{S} \cdot \boldsymbol{N}_{\mathrm{r}}\mathrm{d}A_{\mathrm{r}} = \boldsymbol{F}_{\mathrm{E}} \cdot \boldsymbol{S}_{\mathrm{E}} \cdot \boldsymbol{N}_{\mathrm{i}}\mathrm{d}A_{\mathrm{i}}$. Moreover, assuming incompressible plastic deformation it follows for the plastic Jacobian determinant $J_{\mathrm{P}} = \sqrt{\det(\overline{\boldsymbol{G}}_{\alpha\beta})/\det(G_{AB})}\det([F_{\mathrm{P}}]^{\alpha}_{.A}) = 1$ and accordingly for the total Jacobian determinant $J = J_{\mathrm{E}} = \sqrt{\det(g_{ab})/\det(\overline{\boldsymbol{G}}_{\alpha\beta})}\det([F_{\mathrm{E}}]^{a}_{.\alpha})$, where it is generally required that both are non-negative and non-zero, i.e., $J_{\mathrm{P}} > 0$ and $J_{\mathrm{E}} > 0$. The relation between infinitesimal volume elements remains therefore as $\mathrm{d}v = J_{\mathrm{E}}J_{\mathrm{P}}\mathrm{d}V_{\mathrm{r}} = J\mathrm{d}V_{\mathrm{r}}$ which implies that there is no volume change between reference and intermediate configuration, i.e., $\mathrm{d}V_{\mathrm{i}} = \mathrm{d}V_{\mathrm{r}}$.

An extension of the here presented continuum mechanical framework towards the description of the kinematics of material surfaces is given, e.g., in [227]. For many applications, the use of Cartesian coordinates is sufficient as it simplifies the description of kinematics considerably. In such a case, the basis vectors are denoted as $\boldsymbol{e}_A = \boldsymbol{G}_A = \delta^a_{.A}\boldsymbol{g}_a$ and $\boldsymbol{e}^A = \boldsymbol{G}^A = \delta^A_{.a}\boldsymbol{g}^a$ with $g^a_{.A} = \delta^a_{.A}$, $g^A_{.a} = \delta^A_{.a}$, $g_{ab} = \delta_{ab}$, and $G_{AB} = \delta_{AB}$.

2.8 Deformation-rate measures and internal stress power

Energetically conjugate pairs of stress and strain measures determine the internal work of a system. Its rate, the rate of internal work $\mathcal{P}$ (per unit mass), plays an important role in the formulation of the first and second law of thermodynamics as well as in the formulation of the principle of virtual power. In the following, the focus is directed on the definition of suitable deformation-rate and strain-rate measures which form a stress power expression together with a conjugate stress tensor. Starting point is the material velocity gradient $\dot{\boldsymbol{F}}$ which can be expressed in the following way by applying Schwarz' theorem

$$\dot{\boldsymbol{F}} = \frac{\partial}{\partial t}\frac{\partial \boldsymbol{x}}{\partial \boldsymbol{X}} = \frac{\partial}{\partial \boldsymbol{X}}\frac{\partial \boldsymbol{x}}{\partial t} = \nabla_{\mathrm{r}}\boldsymbol{v} = \frac{\partial \boldsymbol{v}}{\partial \boldsymbol{x}} \cdot \frac{\partial \boldsymbol{x}}{\partial \boldsymbol{X}} = \boldsymbol{l} \cdot \boldsymbol{F}. \tag{2.81}$$

Here, $\boldsymbol{v} = \dot{\boldsymbol{x}}$ is the velocity vector defined as the material time derivative of the spatial position vector and $\boldsymbol{l}$ denotes the spatial velocity gradient tensor. The symmetric and antisymmetric part of $\boldsymbol{l} = \boldsymbol{d}+\boldsymbol{w}$ are defined as the spatial deformation-rate tensor $\boldsymbol{d} = (\boldsymbol{l})_{\mathrm{sym}} = 1/2[\boldsymbol{l}+\boldsymbol{l}^{\mathrm{T}}]$ and the spin tensor $\boldsymbol{w} = (\boldsymbol{l})_{\mathrm{skw}} = 1/2[\boldsymbol{l}-\boldsymbol{l}^{\mathrm{T}}]$ respectively. Hence, the rate of the right Cauchy-Green tensor can be expressed as

$$\dot{\boldsymbol{C}} = \boldsymbol{F}^{\mathrm{T}} \cdot \dot{\boldsymbol{F}} + \dot{\boldsymbol{F}}^{\mathrm{T}} \cdot \boldsymbol{F} = \boldsymbol{F}^{\mathrm{T}} \cdot [\boldsymbol{l} + \boldsymbol{l}^{\mathrm{T}}] \cdot \boldsymbol{F} = 2\boldsymbol{F}^{\mathrm{T}} \cdot \boldsymbol{d} \cdot \boldsymbol{F}, \tag{2.82}$$

where

$$\dot{\boldsymbol{E}} = \boldsymbol{F}^{\mathrm{T}} \cdot \boldsymbol{d} \cdot \boldsymbol{F} = \frac{1}{2}\dot{\boldsymbol{C}}. \tag{2.83}$$

With these definitions, the specific stress power can be expressed by the following energetically conjugate pairs (without proof)

$$\mathcal{P} = \frac{1}{\rho_{\mathrm{c}}}\boldsymbol{\sigma} : \boldsymbol{d} = \frac{1}{\rho_{\mathrm{r}}}\boldsymbol{\tau} : \boldsymbol{d} = \frac{1}{\rho_{\mathrm{r}}}\boldsymbol{P} : \dot{\boldsymbol{F}} = \frac{1}{\rho_{\mathrm{r}}}\boldsymbol{P} : \dot{\boldsymbol{E}}, \tag{2.84}$$

where ρ denotes the density of the corresponding configuration and $\boldsymbol{\sigma} : \boldsymbol{l} = \boldsymbol{\sigma} : \boldsymbol{d}$ since $\boldsymbol{\sigma} : \boldsymbol{w} = 0$, see for instance Bertram [28]. As a result of the multiplicative decomposition given by Eq. (2.64), $\boldsymbol{l}$ can be additively decomposed into an elastic and a plastic part, i.e.,

$$\boldsymbol{l} = \left[\dot{\boldsymbol{F}}_{\mathrm{E}} \cdot \boldsymbol{F}_{\mathrm{P}} + \boldsymbol{F}_{\mathrm{E}} \cdot \dot{\boldsymbol{F}}_{\mathrm{P}}\right] \cdot \boldsymbol{F}^{-1} = \boldsymbol{l}_{\mathrm{E}} + \boldsymbol{l}_{\mathrm{P}}, \tag{2.85}$$

where $\boldsymbol{l}_{\mathrm{E}} = \dot{\boldsymbol{F}}_{\mathrm{E}} \cdot \boldsymbol{F}_{\mathrm{E}}^{-1}$ is the elastic part of the spatial velocity gradient and $\boldsymbol{l}_{\mathrm{P}} = \boldsymbol{F}_{\mathrm{E}} \cdot \boldsymbol{L}_{\mathrm{P}} \cdot \boldsymbol{F}_{\mathrm{E}}^{-1}$ represents the push-forward of the (intermediate) plastic velocity gradient $\boldsymbol{L}_{\mathrm{P}}$. In the context of crystal plasticity, $\boldsymbol{L}_{\mathrm{P}}$ is defined as

$$\boldsymbol{L}_{\mathrm{P}} = \dot{\boldsymbol{F}}_{\mathrm{P}} \cdot \boldsymbol{F}_{\mathrm{P}}^{-1} = \sum_{\alpha}^{n_\alpha} \nu_\alpha \boldsymbol{s} \otimes \boldsymbol{n}_\alpha. \tag{2.86}$$

Here, the sum of plastic slip rates ν_α on corresponding slip systems $\alpha \in [1, n_\alpha]$ defines the evolution of plastic deformation (e.g. Rice [211]). Further,

$$\boldsymbol{d} = \boldsymbol{d}_{\mathrm{E}} + \boldsymbol{d}_{\mathrm{P}}, \quad \boldsymbol{w} = \boldsymbol{w}_{\mathrm{E}} + \boldsymbol{w}_{\mathrm{P}} \tag{2.87}$$

follows from Eq. (2.85) where $\boldsymbol{d}_{\mathrm{E}} = (\boldsymbol{l}_{\mathrm{E}})_{\mathrm{sym}} = 1/2[\boldsymbol{l}_{\mathrm{E}} + \boldsymbol{l}_{\mathrm{E}}^{\mathrm{T}}]$ and $\boldsymbol{d}_{\mathrm{P}} + \boldsymbol{w}_{\mathrm{P}} = \boldsymbol{F}_{\mathrm{E}} \cdot \boldsymbol{L}_{\mathrm{P}} \cdot \boldsymbol{F}_{\mathrm{E}}^{-1}$, cf. Asaro [7]. In analogy to Eq. (2.82) and Eq. (2.83), it follows furthermore that

$$\dot{\boldsymbol{C}}_{\mathrm{E}} = 2\boldsymbol{F}_{\mathrm{E}}^{\mathrm{T}} \cdot \boldsymbol{d}_{\mathrm{E}} \cdot \boldsymbol{F}_{\mathrm{E}} = 2\dot{\boldsymbol{E}}_{\mathrm{E}}. \tag{2.88}$$

The additive split of $\boldsymbol{l}$ enables an equivalent split of the specific stress power into an elastic $\mathcal{P}_{\mathrm{E}}$ and a plastic part $\mathcal{P}_{\mathrm{P}}$, i.e., $\mathcal{P} = \mathcal{P}_{\mathrm{E}} + \mathcal{P}_{\mathrm{P}}$. Using Eq. (2.78), an intermediate expression for the stress power is obtained based on the relation

$$\boldsymbol{\tau} : \boldsymbol{d} = \boldsymbol{\tau} : \left[\boldsymbol{d}_{\mathrm{E}} + \left(\boldsymbol{F}_{\mathrm{E}} \cdot \boldsymbol{L}_{\mathrm{P}} \cdot \boldsymbol{F}_{\mathrm{E}}^{-1}\right)_{\mathrm{sym}}\right] = \boldsymbol{S}_{\mathrm{E}} : \left[\frac{1}{2}\dot{\boldsymbol{C}}_{\mathrm{E}} + \boldsymbol{C}_{\mathrm{E}} \cdot \boldsymbol{L}_{\mathrm{P}}\right], \tag{2.89}$$

which finally gives

$$\mathcal{P}_{\mathrm{E}} = \frac{1}{2\rho_{\mathrm{i}}} \boldsymbol{S}_{\mathrm{E}} : \dot{\boldsymbol{C}}_{\mathrm{E}} = \frac{1}{\rho_{\mathrm{i}}} \boldsymbol{S}_{\mathrm{E}} : \dot{\boldsymbol{E}}_{\mathrm{E}} \quad \text{and} \quad \mathcal{P}_{\mathrm{P}} = \frac{1}{\rho_{\mathrm{i}}} \boldsymbol{S}_{\mathrm{E}} : \boldsymbol{C}_{\mathrm{E}} \cdot \boldsymbol{L}_{\mathrm{P}}. \tag{2.90}$$

Note that plastic incompressibility implies $\rho_{\mathrm{r}} = \rho_{\mathrm{i}}$. In the framework of crystal plasticity it is convenient to express the plastic stress power in terms of the (intermediate) Mandel stress tensor (Mandel [169]) defined as

$$\boldsymbol{M}_{\mathrm{E}} = \boldsymbol{C}_{\mathrm{E}} \cdot \boldsymbol{S}_{\mathrm{E}}. \tag{2.91}$$

With that, the plastic part of the specific stress power yields

$$\mathcal{P}_{\mathrm{P}} = \frac{1}{\rho_{\mathrm{i}}} \boldsymbol{M}_{\mathrm{E}} : \boldsymbol{L}_{\mathrm{P}}. \tag{2.92}$$

A stress power expression in which $\boldsymbol{M}_{\mathrm{E}}$ is conjugate to the plastic velocity gradient $\boldsymbol{L}_{\mathrm{P}}$ was first used by Mandel [167].

3 Elastic and plastic modeling aspects of crystalline materials

The objective of this chapter is to provide some insight about the continuum-based modeling of crystal plasticity. First, some general crystallographic relations are described involving the geometrical representation of slip and twin systems along with the continuum-like approximation of dislocations. These relations are used to describe the relevant deformation mechanisms at the continuum level, namely dislocation glide and twinning. Crystallographic slip evolves as a consequence of dislocation motion, accumulation, and interactions. In view of non-local crystal plasticity, slip gradients associated with continuum measures of geometrically necessary dislocation (GND) densities are considered in the framework. As a consequence, the crystallographic slip is affected by stresses associated with higher-order gradients. In relation to the characteristic length scale of the material, this introduces a size dependence within the hardening relation. Twinning is considered as a shear deformation associated with the glide of twin partials. A detailed description of the twinning model is provided in Chapter 7.

With regard to the elastic deformation behavior of crystals, the directional dependence of elastic properties is incorporated via a hyperelastic constitutive law fed by measurable elastic constants. With focus on the symmetry of hcp crystals, an anisotropic variant of the Neo-Hookean model is developed in extension to the commonly applied isotropic Neo-Hookean model. The new model is used to describe the directional dependence of elastic properties in terms of transverse isotropy. A numerical example illustrates the material response of Mg with varying crystallographic orientation with respect to the loading direction.

Furthermore, attention is paid towards the thermodynamic consistent formulation of gradient crystal plasticity. Part of the constitutive framework is the continuum-based description of dislocations. Two populations of dislocations are distinguished according to their impact on the work hardening behavior in terms of size-independent (local) and size-dependent (non-local) hardening contributions. The later is introduced via densities of geometrically necessary dislocations whose accumulations due to deformation incompatibilities generates additional resistance to dislocation glide. As is discussed, the modeling approach requires additional evolution equations at the nodal level according to the number of considered slip systems along with associated boundary conditions. Characteristic features of the model are finally emphasized by means of a symmetric dislocation pile-up problem.

3.1 Crystallographic description of deformation

Dislocation glide is the primary mechanism by which crystalline materials deform plastically. This process is explained by the motion or slip of dislocations through the material on well-defined crystallographic slip systems. The activation of slip is generally driven by the resolved shear stress and becomes evident in terms of slip traces or lines. Often, the totality of densely located slip lines is termed slip band. Nevertheless, depending on many factors such as crystallographic orientation, temperature, strain rate, chemical composition, etc., mechanical twinning induced by the deformation can play an essential role in the deformation behavior of crystalline solids. While the geometric structure of a twin system is similar to the one of a slip system, its activation is generally not only driven by the resolved shear stress. A twin system provides information about how twin and parent phases of the crystal are related to each other. It is obvious that an accurate treatment of such crystallographic information is important. For that reason, the conventions for indicating crystallographic directions and planes are briefly recalled in this section. With respect to gradient crystal plasticity models, it is also important to specify the geometry of dislocations which is represented at the continuum level by perfect rectangular shaped dislocation loop structures. To this end, the orientation of the dislocation line direction gives rise to distinguish the character of each dislocation loop segment as will be pointed out.

3.1.1 Crystal structures of metals

Except metallic glasses, metals and alloys are formed by well-arranged atomic structures - the crystals. In its idealized configuration, i.e., assuming perfect (defect-free) and solid conditions, a crystal is build up by periodic sequences of unit cells in all three spatial directions. Upon mathematical symmetry deliberations, there are 14 different possibilities to arrange atoms in a periodic, regular, and repeating structure called Bravais lattices [34]. These 14 Bravais lattices can be further categorized into seven crystal systems (see, e.g. Hahn [100]). The majority of common metals are built up by one of the unit cells depicted in Fig. 3.1. In the most general case (not depicted in the figure), a unit cell is characterized by six lattice parameters $\{\mathsf{a},\mathsf{b},\mathsf{c},\alpha,\beta,\gamma\}$ where $\mathsf{a}=|\mathbf{a}|$, $\mathsf{b}=|\mathbf{b}|$, and $\mathsf{c}=|\mathbf{c}|$ denote the dimensions of the unit cell, each in the respective direction of a basis vector, and $\alpha=\angle(\mathbf{b},\mathbf{c})$, $\beta=\angle(\mathbf{a},\mathbf{c})$, and $\gamma=\angle(\mathbf{a},\mathbf{b})$ are the angles between the lattice basis vectors.

The type of unit cell of which a lattice is build up results in different mechanical properties of the bulk material. While face-centered cubic (fcc) materials like Cu, Au, and Ag show in general a high formability, metals having a body-centered cubic (bcc) crystal lattice, for instance α-Fe, are rather brittle. Metals with a hexagonal close-packed (hcp) lattice structure, such as Mg or Ti, are even more limited in their ability to deform plastically. Due to the low crystal symmetry, additional deformation modes in terms of twinning are often observed in hcp metals whereas their activation depends strongly on the c/a ratio of the lattice parameters.

3.1.2 Lattice planes and directions

A three-dimensional crystal lattice is defined via the linear combination of basis vectors $\{\mathbf{a},\mathbf{b},\mathbf{c}\}$ scaled by a triple of integers u,v,w where each is a multiple of the constant interatomic distance in the corresponding direction. In case of fcc or bcc crystals, the lattice parameters are given by the set $\{a,a,a,\pi/2,\pi/2,\pi/2\}$ and the basis vectors are $\{\boldsymbol{a}_1,\boldsymbol{a}_2,\boldsymbol{a}_3\}$,

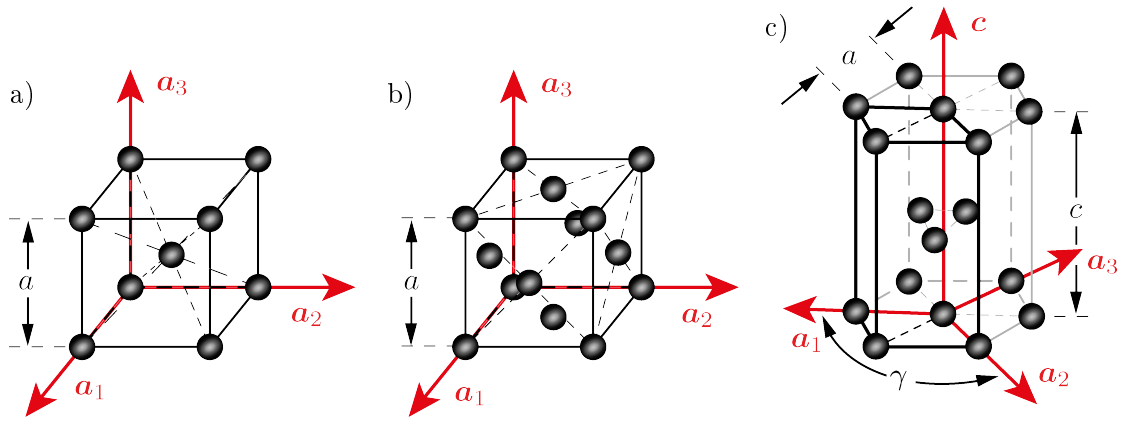

Figure 3.1: Common crystal lattice structures of metallic materials: a) body-centered cubic (bcc), b) face-centered cubic (fcc), c) hexagonal close-packed (hcp) crystal lattice.

cf. Fig. 3.1 a) and b). In case of the hcp crystal lattice, the lattice parameters of a primitive hexagonal unit cell (bold line) are given by the set $\{a, a, c, \pi/2, \pi/2, 2/3\pi\}$ and the basis vectors are denoted as $\{\boldsymbol{a}_1, \boldsymbol{a}_2, \boldsymbol{c}\}$, cf. Fig. 3.1 c). Then, an arbitrary point in the lattice is determined by the position vector

$$\boldsymbol{s}_{[uvw]} = u\boldsymbol{a}_1 + v\boldsymbol{a}_2 + w\boldsymbol{c} = s_i\boldsymbol{a}_i, \tag{3.1}$$

where the subscription '$[uvw]$' is used to distinguish between direction vectors associated with different coordinate systems.

Crystallographic directions are typically indicated in the form $[uvw]$ whereas sets of crystallographically equivalent directions are denoted as $<uvw>$. Planes are specified by its inverse intercepts along the lattice vectors, the so-called Miller indices h, k, l [176]. In contrast, individual planes are denoted in the form (hkl) and families of crystallographically equivalent planes are written as $\{hkl\}$. The plane normal vector is expressed with respect to the reciprocal (or dual) basis $\{\boldsymbol{a}_1^*, \boldsymbol{a}_2^*, \boldsymbol{c}^*\}$ which reads

$$\boldsymbol{n}_{(hkl)}^* = h\boldsymbol{a}_1^* + k\boldsymbol{a}_2^* + l\boldsymbol{c}^* = n_i^*\boldsymbol{a}_i^*. \tag{3.2}$$

Each reciprocal lattice vector is constructed by the cross product between two direct basis vectors such that $\boldsymbol{a}_i \cdot \boldsymbol{a}_j^* = \delta_{ij}$ (see, e.g., De Graef [63]). The reciprocal lattice vectors can be expressed with respect to the direct lattice as follows:

$$\begin{aligned} \boldsymbol{a}_1^* &= \frac{\boldsymbol{a}_2 \times \boldsymbol{c}}{\boldsymbol{a}_1 \cdot [\boldsymbol{a}_2 \times \boldsymbol{c}]} = \frac{2[2\boldsymbol{a}_1 + \boldsymbol{a}_2]}{3a^2}, \\ \boldsymbol{a}_2^* &= \frac{\boldsymbol{c} \times \boldsymbol{a}_1}{\boldsymbol{a}_1 \cdot [\boldsymbol{a}_2 \times \boldsymbol{c}]} = \frac{2[\boldsymbol{a}_1 + 2\boldsymbol{a}_2]}{3a^2}, \\ \boldsymbol{c}^* &= \frac{\boldsymbol{a}_1 \times \boldsymbol{a}_2}{\boldsymbol{a}_1 \cdot [\boldsymbol{a}_2 \times \boldsymbol{c}]} = \frac{\boldsymbol{c}}{c^2}. \end{aligned} \tag{3.3}$$

If the Miller indices are interpreted as components of a vector expressed in terms of the (direct) basis vectors $\boldsymbol{a}_i$, i.e., $\boldsymbol{n}_{(hkl)} = h\boldsymbol{a}_1 + k\boldsymbol{a}_2 + l\boldsymbol{c}$, it is not guaranteed that the direction of $\boldsymbol{n}_{(hkl)}$ is normal to the corresponding plane, i.e., $\boldsymbol{n}_{(hkl)} \nparallel \boldsymbol{n}_{(hkl)}^*$ in general. Directions and planes of hcp crystal structures are therefore indicated by the four index notation as will be pointed

out next. For this purpose, a forth lattice vector $\boldsymbol{a}_3 = -[\boldsymbol{a}_1 + \boldsymbol{a}_2]$ is introduced such that equidistant spacings are obtained in each of the three close-packed directions, cf. Fig. 3.1 c). Then, with respect to the extended hexagonal basis, a single direction is specified in the form $[u'v't'w']$ leading to a component representation written as

$$\boldsymbol{s}_{[u'v't'w']} = u'\boldsymbol{a}_1 + v'\boldsymbol{a}_2 + t'\boldsymbol{a}_3 + w'\boldsymbol{c} = s_I\boldsymbol{a}_I, \tag{3.4}$$

where $t' = -[u' + v']$. The relation between the four $[u'v't'w']$ and three index notation $[uvw]$ is given by the following set of equations

$$u = u' - t' = 2u' + v', \qquad v = v' - t' = 2v' + u', \qquad w = w'. \tag{3.5}$$

For the inverse relations, it can be found that

$$u' = \frac{1}{3}[2u - v], \qquad v' = \frac{1}{3}[2v - u], \qquad t' = -\frac{1}{3}[u + v], \qquad w' = w. \tag{3.6}$$

Fig. 3.2 a) shows some exemplary direction and normal vectors within the basal plane (plane normal to the c-axis). By comparing the three and four index notation, one can find that only the latter allows to define sets of crystallographically equivalent members with respect to the hcp crystal lattice.

Following Okamoto and Thomas [191], there are four reciprocal basis vectors $\{\boldsymbol{A}_1^*, \boldsymbol{A}_2^*, \boldsymbol{A}_3^*, \boldsymbol{C}^*\}$ which define the plane normal vector with respect to the hexagonal coordinate system as

$$\boldsymbol{n}^*_{(h'k'i'l')} = h'\boldsymbol{A}_1^* + k'\boldsymbol{A}_2^* + i'\boldsymbol{A}_3^* + l'\boldsymbol{C}^* = n_I^*\boldsymbol{A}_I^*, \tag{3.7}$$

where the components (h', k', i', l') are known as the Miller-Bravais indices with $i' = -[h' + k']$. The constructed normal vector must be equivalent to the one defined by Eq. (3.2), i.e., $\boldsymbol{n}^*_{(hkl)} \parallel \boldsymbol{n}^*_{(h'k'i'l')}$, cf. for example the textbook of De Graef and Mc Henry [64]. The directional equivalence is also evident from the illustration in Fig. 3.2 b). With that, the following relations can be obtained

$$\boldsymbol{A}_1^* = \frac{2}{3a^2}\boldsymbol{a}_1, \quad \boldsymbol{A}_2^* = \frac{2}{3a^2}\boldsymbol{a}_2, \quad \boldsymbol{A}_3^* = \frac{2}{3a^2}\boldsymbol{a}_3, \quad \boldsymbol{C}^* = \frac{\boldsymbol{c}}{c^2}. \tag{3.8}$$

From that, another benefit of using the four index notation can be concluded. If Miller-Bravais indices $(h'k'i'l')$ are taken as the components of a vector with respect to the direct basis vectors, then this vector can be interpretation as a normal vector of the plane indicated by the corresponding indices since $\boldsymbol{a}_I \parallel \boldsymbol{A}_I^*$, cf. Fig. 3.2 b). This advantage is gone for the reciprocal space defined by the reciprocal base $\{\boldsymbol{a}_i^*\}$. In contrast, with respect to cubic crystal structures, direct and reciprocal lattice vectors coincide a priori due to the orthonormal natur of the basis, i.e., $\{\boldsymbol{a}_i\} = \{\boldsymbol{a}_i^*\}$.

Because crystallographic directions and normal vectors are processed during numerical calculations in Cartesian coordinates, additional transformation relations are required. The transformation rules for directions and normal vectors are defined between the three index notation and the Cartesian representation (given in terms of $\boldsymbol{s}_{[xyz]}$ for direction vectors and $\boldsymbol{n}_{[xyz]}$ for plane normal vectors) as

$$\boldsymbol{s}_{[xyz]} = \boldsymbol{A} \cdot \boldsymbol{s}_{[uvw]} \quad \text{and} \quad \boldsymbol{n}_{[xyz]} = \boldsymbol{n}_{[hkl]} \cdot \boldsymbol{B}, \tag{3.9}$$

where the actual form of the transformation matrices $\boldsymbol{A}$ and $\boldsymbol{B}$ depends on the relative orien-

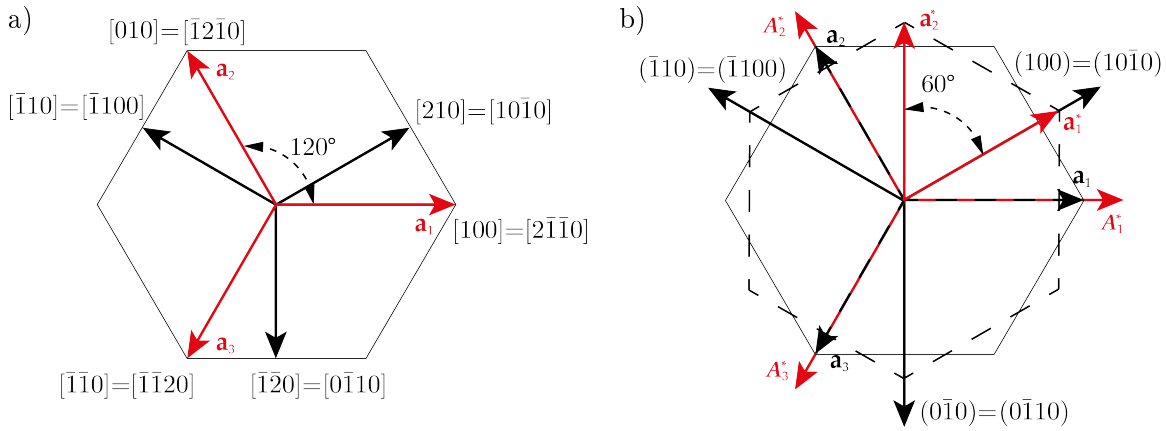

Figure 3.2: Exemplary illustration of a) direction vectors and b) plane normal vectors within the basal plane of the hcp lattice. As can be seen, the four index notation has an advantage over the three index notation as it allows to define sets of crystallographically equivalent members.

tation of both coordinate systems to each other. By introducing the standard (orthonormal) basis $\boldsymbol{e}_i$ such that $\boldsymbol{e}_1 \parallel \boldsymbol{a}_1$ and $\angle(\boldsymbol{e}_2, \boldsymbol{a}_2) = 30°$, it follows that

$$\boldsymbol{A} = \begin{bmatrix} 1 & -\frac{1}{2} & 0 \\ 0 & \frac{\sqrt{3}}{2} & 0 \\ 0 & 0 & \frac{c}{a} \end{bmatrix} \quad \text{and} \quad \boldsymbol{B} = \boldsymbol{A}^{-1} = \begin{bmatrix} 1 & \frac{1}{\sqrt{3}} & 0 \\ 0 & \frac{2}{\sqrt{3}} & 0 \\ 0 & 0 & \frac{a}{c} \end{bmatrix}. \tag{3.10}$$

3.1.3 Schmid's law

The mechanism of slip describes the relative motion of two regions of a crystal with respect to each other. This process is usually observed to takes place in directions of densest atomic packing and on close-packed planes. In this light, the actual slip process initiates if the stress magnitude resolved on a certain slip system overcomes a specific stress barrier. This barrier or resistance is referred to as the critical resolved shear stress $Y_{\alpha 0}$ (or yield limit) upon which plastic deformation initiates in terms of dislocation slip. This concept has proven itself to be well suited to predict the onset of slip in most crystalline materials and is known as the Schmid's law [215] (see also Schmid and Boas [216]). Occasional deviations from this concept have been observed, in particular, for bcc metals and alloys (see, e.g., Christian [50]) but are not further discussed here.

Typical slip systems for fcc and hcp crystals are illustrated in Fig. 3.3 a) and respectively b) together with its designation in the corresponding index notation. While fcc materials such as Cu provide 12 possible slip systems, all having a very low yield limit of ≈ 1.5 MPa (Basinski and Basinski [20]), the ductility of hcp crystals such as Mg is mainly determined by basal slip as this slip mode has by far the lowest critical resolved shear stress compared to prismatic or pyramidal slip modes. The predominance of basal slip becomes more obvious when comparing the ratios between yield stresses of common slip systems. For instance, ratios of $Y_{\text{bas}} : Y_{\text{pri}} : Y_{\pi 2} \approx 1 : 11 : 29$ have been identified on the basis of available experimental data

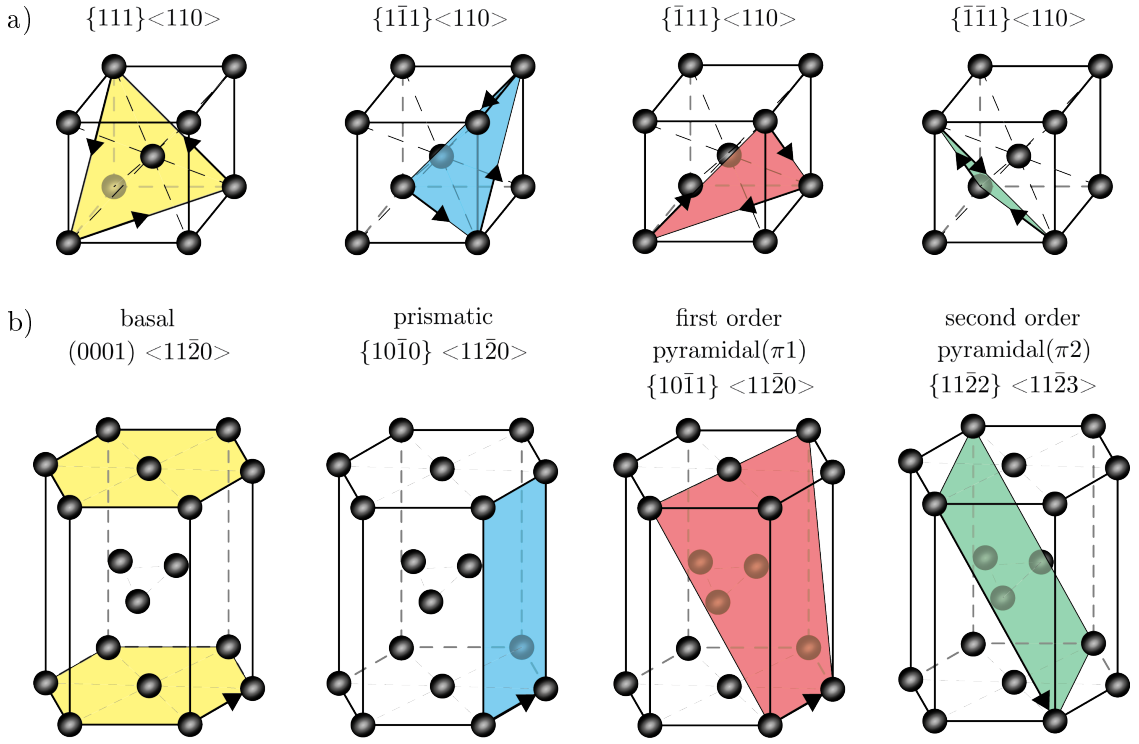

Figure 3.3: Common slip systems in a) fcc crystals and b) hcp crystals. The indicated slip directions are arbitrary chosen as slip deformation is a bidirectional mechanism.

for magnesium single crystals and used in numerical computations, see [110]. These values indicate the difficulty of non-basal slip mode activation in Mg clearly.

The resolved shear stress τ_α (Schmid stress) is obtained as the projection of the applied stress onto the slip system. For the case of uniaxial tension, the relation between applied tensile stress σ and the resolved shear stress τ_α is given as

$$\tau_\alpha = \sigma \cos(\phi_n) \cos(\phi_s) = \sigma f_\alpha, \tag{3.11}$$

where the orientation of the slip system is specified by the angle ϕ_s between the loading direction and the slip plane normal $\boldsymbol{n}_\alpha$ and by the angle ϕ_s between the loading direction and the slip direction $\boldsymbol{s}_\alpha$, cf. the illustration in Fig. 3.4. The factor by which the macroscopically applied stress is resolved onto the slip system is called Schmid factor f_α. For an arbitrary load condition, the resolved shear stress τ_α is calculated, e.g., as the projection of the (intermediate) Mandel stress tensor onto the corresponding slip system denoted as $\mathbb{S}_\alpha = \boldsymbol{s}_\alpha \otimes \boldsymbol{n}_\alpha$ or, equivalently, the projection of the Kirchhoff stress tensor onto the deformed slip system $\widehat{\mathbb{S}}_\alpha = \widehat{\boldsymbol{s}}_\alpha \otimes \widehat{\boldsymbol{n}}_\alpha$, which reads

$$\tau_\alpha = \boldsymbol{M}_{\mathrm{E}} : \mathbb{S}_\alpha = \boldsymbol{\tau} : \widehat{\mathbb{S}}_\alpha. \tag{3.12}$$

For arbitrary three-dimensional stress states, the Schmid factor is obtained by normalizing the resolves shear stress by the tensorial norm of the applied stress tensor, i.e.,

$$f_\alpha = \frac{\boldsymbol{M}_{\mathrm{E}} : \mathbb{S}_\alpha}{\|\boldsymbol{M}_{\mathrm{E}}\|} = \frac{\boldsymbol{\tau} : \widehat{\mathbb{S}}_\alpha}{\|\boldsymbol{M}_{\mathrm{E}}\|} = \frac{\tau_\alpha}{\|\boldsymbol{M}_{\mathrm{E}}\|} = \frac{\tau_\alpha}{\|\boldsymbol{\tau}\|}. \tag{3.13}$$

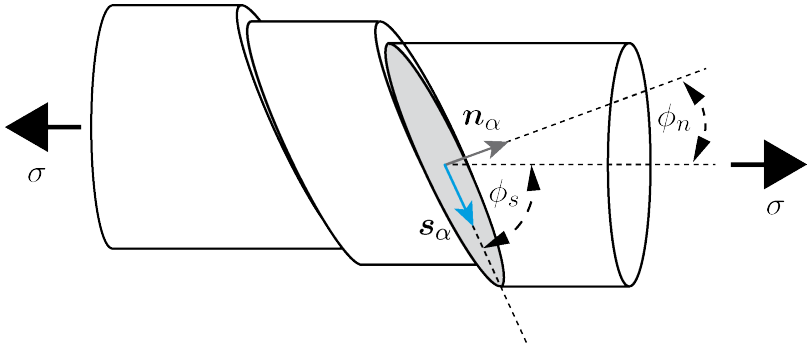

Figure 3.4: Illustration of Schmid's law of resolved shear stress for the case of uniaxial tension. The externally applied stress is resolved on the slip system specified by the orientation angles ϕ_n and ϕ_s.

3.1.4 Geometric twinning elements in hcp crystals

A twin represents a reoriented region of a crystal whose lattice structure is a mirror image of the original (parent) lattice structure, cf. Fig. 3.5 a). In this work, only coherent twin boundaries are under consideration, i.e., atoms on the mirror plane (purple plane) having perfect atomic match. Under the action of an externally applied mechanical load, a twin is formed by the cooperative displacement (and shuffling) of atoms. The mirror plane which can be viewed as the twin boundary/interface, is characterized by the normal vector $\boldsymbol{n}_\eta$. The traveled distance in direction of shift, i.e., in the twinning shear direction $\boldsymbol{s}_\eta$, is proportional to its normal distance to the twin boundary. Similar as in the description of slip systems, the vectors $\boldsymbol{s}_\eta$ and $\boldsymbol{n}_\eta$ form a twin system.

In the classical description of twinning according to Bilby and Crocker [30], the geometric elements $\{\boldsymbol{K}_1, \boldsymbol{K}_2, \boldsymbol{\eta}_1, \boldsymbol{\eta}_2\}$ are used to indicate characteristic planes and directions, see also the indications in Fig. 3.5 a). Here, $\boldsymbol{K}_1$ denotes the first undistorted plane (purple plane) characterized in terms of the normal vector $\boldsymbol{n}_\eta$, $\boldsymbol{K}_2$ is the second undistorted plane (blue plane), $\boldsymbol{\eta}_1 \parallel \boldsymbol{s}_\eta$ indicates the direction of shear, and $\boldsymbol{\eta}_2$ is the direction within the second undistorted plane perpendicular to the intersection of $\boldsymbol{K}_1$ and $\boldsymbol{K}_2$. In addition, the plane of shear $\boldsymbol{S}$ is often indicated (green plane).

Although a particular twinning mode is uniquely defined via either of the pair $\{\boldsymbol{K}_1, \boldsymbol{\eta}_2\}$ or $\{\boldsymbol{K}_2, \boldsymbol{\eta}_1\}$, the set $\{\boldsymbol{s}_\eta, \boldsymbol{n}_\eta\}$ along with the twinning shear magnitude η_0 of the corresponding twinning mode are used in this work for all computational purposes. With respect to hcp metals, η_0 is determined in terms of the lattice parameters a and c as

$$\eta_0 = \frac{3a^2 - c^2}{\sqrt{3}ac}. \tag{3.14}$$

Due to the crystallographic reorientation of the lattice within the twinned volume relative to the untwinned lattice (parent), two sets of lattice vectors must be distinguished. The parent crystal orientation is specified by the set of parent lattice vectors $\{\boldsymbol{s}_\alpha, \boldsymbol{t}_\alpha, \boldsymbol{n}_\alpha\}$ whereas the twin orientation is specified by the set of reoriented lattice vectors denoted as $\{\tilde{\boldsymbol{s}}_\alpha, \tilde{\boldsymbol{t}}_\alpha, \tilde{\boldsymbol{n}}_\alpha\}$. Fig. 3.5 b) shows a widely observed twinning mode in magnesium, the $\{10\bar{1}2\}$ $<10\bar{1}1>$ tensile twin system, see, e.g. Barnett [18]. This twinning mode is characterized by a twin orientation whose lattice vectors are obtained by a reflection of the parent lattice vectors across the twinning plane $\boldsymbol{K}_1$. Hence, the reoriented lattice vectors are determined by the (improper) orthogonal

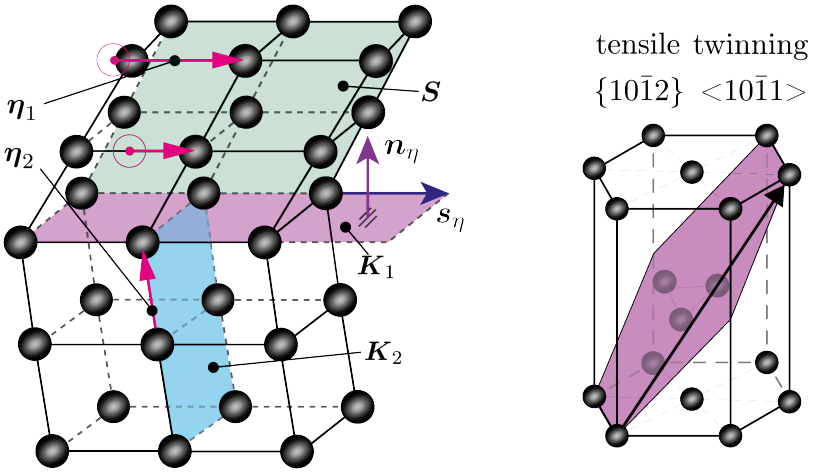

Figure 3.5: Schematic illustration of a) the geometrical twinning elements and b) the tensile twin system which plays a crucial role, for instance in Mg.

transformation defined as

$$\tilde{\boldsymbol{s}}_\alpha = \boldsymbol{Q}_\eta \cdot \boldsymbol{s}_\alpha, \quad \tilde{\boldsymbol{t}}_\alpha = \boldsymbol{Q}_\eta \cdot \boldsymbol{t}_\alpha, \quad \tilde{\boldsymbol{n}}_\alpha = \boldsymbol{Q}_\eta \cdot \boldsymbol{n}_\alpha, \tag{3.15}$$

where

$$\boldsymbol{Q}_\eta = 2\boldsymbol{n}_\eta \otimes \boldsymbol{n}_\eta - \boldsymbol{I}, \tag{3.16}$$

is the transformation matrix with $\boldsymbol{Q}_\eta = \boldsymbol{Q}_\eta^{\mathrm{T}} = \boldsymbol{Q}_\eta^{-1}$, $\det(\boldsymbol{Q}_\eta) = 1$ (proper orthogonal transformation), cf., for instance Clayton [54]. Other orientation relations than the one considered above can be found, e.g., in [30]. Because all twinning elements of the tensile twinning mode are rational ($\boldsymbol{K}_1 = \{10\bar{1}2\}$, $\boldsymbol{K}_2 = \{\bar{1}012\}$, $\eta_1 = \langle 10\bar{1}1>$, $<\eta_1 = 10\bar{1}\bar{1}>$), the tensile twinning mode is associated with compound twins.

3.1.5 Continuum description of dislocations

A common and meaningful definition of dislocations is obtained by means of the Burgers circuit [39]. As depicted in Fig. 3.6 a), an arbitrary chosen closed loop formed by a path of nearest atoms using the right-hand rule (see, e.g., Rösler [213]) defines a Burgers circuit indicated as $\mathcal{C}$. When running the same path in a relaxed or perfect crystal, the circuit fails to close if at least one dislocation is enclosed, cf. Fig. 3.6 b). The resulting gap between start and end point (framed atoms) can be described in terms of a translation vector called the Burgers vector $\boldsymbol{b}_\alpha$. From this concept it is obvious that during the motion of a dislocation though the crystal, the regularity of the atomic structure is temporary lost along the dislocation line. For that reason, dislocations can be understand as line defects. Their presence is accompanied by a distortion of the local environment so that additional elastic energy is stored in corresponding regions.

The total dislocation line can be sectioned into edge, screw , and mixed dislocation zones or segments. In view of a continuum representation of dislocations, an idealized dislocation form is assumed in which mixed dislocations are neglected. Then, an essential difference between

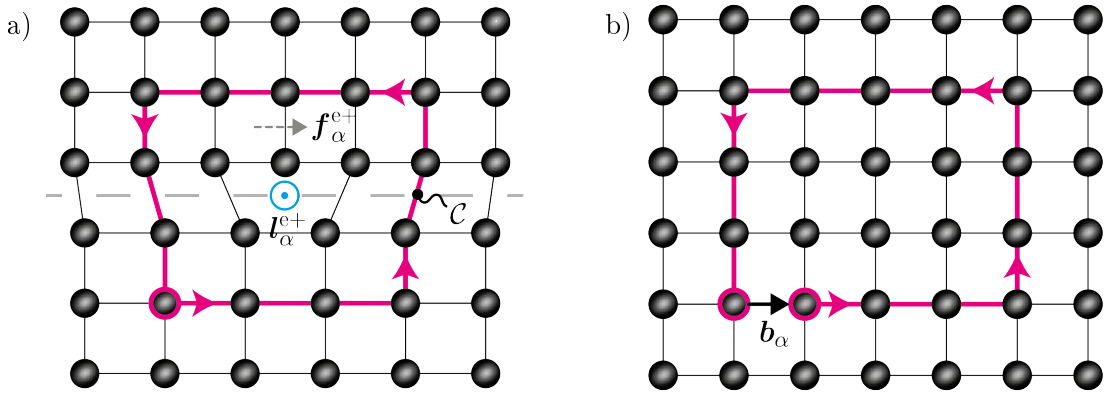

Figure 3.6: Definition of dislocations by means of the Burgers circuit: a) Burgers circuit $\mathcal{C}$ around a positive edge dislocation. b) resulting Burgers vector $\boldsymbol{b}_\alpha$ for the relaxed configuration.

edge and screw dislocations can be drawn according to their elastic energy ratio which is

$$\frac{E^{\mathrm{e}}}{E^{\mathrm{s}}} = \frac{1}{1-\nu}. \tag{3.17}$$

Here, E^{e} and E^{s} denote the elastic energy stored per unit length of the edge and screw dislocation segment, respectively, see for instance Hull and Bacon [106]. Consequently, there is a tendency to form screw dislocations rather than edge dislocations. However, from stability reasons, dislocations cannot be pure screw and, hence, there is always an intermediate dislocation containing a screw and an edge segment.

The type or character of the dislocation can be identified using the dislocation line sense and its relative orientation with respect to the Burgers vector. As mentioned above, the right-hand rule is used to determine the Burgers vector. This implies that the dislocation line direction $\boldsymbol{l}_\alpha^{e+}$ is pointing out of the drawing plane. Consequently, the direction of movement (slip) $\boldsymbol{s}_\alpha$ and thus the direction of the flow vector $\boldsymbol{f}_\alpha^{e+}$ are parallel to $\boldsymbol{b}_\alpha$ where

$$\boldsymbol{b}_\alpha = |\boldsymbol{b}_\alpha|\boldsymbol{s}_\alpha = b_\alpha \boldsymbol{s}_\alpha. \tag{3.18}$$

In fact, $\boldsymbol{f}_\alpha^{e+}$ indicates the direction in which the upper part of the crystal is sheared relative to the lower part as indicated in Fig. 3.7 a). This allows to define the dislocation character as positive edge. Note also that the slip plane normal has to point towards the extra half plane. In conclusion, the following characteristics can be summarized for edge dislocations:

$$\boldsymbol{b}_\alpha \parallel \boldsymbol{f}_\alpha^{e+}, \quad \boldsymbol{b}_\alpha \perp \boldsymbol{l}_\alpha^{e+}, \quad \boldsymbol{n}_\alpha = \frac{\boldsymbol{l}_\alpha^{e+} \times \boldsymbol{b}_\alpha}{|\boldsymbol{l}_\alpha^{e+} \times \boldsymbol{b}_\alpha|}. \tag{3.19}$$

The deformation as produced by slip of an edge dislocation, can be generated by the motion of a screw dislocation, see Fig. 3.7 b). When fixing the line sense with respect to the previous case, then the line direction of the positive screw dislocation $\boldsymbol{l}_\alpha^{s+}$ is oriented parallel to the Burgers vector $\boldsymbol{b}_\alpha$. Further, according to the direction of flow $\boldsymbol{f}_\alpha^{s+}$, the positive screw dislocation is associated with a right-handed screw dislocation. Henceforth, the direction in which positive screw dislocations are moving is defined as the transverse slip direction $\boldsymbol{t}_\alpha \parallel \boldsymbol{f}_\alpha^{s+}$, defined as

$$\boldsymbol{t}_\alpha = \boldsymbol{n}_\alpha \times \boldsymbol{s}_\alpha. \tag{3.20}$$

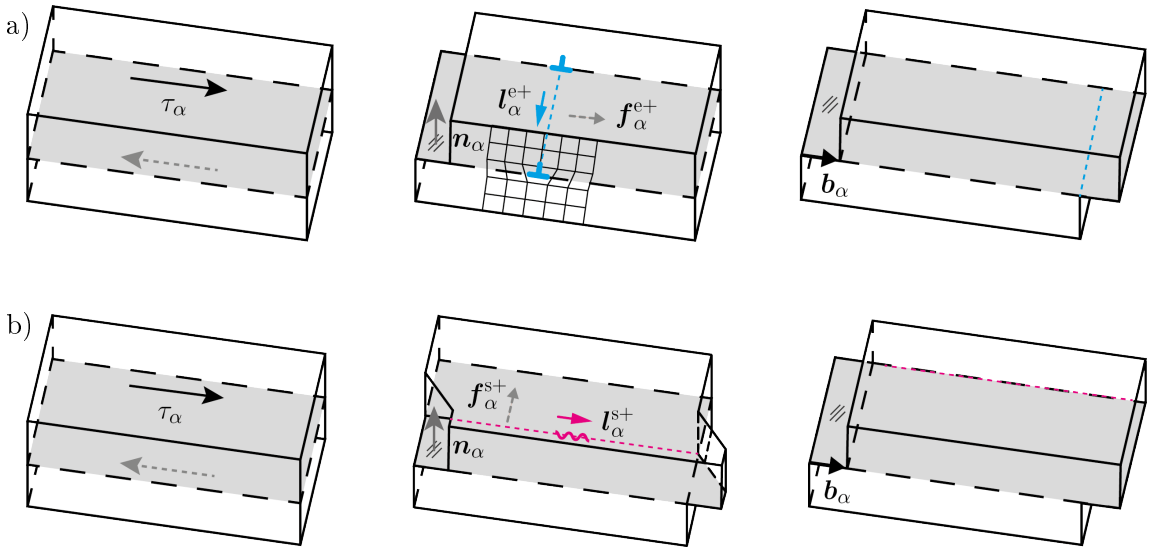

Figure 3.7: Accommodation of plastic deformation via a) positive edge dislocation slip and b) right-handed screw dislocation slip.

In this connection notice that, in particular for fcc crystals, screw dislocation are not uniquely bound to one single slip plane but are rather free to cross slip. Since this mechanism would go beyond the scope of this section, the reader is referred to, e.g., Kubin [146]. In summary, following conditions are associated with a positive screw dislocation character

$$\boldsymbol{b}_\alpha \perp \boldsymbol{f}_\alpha^{e+}, \quad \boldsymbol{b}_\alpha \parallel \boldsymbol{l}_\alpha^{s+}, \quad \boldsymbol{l}_\alpha^{s+} \times \boldsymbol{b}_\alpha = \boldsymbol{0}. \tag{3.21}$$

As a result of the above introduced idealization of dislocations in terms of pure edge and screw segments, the dislocation loop can be interpreted as a planar and rectangular shaped approximation as is drawn in Fig. 3.8.

3.2 Crystal elasticity

According to Schmid's law [216], crystals undergo pure elastic deformation until the critical stress level of the most favorable or the most easy to activate slip system is reached. The thereby induced mechanical stress results in a deviation of interatomic distances and/or orientations and, hence, causes a change in corresponding interatomic forces. This elastic distortion of the crystal lattice can be considered as a thermodynamically reversible and non-linear process, i.e., the atoms will always return to their initial position after the removal of external load without any internal dissipation of energy.

Depending on the type of crystal lattice, interatomic bonds can be stronger or weaker in different spatial directions. This anisotropy of interatomic bonds determines the elastic properties of the material in different spatial directions. The degree of elastic anisotropy is quantified by the anisotropy factor, calculated from orientation-dependent elastic constants, see for instance Tromans [243]. In continuum-based theories, the mechanisms associated with crystal elasticity are addressed in a phenomenological manner by postulating a hyperelastic potential $\psi_{\mathrm{i}}^{\mathrm{el}}$. This potential describes the elastically stored free energy per unit volume by taking into account the information about the materials symmetry group at the same time.

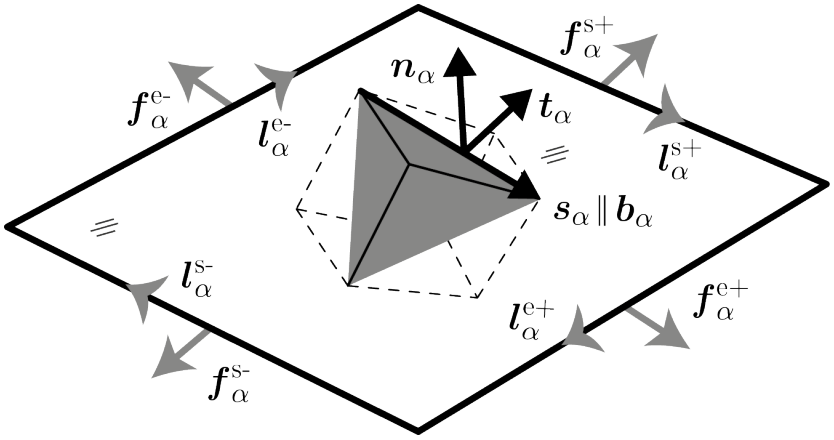

Figure 3.8: Planar and rectangular shaped idealization of a dislocation loop. Illustration refers to a fcc crystal and indicates the conventions used to define the zonal characters of the dislocation.

3.2.1 Isotropic hyperelasticity

In many cases, the elastic material response is assumed to be isotropic. This is either done for reasons of simplicity or due to the fact that the resulting error is expected to be small and therefore acceptable for the particular context. In general, the symmetry group $\mathcal{G}_{\mathrm{iso}}$ of an isotropic material comply with the full special orthogonal group $\mathcal{SO}(3) \coloneqq \{\boldsymbol{Q}_{\mathrm{iso}} | \boldsymbol{Q}_{\mathrm{iso}} \cdot \boldsymbol{Q}_{\mathrm{iso}}^{\mathrm{T}} = \boldsymbol{I} \vee \det(\boldsymbol{Q}_{\mathrm{iso}}) = 1\}$, i.e., $\mathcal{G}_{\mathrm{iso}} = \mathcal{SO}(3)$. Then, the free energy is a scalar-valued isotropic function of the symmetric tensor $\boldsymbol{C}_{\mathrm{E}}$. Furthermore, the principle of objectivity requires that

$$\psi_{\mathrm{i}}^{\mathrm{el}}(\boldsymbol{C}_{\mathrm{E}}) = \psi_{\mathrm{i}}^{\mathrm{el}}(\boldsymbol{Q}_{\mathrm{iso}} \cdot \boldsymbol{C}_{\mathrm{E}} \cdot \boldsymbol{Q}_{\mathrm{iso}}^{\mathrm{T}}) \ , \ \forall \boldsymbol{Q}_{\mathrm{iso}} \in \mathcal{G}_{\mathrm{iso}}, \tag{3.22}$$

Hence, $\psi_{\mathrm{i}}^{\mathrm{el}}$ remains invariant under arbitrary orthogonal transformations $\boldsymbol{Q}_{\mathrm{iso}}$ because the right Cauchy-Green stretch tensor $\boldsymbol{C}_{\mathrm{E}}$ remains unaltered. As a result, $\psi_{\mathrm{i}}^{\mathrm{el}}$ can be expressed in terms of the principal invariants of its argument, i.e.,

$$\psi_{\mathrm{i}}^{\mathrm{el}}(\boldsymbol{C}_{\mathrm{E}}) = \psi_{\mathrm{i}}^{\mathrm{el}}(I_1(\boldsymbol{C}_{\mathrm{E}}), I_2(\boldsymbol{C}_{\mathrm{E}}), I_3(\boldsymbol{C}_{\mathrm{E}})), \tag{3.23}$$

where the principal invariants of $\boldsymbol{C}_{\mathrm{E}}$ are defined as

$$I_1(\boldsymbol{C}_{\mathrm{E}}) = \mathrm{tr}(\boldsymbol{C}_{\mathrm{E}}), \quad I_2(\boldsymbol{C}_{\mathrm{E}}) = \mathrm{tr}(\mathrm{cof}(\boldsymbol{C}_{\mathrm{E}})), \quad I_3(\boldsymbol{C}_{\mathrm{E}}) = \det(\boldsymbol{C}_{\mathrm{E}}) = J_{\mathrm{E}}^2. \tag{3.24}$$

A widely used free energy function to describe the non-linear elastic material response of materials is of Neo-Hookean type. A particular form is for example

$$\psi_{\mathrm{i}}^{\mathrm{el}}(\boldsymbol{C}_{\mathrm{E}}) = \frac{1}{2}\mu\left[I_1 - 3\right] - \mu \ln(J) + \frac{1}{2}\lambda \ln(J_{\mathrm{E}})^2, \tag{3.25}$$

which leads to the following relation for the secon Piola-Kirchhoff stress tensor

$$\boldsymbol{S}_{\mathrm{E}} = 2\frac{\partial \psi_{\mathrm{i}}^{\mathrm{el}}}{\partial \boldsymbol{C}_{\mathrm{E}}} = \mu\left[\boldsymbol{I} - \boldsymbol{C}_{\mathrm{E}}^{-1}\right] + \lambda \ln(J_{\mathrm{E}})\boldsymbol{C}_{\mathrm{E}}^{-1}, \tag{3.26}$$

with μ and λ being the (isotropic) Lamé constants.

3.2.2 Elastic anisotropy of hcp crystals

The anisotropic elastic response of hcp single crystals can be described by means of five independent material parameters $\{C_{11}, C_{12}, C_{13}, C_{33}, C_{44}\}$, i.e., in terms of transverse isotropy. In this case, the material response is constant for rotational symmetric loading with respect to the axis of transverse isotropy[1] $\boldsymbol{A}_\mathrm{i} \| < c >$ and $|\boldsymbol{A}_\mathrm{i}| = 1$. For that reason the basal plane is referred to as the plane of isotropy. As a consequence, elastic properties such as the Young's modulus E^ϕ vary with angle $\phi \in [0, \pi]$, measured between $\boldsymbol{A}_\mathrm{i}$ and the direction of applied load. In other words, the structural characteristics of the crystal are preserved for arbitrary rotations $\boldsymbol{Q}_{<c>}$ around $\boldsymbol{A}_\mathrm{i}$, and, by any reflection $\boldsymbol{Q}_\mathrm{bas}$ across the basal plane. Together, these transformations define the symmetry group $\mathcal{G}_\mathrm{tri} = \{\boldsymbol{Q}_{<c>}, \boldsymbol{Q}_\mathrm{bas}\}$. Following Spencer [228], $\psi_\mathrm{i}^\mathrm{el}$ is required to be an isotropic invariant of the elastic right Cauchy-Green stretch tensor $\boldsymbol{C}_\mathrm{E}$ and the material unit vector $\boldsymbol{A}_\mathrm{i}$. Here, the objectivity requirement for transversely isotropic materials is formulated in terms of the structural tensor of transverse isotropy defined as the dyadic product $\boldsymbol{A}_\mathrm{i} \otimes \boldsymbol{A}_\mathrm{i}$, i.e.,

$$\psi_\mathrm{i}^\mathrm{el}(\boldsymbol{C}_\mathrm{E}, \boldsymbol{A}_\mathrm{i} \otimes \boldsymbol{A}_\mathrm{i}) = \psi_\mathrm{i}^\mathrm{el}(\boldsymbol{Q} \cdot \boldsymbol{C}_\mathrm{E} \cdot \boldsymbol{Q}^\mathrm{T}, \boldsymbol{Q} \cdot [\boldsymbol{A}_\mathrm{i} \otimes \boldsymbol{A}_\mathrm{i}] \cdot \boldsymbol{Q}^\mathrm{T}),\ \forall \boldsymbol{Q} \in \mathcal{G}_\mathrm{tri} \subset \mathcal{SO}(3). \tag{3.27}$$

Accordingly, $\psi_\mathrm{i}^\mathrm{el}$ can be expressed in terms of five independent principal invariants, i.e.,

$$\psi_\mathrm{i}^\mathrm{el}(\boldsymbol{C}_\mathrm{E}, \boldsymbol{A}_\mathrm{i} \otimes \boldsymbol{A}_\mathrm{i}) = \psi_\mathrm{i}^\mathrm{el}(I_1(\boldsymbol{C}_\mathrm{E}), I_2(\boldsymbol{C}_\mathrm{E}), I_3(\boldsymbol{C}_\mathrm{E}), I_4(\boldsymbol{C}_\mathrm{E}, \boldsymbol{A}_\mathrm{i}), I_5(\boldsymbol{C}_\mathrm{E}, \boldsymbol{A}_\mathrm{i})), \tag{3.28}$$

where the (pseudo) invariants I_4 and I_5 accounting for the anisotropy, are defined as

$$I_4(\boldsymbol{C}_\mathrm{E}, \boldsymbol{A}_\mathrm{i}) = \boldsymbol{C}_\mathrm{E} : [\boldsymbol{A}_\mathrm{i} \otimes \boldsymbol{A}_\mathrm{i}]\,, \quad I_5(\boldsymbol{C}_\mathrm{E}, \boldsymbol{A}_\mathrm{i}) = \boldsymbol{C}_\mathrm{E}^2 : [\boldsymbol{A}_\mathrm{i} \otimes \boldsymbol{A}_\mathrm{i}]\,. \tag{3.29}$$

By means of the above defined invariants, the free energy can be decomposed into an isotropic part and a transverse isotropic (anisotropic) part, here, in the following sense

$$\psi_\mathrm{i}^\mathrm{el}(I_1, I_2, I_3, I_4, I_5) = \psi_\mathrm{i}^\mathrm{el,iso}(I_1, I_2, I_3) + \psi_\mathrm{i}^\mathrm{el,aniso}(I_3, I_4, I_5), \tag{3.30}$$

or equivalently as

$$\psi_\mathrm{i}^\mathrm{el}(\boldsymbol{C}_\mathrm{E}, \boldsymbol{A}_\mathrm{i} \otimes \boldsymbol{A}_\mathrm{i}) = \psi_\mathrm{i}^\mathrm{el,iso}(\boldsymbol{C}_\mathrm{E}) + \psi_\mathrm{i}^\mathrm{el,aniso}(\boldsymbol{C}_\mathrm{E}, \boldsymbol{A}_\mathrm{i} \otimes \boldsymbol{A}_\mathrm{i}). \tag{3.31}$$

In conformity with Eq. (3.25), the isotropic part reads

$$\psi_\mathrm{i}^\mathrm{el,iso} = \frac{1}{2}\mu^\perp\,[I_1 - 3 - 2\ln(J_\mathrm{E})] + \frac{1}{2}\lambda^\perp \ln(J_\mathrm{E})^2, \tag{3.32}$$

where $\mu^\perp$ and $\lambda^\perp$ denote the Lamé parameters associated with in-plane elastic properties (plane of isotropy), i.e., elatic properties in arbitrary directions normal to $\boldsymbol{A}_\mathrm{i}$. Further, a fully non-linear Neo-Hookean-like formulation for transversely isotropic material behavior is obtained as an extension of the linear elastic case presented by Spencer [228], see also Spencer [229]. In this, linear elastic transverse isotropy is described by the following free energy function:

$$\psi_\mathrm{lin}^\mathrm{el,aniso} = \alpha\,[\boldsymbol{\epsilon} : \boldsymbol{a} \otimes \boldsymbol{a}]\,\mathrm{tr}(\boldsymbol{\epsilon}) + 2\beta\,\left[\boldsymbol{\epsilon}^2 : \boldsymbol{a} \otimes \boldsymbol{a}\right] + \frac{1}{2}\delta\,[\boldsymbol{\epsilon} : \boldsymbol{a} \otimes \boldsymbol{a}]^2\,. \tag{3.33}$$

[1] For lattice preserving plastic deformation it follows that $\boldsymbol{A}_\mathrm{r} = \boldsymbol{A}_\mathrm{i}$, i.e., the referential unit vector $\boldsymbol{A}_\mathrm{r}$ remains unaltered with respect to the intermediate configuration.

Each term is quadratic with respect to the infinitesimal strain tensor $\boldsymbol{\epsilon}$, resulting in a constant anisotropic contribution to the stiffness tensor; $\boldsymbol{a}$ denotes the axis of transverse isotropy. In the current framework of finite deformations, these terms are replaced by equivalent expressions using the pseudo invariants given by Eq. (3.29). In addition, the first invariant of $\boldsymbol{C}_E$ is replaced by $\ln(J_\mathrm{E})$ in order to satisfy the growth condition for compressive loading in equivalence to the isotropic Neo-Hookean model [104]. With that, the transversely isotropic energy contribution of Neo-Hookean type yields

$$\psi_\mathrm{i}^{\mathrm{el,aniso}} = \alpha\,[I_4 - 1]\ln(J_\mathrm{E}) + 2\beta\,[I_5 - 2I_4 + 1] + \frac{1}{2}\delta\,[I_4 - 1]^2\,. \tag{3.34}$$

The anisotropic elastic free energy is fully non-linear and suitable for large compressive strains: The first term couples isotropic and anisotropic energy contributions and accounts for the volume ratio J_E in a highly non-linear manner. The second term is closely related to shear properties on planes parallel to the isotropy axis. The third term accounts for non-linear stretch in direction of the axis of transverse isotropy.

The second Piola-Kirchhoff stress tensor $\boldsymbol{S}_\mathrm{E}$ is split in analogy to the free energy, i.e.,

$$\boldsymbol{S}_\mathrm{E} = 2\left[\frac{\partial\psi_\mathrm{i}^{\mathrm{el,iso}}}{\partial\boldsymbol{C}_\mathrm{E}} + \frac{\partial\psi_\mathrm{i}^{\mathrm{el,aniso}}}{\partial\boldsymbol{C}_\mathrm{E}}\right] = \boldsymbol{S}_\mathrm{E}^{\mathrm{iso}} + \boldsymbol{S}_\mathrm{E}^{\mathrm{aniso}}. \tag{3.35}$$

The isotropic part is similar to Eq. (3.26) and reads

$$\boldsymbol{S}_\mathrm{E}^{\mathrm{iso}} = \mu^\perp\left[\boldsymbol{I} - \boldsymbol{C}_\mathrm{E}^{-1}\right] + \lambda^\perp\ \ln(J_\mathrm{E})\boldsymbol{C}_\mathrm{E}^{-1}. \tag{3.36}$$

The anisotropic part yields

$$\begin{aligned}\boldsymbol{S}_\mathrm{E}^{\mathrm{aniso}} &= \alpha\left[2\ln(J_\mathrm{E})\boldsymbol{A}_\mathrm{i}\otimes\boldsymbol{A}_\mathrm{i} + [I_4 - 1]\,\boldsymbol{C}_\mathrm{E}^{-1}\right]\\ &\quad + 4\beta\left[\boldsymbol{A}_\mathrm{i}\otimes\boldsymbol{C}_\mathrm{E}\cdot\boldsymbol{A}_\mathrm{i} + \boldsymbol{C}_\mathrm{E}\cdot\boldsymbol{A}_\mathrm{i}\otimes\boldsymbol{A}_\mathrm{i} - 2\boldsymbol{A}_\mathrm{i}\otimes\boldsymbol{A}_\mathrm{i}\right]\\ &\quad + 2\delta\,[I_4 - 1]\,\boldsymbol{A}_\mathrm{i}\otimes\boldsymbol{A}_\mathrm{i}.\end{aligned} \tag{3.37}$$

As expected, in the absence of strain (undeformed state), both, the elastic free energy as well as the resulting stress tensor vanish. Finally, a relation between elastic constants and elastic model parameters shall be established. In this respect, the elastic stiffness tensor becomes

$$\begin{aligned}\mathbb{C}_\mathrm{E} &= 4\frac{\partial^2\psi_\mathrm{i}^{\mathrm{el,aniso}}}{\partial\boldsymbol{C}_\mathrm{E}\partial\boldsymbol{C}_E}\\ &= 2\alpha\left[\boldsymbol{C}_\mathrm{E}^{-1}\otimes\boldsymbol{A}\otimes\boldsymbol{A} + \boldsymbol{A}\otimes\boldsymbol{A}\otimes\boldsymbol{C}_E^{-1} + [I_4 - 1]\,\mathcal{C}_\mathrm{E}\right]\\ &\quad + 8\beta\left[\boldsymbol{A}\otimes\boldsymbol{A}\cdot\mathcal{I} + \mathcal{I}\cdot\boldsymbol{A}\otimes\boldsymbol{A}\right]\\ &\quad + 4\delta\boldsymbol{A}\otimes\boldsymbol{A}\otimes\boldsymbol{A}\otimes\boldsymbol{A},\end{aligned} \tag{3.38}$$

where the components of $\mathcal{C}_\mathrm{E}$ read

$$[\mathcal{C}_\mathrm{E}]_{ijkl} = \frac{\partial[\boldsymbol{C}_\mathrm{E}^{-1}]_{ij}}{\partial[\boldsymbol{C}_\mathrm{E}]_{kl}} = -\frac{1}{2}\left[[\boldsymbol{C}_\mathrm{E}^{-1}]_{ik}[\boldsymbol{C}_\mathrm{E}^{-1}]_{jl} + [\boldsymbol{C}_\mathrm{E}^{-1}]_{il}[\boldsymbol{C}_\mathrm{E}^{-1}]_{jk}\right] \tag{3.39}$$

with

$$[\mathcal{I}]_{ijkl} = \frac{\partial[\boldsymbol{I}]_{ij}}{\partial[\boldsymbol{I}]_{kl}} = \frac{1}{2}\left[[\boldsymbol{I}]_{ik}[\boldsymbol{I}]_{jl} + [\boldsymbol{I}]_{il}[\boldsymbol{I}]_{jk}\right]. \tag{3.40}$$

Using the vector notation (Voigt), the elastic constants are rewritten as $[\mathcal{C}]_{1111} \rightarrow C_{11}$, $[\mathcal{C}]_{3333} \rightarrow C_{33}$, $[\mathcal{C}]_{2323} \rightarrow C_{44}$, $[\mathcal{C}]_{1122} \rightarrow C_{12}$, $[\mathcal{C}]_{1133} \rightarrow C_{13}$, and $[\mathcal{C}]_{1212} \rightarrow C_{66}$. Considering transverse isotropy with respect to the $\boldsymbol{X}_3$-axis, the relation between elastic constants and elastic model parameters yields

$$\begin{aligned} C_{11} &= \lambda^{\perp} + 2\mu^{\perp}, \\ C_{12} &= \lambda^{\perp}, \\ C_{13} &= 2\alpha + \lambda^{\perp}, \\ C_{33} &= 4\alpha + 16\beta + 4\delta + \lambda^{\perp} + \mu^{\perp}, \\ C_{44} &= 4\beta + \mu^{\perp}, \\ C_{66} &= [C_{11} - C_{12}]/2. \end{aligned} \tag{3.41}$$

From this, the elastic model parameters are determined as

$$\begin{aligned} \mu^{\perp} &= [C_{11} - C_{12}]/2, \\ \lambda^{\perp} &= C_{12}, \\ \alpha &= [C_{13} - C_{12}]/2, \\ \beta &= [2C_{44} - C_{11} + C_{12}]/8, \\ \delta &= [C_{11} + C_{33}]/4 - C_{13}/2 - C_{44}. \end{aligned} \tag{3.42}$$

3.2.3 Numerical example - elastic anisotropy of Mg single crystal

The anisotropic elastic response is investigated for pure Mg by focusing on three different tensile load scenarios: 1) parallel to the c-axis, 2) 45° with respect to the the basal plane, and 3) parallel to the basal plane. Experimentally determined (adiabatic) elastic constants for Mg single crystals are taken from Long and Smith [160]: $C_{11} = 59.7$ MPa, $C_{33} = 61.7$ MPa, $C_{44} = 16.4$ MPa, $C_{12} = 26.2$ MPa, and $C_{13} = 21.7$ MPa. A round tensile specimen is used as an illustrative application (see the inclusion in Fig. 3.9) which is loaded displacement-controlled by an increment of 250 mm. The geometry is defined by the specimen diameter $D_0 = 20$ mm, grip diameter $D_1 = 24$ mm, gauge length $L_0 = 100$ mm, parallel length $L_1 \approx 120$ mm, grip length $L_2 = 60$ mm, and total length $L_3 = 250$ mm. Further, a fillet radius of $R = 4$ mm has been used. The material response is illustrated in Fig. 3.9 for all three crystal orientations using the volume averaged Cauchy stress

$$[\overline{\boldsymbol{\sigma}}]_{22} = \frac{1}{v}\int [\boldsymbol{\sigma}]_{22}\mathrm{dv} \tag{3.43}$$

and the volume averaged logarithmic stretch

$$\ln([\overline{\boldsymbol{U}}]_{22}) = \ln\left(\frac{1}{v}\int [\boldsymbol{U}]_{22}\mathrm{dv}\right). \tag{3.44}$$

As can be seen, the elastic response differs drastically at large deformations between all three crystal orientations. For that reason, the crystal anisotropy of Mg has to be taken into account, for instance, in cases when tensile twinning is likely to occure with high volume fraction. In this respect, the angle between the c-axis and the loading direction can change drastically within the twinned volume due to considerable lattice reorientation of approx. 86.3° for tensile twinning in Mg, cf. [255].

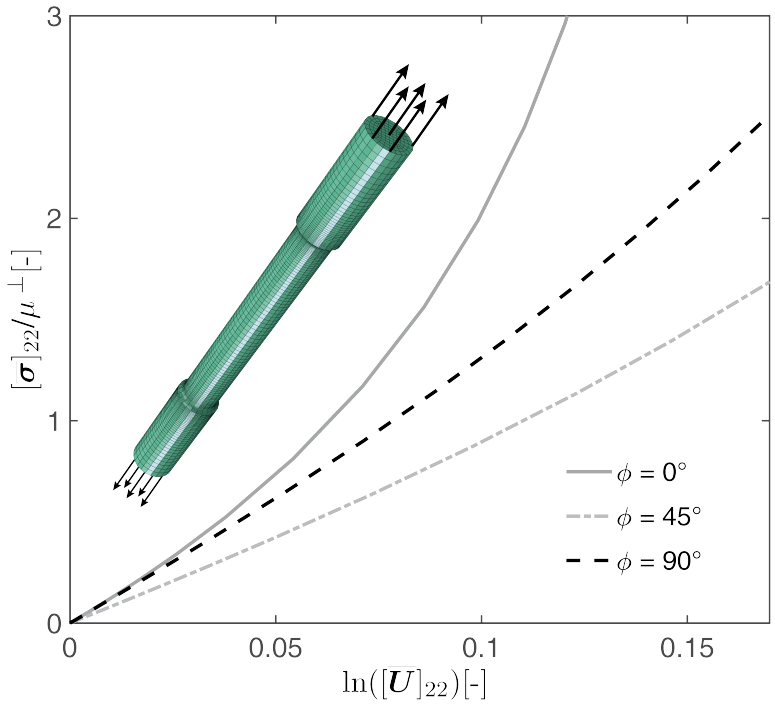

Figure 3.9: Normalized elastic stress-strain response of a round tensile specimen for three different crystal orientations: $\phi = 0°$, $\phi = 45°$, and $\phi = 90°$, where ϕ is the loading angle measured between the loading direction and the axis of transverse isotropy $\boldsymbol{A}_{\text{r}} \| < c >$.

3.3 Crystal plasticity at small scales

According to Ashby [9], plasticity in crystals is affected by two different populations of dislocations. Although there is no experimental possibility to distinguish these populations, they are very well characterized. Statistically stored dislocations evolve from random trapping processes during homogeneous plastic deformation. Their accumulation is therefore associated with plastic strain. In contrast, geometrically necessary dislocations accumulate in case of inhomogeneous plastic deformation in order to preserve lattice compatibility. Since the density of stored GNDs can be related to plastic strain gradients (Kröner [143]), it can be taken as a measure for lattice curvature (e.g. [31, 144]). The role of GNDs becomes significant as the characteristic material length scale l shrinks. The most prominent example is the average grain size in polycrystalline material systems as it controls the dislocation pile-up behavior and, in turn, the resulting size effect named after Hall [102] and Petch [203].

3.3.1 Statistically stored dislocations

Although SSDs do not directly lead to size-dependent hardening (but may enhance such effects indirectly via interaction mechanisms), their density relative to the density of GNDs allows for a meaningful interpretation of the underlying micromechanics when analyzing the deformation behavior of small-scaled crystals which is different compared to bulk-sized crystals due to geometrical confinements of plastic zones. Keeping in mind that dislocations are carrying the plastic deformation while expanding in a loop-like setting, such individual or discrete dislocations are not resolved in continuum-based crystal plasticity models but are rather considered

in terms of locally averaged densities. The prominent relation by which SSD densities ζ_α are related to plastic slip rates ν_α was established by Orowan [193] and reads

$$\nu_\alpha = \zeta_\alpha b_\alpha \bar{v}_\alpha, \tag{3.45}$$

where $\bar{v}_\alpha$ is the average line velocity. Ohashi [190] used this relation to derive an evolution equation for SSD densities by relating an average lifetime after which dislocations are trapped to its mean free path L_α which is allocated to the dislocation during this time. Then, the rate of the SSDs density can be expressed in terms of

$$\dot{\zeta}_\alpha = \frac{\nu_\alpha}{b_\alpha L_\alpha}, \tag{3.46}$$

where $L_\alpha = \hat{L}_\alpha(\{\zeta_\alpha\}, \{g_\alpha\})$ is a function of both, SSD ζ_α and GND g_α densities. For further details see also Kuhlmann-Wilsdorf [148]. A similar representation based on an equivalent plastic strain formulation instead of a slip-system-based formulation was used by Fleck et al. [80] and Brinckmann et al. [35]. In [111], an effective SSD density ζ^{eff} is calculated based on the effective accumulated plastic slip γ^{eff} defined as

$$\gamma^{\text{eff}} = \sqrt{\sum_\alpha \gamma_\alpha^2}, \quad \text{with} \quad \gamma_\alpha = \int \nu_\alpha \mathrm{d}t. \tag{3.47}$$

Together with the mean distance between forest dislocations denoted as $\tilde{l}$, an approximation of the total SSD density can be established as

$$\dot{\zeta}^{\text{eff}} = \frac{1}{\tilde{l}} \sqrt{\sum_\alpha \left[\frac{\nu_\alpha}{b_\alpha}\right]^2}. \tag{3.48}$$

Here, $\tilde{l}$ is taken as a constant value which is reasonable as long as the focus remains within a moderate strain regime. It is worth mentioning that with respect to crystal plasticity models where work hardening is formulated in terms of ν_α rather than $\dot{\zeta}_\alpha$, the SSD density can be computed during postprocessing. Moreover, the population of the effective SSD density relative to the effective GND density enables a direct estimation of the extent to which the size has an influence on the micromechanic behavior, e.g. [111]. More complex formulations for SSD densities are available for dislocation-based models including, for instance, the dislocation annihilation model of Essmann and Mughrabi [75], see also Evers et al. [78].

3.3.2 Geometrically necessary dislocations

Densities of GNDs $g_{\text{i}\alpha}$ are stored in the material to accomplish lattice incompatibility (Nye [186]). They represent lattice imperfections and act therefore as additional obstacles to dislocation motion. Considering both dislocation populations, the total dislocation density becomes

$$\rho_\alpha = \zeta_\alpha + g_{\text{i}\alpha}. \tag{3.49}$$

An effective continuum measure for estimating GND densities is attributed to Nye [186]. In essence, incompatible plastic deformation is measured in terms of $\text{Curl}_\text{r} \boldsymbol{F}_\text{P}$ whereas compatible plastic deformation is obtained for $\text{Curl}_\text{r} \boldsymbol{F}_\text{P} = \boldsymbol{0}$ (Shizawa and Zbib[225], Acharya and Bassani [1], Cermelli and Gurtin [42], Svendsen [237]). Then, the net sum of Burgers vectors $\mathfrak{b}(\mathcal{C})$

around an arbitrary closed curve $\mathcal{C}$ (Burgers circuit) in the reference configuration is obtained as

$$\mathfrak{b}(\mathcal{C}) = \oint_{\mathcal{C}} \boldsymbol{F}_{\mathrm{P}} \cdot \mathrm{d}\boldsymbol{X} = \int_{A_{\mathrm{r}}} \mathrm{Curl}_{\mathrm{r}}(\boldsymbol{F}_{\mathrm{P}}) \cdot \mathrm{d}\boldsymbol{A}_{\mathrm{r}} = \int_{A_{\mathrm{r}}} \mathrm{Curl}_{\mathrm{r}}(\boldsymbol{F}_{\mathrm{P}}) \cdot \boldsymbol{N}_{\mathrm{r}} \mathrm{d}A_{\mathrm{r}}, \tag{3.50}$$

where the material surface A_{r} is bounded by $\mathcal{C} = \partial A_{\mathrm{r}}$ via Stokes' theorem. Indeed,

$$\boldsymbol{G}_{\mathrm{r}} = \mathrm{Curl}_{\mathrm{r}}(\boldsymbol{F}_{\mathrm{P}}) \tag{3.51}$$

represents the mixed (intermediate-referential) form of the dislocation tensor and, hence, $\boldsymbol{G}_{\mathrm{r}} \cdot \boldsymbol{N}_{\mathrm{r}}$ represents an intermediate vector which is measured per unit reference area $\mathrm{d}A_{\mathrm{r}}$. Aiming on a slip-system-based formulation, Eq. (3.50) may be written as

$$\mathfrak{b}_\alpha(\mathcal{C}) = \int_{A_{\mathrm{r}}} \boldsymbol{s}_\alpha \cdot \boldsymbol{G}_{\mathrm{r}} \cdot \boldsymbol{N}_{\mathrm{r}} \mathrm{d}A_{\mathrm{r}}, \tag{3.52}$$

with the decomposition (cf. [237])

$$\mathfrak{b}(\mathcal{C}) = \sum_\alpha \mathfrak{b}_\alpha(\mathcal{C}) \boldsymbol{s}_\alpha \tag{3.53}$$

of the total net sum of Burgers vectors into slip-system-based net sum Burgers vectors $\mathfrak{b}_\alpha(\mathcal{C})$. Finally, a fully intermediate representation of $\mathfrak{b}_\alpha$ is archived by mapping the referential surface element on the intermediate configuration via Eq. (2.80). This gives

$$\mathfrak{b}_\alpha(\mathcal{C}) = \int_{A_{\mathrm{i}}} \boldsymbol{s}_\alpha \cdot \boldsymbol{G}_{\mathrm{i}} \cdot \boldsymbol{N}_{\mathrm{i}} \, \mathrm{d}A_{\mathrm{i}}, \tag{3.54}$$

where $\boldsymbol{G}_{\mathrm{i}}$ represents the intermediate dislocation tensor defined as

$$\boldsymbol{G}_{\mathrm{i}} = \boldsymbol{G}_{\mathrm{r}} \cdot \boldsymbol{F}_{\mathrm{P}}^{\mathrm{T}}, \tag{3.55}$$

cf. [42]. Furthermore, with respect to a single slip system, $\mathfrak{b}_\alpha$ can be related to a corresponding GND density g_α. In fact, there is a unique combination of dislocation densities which forms the dislocation tensor. Recalling the definition of $\boldsymbol{L}_{\mathrm{P}}$ by Eq. (2.86), the rate of the mixed dislocation tensor becomes

$$\begin{aligned} \dot{\boldsymbol{G}}_{\mathrm{r}} = \mathrm{Curl}_{\mathrm{r}}(\dot{\boldsymbol{F}}_{\mathrm{P}}) &= \sum_\alpha \boldsymbol{s}_\alpha \otimes [\nabla_{\mathrm{r}} \nu_\alpha \times \boldsymbol{F}_{\mathrm{P}}^{\mathrm{T}} \cdot \boldsymbol{n}_\alpha] + \nu_\alpha \boldsymbol{s}_\alpha \otimes \boldsymbol{G}_{\mathrm{r}}^{\mathrm{T}} \cdot \boldsymbol{n}_\alpha \\ &= \sum_\alpha b_\alpha \boldsymbol{s}_\alpha \otimes \dot{\boldsymbol{g}}_{\mathrm{r}\alpha}, \end{aligned} \tag{3.56}$$

where $b_\alpha = |\boldsymbol{b}_\alpha|$ and $\boldsymbol{g}_{\mathrm{r}\alpha}$ denotes the mixed form of the GND density of slip system α measured as line length per unit reference volume such that

$$\dot{\boldsymbol{g}}_{\mathrm{r}\alpha} = \frac{1}{b_\alpha} \nabla_{\mathrm{r}} \nu_\alpha \times \boldsymbol{F}_{\mathrm{P}}^{\mathrm{T}} \cdot \boldsymbol{n}_\alpha + \sum_\beta \nu_\alpha \left[\boldsymbol{s}_\beta \cdot \boldsymbol{n}_\alpha \right] \boldsymbol{g}_{\mathrm{r}\beta}. \tag{3.57}$$

This relation is referred to as the continuum model in [237] and contains, from left to right, an Ashby-like gradient term (see, for instance Evers et al. [78]) and a dislocation interaction term. With Eq. (3.55), the evolution of the intermediate dislocation tensor $\boldsymbol{G}_{\mathrm{i}}$ may be written

as

$$\dot{\boldsymbol{G}}_{\mathrm{i}} = \dot{\boldsymbol{G}}_{\mathrm{r}} \cdot \boldsymbol{F}_{\mathrm{P}}^{\mathrm{T}} + \boldsymbol{G}_{\mathrm{i}} \cdot \boldsymbol{L}_{\mathrm{P}}^{\mathrm{T}} = \sum_{\alpha} b_{\alpha} \boldsymbol{s}_{\alpha} \otimes \dot{\boldsymbol{g}}_{\mathrm{i}\alpha}. \tag{3.58}$$

In this respect, the intermediate form of the GND density takes the form

$$\dot{\boldsymbol{g}}_{\mathrm{i}\alpha} = \frac{1}{b_{\alpha}} \nabla_{\mathrm{i}} \nu_{\alpha} \times \boldsymbol{n}_{\alpha} + \sum_{\beta} \left[\nu_{\alpha} \left[\boldsymbol{s}_{\beta} \cdot \boldsymbol{n}_{\alpha} \right] \boldsymbol{g}_{\mathrm{i}\beta} + \nu_{\beta} \left[\boldsymbol{g}_{\mathrm{i}\alpha} \cdot \boldsymbol{n}_{\beta} \right] \boldsymbol{s}_{\beta} \right], \tag{3.59}$$

cf. Bargmann et al. [17]. The projection of $\dot{\boldsymbol{g}}_{\mathrm{i}\alpha}$ onto the slip system basis $\{\boldsymbol{s}_{\alpha}, \boldsymbol{t}_{\alpha}, \boldsymbol{n}_{\alpha}\}$ yields the evolution equations of the three (scalar-valued) components of the GND density, namely the screw GND density $g_{\mathrm{i}\alpha}^{\mathrm{s}}$, the in-plane edge GND density $g_{\mathrm{i}\alpha}^{\mathrm{e}}$, and the normal to slip plane edge GND density $g_{\mathrm{i}\alpha}^{\mathrm{e}\perp}$ reading

$$\begin{aligned}
\dot{g}_{\mathrm{i}\alpha}^{\mathrm{s}} &= \boldsymbol{s}_{\alpha} \cdot \dot{\boldsymbol{g}}_{\mathrm{i}\alpha} = \sum_{\beta} \left[\nu_{\alpha} \left[\boldsymbol{s}_{\beta} \cdot \boldsymbol{n}_{\alpha} \right] g_{\mathrm{i}\alpha}^{\mathrm{s}} + \nu_{\beta} \left[\boldsymbol{g}_{\mathrm{i}\alpha} \cdot \boldsymbol{n}_{\beta} \right] \left[\boldsymbol{s}_{\beta} \cdot \boldsymbol{s}_{\alpha} \right] \right] + \frac{1}{b_{\alpha}} \nabla_{\mathrm{i}} \nu_{\alpha} \cdot \boldsymbol{t}_{\alpha}, \\
\dot{g}_{\mathrm{i}\alpha}^{\mathrm{e}} &= \boldsymbol{t}_{\alpha} \cdot \dot{\boldsymbol{g}}_{\mathrm{i}\alpha} = \sum_{\beta} \left[\nu_{\alpha} \left[\boldsymbol{s}_{\beta} \cdot \boldsymbol{n}_{\alpha} \right] g_{\mathrm{i}\alpha}^{\mathrm{e}} + \nu_{\beta} \left[\boldsymbol{g}_{\mathrm{i}\alpha} \cdot \boldsymbol{n}_{\beta} \right] \left[\boldsymbol{s}_{\beta} \cdot \boldsymbol{t}_{\alpha} \right] \right] - \frac{1}{b_{\alpha}} \nabla_{\mathrm{i}} \nu_{\alpha} \cdot \boldsymbol{s}_{\alpha}, \\
\dot{g}_{\mathrm{i}\alpha}^{\mathrm{e}\perp} &= \boldsymbol{n}_{\alpha} \cdot \dot{\boldsymbol{g}}_{\mathrm{i}\alpha} = \sum_{\beta} \left[\nu_{\alpha} \left[\boldsymbol{s}_{\beta} \cdot \boldsymbol{n}_{\alpha} \right] g_{\mathrm{i}\alpha}^{\mathrm{e}\perp} + \nu_{\beta} \left[\boldsymbol{g}_{\mathrm{i}\alpha} \cdot \boldsymbol{n}_{\beta} \right] \left[\boldsymbol{s}_{\beta} \cdot \boldsymbol{n}_{\alpha} \right] \right].
\end{aligned} \tag{3.60}$$

The total slip system-based GND density is obtained as

$$g_{\mathrm{i}\alpha} = |\boldsymbol{g}_{\mathrm{i}\alpha}| = \sqrt{[g_{\mathrm{i}\alpha}^{\mathrm{s}}]^2 + [g_{\mathrm{i}\alpha}^{\mathrm{e}}]^2 + [g_{\mathrm{i}\alpha}^{\mathrm{e}\perp}]^2}. \tag{3.61}$$

By taking $\mathrm{Curl}_{\mathrm{r}}(\gamma_{\alpha} \boldsymbol{s}_{\alpha} \otimes \boldsymbol{n}_{\alpha})$ as a measure for incompatible plastic deformation rather than $\mathrm{Curl}_{\mathrm{r}}(\boldsymbol{F}_{\mathrm{P}})$, the Ashby-like version of vector-valued GND densities $\dot{\boldsymbol{g}}_{\mathrm{i}\alpha} = b_{\alpha}^{-1} \nabla_{\mathrm{i}} \nu_{\alpha} \times \boldsymbol{n}_{\alpha}$ can be derived. In [237], this approach is referred to as the glide-system model. In this case, the component representations of Eq. (3.60) becomes

$$\begin{aligned}
\dot{g}_{\mathrm{i}\alpha}^{\mathrm{s}} &= \frac{1}{b_{\alpha}} \nabla_{\mathrm{i}} \nu_{\alpha} \cdot \boldsymbol{t}_{\alpha}, \\
\dot{g}_{\mathrm{i}\alpha}^{\mathrm{e}} &= -\frac{1}{b_{\alpha}} \nabla_{\mathrm{i}} \nu_{\alpha} \cdot \boldsymbol{s}_{\alpha}, \\
\dot{g}_{\mathrm{i}\alpha}^{\mathrm{e}\perp} &= 0,
\end{aligned} \tag{3.62}$$

i.e., dislocation interactions are neglected and GND densities parallel to the slip plane normals vanish. Due to the sign convention within Eqs. (3.60) and (3.62), left-handed screw dislocations are defined as positive. In contrast to this, some authors (e.g. Arsenlis and Parks [4]) define right-handed screw dislocations as positive by projecting the plastic slip gradient on the line direction $\boldsymbol{l}_{\alpha}^{\mathrm{e}+} = \boldsymbol{s}_{\alpha} \times \boldsymbol{n}_{\alpha} = -\boldsymbol{t}_{\alpha}$ of the positive edge segment. The vector $-\boldsymbol{t}_{\alpha}$ (or equivalently the vector $\boldsymbol{l}_{\alpha}^{\mathrm{e}+}$) is sometimes denoted as $\boldsymbol{p}_{\alpha}$ (see, [4]). Following this, the evolution equation for screw GND densities becomes

$$\dot{g}_{\mathrm{i}\alpha}^{\mathrm{s}} = \frac{1}{b_{\alpha}} \nabla_{\mathrm{i}} \nu_{\alpha} \cdot \boldsymbol{p}_{\alpha} = -\frac{1}{b_{\alpha}} \nabla_{\mathrm{i}} \nu_{\alpha} \cdot \boldsymbol{t}_{\alpha}. \tag{3.63}$$

This sign convention is used henceforth for the definition of screw GND densities as it conforms with the description of dislocations introduced previously, cf. Fig. 3.8.

3.3.3 Numerical example - formation of a GND loop

In order to illustrate the continuum-based prediction of GND densities during inhomogeneous deformation, attention is laid on a simple shear problem of a cube whose exterior is modeled as impenetrable boundaries to dislocation motion. As a result, plastic deformation is forced to localize in the center of the cube due to strong dislocation pile-ups along the boundaries. Details on boundary conditions are discussed in section 3.3.8 and exact model parameters are not provided for the sake of simplicity. The orientation of the single slip configuration is provided in Fig. 3.10 a). The associated distribution of the GND density is presented in Fig. 3.10 b) in terms of the sum of both dislocation components $g^{\mathrm{e}}_{\mathrm{i}\alpha} + g^{\mathrm{s}}_{\mathrm{i}\alpha}$ along with a sketch of a rectangular dislocation loop which indicates the positive line sense. The summation is used to illustrate the sign sense of both dislocation components. As can be seen, the results mimic a dislocation loop consisting of positive and negative screw and edge dislocation segments. Notice that the upper half of the cube is hidden for better visualization in both plots and GNDs normal to the slip plane are neglected.

3.3.4 Thermodynamic framework of strain gradient crystal plasticity

A thermodynamic consistent formulation is employed in which the energy storage per unit volume with respect to the intermediate configuration is assumed to be additively split in the following way

$$\psi_{\mathrm{i}}(\boldsymbol{C}_{\mathrm{E}}, \{\gamma_\alpha\}, \{\nabla_{\mathrm{i}}\gamma_\alpha\}) = \psi^{\mathrm{el}}_{\mathrm{i}}(\boldsymbol{C}_{\mathrm{E}}) + \psi^{\mathrm{l}}(\{\gamma_\alpha\}) + \psi^{\mathrm{g}}_{\mathrm{i}}(\{\nabla_{\mathrm{i}}\gamma_\alpha\}), \tag{3.64}$$

where $\psi^{\mathrm{el}}_{\mathrm{i}}$ is the elastic energy storage, ψ^{l} represents the local energy storage due to dislocation glide (plastic slip)[2], and $\psi^{\mathrm{g}}_{\mathrm{i}}$ denotes the energy storage associated with accumulation of GNDs as a result of inhomogeneous deformation (plastic strain gradients). The dimension of the sets $\{\gamma_\alpha\}$ and $\{\nabla_{\mathrm{i}}\gamma_\alpha\}$ is specified by the number of admissible slip systems $\alpha = 1, ..., n_\alpha$.

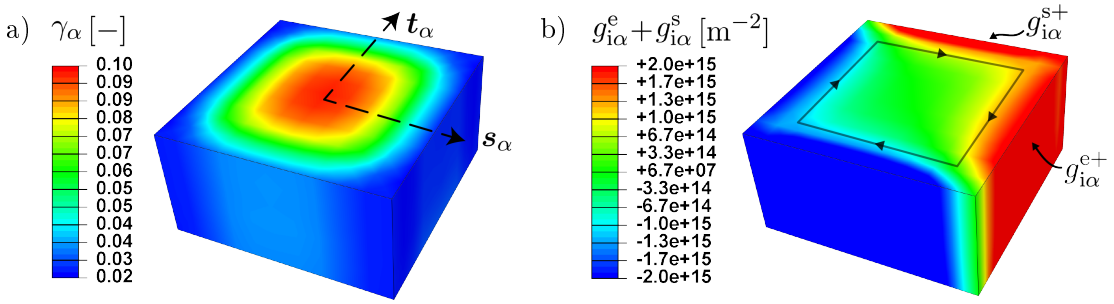

Figure 3.10: Simple shearing of a single crystalline cube (upper half is hidden) with single slip configuration as indicated in the contour plot a) showing the distribution of plastic slip γ_α. The sign convention for screw and edge dislocations is exemplified in the contour plot b) showing the GND density in terms of the sum of both dislocation components $g^{\mathrm{e}}_{\mathrm{i}\alpha} + g^{\mathrm{s}}_{\mathrm{i}\alpha}$. The computed GND density mimics a dislocation loop as indicated by the line loop.

[2] In an alternative approach which is based on the microforce balance (Gurtin [94]), the local hardening contribution is inherent in the definition of the dissipative microforce, cf. Chapter 7. Nevertheless, the energetic approach followed here results in a similar hardening relation as is discussed, for instance, in [69]

Considering quasi-static, isothermal conditions, the dissipation inequality reads

$$\mathcal{D} = \int_{\mathcal{B}_\mathrm{i}} \left[\rho_\mathrm{i} \mathcal{P} - \Upsilon_\mathrm{i}(\dot{\boldsymbol{C}}_\mathrm{E}, \{\nu_\alpha\}, \{\nabla_\mathrm{i}\nu_\alpha\}) \right] \mathrm{d}V_\mathrm{i} \geq 0, \tag{3.65}$$

Recalling Eqs. (2.90) and (2.92), the stress power per unit mass is split as

$$\mathcal{P} = \mathcal{P}_\mathrm{E} + \mathcal{P}_\mathrm{P} = \frac{1}{\rho_\mathrm{i}} \left[\frac{1}{2} \boldsymbol{S}_\mathrm{E} : \dot{\boldsymbol{C}}_\mathrm{E} + \boldsymbol{M}_\mathrm{E} : \boldsymbol{L}_\mathrm{P} \right]. \tag{3.66}$$

With the energy storage rate density Υ_i reading

$$\Upsilon_\mathrm{i} = \frac{\partial \psi_\mathrm{i}^\mathrm{el}}{\partial \boldsymbol{C}_\mathrm{E}} : \dot{\boldsymbol{C}}_\mathrm{E} + \sum_\alpha \left[\frac{\partial \psi^\mathrm{l}}{\partial \gamma_\alpha} \nu_\alpha + \frac{\partial \psi_\mathrm{i}^\mathrm{g}}{\partial \nabla_\mathrm{i} \gamma_\alpha} \cdot \nabla_\mathrm{i} \nu_\alpha \right], \tag{3.67}$$

the reduced dissipation inequality is obtained as

$$\mathcal{D}_\mathrm{red} = \int_{\mathcal{B}_\mathrm{i}} \left[\boldsymbol{M}_\mathrm{E} : \boldsymbol{L}_\mathrm{P} - \sum_\alpha \left[\kappa_\alpha \, \nu_\alpha + \boldsymbol{\kappa}_\alpha \cdot \nabla_\mathrm{i} \nu_\alpha \right] \right] \mathrm{d}V_\mathrm{i} \geq 0. \tag{3.68}$$

In accordance to Ekh et al. [70], the scaler-valued microstress $\kappa_\alpha = \partial \psi^\mathrm{l} / \partial \gamma_\alpha$ and the back-stress vector (or vector-valued microstress) $\boldsymbol{\kappa}_\alpha = \partial \psi_\mathrm{i}^\mathrm{g} / \partial \nabla_\mathrm{i} \gamma_\alpha$ are introduced work conjugate to ν_α and $\nabla_\mathrm{i} \nu_\alpha$ respectively. Following standard thermodynamic arguments, the (intermediate) second Piola-Kirchhoff stress must satisfy $\boldsymbol{S}_\mathrm{E} = 2 \, \partial \psi_\mathrm{i} / \partial \boldsymbol{C}_\mathrm{E}$. Then, integration by parts and application of Gauss' theorem lead to

$$\mathcal{D}_\mathrm{red} = \int_{\mathcal{B}_\mathrm{i}} \left[\boldsymbol{M}_\mathrm{E} : \boldsymbol{L}_\mathrm{P} - \sum_\alpha \left[\kappa_\alpha - \mathrm{Div}_\mathrm{i}(\boldsymbol{\kappa}_\alpha) \right] \nu_\alpha \right] \mathrm{d}V_\mathrm{i} - \int_{\partial \mathcal{B}_\mathrm{i}} \sum_\alpha \nu_\alpha \, \boldsymbol{\kappa}_\alpha \cdot \boldsymbol{N}_\mathrm{i} \mathrm{d}A_\mathrm{i} \geq 0, \tag{3.69}$$

where $\boldsymbol{N}_\mathrm{i}$ denotes the outward pointing normal vector. A more restrictive validity of the dissipation inequality is obtained by its local form. With respect to the bulk dissipation, this gives

$$\mathcal{D}_\mathrm{red}^\mathrm{L} = \boldsymbol{M}_\mathrm{E} : \boldsymbol{L}_\mathrm{P} - \sum_\alpha \left[\kappa_\alpha - \mathrm{Div}_\mathrm{i}(\boldsymbol{\kappa}_\alpha) \right] \nu_\alpha = \sum_\alpha \left[\tau_\alpha - \kappa_\alpha + \mathrm{Div}_\mathrm{i}(\boldsymbol{\kappa}_\alpha) \right] \nu_\alpha \geq 0 \quad \text{in} \quad \mathcal{B}_\mathrm{i}, \tag{3.70}$$

where $\tau_\alpha = \boldsymbol{M}_\mathrm{E} : \mathbb{S}_\alpha$. With respect to the boundary dissipation, one obtains

$$\mathcal{D}_\mathrm{red}^\mathrm{L(b)} = - \sum_\alpha \nu_\alpha \, \boldsymbol{\kappa}_\alpha \cdot \boldsymbol{N}_\mathrm{i} = \sum_\alpha \nu_\alpha \, \kappa_\alpha^\mathrm{(b)} \geq 0 \quad \text{on} \quad \partial \mathcal{B}_\mathrm{i}, \tag{3.71}$$

in which $\kappa_\alpha^\mathrm{(b)} = - \boldsymbol{\kappa}_\alpha \cdot \boldsymbol{N}_\mathrm{i}$ denotes the micro-boundary stress. For homogeneous plastic deformation, i.e., $\boldsymbol{\kappa}_\alpha = \boldsymbol{0}$, Eq. (3.70) reduces to

$$\mathcal{D}_\mathrm{red}^\mathrm{L} = \sum_\alpha \left[\tau_\alpha - \kappa_\alpha \right] \nu_\alpha \geq 0 \quad \text{in} \quad \mathcal{B}_\mathrm{i}, \tag{3.72}$$

and the boundary contribution in Eq. (3.71) vanishes completely. Further on, the onset of plastic slip is steered by the space of admissible stresses

$$\mathcal{E} = \{ \boldsymbol{M}_\mathrm{E} | \phi_\alpha(\tau_\alpha, R_\alpha) \leq 0 \}, \tag{3.73}$$

which represents, in general, a convex but not necessarily smooth elastic domain whose bound-

ary $\phi_\alpha(\tau_\alpha, R_\alpha) = 0$ is the yield surface. In this respect, the initiation of plastic yield is controlled by a set of yield functions of the form

$$\phi_\alpha(\tau_\alpha, R_\alpha) = \tau_\alpha - R_\alpha(\gamma_\alpha, \nabla_{\mathrm{i}}\gamma_\alpha), \tag{3.74}$$

where $R_\alpha = \kappa_\alpha - \mathrm{Div}_{\mathrm{i}}(\boldsymbol{\kappa}_\alpha) + Y_{\alpha 0}$ reflects the current slip system resistance and $R_\alpha(\gamma_\alpha = 0) = Y_{\alpha 0}$ comply with the initial yield limit (or critical resolved shear stress) $Y_{\alpha 0}$ of the slip system in the absence of plastic slip.

3.3.5 Plastic flow rule

The flow rule is handled as a viscoplastic regularization of the rate-independent case. This has the benefit that laborious identification of active slip systems is avoided. An appropriate algortihm for determination of active systems has been proposed, e.g., by Miehe and Schröder [175]. In case of a viscoplastic approach, overstress states, i.e., $\tau_\alpha - R_\alpha > 0$ are generally allowed and regularized, for instance, via a power law relation. A common choice is the viscoplastic law of Perzyna type [202], i.e.,

$$\nu_\alpha = \nu_0 \left[\frac{< \phi_\alpha >}{C_0} \right]^m. \tag{3.75}$$

Here, the plastic slip rate ν_α is related to a reference shear rate ν_0 and a reference drag stress C_0. The brackets $< \phi_\alpha >= 1/2\ [\phi_\alpha\ + |\phi_\alpha|]$ define a non-negative and monotonically increasing ramp function and ensure that $\nu_\alpha > 0$ if $\tau_\alpha > R_\alpha$. As a consequence, opposite slip directions must be considered as independent slip systems. Furthermore, the parameter m denotes the rate sensitivity exponent of the stress ratio. If desired, strain-rate dependence can be minimized by taking $[C_0]^m/\nu_0 \to 0$ [70]. A value of $m \geq 20$ can be used to obtain a rate-independent response. In addition, ν_0 is usually of the same order as the macroscopically applied strain rate.

Another frequently applied power law relation goes back to Hutchinson [113], see also Asaro [7] and Peirce et al. [199]. With respect to the current strain gradient-extended theory, this power law function becomes

$$\nu_\alpha = \nu_0 \left[\frac{|\pi_\alpha|}{r_\alpha} \right]^m \mathrm{sgn}(\pi_\alpha). \tag{3.76}$$

In contrast to Eq. (3.75), each slip system is treated bidirectional, i.e., an activation of slip in negative direction is allowed, and therefore, $\nu_\alpha < 0$ is possible. Furthermore, π_α denotes the microforce power conjugate to ν_α in the theory of Gurtin [93]. In the current context, $\pi_\alpha = \tau_\alpha + \mathrm{Div}_{\mathrm{i}}(\boldsymbol{\kappa}_\alpha)$ and $r_\alpha = \kappa_\alpha + Y_{\alpha 0}$ denotes the current slip system resistance associated with random tripping processes of SSDs. Besides the above presented viscoplastic flow relations, there is a number of other prominent formulations, see for instance [43].

3.3.6 Local hardening models

Local hardening models account for the size-independent hardening behavior of crystalline materials as a result of dislocation motion. In fact, these models capture isotropic self and cross (latent) hardening in a phenomenological manner in case of multi slip activation. In contrast to dislocation-based models (e.g. Kuhlmann-Wilsdorf [149], Ma and Rooters [162]),

the hardening stage is here characterized by the set of accumulated plastic slip variables γ_α, cf. Eq. $(3.47)_2$. As a result, it follows that $\gamma_\alpha \geq 0$, independent of the chosen viscoplastic power law and, hence, independent of the sign of ν_α.

Neglecting the interaction relations within the evolution equations for GND densities, the local hardening law is solely derived from the local free energy contribution ψ^{l}, i.e.,

$$\kappa_\alpha = \frac{\partial \psi^{\mathrm{l}}}{\partial \gamma_\alpha}, \tag{3.77}$$

cf. Ekh et al. [70]. Assuming a linear hardening relation according to Taylor [242], a potential which satisfies this and accounts for slip system interactions reads

$$\psi^{\mathrm{l}} = \frac{1}{2} \sum_{\alpha,\beta} \gamma_\alpha \; H^{\mathrm{l}}_{\alpha\beta} \gamma_\beta, \tag{3.78}$$

cf. Bargmann et al. [17]. Here, $H^{\mathrm{l}}_{\alpha\beta} = q_{\alpha\beta} H^{\mathrm{l}}_{\alpha 0}$ is the local hardening matrix defined by the interaction coefficients $q_{\alpha\beta}$ and the local hardening modulus $H^{\mathrm{l}}_{\alpha 0}$. Accordingly, self hardening is active if $\alpha = \beta$ with $q_{\alpha\beta} = 1$ while latent hardening occurs if $\alpha \neq \beta$ with $q_{\alpha\beta} \neq 0$. As a result of Eq. (3.78), the associated microstress is derived as

$$\kappa_\alpha = \sum_\beta H^{\mathrm{l}}_{\alpha\beta} \gamma_\beta, \tag{3.79}$$

see also [8]. Hence, slip systems on which dislocations have evolved during active glide stages lead to hardening of neighboring slip systems in terms of additional impediment to dislocation motion, i.e., additional to the self hardening contribution. For further details regarding the choice of coefficients $q_{\alpha\beta}$ see, e.g., [62, 137].

Another common hardening model is referred to as Voce-hardening [250] and is characterized by a saturation behavior of the stress-strain response. An exemplary energy format reads

$$\psi^{\mathrm{l}} = \sum_\alpha \left[\gamma_\alpha \Delta H^{\mathrm{l}}_\alpha + \frac{\Delta H^{\mathrm{l}}_\alpha}{c_{\mathrm{sat}}} \left[\exp\left(-c_{\mathrm{sat}} \sum_\beta \gamma_\beta \right) - 1 \right] \right], \tag{3.80}$$

see Husser and Bargmann [109], Klusemann [134]. Here, c_{sat} is the saturation rate parameter and $\Delta H^{\mathrm{l}}_\alpha = H^{\mathrm{l}}_{\alpha 0} - Y_{\alpha 0}$ is the saturation stress defined as the difference between the local hardening modulus $H^{\mathrm{l}}_{\alpha 0}$ and the initial yield resistance Y_α of the slip system. This particular choice for the local free energy results in the following microstress definition

$$\kappa_\alpha = \Delta H^{\mathrm{l}}_\alpha \left[1 - \exp\left(-c_{\mathrm{sat}} \sum_\beta \gamma_\beta \right) \right]. \tag{3.81}$$

In this model, latent hardening is steered by the total accumulated plastic slip $\sum_\beta \gamma_\beta$ in the material, i.e., plastic slip from neighboring slip systems are considered a priori. Hence, the saturation rate becomes accelerated by high latent slip activity. Alternatively, latent hardening contributions can be excluded from the exponential hardening relation and considered as linear contribution similar to Eq. (3.79), cf. [110]. Other phenomenological hardening models were suggested, among others, by Peirce et al. [198], Brown et al. [36], Wu et al. [257].

3.3.7 Size-dependent hardening

For loading conditions, particularly with pronounced heterogeneous plastic deformation, an extra storage of dislocations (in addition to stored SSDs) is required due to geometrically necessity reasons [78]. Consequently, the mobility of dislocations is more impaired which is typically reflected by an enhanced strain hardening rate and/or yield limit. The microstress $\boldsymbol{\kappa}_\alpha$ can generally be assumed to comprise an energetic and a dissipative contribution, see e.g., Gurtin and Anand [96], Reddy [209], Niordson and Kysar [182], Bargmann et al. [15]. In this work, the dissipative part is neglected such that $\boldsymbol{\kappa}_\alpha$ is purely energetic, i.e.,

$$\boldsymbol{\kappa}_\alpha = \frac{\partial \psi_{\mathrm{i}}^{\mathrm{g}}}{\partial \nabla_{\mathrm{i}} \gamma_\alpha}. \tag{3.82}$$

Following Bargmann et al. [17], the corresponding free energy contribution $\psi_{\mathrm{i}}^{\mathrm{g}}$ can be formulated in terms of the GND density vector $\boldsymbol{g}_{\mathrm{i}\alpha}$. Assuming a quadratic defect energy format, a general expression which couples GND densities among neighboring slip systems yields

$$\psi_{\mathrm{i}}^{\mathrm{g}} = \frac{1}{2} \sum_{\alpha,\beta} l_\alpha l_\beta H_0^{\mathrm{g}} \left[\boldsymbol{b}_\alpha \cdot \boldsymbol{b}_\beta\right] \left[\boldsymbol{g}_{\mathrm{i}\alpha} \cdot \boldsymbol{g}_{\mathrm{i}\beta}\right], \tag{3.83}$$

in which H_0^{g} is the gradient hardening modulus. Notice that the components of $\boldsymbol{g}_{\mathrm{i}\alpha}$ are related to the Cartesian basis and thus do not give direct interpretation of the edge and screw dislocation density distribution. From an application point of view, it is convenient to replace the Cartesian GND density vector components by the projections onto characteristic directions, i.e., $\boldsymbol{g}_{\mathrm{i}\alpha} = [g_{\mathrm{i}\alpha}^{\mathrm{s}}, g_{\mathrm{i}\alpha}^{\mathrm{e}}, g_{\mathrm{i}\alpha}^{\mathrm{e}\perp}] = [\boldsymbol{s}_\alpha \cdot \boldsymbol{g}_{\mathrm{i}\alpha}, \boldsymbol{t}_\alpha \cdot \boldsymbol{g}_{\mathrm{i}\alpha}, \boldsymbol{n}_\alpha \cdot \boldsymbol{g}_{\mathrm{i}\alpha}]$, cf. Eq. (3.60). Often, the Ashby-like component representation is of practical interest as it gives a reasonable approximation in many scenarios. Hence, in spirit of the Ashby model, Eq. (3.83) can be formulated as

$$\begin{aligned} \psi_{\mathrm{i}}^{\mathrm{g}} &= \frac{1}{2} \sum_{\alpha,\beta} l_\alpha l_\beta \left[\boldsymbol{b}_\alpha \cdot \boldsymbol{b}_\beta\right] \left[H_0^{\mathrm{e}} \left[\boldsymbol{s}_\alpha \cdot \boldsymbol{g}_{\mathrm{i}\alpha}\right] \left[\boldsymbol{s}_\beta \cdot \boldsymbol{g}_{\mathrm{i}\beta}\right] + H_0^{\mathrm{s}} \left[\boldsymbol{t}_\alpha \cdot \boldsymbol{g}_{\mathrm{i}\alpha}\right] \left[\boldsymbol{t}_\beta \cdot \boldsymbol{g}_{\mathrm{i}\beta}\right]\right] \\ &= \frac{1}{2} \sum_{\alpha,\beta} l_\alpha l_\beta \left[\boldsymbol{b}_\alpha \cdot \boldsymbol{b}_\beta\right] \left[H_0^{\mathrm{e}} g_{\mathrm{i}\alpha}^{\mathrm{e}} g_{\mathrm{i}\beta}^{\mathrm{e}} + H_0^{\mathrm{s}} g_{\mathrm{i}\alpha}^{\mathrm{s}} g_{\mathrm{i}\beta}^{\mathrm{s}}\right]. \end{aligned} \tag{3.84}$$

Here, hardening associated with edge and screw GND densities is distinguished by introducing appropriate gradient hardening moduli denoted as H_0^{e} and H_0^{s}. The ratio between the gradient moduli is chosen in accordance to the ratio of the elastic strain energy between both dislocation components. With focus on isotropic crystals, the relation between the hardening moduli can be simplified as

$$H_0^{\mathrm{s}} = [1 - \nu] H_0^{\mathrm{e}}, \tag{3.85}$$

in which ν denotes Poisson's ratio, cf. Husser et al. [112]. Since $H_0^{\mathrm{e}} > H_0^{\mathrm{s}}$, a higher population of screw GNDs is likely. Considering the above derived defect energy, a general expression for the microstress vector can be established as

$$\begin{aligned} \boldsymbol{\kappa}_\alpha &= \frac{\partial \psi_{\mathrm{i}}^{\mathrm{g}}}{\partial \nabla_{\mathrm{i}} \gamma_\alpha} = \frac{\partial \psi_{\mathrm{i}}^{\mathrm{g}}}{\partial g_{\mathrm{i}\alpha}^{\mathrm{e}}} \frac{\partial g_{\mathrm{i}\alpha}^{\mathrm{e}}}{\partial \nabla_{\mathrm{i}} \gamma_\alpha} + \frac{\partial \psi_{\mathrm{i}}^{\mathrm{g}}}{\partial g_{\mathrm{i}\alpha}^{\mathrm{s}}} \frac{\partial g_{\mathrm{i}\alpha}^{\mathrm{s}}}{\partial \nabla_{\mathrm{i}} \gamma_\alpha} \\ &= \sum_\beta l_\alpha l_\beta \left[\boldsymbol{b}_\alpha \cdot \boldsymbol{b}_\beta\right] H_0^{\mathrm{e}} \left[\frac{\partial g_{\mathrm{i}\alpha}^{\mathrm{e}}}{\partial \nabla_{\mathrm{i}} \gamma_\alpha} + [1 - \nu] \frac{\partial g_{\mathrm{i}\alpha}^{\mathrm{s}}}{\partial \nabla_{\mathrm{i}} \gamma_\alpha}\right]. \end{aligned} \tag{3.86}$$

Other free energy formats have been proposed, among others, by Gurtin [95], Ertürk et al. [74], Bayerschen and Bölke [22]. Backstress expressions which are physically motivated but not derived from an energetic potential have been considered, e.g., by Evers et al. [77], Bayley et al. [24]. In such expressions, the interaction relations between dislocations are established on the basis of physical interpretations. The backstress $\tau_{\mathrm{i}}^{\mathrm{b}}$ of such non-work-conjugate theories can be related the energetic microstress vector as $\tau_{\mathrm{i}}^{\mathrm{b}} = -\mathrm{Div}_{\mathrm{i}}(\boldsymbol{\kappa}_\alpha)$, cf. Kuroda and Tvergaard [153], Ertürk et al. [74].

3.3.8 Boundary conditions

In the here presented framework of strain gradient crystal plasticity, GND densities are treated as nodal degrees of freedom. This leads to strongly coupled field equations for which the evolution of GND densities has to be solved in addition to the balance of linear momentum. As a consequence of taking GND densities as additional degrees of freedom, additional boundary conditions have to be defined for crystallographic slips (natural) and/or GND densities (essential). The microscopically free (microfree) and microscopically hard (microhard) boundary conditions are defined as

$$\dot{g}_{\mathrm{i}\alpha}^{\mathrm{e}} = \dot{g}_{\mathrm{i}\alpha}^{\mathrm{s}} = 0 \quad \text{on} \quad \partial\mathcal{B}_{\mathrm{i}}^{\mathrm{g}} \tag{3.87}$$

and

$$\nu_\alpha \boldsymbol{N}_{\mathrm{i}} \cdot \boldsymbol{s}_\alpha = \boldsymbol{N}_{\mathrm{i}} \cdot \boldsymbol{t}_\alpha = 0 \quad \text{on} \quad \partial\mathcal{B}_{\mathrm{i}}^{\nu}, \tag{3.88}$$

respectively where $\partial\mathcal{B}_{\mathrm{i}} = \partial\mathcal{B}_{\mathrm{i}}^{\mathrm{g}} \cup \partial\mathcal{B}_{\mathrm{i}}^{\nu}$, see for instance Gurtin and Needleman [98], Kuroda and Tvergaard [153]. As a result of the considered implementation approach, the boundary conditions given by Eq. (3.88) are only fulfilled in a weak sense, i.e., the conditions are not fulfilled point wise but rather in the sense of an integral average over the corresponding domain. In contrast, the conditions given by Eq. (3.87) are strongly fulfilled. For the sake of completeness, it should be mentioned that an alternative finite element approach with nodal plastic slip variables and local GND densities is conceivable and would lead to opposite characteristics, cf. Klusemann et al. [135] and Kuroda [3]. Moreover, advanced (non-standard) boundary conditions have been proposed for (inner) grain boundaries, see [69, 173, 195, 201]. Advanced boundary conditions associated with single crystal surfaces are discussed in detail in Chapter 6.

3.3.9 Numerical example - symmetric double pile-up of dislocations

The presented gradient-enhanced crystal plasticity model is applied to a one-dimensional problem in order to illustrate the symmetric pile-up behavior of dislocations at impenetrable boundaries. Without further details, the theoretical framework is reduced to the one-dimensional case. A (single crystalline) micron-sized truss member of constant cross section and length $L_0 = 100$ µm is considered which is subjected to a tensile deformation along the X_1-direction. The truss is approximated by 1,000 2-node (linear) truss elements, each having a single integration point. Microhard conditions are imprinted at both ends, cf. Eq. (3.88). The truss is fixed at one end whereas the other end is free to move, i.e.,

$$\begin{aligned} &[\boldsymbol{u}]_1(X_1 = 0) = 0, \\ &[\boldsymbol{u}]_1(X_1 = L_0) = 10 \text{ µm} \ . \end{aligned} \tag{3.89}$$

A single slip system with perfect orientation is taken into account. The Schmid factor in this case is maximum, i.e. $f_\alpha = 0.5$. Hence, for the one-dimensional case, the resolved shear stress becomes $\tau_\alpha = 1/2[\boldsymbol{M}_{\mathrm{E}}]_{11}$. Moreover, the following set of material parameters is considered for the computations: $E = 200$ GPa, $\nu = 0.3$, $H^{\mathrm{l}}_{\alpha 0} = 1$ GPa, $H^{\mathrm{g}}_0 = 100$ GPa, $b = 0.256$ nm, $m = 20$, $C_0 = 1$ MPa, and $\nu_0 = 10^{-3}$ s^{-}1.

First, the focus is on the impact of the gradient effect on the stress-strain response which is presented in terms of $[\boldsymbol{P}]_{11}$ normalized by the yield limit $Y_{\alpha 0}$ and $[\boldsymbol{F}]_{11} - 1$, cf. Fig. 3.11. By varying the internal length scale parameter l, the material response exhibits a size-dependent behavior. The size effect can be therefore quantified by the ratio l/L_0. A size-independent response is obtained in the limiting case if $l/L_0 \to 0$. For cases when $l/L_0 > 0$, an increased work-hardening rate is observed. This size effect is similar to the Hall-Petch effect [102, 203] in polycrystals where the internal length scale is associated with the average grain size. For that reason, the current single crystalline problem is comparable to a single grain surrounded by high angle boundaries.

As next, the distribution of dislocation densities is investigated in order to establish a correlation between macroscopic response and microstructural evolution of dislocations. Fig. 3.12 a) and b) show the distribution of GNDs and respectively SSDs along the truss length. From Fig. 3.12 a), it can be seen that the material strength scales with the density of GNDs which are piling up along the hard boundaries. Here, the GND density is computed as $\dot{g}_{\mathrm{i}\alpha} = b^{-1}\mathrm{d}\nu_\alpha/\mathrm{d}X_1$. With increasing ratio l/L_0, the internal length scale approaches the characteristic dimension of the sample. As a result, the pile up length increases and pile ups of opposite sign approach each other. This affects the plastic deformation behavior as can be seen from the resulting SSD density distribution in Fig. 3.12 b), which is calculated as $\dot{\zeta}_\alpha = b^{-1}\tilde{l}^{-1}\nu_\alpha$ using $\tilde{l} = 1$ µm, cf. Eq. (3.48). In conclusion, an homogeneously deforming crystal tends to localize as a result of size reduction as plastic strain gradients arise from piling up dislocations.

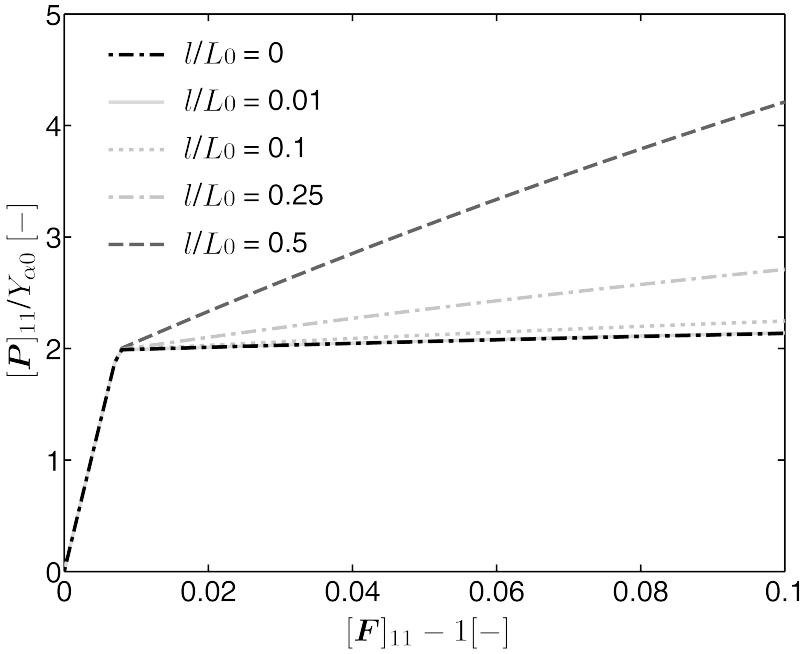

Figure 3.11: Normalized stress-strain response of a one-dimensional micron-sized truss experiencing a strengthening effect due to size-dependent hardening during tensile loading.

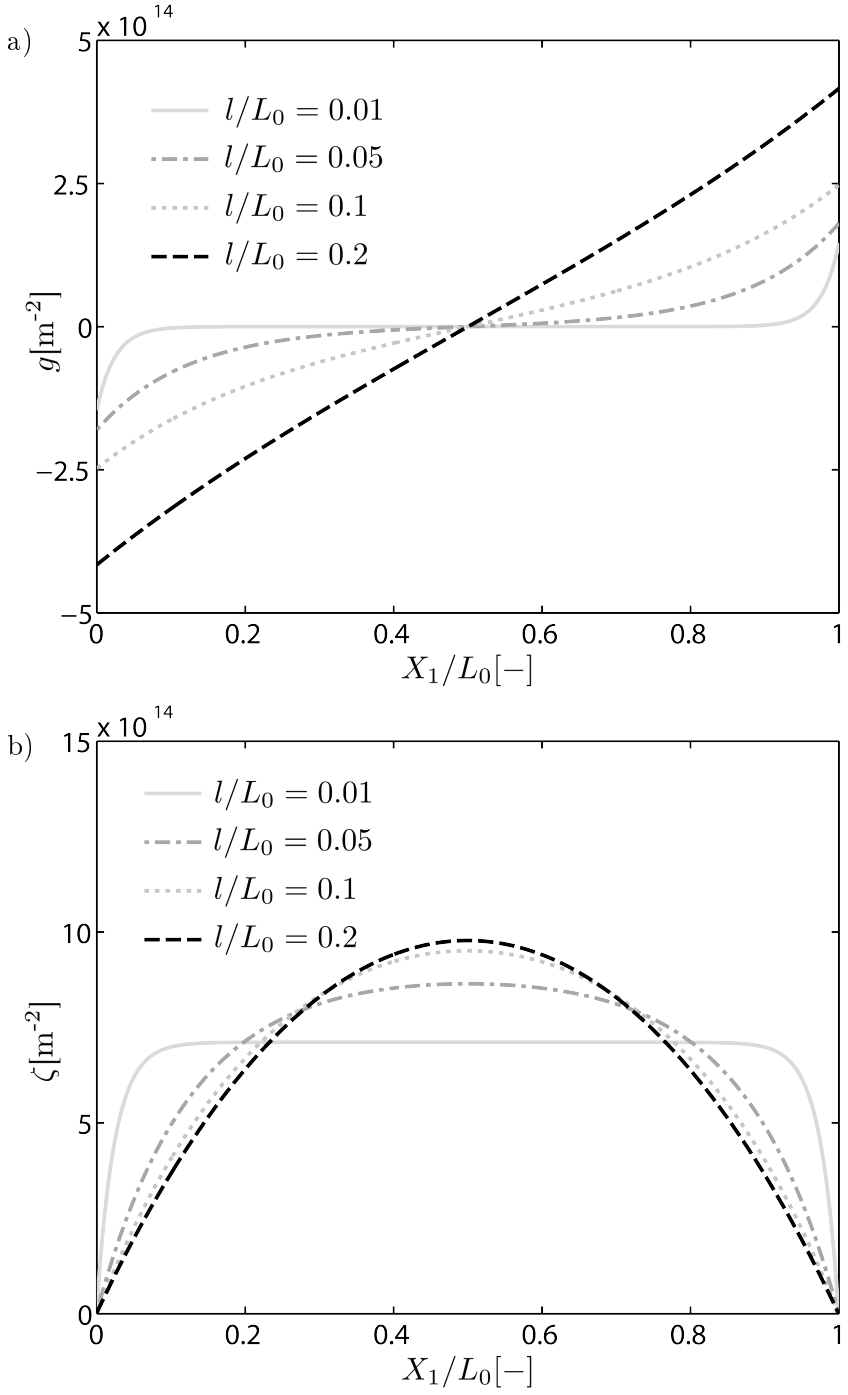

Figure 3.12: Distribution of a) the GND density and b) the SSD density along the normalized position of the truss and for different ratios l/L_0. A high l/L_0 ratio corresponds to a small sample dimension resulting in extensive GND storage and plastic slip localization.

4 Analysis of slip band formation during compression of micron-sized crystals

A finite-deformation strain gradient crystal plasticity model is implemented in a three-dimensional finite-element framework in order to analyze the deformation behavior and the stress-strain response of magnesium single crystals under c-axis orientation. The potential-based and thermodynamically consistent material model is formulated in a non-local and non-linear inelastic context in which dislocation densities are introduced via plastic strain gradients. Experiments have shown that the internal length scale of the microstructure starts to affect the overall stress-strain response when the sample size decreases to the micron scale. As a consequence, strain gradients develop, leading to an additional energetic-like hardening effect which results in an increase of the macroscopic strength with decreasing crystal size. In the case of uniaxial compression of c-axis-oriented single crystal micropillars, the model is able to predict the discrete dislocation glide in terms of a band-shaped slip zone. Two different pillar sample sizes are taken into account in order to investigate the intrinsic size effect during plastic deformation where the crystallographic orientation leads to the activation of pyramidal $\{11\bar{2}2\}$ $<11\bar{2}3>$ slip systems as reported in various experimental studies. The interaction of those slip systems is expressed in terms of latent hardening and excess dislocation development. A comparison between numerical results and corresponding experimental data is presented.

The content of this chapter has been published in [E. Husser, E. Lilleodden, S. Bargmann, *Computational modeling of intrinsically induced strain gradients during compression of c-axis-oriented magnesium single crystal*, Acta Materialia, 71, 206-219, 2014] and may include some modifications.

4.1 Introduction

Alternative light-weight materials such as magnesium will become more important in the future. Due to its low density and high strength-to-weight ratio, magnesium provides a high potential for a wide range of applications. Especially in high-tech functional materials, a fundamental knowledge about the microstructure is required to optimize the performance. The hexagonal close-packed lattice structure of magnesium represents still a major challenge since its deformation behavior is more complex compared to that of face-centered cubic metals. For that reason, a wide range of experimental studies has been performed in order to get a better understanding of the deformation mechanisms and their impact on the macroscopic strength. In this regard, small volume investigations using single crystals are performed under specific boundary conditions by which unwanted micromechanical processes can be excluded in order to focus on a particular deformation mechanism such as non-basal slip activation. Beside basal slip in hcp materials, the investigation of non-basal slip is of great interest since its impact on the mechanical properties must be considered in the material design process. Essential for the activation of non-basal slip systems in single crystals is the crystallographic orientation with respect to the loading direction by which basal slip has no resolved shear stress, e.g., loading parallel [210, 260] or perpendicular [187, 232] to the basal plane.

Apart from slip activation, the material response is strongly influenced by the size of the sample if dimensions are reduced to the micrometer range. In the literature, different kinds of size effects have been observed. To this extent, an extensive review with respect to different crystalline and amorphous metals is provided by Greer and De Hosson [88]. A meaningful distinction of size-dependent strengthening effects was illustrated by Sevillano [221, 222]. Here, size effects are classified into two types. According to Sevillano, extrinsic size effects are characterized by externally imposed plastic strain gradients, which are resolved by the storage of geometrically necessary dislocations, see [9, 80, 186]. As a consequence of the GND storage, size-dependent work hardening becomes significant if the gradient in plastic slip is significant or equivalently if the deformation length-scale is small relative to distributed plastic strain. Typical examples for deformation length-scales are the penetration depth in micro- and nanoindentation tests [184, 251], the beam thickness in microbending tests [81], and the wire diameter in microtorsion tests [80]. In particular, the storage of GNDs causes an additional energetic-like hardening effect which increases the macroscopic strength with decreasing sample size. Since such length scale-dependent hardening is not mapped by conventional crystal plasticity theory, a great variety of strain gradient crystal plasticity models have been developed. In those, the strain gradient is introduced into the mathematical model and, in many cases, associated with GNDs. Large deformation strain gradient crystal plasticity models have been formulated by, e.g., [17, 25, 57, 95, 153, 156, 194]. In contrast to extrinsic size effects, intrinsic size effects do not require the presence of mesoscopic plastic strain gradients but rather result from the interference of a plastic process zone with any internal (microstructural) length-scale [221], such as the average inter-dislocation distance, the inter-particle distance, or the physical size limited by free surfaces.

This contribution aims at the computational modeling of c-axis-oriented magnesium single crystal where strain gradients are imposed intrinsically, due to the small sample size and the large microstructural length associated with the low dislocation density, single crystalline structure. For this purpose, a finite-deformation strain gradient crystal plasticity model is implemented into a three-dimensional finite element framework. While there have been several numerical studies of microcompression of fcc single crystals, to the authors' knowledge no such studies have been applied to hcp systems. For instance, Raabe and Roters [208] investi-

gated the effect of different initial crystal orientations, diameter-to-height ratios, and friction coefficients on the deformation behavior of copper single crystals using conventional crystal plasticity. In the work of Shade et al. [223], lateral constraint effects of single-slip oriented nickel-base superalloy single crystals were studied, also using conventional crystal plasticity. It turned out that the lateral constraint has a significant effect on the strain hardening behavior. However, in both studies, the effects of GND induced plastic slip gradients as described by Nye [186] were not considered. For this reason a deformation mode typical observed in micro-compressed single crystals, which is characterized by a localization of several slip systems, cannot be reproduced. Recently, Kuroda [152] presented a numerical example using a strain gradient theory that is based on the same single-slip oriented nickel-base superalloy as investigated in [223]. It has been shown that the consideration of the gradient effect is essential for the formation of a particular deformation mode which is composed of a band-shaped slip zone and two dead zones. In this context, the study showed how various parameters, such as different macroscopic and microscopic boundary conditions as well as different length-scale to pillar diameter ratios, influence the deformation mode. In delimitation to this, we are focusing on a specific set of parameters in order to validate the here applied strain gradient crystal plasticity model according to micromechanical testing of magnesium singly crystal. Resulting stress-strain curves of two representative sample sizes are directly related to experimental data of Lilleodden [157]. In addition, multiple slip including slip system interactions in terms of latent hardening and latent dislocation nucleation resistance is considered.

4.2 Micromechanics of single-crystal magnesium under c-axis compression

Due to its hcp crystal structure, crystallographic slip in magnesium primarily occurs on the (0001) basal plane where the close-packed slip directions are of type $\{11\bar{2}0\}$. However, many experimental observations have shown that non-basal slip takes place, especially if the loading direction is parallel or perpendicular to the basal plane. In this contribution, the relevant crystallographic orientation of magnesium single crystal is the c-axis- or (0001)-orientation as illustrated in Fig. 4.1. Note that the direction of the c-axis is coincident with the direction of the $<c>$ Burgers vector, and is aligned with the loading axis of the indenter. Consequently, slip systems including the $<a>$ Burgers vector, such as the basal slip systems have zero Schmid factor, i.e. they have no resolved shear stress. Therefore, those slip systems cannot contribute to a vertical deformation along the c-axis necessitating the activation of less easily activated slip systems. As reported first by Obara et al. [187] and Stohr and Poirier [232], pyramidal $\{11\bar{2}2\} < 11\bar{2}3 >$ slip, hereafter referred to as $\pi 2$ slip, was observed during compression tests of magnesium single crystal along the c-axis. Due to the symmetry along the c-axis, six $\pi 2$ slip systems are exposed to the same stress. The simultaneous activation of six slip systems leads to a strong work-hardening behavior due to slip system interaction processes.

Recent microcompression studies by Lilleodden [157] and Byer et al. [40] confirm that $\pi 2$ slip is the predominant deformation mechanism during c-axis compression of magnesium single crystals. Lilleodden also investigated the influence of the pillar diameter and determined a strong dependency of yield stress on the crystal size while the observed deformation characteristics remained qualitatively the same for all diameters. The size-dependent yield stress characteristic is illustrated in Fig. 4.2 on the basis of three different nominal sample diameters (2.1 µm, 6.1 µm, 10 µm), where three experimental data sets are presented for each size. The shown yield stresses have been obtained by analyzing the slope of the load-displacement data

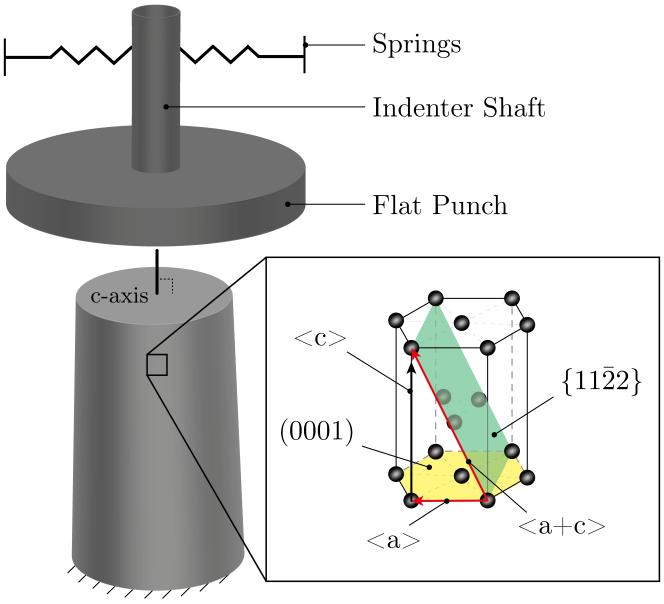

Figure 4.1: Schematic illustration of the microcompression set-up including the crystallographic orientation. The loading axis is perpendicular to the (0001) basal plane. Thus, basal slip in {11$\bar{2}$0} directions (<a> Burgers vector) is prevented. Instead, pyramidal {11$\bar{2}$2} planes are preferred and slip in < 11$\bar{2}$3 > directions (<$a+c$> Burgers vector) is activated.
Reprinted from [111] with permission from Elsevier, Copyright 2014.

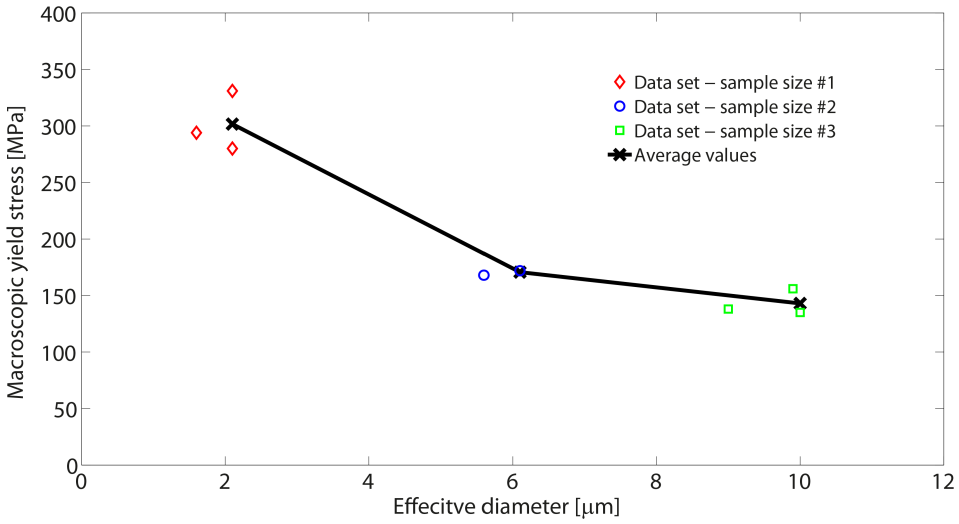

Figure 4.2: Experimental yield stress data [157] for three different nominal sample diameters: 2.1 µm, 6.1 µm, and 10 µm. Averaged values for the 2.1 µm and 6.1 µm pillars are determined as 300 MPa and 170 MPa, respectively.
Reprinted from [111] with permission from Elsevier, Copyright 2014.

and taking the macroscopic yield point as the point corresponding to a 50% decrease in stiffness from the maximum slope. Moreover, for each nominal diameter, an average value for the macroscopic yield stress is drawn in the diagram and taken as input for numerical simulations.

In order to explain the mechanism leading to this effect, let us first consider polycrystals, and the well-known size effect associated with the findings of Hall [102] and Petch [203], e.g. the grain-size-dependent hardening. In this case, grain boundaries can be envisaged as insurmountable obstacles to dislocation motion. The resulting dislocation pile-ups cause inhomogeneous plastic deformation which in turn results in a reorientation of the crystal lattice. According to Ashby [9], GNDs need to accumulate in such regions to preserve lattice compatibility and lead to localized lattice rotation. The resulting hardening effect rises with decreasing sample size due to the grain boundary surface to volume ratio. However, as pointed out in Ref. [221], the Hall-Petch effect is a mixed type size effect which shows both a size-dependent yield stress characteristic caused by dislocation pile-up and a size-dependent work-hardening behavior due to GND storage. Here, the average grain size represents the internal length-scale of the polycrystalline sample. With respect to single crystal, there are no such grain boundaries and dislocations can freely move through the surface. But as already indicated in Fig. 4.1, plastic slip is constrained at the top of the pillar due to contact. Therefore, a similar pile-up effect can be expected in the top region of the pillar despite the free surfaces in the radial direction. Likewise, the region below the pillar is subjected to minimal stresses such that an indirect constraint in plastic flow develops in the lower region of the pillar. The microcompression loading condition therefore is associated with intrinsic strain gradients rather than an extrinsic effect, since no external gradient in plastic strain is directly imposed; internal length-scales are taken to be responsible for the observed size effect. More specifically, the plastic process size is limited by the size of the pillar [221], and constrained at the top and bottom of the pillar, and the parameter expected to govern the strength of the size effect is the ratio of microstructural length l_α to nominal diameter D_m of the micropillar; for the case $l_\alpha / D_\mathrm{m} \approx 0$, the yield stress is size independent.

Due to the aforementioned constraints at the top and bottom of the pillar, microcompressive loading leads to an inhomogeneous deformation of the sample in terms of band-shaped slip. As previously stated, the experimental results in Ref. [157] show no drastic effect on the hardening rate while reducing the sample size. Therefore, the effect of GND storage is responsible for a strongly localized deformation mode, as highlighted in Ref. [152], rather than causing an increased work-hardening rate. Additionally, the characteristic of the deformation mode is influenced by the friction conditions, as investigated by Shade et al. [223] for microcompression of a single-crystal nickel superalloy. Here, it was found that a lateral constraint of the pillar top (Coulomb friction coefficient of 1.0) causes large bands of disoriented regions and, finally, an intensified inhomogeneous plastic deformation. The influence of a high friction coefficient is clearly pointed out in Ref. [157] in which the center section of the pillar undergoes a massive shear off after reaching a critical strain level while the upper section remained aligned with the original axis due to high contact friction.

The present work is focused on magnesium micropillars as used in the experiments of Lilleodden [157]. The micropillars are created from bulk material using a focused ion beam (FIB). This method results in a slightly larger base diameter than top diameter as depicted in the scanning electron microscopy (SEM) images in Fig. 4.3 for a representative pillar geometry. Compression tests are conducted by a nanoindenter equipped with a circular flat punch of 15 µm diameter and tests are run at a nominal displacement rate of 0.001 s^{-1}, i.e., under quasi-static conditions.

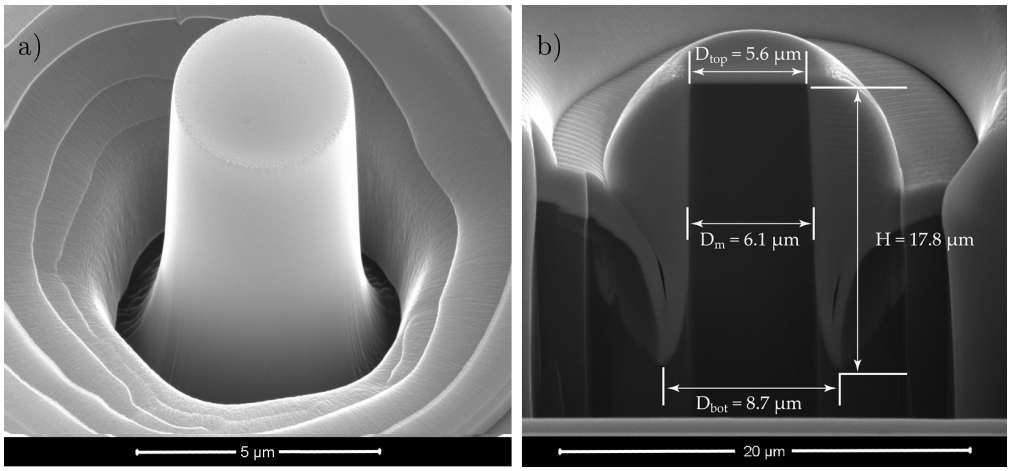

Figure 4.3: Scanning electron microscope images (taken from [157]) of a representative micropillar of a nominal diameter of 6.1 µm showing a) the predeformed micropillar geometry and b) its corresponding FIB machined cross section.
Reprinted from [111] with permission from Elsevier, Copyright 2014.

4.3 Constitutive description

The non-local crystal plasticity model considered to model the size-affected deformation behavior of single crystalline micropillars is based on the full continuum model of the vector-valued GND density. Recalling Eq. (3.60), the GND density consists of in-plane edge and screw components as well as a normal to slip plane edge component. However, only the in-plane edge component $g^{\mathrm{e}}_{\mathrm{i}\alpha}$ of the dislocation density field is considered in the following. As a result, Eq. $(3.60)_2$ reduces to

$$\dot{g}^{\mathrm{e}}_{\mathrm{i}\alpha} = \sum_{\beta} \nu_\alpha \left[\boldsymbol{s}_\beta \cdot \boldsymbol{n}_\alpha\right] g^{\mathrm{e}}_{\mathrm{i}\beta} - \frac{1}{b} \nabla_{\mathrm{i}} \nu_\alpha \cdot \boldsymbol{s}_\alpha, \tag{4.1}$$

where $b = b_\alpha$ denotes the amplitude of the Burgers vector in any of the six $<a+c>$-directions. Notice that the second interaction term in Eq. $(3.60)_2$ is neglected due to the above made assumption. While the second term in Eq. (4.1) corresponds to GND accumulation associated with inhomogeneous plastic deformation, the first term accounts for GND storage as a result of dislocation interaction mechanisms between active $\pi 2$ systems. In this regard, the presence of dislocations with respect to slip systems β leads to a reduced gradient effect with respect to slip system α since both terms are of opposite sign. This effect can be interpreted as latent dislocation nucleation resistance. This modeling approach for interactions between dislocations is quite different from other approaches in the literature, compare for instance Evers et al. [78]. The relation between the intermediate gradient and the material gradient of the plastic slip rate is of particular importance and is given as

$$\nabla_{\mathrm{i}} \nu_\alpha = \boldsymbol{F}_{\mathrm{P}}^{-\mathrm{T}} \cdot \nabla_{\mathrm{r}} \nu_\alpha. \tag{4.2}$$

In terms of a thermodynamic consistent formulation, the hardening effects of strain gradients are introduced as energetic-like processes within the free energy density ψ_{i} which is assumed to be additively decomposed according to Eq. (3.64), i.e. in an elastic contribution $\psi^{\mathrm{el}}_{\mathrm{i}}$, a

(local) strain hardening contribution ψ^{l}, and a (non-local) gradient hardening contribution $\psi^{\mathrm{g}}_{\mathrm{i}}$. The elastic energy contributions is chosen to mimic an isotropic (compressible) Neo-Hookean response which is captured by the form presented in Eq. (3.25). Local hardening is defined via a linear hardening relation which is comprised of self and latent hardening contributions, cf. Eq. (3.78). Moreover, the screw GND density component within the defect energy in Eq. (3.84) is neglected. Hence the energy expression reduces to

$$\psi^{\mathrm{g}}_{\mathrm{i}} = \frac{1}{2} b^2 l^2 \sum_{\alpha,\beta} H^{\mathrm{g}}_0 g^{\mathrm{e}}_{\mathrm{i}\alpha} g^{\mathrm{e}}_{\mathrm{i}\beta}. \tag{4.3}$$

Size-dependent effects are governed by the internal length-scale parameters which is assumed to be the same for all considered slip systems in the current context, i.e., $l = l_\alpha = l_\beta$. In accordance to Ekh et al. [70], the micro-hardening stress vector is determined as $\boldsymbol{\kappa}_\alpha = \partial\psi_{\mathrm{i}}/\partial\nabla_{\mathrm{i}}\gamma_\alpha$. In extension to [70], the scalar-valued microstress in the current framework is determined by two contributions which is due to the interaction between active plastic slip rates and GND densities of latent slip systems, i.e.,

$$\kappa_\alpha = \frac{\partial\psi^{\mathrm{l}}_{\mathrm{i}}}{\partial\gamma_\alpha} + \frac{\partial\psi^{\mathrm{g}}_{\mathrm{i}}}{\partial g^{\mathrm{e}}_{\mathrm{i}\alpha}} \frac{\partial g^{\mathrm{e}}_{\mathrm{i}\alpha}}{\partial\gamma_\alpha}. \tag{4.4}$$

In order to account for kinetic effects on the hardening behavior, e.g., rate-dependent dislocation nucleation, the model is based on a dissipation potential $\chi_{\mathrm{i}}(\{\nu_\alpha\})$ of the form

$$\chi_{\mathrm{i}} = \sum_\alpha \left[Y_\alpha \nu_\alpha + \frac{m}{m+1} C_0 \nu_0 \left[\frac{\nu_\alpha}{\nu_0} \right]^{\frac{m+1}{m}} \right]. \tag{4.5}$$

Note that the dissipation principle is sufficiently satisfied if the dissipation potential χ_{i} is non-negative and separately convex in its arguments, see [226]. Following Svendsen and Bargmann [238], the relevant field relations are derived from the rate potential

$$r_{\mathrm{i}} = \Upsilon_{\mathrm{i}} + \chi_{\mathrm{i}}. \tag{4.6}$$

where Υ_{i} is determined via Eq. (3.67). Assuming quasi-static, isothermal conditions and neglecting body forces and external supplies, the variation of the rate potential Eq. (4.5) yields the following field relations

$$\begin{aligned} \mathbf{0} &= \mathrm{Div}_{\mathrm{i}}(\boldsymbol{F}_{\mathrm{E}} \cdot \boldsymbol{S}_{\mathrm{E}}), \\ \nu_\alpha &= \nu_0 \left[\frac{\langle \tau_\alpha - \kappa_\alpha + \mathrm{Div}_{\mathrm{i}}(\boldsymbol{\kappa}_\alpha) - Y_\alpha \rangle}{C_0} \right]^m. \end{aligned} \tag{4.7}$$

For a detailed derivation, see Bargmann et al. [17]. These field relations represent the balance of linear momentum and the evolution equation for the plastic slip rate, i.e., the viscoplastic flow rule. It should be noticed that $\mathrm{Div}_{\mathrm{i}}(\boldsymbol{F}_{\mathrm{E}} \cdot \boldsymbol{S}_{\mathrm{E}}) = \mathrm{Div}_{\mathrm{r}}(\boldsymbol{P})$.

4.4 Finite element model

Numerical computations are done using the finite element analysis program Abaqus. The constitutive relations for the strain gradient crystal plasticity model presented here are implemented into the subroutine UEL (User ELement). As depicted in Fig. 4.4, the finite-element

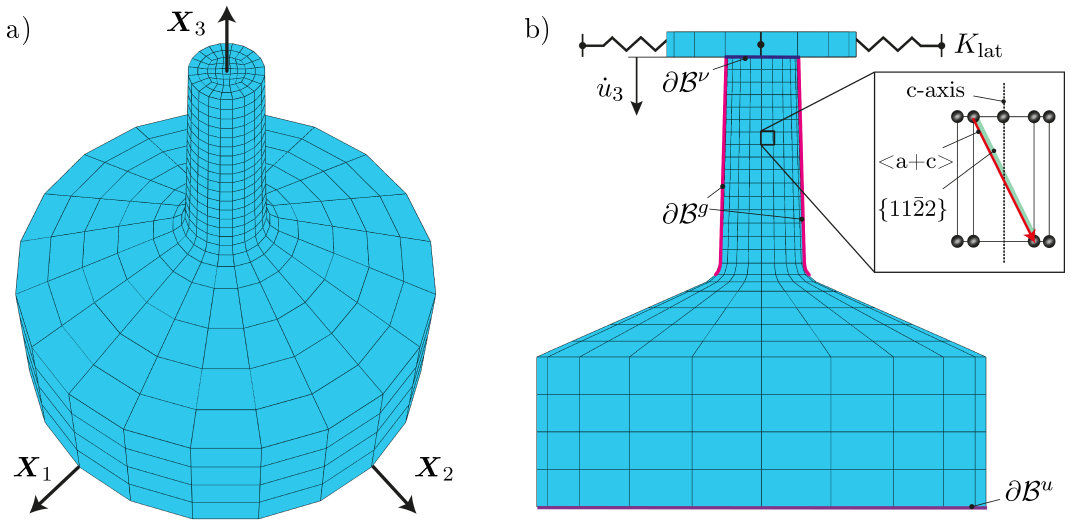

Figure 4.4: Finite element model consisting of micropillar, surrounding bulk substrate, rigid punch, and lateral springs. a) Perspective view of the micropillar sample; b) side view showing boundaries and the crystallographic orientation of the single crystal.
Reprinted from [111] with permission from Elsevier, Copyright 2014.

model consists of a micropillar sample connected to bulk material, and a punch connected to four laterally placed spring elements. In total, 1755 brick elements with 2128 nodes are used for meshing pillar and bulk material, resulting in a total number of 19,152 degrees of freedom (3 displacements + 6 GND densities). Including the bulk substrate in the finite-element model provides more realistic boundary conditions since the bottom of the pillar deforms elastically. The micropillar and the bulk material have the same crystallographic orientation. The punch is modeled as rigid and is tied to the top surface of the micropillar in order to reflect Coulomb friction with a coefficient of 1.0. The pillar-bulk junction is curved to reduce sharp changes in geometry such that artificial stress peaks at the surrounding junction are prevented.

The axial displacement is assigned to the entire rigid punch by a predefined displacement rate $\dot{u}_3$, against the $\boldsymbol{X}_3$-direction. Additionally, the rigid punch is laterally constrained by four spring elements of stiffness K_{lat}, located at the outer points of the punch along the $\boldsymbol{X}_1$ and $\boldsymbol{X}_2$ directions. The bottom surface of the bulk substrate $\partial\mathcal{B}^u$ is constrained by:

$$\begin{aligned} u_1 &= 0 \quad \text{along} \quad X_2 = 0 \quad \text{on } \partial\mathcal{B}^u, \\ u_2 &= 0 \quad \text{along} \quad X_1 = 0 \quad \text{on } \partial\mathcal{B}^u, \\ u_3 &= 0 \quad \text{on } \partial\mathcal{B}^u. \end{aligned} \tag{4.8}$$

With respect to boundary conditions for the micromechanical problem, microhard boundary conditions, cf. Eq. (3.88), are chosen for the top surface $\partial\mathcal{B}^{\nu}$ of the micropillar. Hence, the plastic slip rate ν_α becomes constrained such that dislocation flow through that boundary is prevented. Consequently, an accumulation, i.e., pile up, of GNDs results. Note that similar boundary conditions arise naturally in the bulk substrate due to a sudden drop of acting stresses. With regard to the lateral surface $\partial\mathcal{B}^g$, the GND density rates $\dot{g}^{\mathrm{e}}_\alpha$ are constrained by microfree conditions, cf. Eq. (3.87). Thus, the GND densities are forced not to pile up along the lateral surfaces but rather to flow through the surfaces without any interaction and allow it to deform plastically.

The top surface of the micropillar can alternatively be defined as microfree. The influence of this approach on the deformation mode was investigated in [152]. However, such an approach would imply that the contact surface of the sample can freely deform. This is highly unrealistic since the deformation is imposed here. For the here considered case, all slip plane are intersecting the contact surface. Hence, in consideration of the experimental set-up, a microhard top surface is assumed for the following simulations.

4.5 Numerical results and discussion

The numerical solution of the presented model is approached via a dual-mixed finite element method as proposed by Ekh et al. [70], see also Svedberg and Runesson [236]. In that sense, the balance of linear momentum Eq. $(4.7)_1$ and the evolution equations for GND densities Eq. (4.1) are taken as global field equations in space and solved with a monolithic Newton-Raphson iteration scheme. Furthermore, an implicit time integration procedure is applied where both the local relations and the global field relations are discretized in time with an implicit finite-difference method. Trilinear (8-node) brick elements with $2 \times 2 \times 2$ Gauss points are chosen for discretization in space. Both fields, the mechanical displacements $\boldsymbol{u}$ and the GND densities g^{e}_{α}, are interpolated linearly with the same shape functions. Note that in addition to the three translational degrees of motion, each node contains dislocation densities as enhanced degrees of freedom according to the number of considered slip systems.

4.5.1 Material parameters

Two representative micropillars of different size are considered in the numerical simulations. The size of the micropillar is characterized by the middle diameter. The larger sample has a nominal diameter of 6.1 µm (cf. Fig. 4.3), whereas the smaller sample has a nominal diameter of 2.1 µm. For both specimens, the nominal height to mid-plane diameter ratio is approximately 3:1. A total engineering strain of 5 % is applied in both simulations using a nominal strain rate of 0.001 s^{-1} [157]. With respect to the elasticity parameter, a Young's modulus of 45 GPa is adopted, as was found from partial unloading tests conducted at about 1% total strain [157]. The Poisson ratio is taken as $\nu = 0.35$ according to [11]. Macroscopic yield stresses have been detected from the provided data and stated in Table 4.1. Further, a lateral stiffness of $K_{\mathrm{lat}} = 13$ kN/mm is taken from nanoindenter calibration data.

During compression, a simultaneous activation of six $\pi 2$ slip systems is assumed, consistent with experimental observations [40, 157, 187, 232]. Here, latent hardening coefficients are used in order to model a physical deformation behavior where one slip system becomes dominant during deformation. In particular, hardening coefficients are chosen as $q_{\alpha\beta} = 1$ for $\alpha = \beta$ (self hardening) as well as $q_{\alpha\beta} = 0.25$ and $q_{\alpha\beta} = 2$ in case of latent hardening ($\alpha \neq \beta$) along the preferred slip system and the stagnating systems, respectively. This strategy is reasonable, because if a lattice disorientation is used in order to control the multiple slip activation, some variation of the crystallographic orientation might lead to a non-neglectable increase of the Schmid factor for basal slip.

Experimental data shows that the sample size of the micropillar has an influence on the macroscopic yield stress $\overline{Y}$. According to the here considered (0001) orientation leading to $\pi 2$ slip activation, the relation between macroscopic and microscopic yield stress is given by $Y_{\alpha} = f_{\pi 2}\overline{Y}$, where $f_{\pi 2} = 0.45$ represents the corresponding Schmid factor. The internal

Table 4.1: Elasticity and process parameters used for numerical simulations.

nominal pillar diameter	D_{m}	6.1	2.1	µm
macroscopic yield stress	$\overline{Y}$	170	300	MPa
Young's modulus	E	45	45	GPa
Poisson's ratio	ν	0.35	0.35	-
engineering strain	$\varepsilon_{\mathrm{eng}}$	0.05	0.05	-
nominal strain rate	$\dot{\varepsilon}_{\mathrm{eng}}$	0.001	0.001	s^{-1}
lateral stiffness	K_{lat}	13	13	kN/mm

length-scale parameter is assumed to be $l = 1$ µm for all slip systems. This assumption is consistent with findings of Begley and Hutchinson [26] where values for soft metals have been found to be about 1.6 µm and for hard metals to be in the range between 0.5 and 1 µm. In this sense, hcp metals such as pure magnesium can easily be assigned to the class of hard metals. Furthermore, a value of 1 µm indicates good agreement with the observed size effect when quantifying the impact of the internal length on the yield stress by the quotient l/D_{m}. With regard to the three different pillar sizes (2.1 µm, 6.1 µm, and 10 µm) which have been examined in [157], the quotient becomes 0.476, 0.164, and 0.1. The strong increase of the quotient from the 6.1 µm sample to the 2.1 µm sample is in accordance with the high jump in the yield stress, whereas the yield stress difference between the 6.1 µm sample and the 10 µm sample is comparatively small. Note that an infinitely large sample would lead to a quotient of ≈ 0, indicating no internal effects on the deformation process.

According to the quasi-static loading condition, the viscoplastic material response is modeled as rate-independent using a rate sensitivity exponent of $m = 1/0.05 = 20$. The drag stress and reference shear rate are taken to be $C_0 = 10$ MPa and $\nu_0 = 10^{-3}$ s, respectively. Moreover, the amplitude of the Burgers vector is calculated as $b = \sqrt{a^2 + c^2}$, where the lattice constants are $a = 0.3203$ nm and $c = 0.52002$ nm [117]. A summary of the here used material parameters is given in Table 4.2.

4.5.2 Strain gradient effect on deformation behavior

A quantification of plastic deformation due to dislocation glide is done using the accumulated plastic slip γ_α, which is defined as the time integral over the plastic slip rate, cf. Eq. (3.47). With respect to multiple slip activation, an appropriate assessment of the total plastic deformation is provided by taking the effective accumulated plastic slip γ^{eff} into account, cf. Eq. (3.47).

The deformation mode during compression is first analyzed by comparing the results between conventional crystal plasticity without any internal length-scale consideration and gradient-enhanced crystal plasticity. In both cases, latent hardening is active such that the deformation is mainly driven by one favorable slip system. Fig. 4.5 shows the computed effective accumulated plastic slip γ^{eff} at the final strain state of 5 %. It can be seen that the deformation mode predicted by the gradient theory is characterized by a band-shaped slip zone which corresponds to the most intensive glide zone of the single crystal, cf. Fig. 4.5 b). In contrast to

Table 4.2: Material parameters used for numerical simulations.

nominal pillar diameter	D_{m}	6.1	2.1	µm
microscopic yield stress	Y_α	76.5	135	MPa
local hardening modulus	H_0^{l}	720	720	MPa
gradient hardening modulus	H_0^{g}	26.5	26.5	GPa
drag stress	C_0	10	10	MPa
rate sensitivity exponent	m	20	20	-
reference shear rate	ν_0	10^{-3}	10^{-3}	s^{-1}
internal length scale parameter	l	1	1	µm
amplitude of Burgers vector	b	0.61075	0.61075	nm

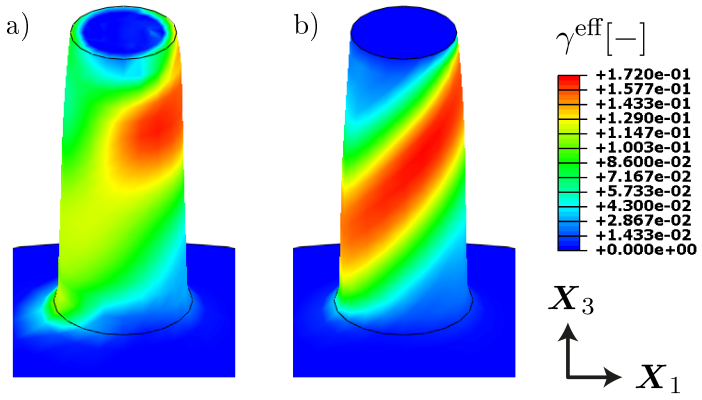

Figure 4.5: Contour plots showing effective accumulated plastic slip distribution γ^{eff} at 5 % nominal strain for the 6.1 µm sample. Deformation mode differs strongly when comparing results predicted by a) conventional crystal plasticity ($l = 0$) and b) strain gradient-enhanced crystal plasticity. The gradient effect leads to a pronounced slip band as observed in experiments.
Reprinted from [111] with permission from Elsevier, Copyright 2014.

this, the conventional approach shows a complete different response, see Fig. 4.5 a). Here, the internal length-scale ($l = 0$) has no influence on the overall plastic process.

When comparing the initial state of plastic deformation of both theories, it is obvious that the localization of plastic deformation takes place at different zones. In the case of $l = 0$, the localization occurs in the left upper corner at the beginning of the deformation and shifts to the right side at about two thirds of the height. Fig. 4.6 a) illustrates the initial plastic deformation process at two different strain states using the accumulated plastic slip of the most preferred slip system $\boldsymbol{s}_\alpha$. Here, the plastic deformation of the top corner is due to the missing micro-hard conditions within the conventional theory. In comparison to the gradient-enhanced model, the localization of plastic deformation starts at the right upper corner where the cross section area of the pillar is minimal and develops strongly in direction of the corresponding slip system $\boldsymbol{s}_\alpha$, see Fig. 4.6 b).

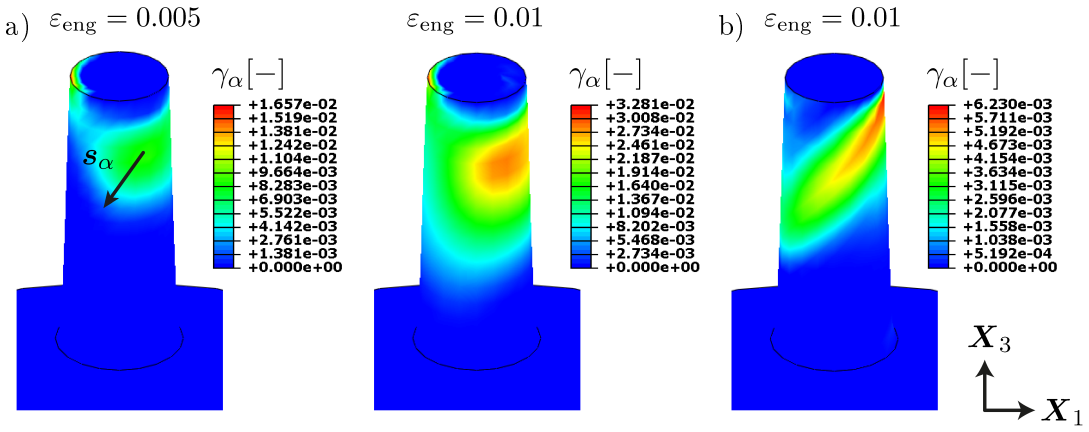

Figure 4.6: Contour plots showing accumulated plastic slip distribution γ_α of the preferred slip system α. Localization of plastic deformation is presented for a) conventional crystal plasticity at 0.5 % and 1 % nominal strain and for b) strain gradient-enhanced crystal plasticity at 1 % nominal strain. The strain gradient theory shows a much more realistic glide deformation where the plastic slip γ_α develops strongly in the corresponding slip system direction $\boldsymbol{s}_\alpha$. Reprinted from [111] with permission from Elsevier, Copyright 2014.

The formation of the plastic slip band is caused by the backstress-like stresses $\text{Div}_{\text{i}}(\boldsymbol{\kappa}_\alpha)$. According to that, the effective shear stress, here defined as $\tau_\alpha^{\text{eff}} = [\tau_\alpha - S_\alpha]^m/[C_0]^m$, indicates a similar formation of a band-shaped zone as illustrated in Fig. 4.7. Its development shows that the stress band formation is almost completed at around 0.65 % nominal strain, just after the elastic limit has been reached. During deformation, the local stress band widens downwards whereas the intensity of τ_α^{eff} decreases continuously. By comparing the distribution of τ_α^{eff} at 1.5 % and 5 % nominal strain, it is seen that the local stress field reaches a plateau. As a consequence, the development of the plastic slip band expressed by γ_α stagnates such that a further deformation would not lead to an evident change in the characteristic of the band-shaped zone.

4.5.3 Influence of sample size variation

The deformation mode obtained by gradient-enhanced crystal plasticity has two major characteristics. Firstly, a localization of plastic flow into a slip band can be observed. Additionally, that slip band formation leads to the effect that some regions do not deform plastically. That kind of deformation mode comprising a highly deformed slip zone and two death zones was also computed by Kuroda [152] using a strain gradient approach within a different constitutive framework. However, by varying the sample size, i.e. going form 6.1 µm to 2.1 µm, the deformation characteristic becomes even more intensive. This is illustrated in Fig. 4.8 by comparing the results of both sample sizes at nominal strain states of 2.5 %, 4 %, and 5 %.

As can be seen, the gradient effect leads to a pronounced slip band formation. With regard to the smaller sample, the obtained deformation mode shows a more concentrated slip band and larger death regions. This is due to the fact that the influence of the internal length-scale is increased in the smaller sample in terms of an higher gradient contribution in the micro hardening stresses.

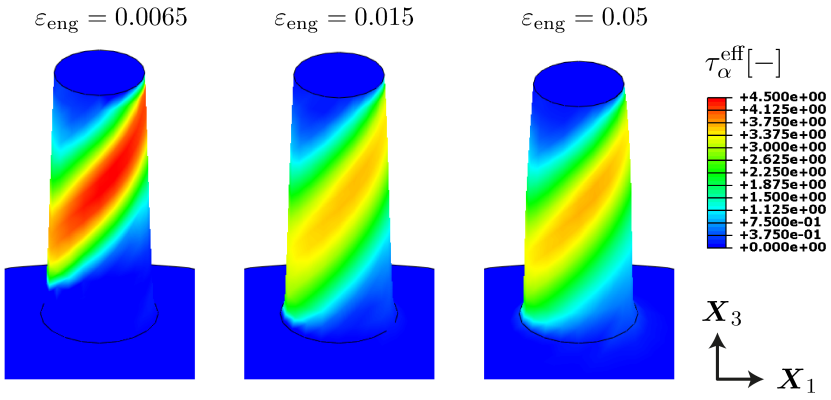

Figure 4.7: Contour plots showing effective shear stress distribution, here defined as $\tau_\alpha^{\text{eff}} = [\tau_\alpha - S_\alpha]^m/[C_0]^m$ of the preferred slip system α. A stress band forms at the early state of plastic deformation. During deformation, the pronounced band-shaped zone widens downwards whereas its intensity decreases up to a certain level.
Reprinted from [111] with permission from Elsevier, Copyright 2014.

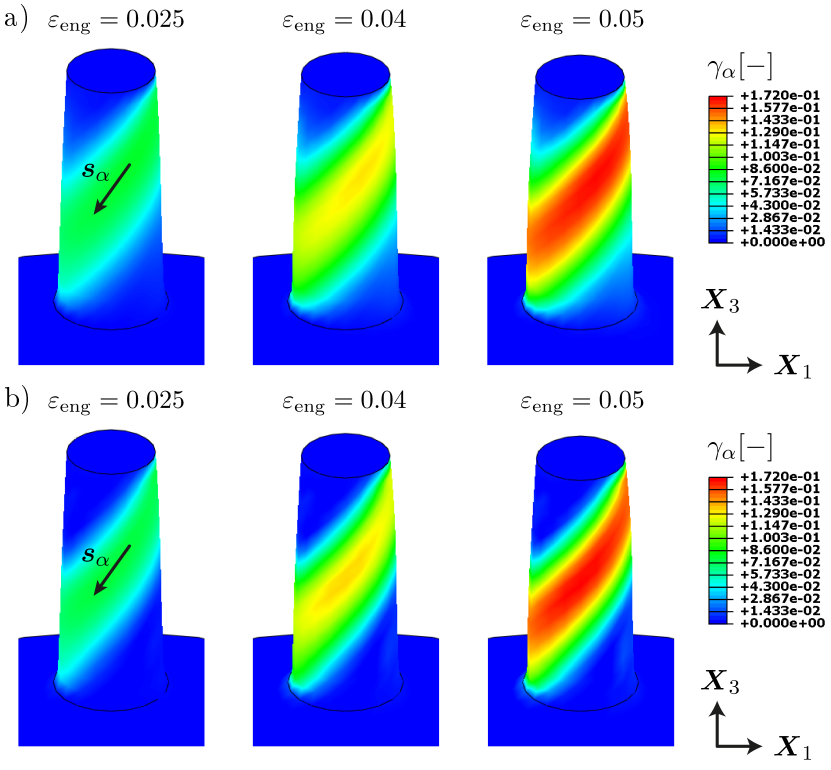

Figure 4.8: Contour plots showing accumulated plastic slip distribution γ_α of the preferred slip system α for a) the 6.1 µm and b) the 2.1 µm pillar. The increased influence of the internal length-scale due to the shrunk sample size leads to a more intensive deformation characteristic in terms of a stronger slip band.
Reprinted from [111] with permission from Elsevier, Copyright 2014.

4.5.4 Analysis of dislocation densities

The final distribution of dislocation densities is compared between both sample sizes as depicted in Fig. 4.9 with respect to the middle cross section ($\boldsymbol{X}_1$-$\boldsymbol{X}_3$ plane). In each case, densities are distinguished with respect to their sign: a) Positive dislocations move in accordance to the defined slip direction $\boldsymbol{s}_\alpha^+$; b) negative dislocations move in the opposite direction $\boldsymbol{s}_\alpha^-$. According to the postulated evolution equation and the considered microscopic boundary conditions, the intrinsically induced strain gradients lead to an accumulation of GNDs in the top and bottom region of the micropillar. Dislocations cannot leave through the top of the pillar due to the predefined micro-hard boundary condition. In contrast to that, an artificial micro-boundary seems to appear in the pillar-bulk connection zone. Here, dislocations move only slightly into the bulk material since the driving stress field drops drastically because of the rapid extending cross section area. Moreover, a slight change in the GND density distribution is obtained when comparing both sample sizes. The contour plots of the smaller sample are less disperse but rather more strongly aligned with the slip direction $\boldsymbol{s}_\alpha$. Calculated values are within an experimental reasonable range of about 10^{12}-$10^{13}\mathrm{m}^{-2}$ [41] and differ only slightly between both samples.

In order to give an approximate estimation of the impact of the GND density, it is helpful to analyze its percentage share in the total dislocation density which in the current context is given by $\rho_\alpha = g^{\mathrm{e}}_{\mathrm{i}\alpha} + \zeta_\alpha$. Recall that the accumulation of SSDs is of statistical nature and can be related to the crystallographic plastic slip [78]. Therefore, although they are not explicitly considered in the model formulation, they are indirectly involved in the local hardening contribution via the plastic slip variables. Following Fleck et al. [80] and Brinckmann et al. [35], an appropriate measure for the effective SSD density is introduced on the basis of the effective accumulated plastic slip γ^{eff}, i.e.,

$$\zeta^{\mathrm{eff}} = \frac{\gamma^{\mathrm{eff}}}{b\tilde{l}}, \tag{4.9}$$

which yields Eq. (3.48) for non-constant Burgers vector magnitudes. Moreover, $\tilde{l} = 0.71$ µm is taken from [2] as the distance between forest dislocations in magnesium. Then, the effective

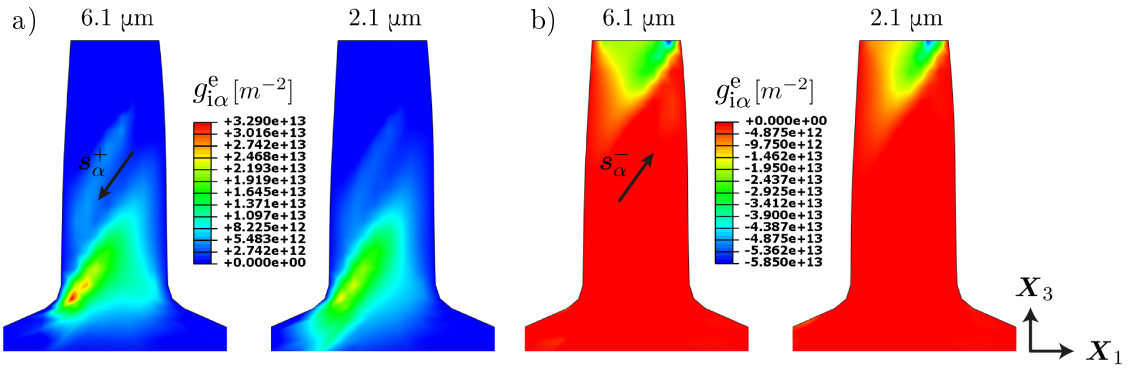

Figure 4.9: Contour plots of GND density distribution $g^{\mathrm{e}}_{\mathrm{i}\alpha}$ of the preferred slip system α within the middle cross section ($\boldsymbol{X}_1$-$\boldsymbol{X}_3$ plane). Plots refer to a) positive and b) negative accumulated dislocation densities and to both (6.1 µm and 2.1 µm) sample sizes, respectively.
Reprinted from [111] with permission from Elsevier, Copyright 2014.

GND density is defined as (considering only edge GND densities)

$$g_{\mathrm{i}}^{\mathrm{eff}} = \sqrt{\sum_{\alpha} [g_{\mathrm{i}\alpha}^{\mathrm{e}}]^2}. \tag{4.10}$$

The Evolution of effective GNDs and SSDs during compression is examined along the central axis in $\boldsymbol{X}_3$-direction of both micropillars for 1 %, 2.5 %, and 5 % nominal strain, respectively. Starting from the bottom of the sample, the central axis intersects characteristic deformation regions, the death zones and the pronounced slip band zone. In Fig. 4.10, computed profiles are shown for a) effective SSD density, b) effective GND density, and c) percentage amount of effective GND density within the total dislocation density $\rho^{\mathrm{eff}} = \zeta^{\mathrm{eff}} + g_{\mathrm{i}}^{\mathrm{eff}}$. All results are plotted along the normalized $\boldsymbol{X}_3$-direction. It can clearly be seen that SSDs mainly accumulate within the single crystal according to the distribution of plastic slip whereas higher concentrations of GNDs are found in the neighborhood of the crystal boundaries. Similar results have been found in the two-dimensional polycrystal example studied by Evers at al. [78]. However, comparing both sample sizes leads to the conclusion that slightly higher SSD density values are computed for the 6.1 µm sample whereas slightly higher GND density values results for the 2.1 µm pillar. When comparing the percentage amount of GNDs for both samples at the final deformation, an increase in gradient hardening due to higher GND accumulation is observed in the death zones of the sample. Moreover, the lateral approach of relative GND peaks indicates the increased influence of the internal length-scale. In other words, the dislocation pile-ups at the top and bottom are moved together in the smaller sample which affects the plastic deformation process of the crystal.

4.5.5 Comparison with experimental data

Fig. 4.11 shows an electron backscattered diffraction (EBSD) analysis of cross-sectional cut along the compression axis of a 5 µm pillar that had been compressed to about 10 % deformation, indicating that the crystal undergoes localized rotation due to dislocation plasticity. The color map in Fig. 4.11 a) shows the local lattice misorientation calculated for each scanning point with respect to the orientation of its surrounding neighbors. The scan was performed using a step size of 100 nm. Since localized lattice rotation is directly related to the accumulation of GNDs [9], a comparison between EBSD analysis and computed GND density distribution enables a more physical interpretation of the observed results. Regions corresponding to a high misorientation are associated with regions of increased GND densities in the simulation as presented in Fig. 4.11 c). The physical reliability of the numerical results are clearly demonstrated by comparing the misorientation distribution along the highlighted vertical path with the distribution of g^{eff} presented in Fig. 4.11 b).

Moreover, computed stress-strain responses are compared with experimental data using three data sets for each sample size. In the following, stress-strain curves are presented in terms of engineering stress σ_{eng} and strain $\varepsilon_{\mathrm{eng}}$. For both, experiments and simulations, the engineering stress is determined as the current force per initial middle cross section area $[\pi D_{\mathrm{m}}^2]/4$ and the engineering strain is defined as the ratio of compression displacement to initial pillar height. Moreover, the data of the initial loading path has been modified for all six sets in order to remove the strains associated with microplasticity prior to large-scale yield, as are associated with contact development and small-scale plasticity [157]. Thus, the strains are shifted in order to capture an elastic loading response with a modulus of 45 GPa, as is used in the simulations. Fig. 4.12 a) and b) show the numerically computed stress-strain curves together

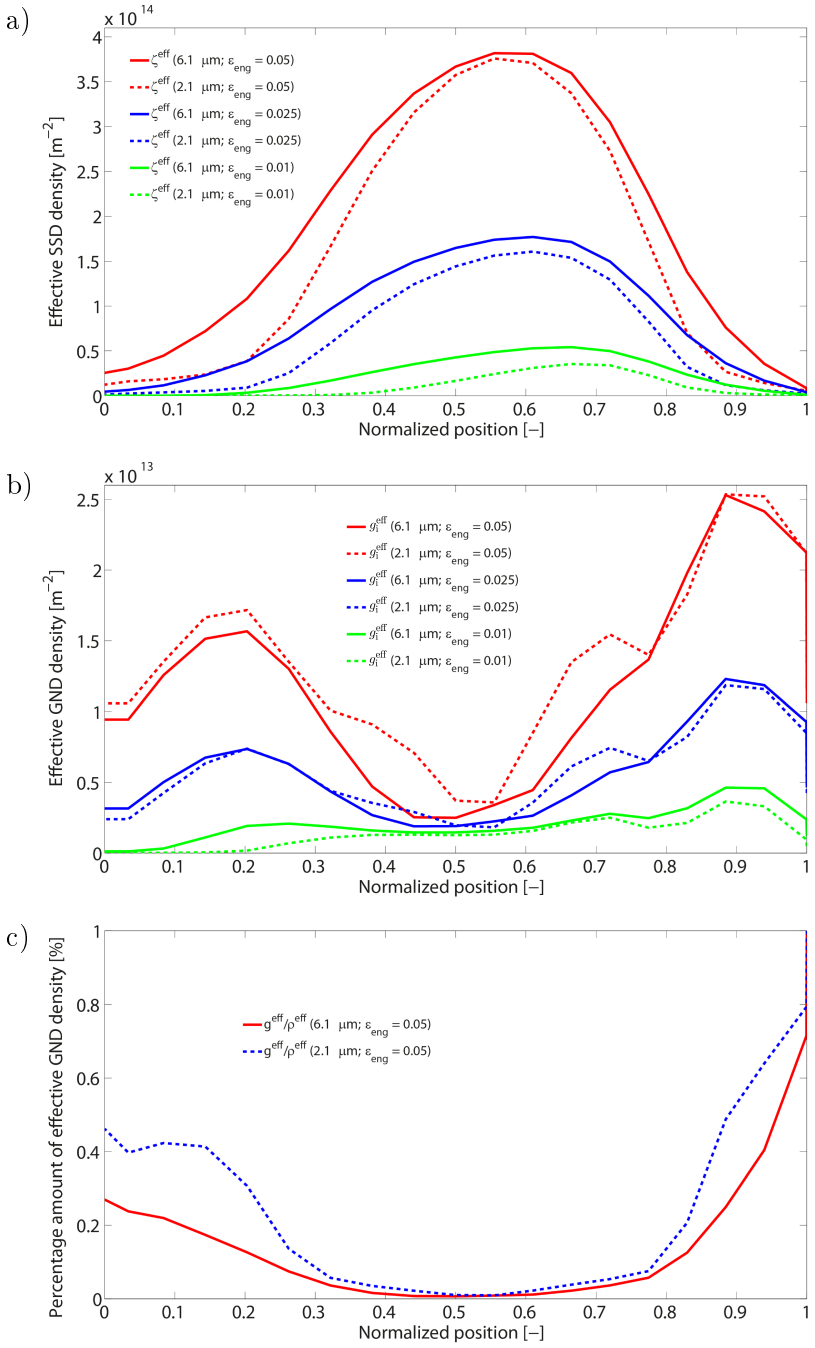

Figure 4.10: Evolution and distribution of a) effective SSD density and b) effective GND density for both sample sizes along the central axis in normalized $\boldsymbol{X}_3$-direction and for 1 %, 2.5 %, and 5 % nominal strain, respectively. Here, the distributions show lateral accumulation of GNDs associated with death zones and central accumulation of SSDs associated with high slipped zones. Moreover, c) the percentage amount of GNDs in contrast to the effective total dislocation density ρ^{eff} is shown for the final strain state. The relative increase of GNDs indicates a stronger influence of the microstructural length on the plastic process zone.
Reprinted from [111] with permission from Elsevier, Copyright 2014.

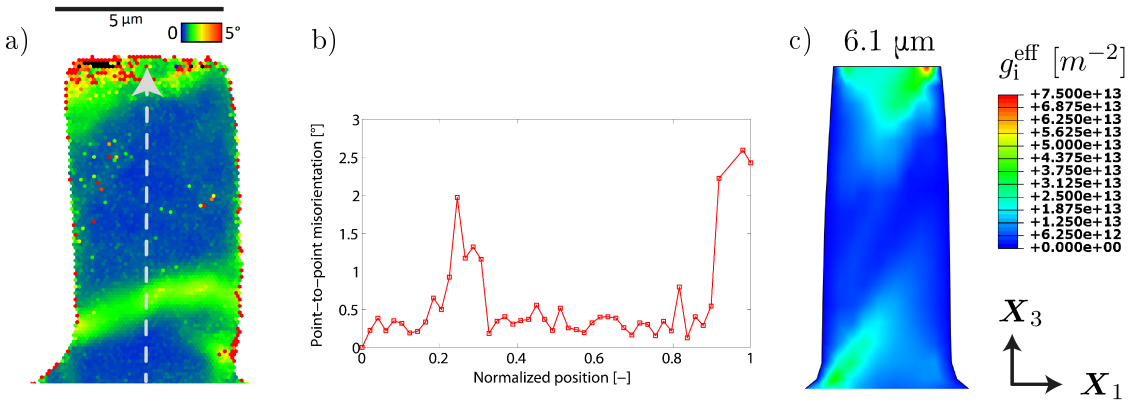

Figure 4.11: EBSD analysis emphasizes qualitatively the physical accordance between simulation and experiment. The local lattice rotation is highlighted within the color map a) for a thinned section of a 5 µm pillar after 10 % deformation. Regions indicating high lattice reorientation are in great accordance with appropriate simulation c) where high GND accumulation can be found in same regions already after 5 % nominal strain. The distribution of lattice misorientation along the highlighted vertical path b) confirms the good agreement when comparing this diagram to the computed GND density along the same path presented in Fig. 4.10 b).
Reprinted from [111] with permission from Elsevier, Copyright 2014.

with corresponding experimental data sets for the 6.1 µm and 2.1 µm sample, respectively. In the case of the large specimen, hardening parameters have been calibrated according to the averaged experimental hardening slope which is nearly linear in the strain interval [0.01,0.045]. As a result, the computed stress-strain curve shows very good agreement with the measured data of the 6.1 µm sample. Inherent to dislocation plasticity, each of the three curves of the smaller specimen show intermittent sequence of horizontal deformation jumps. These discrete strain bursts (or slip avalanches) are not modeled in the standard form of the here presented strain gradient theory. Consequently, a deviation of about 150 MPa is obtained between simulation and experiment at 5 % deformation, even if the work hardening slope remained nearly the same compared with the curve of the 6.1 µm sample. Due to this, another simulation have been performed. In that, strain bursts are successfully integrated in the deformation process in terms of sectionwise pure plastic loading, i.e., the elastic deformation matrix $\boldsymbol{F}_{\mathrm{E}}$ is forced to remain constant for the corresponding strain intervals. This approach is plausible from a physical point of view since sudden appearing strain bursts are associated with a geometrical change caused by a large (plastic) slip step. However, although their occurrence is in general of statistical nature as noted for example by Zaiser and Aifantis [264]. With respect to the deformation mode, we obtain the same characteristics but ca. half the plastic slip magnitude and half the GND density.

4.6 Conclusions

The importance of extended crystal plasticity models has been understood for many years. The present study deals with the computational modeling of microcompression of c-axis-oriented

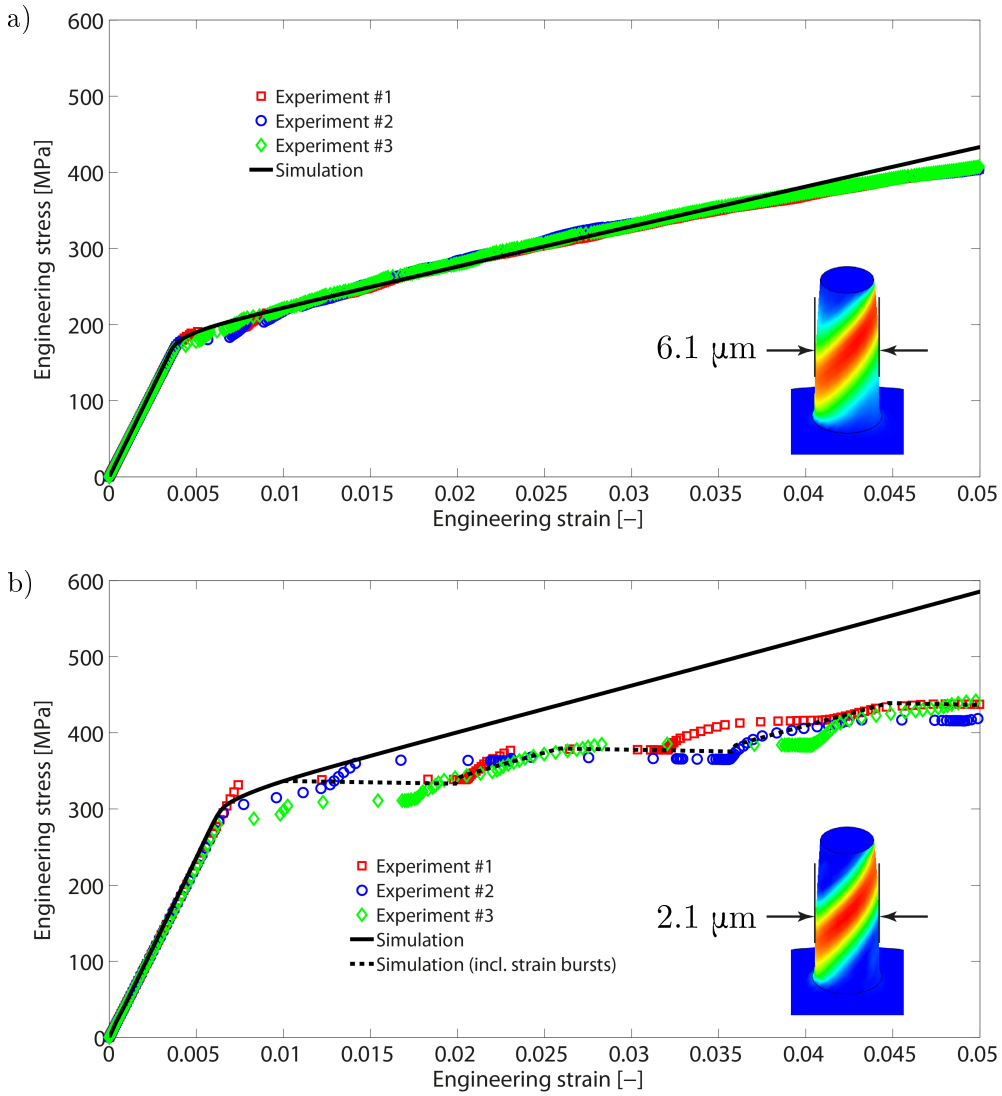

Figure 4.12: Comparison between computed stress-strain curves and experimental data sets for a) 6.1 µm and b) 2.1 µm sample. For each micropillar size, three different data sets are presented to demonstrate repeatability of experiments. Chosen hardening parameters, which have been calibrated according to the averaged experimental hardening slope of the larger sample, results in very good agreement for case a) whilst a final deviation of about 150 MPa is obtained between simulation and experiment in case b) due to intermittent strain bursts. Very good correlation with experimental data sets is obtained when strain bursts are integrated in the simulation in terms of sectionwise pure plastic loading.
Reprinted from [111] with permission from Elsevier, Copyright 2014.

magnesium single crystal using a strain gradient crystal plasticity model. The governing equations are derived in a thermodynamically consistent, large deformation framework. One of the basic physical assumptions upon which the current approach is based is that GND development and more generally local deformation incompatibility results in energy storage in the material. In this case, the free energy necessarily depends on the dislocation density

tensor. The numerical simulations were based on the experimental set-up and the results of Lilleodden [157]. In case of the set-up, essential indenter components such as the flat punch and the lateral stiffness are modeled. The mathematical model accounts for self-hardening, slip system interactions in terms of latent hardening, GNDs, size-dependent hardening behavior and the Bauschinger effect [17].

It was shown that the inclusion of the plastic slip gradient into the free energy enables a reasonable prediction of the plastic slip distribution. Due to the (0001) orientation of the crystal, the numerical simulations are performed with multiple active slip systems and latent hardening was considered. The typical distinct slip band developing in the micropillar is well reproduced by the numerical results. Further, the two zones without lattice rotation at the top, respectively bottom, of the pillar are well captured as well. The general stress-strain behavior was successfully mapped. In the case of the experimentally observed slope for the smaller 2.1 μm pillar sample, horizontal deformation jumps, referred to as discrete strain bursts, appear. Here, microscopic instability effects are responsible for that phenomena leading to a sudden relaxation in the material in terms of dislocation avalanches. These reduce the overall hardening rate such that a typical size effect on the flow stress is not directly observable. According to Zaiser and Aifantis [264] and Csikor et al. [60], strain bursts produce characteristic deformation patterns in the form of slip lines and slip bands. It was indicated how the strain burst phenomena can be integrated into the deformation process. The resulting stress-strain curve, characterized by intermittent bursts, is in strong agreement with the experimental data. Nevertheless, the strain gradient model was able to account for both smooth as well as intermittent discrete hardening behavior. More comprehensive investigations, including strain burst phenomena and their effect on the microstructure, will form future work.

In conclusion, the present work contributes to the ongoing research into understanding the micromechanical behavior of hcp crystals, here, in particular, single-crystal magnesium. The numerical examples were performed in the full three-dimensional setting. The resulting huge number of non-linear and strongly coupled equations to be solved simultaneously were successfully accounted for, including the full account of the coupling of the governing equations.

5 Impact of geometrically necessary storage of dislocations during microbending

The mechanical behavior of single crystalline, micro-sized copper is investigated in the context of cantilever beam bending experiments. Particular focus is on the role of geometrically necessary dislocations during bending-dominated load conditions and their impact on the characteristic bending size effect. Three different sample sizes are considered in this work with main variation in thickness. A gradient extended crystal plasticity model is presented and applied in a three-dimensional finite-element framework considering slip system-based edge and screw components of the dislocation density vector. The underlying mathematical model contains non-standard evolution equations for GNDs, crystal-specific interaction relations, and higher-order boundary conditions. Moreover, two element formulations are examined and compared with respect to size-independent as well as size-dependent bending behavior. The first formulation is based on a linear interpolation of the displacement and the GND density field together with a full integration scheme whereas the second is based on a mixed interpolation scheme. While the GND density fields are treated equivalently, the displacement field is interpolated quadratically in combination with a reduced integration scheme. Computational results indicate that GND storage in small cantilever beams strongly influences the evolution of statistically stored dislocations and, hence, the distribution of the total dislocation density. As a particular example, the mechanical bending behavior in the case of a physically motivated limitation of GND storage is studied. The resulting impact on the mechanical bending response as well as on the predicted size effect is analyzed. Obtained results are discussed and related to experimental findings from the literature.

The content of this chapter has been published in [E. Husser and S. Bargmann, *The role of geometrically necessary dislocations in cantilever beam bending experiments of single crystals*, Materials, 10(3), 289, 2017] and may include some modifications.

5.1 Introduction

Micromechanical testing of small-scaled single crystals has been excessively practiced in the last two decades to study the mechanical size-dependence of diverse materials [6, 88, 141, 246]. Different intrinsic (microstructural) effects have been found to be triggered by the interplay of physical size limitation such as free surfaces and the underlying microstructure in which the initial density of dislocations plays a crucial role. For example, experiments and 3D-discrete dislocation dynamics (DDD) simulations indicated that the size-dependent response of Ni single crystals decreases with increasing starting dislocation density [72]. Further, stable plastic deformation for crystals of ∼360 nm size was achieved and no strengthening effect in the range of 360 nm - 1500 nm was observed for Mo alloy microcrystals [27]. In both cases, the crystals were machined from relatively strong pre-strained bulk. Conversely, a sufficiently low initial dislocation density provokes a rapid starvation of available dislocations [89]. However, this effect becomes dominant if, for instance, the diameter D_m of micropillar samples falls below a critical value (∼1 μm in [89]). In the study of Shan et al. [224], an initial dislocation density of $\sim 10^{15}$ m^{-2} has fallen very fast to zero for $D_\mathrm{m} = 160$ nm whereas already larger samples ($D_\mathrm{m} \geq 250$ nm) were less likely to be dislocation-free after testing. Besides the characteristic sample dimension, the overall crystal size may additionally be considered as suggested recently by El-Awady [71].

With increasing sample size, other mechanisms will superimpose and start to affect or even govern the mechanical behavior. Depending on the geometry of deformation induced into the sample in terms of the applied loading, plastic strain gradients and associated geometrically necessary dislocations therewith, may increase significantly the plastic work hardening. Bending represents a typical deformation mode in which plastic strain gradients are induced extrinsically. Fleck and Hutchinson [79] suggest that the stored density of GNDs is proportional to the curvature of the bended beam. Experiments have found a strong inverse correlation between beam thickness and increase in strength of the material. For instance, an increase in the work hardening behavior with decreasing beam thickness has been reported by Stölken and Evans [233] for thin beams with a variation in thickness between 12.5 μm and 100 μm. Microbending experiments of Motz et al. [179] confirmed the strong correlation between flow stress and beam thickness. The investigated beam sizes varied in thickness between 7.5 μm and 1 μm. In the same work, it was pointed out that a regular alignment of GNDs (as would be expected in pure bending) is insufficient to explain the size effect. The responsible mechanism could be dislocation source limitation as a result of a rapid starvation of initially available dislocations as well as back-stress effects induced by dislocation pile-ups along the neutral axis. Numerical results of 3D-DDD beam bending simulations with thicknesses between 0.5 μm and 1.5 μm revealed that a combination of pile-up of GNDs and source size limitation mimics the experimental data quiet well [180]. These findings indicate the complexity of size-dependent strengthening behavior due to superposition of different mechanisms. Accordingly, it is difficult to independently estimate the size-dependent hardening contribution associated with each mechanism based on experimental data. For that reason, a gradient extended crystal plasticity model is used to investigate the size range (characterized by means of the beam thickness) and the extent to which GNDs affect the size-dependent bending behavior of small-scaled cantilever beams.

The aim of this work is to examine the size-dependent bending response for a range of sample sizes. In particular, we focus on three sample sizes with a variation in thickness between 2.5 μm and 5.0 μm. For this purpose, a higher-order gradient crystal plasticity model is implemented in a three-dimensional finite element framework. Highlights of the model are non-standard

evolution relations for edge and screw components of the slip system-based dislocation density vector, crystal-specific interaction relations, and higher-order gradient boundary conditions. The gradient effect associated with accumulating GND densities is of primary interest. In order to gain additional insights, the size-dependent impact of GNDs on the evolution of SSDs is investigated as well. The mechanical response of cantilever beams is further addressed for the case when the evolution of GNDs saturates due to a physical limitation. The number of dislocations to be stored locally due to compatibility reasons cannot be arbitrary high. Accordingly, a feasible limit for GND storage is introduced. All results are discussed and related to experimental findings from the literature.

5.2 Modeling aspects

The previously presented gradient crystal plasticity model is modified in order to account for the fcc crystal lattice considered in the here studied microbending problem of Cu single crystal. In particular, this involves the evolution equations for GND densities and associated interaction relations within. Moreover, this results in a more complicated definition of the scalar-valued microstress.

5.2.1 Governing equations

The so-called dislocation tensor represents a continuum measurement for GND densities from which the vector-valued GND vector $\dot{\boldsymbol{g}}_{\mathrm{i}\alpha}$ is derived, cf. [42]. Its general form, recall Eq. (3.59), accounts for dislocation collision processes, for instance, interactions between mobile dislocations of active slip systems mimicked by the plastic slip rates and stored dislocations on latent slip systems. For most applications, it is sufficient to account for the edge and screw component of the GND density vector only. Hence, it is assumed that there is no development of plastic slip gradients perpendicular to the slip planes, i.e., $\dot{\boldsymbol{g}}_{\mathrm{i}\alpha} \cdot \boldsymbol{n}_\alpha = 0$ [9]. With respect to fcc crystals, more specific interaction relations are proposed for the edge and screw components of the GND density based on moduli for edge-edge $\iota^{\mathrm{ee}}_{\alpha\beta}$, edge-screw $\iota^{\mathrm{es}}_{\alpha\beta}$, screw-screw $\iota^{\mathrm{ss}}_{\alpha\beta}$, and screw-edge $\iota^{\mathrm{se}}_{\alpha\beta}$ dislocation intersections:

$$\begin{aligned}
\iota^{\mathrm{ee}}_{\alpha\beta} &= |\boldsymbol{s}_\alpha \cdot \boldsymbol{s}_\beta|\, |\boldsymbol{n}_\alpha \times \boldsymbol{n}_\beta|\,, \\
\iota^{\mathrm{es}}_{\alpha\beta} &= |\boldsymbol{s}_\alpha \cdot \boldsymbol{t}_\beta|\, |\boldsymbol{n}_\alpha \times \boldsymbol{n}_\beta|\,, \\
\iota^{\mathrm{ss}}_{\alpha\beta} &= |\boldsymbol{t}_\alpha \cdot \boldsymbol{t}_\beta|\, |\boldsymbol{n}_\alpha \times \boldsymbol{n}_\beta|\,, \\
\iota^{\mathrm{se}}_{\alpha\beta} &= |\boldsymbol{t}_\alpha \cdot \boldsymbol{s}_\beta|\, |\boldsymbol{n}_\alpha \times \boldsymbol{n}_\beta|\,.
\end{aligned} \tag{5.1}$$

In addition, slip coplanarity moduli $\chi_{\alpha\beta}$ are introduced in accordance to previous works (e.g., [7, 15, 99]) as

$$\chi_{\alpha\beta} = \begin{cases} 0 & \text{for} \quad |\boldsymbol{n}_\alpha \times \boldsymbol{n}_\beta| \neq 0 \quad \text{noncoplanar,} \\ 1 & \text{for} \quad |\boldsymbol{n}_\alpha \times \boldsymbol{n}_\beta| = 0 \quad \text{coplanar.} \end{cases} \tag{5.2}$$

In the case of coplanar slip systems, i.e., slip planes of system α and β are parallel to each other, all intersection moduli vanish and slip-system interactions are solely determined by coplanarity moduli. Recall that the GND components are obtained by projecting the plastic slip gradients on the slip directions $\boldsymbol{s}_\alpha$ and the transverse slip directions $\boldsymbol{t}_\alpha$ (see Arsenlis and Parks [4], Gurtin and Anand [97]). Then, under consideration of no development of plastic

slip gradients perpendicular to the slip planes, Eq. (3.59) is substituted by

$$\dot{g}^{\mathrm{e}}_{\mathrm{i}\alpha} = \sum_{\beta} \nu_\alpha \left[g^{\mathrm{e}}_{\mathrm{i}\beta} \left[\iota^{\mathrm{ee}}_{\alpha\beta} + \chi_{\alpha\beta} \right] + g^{\mathrm{s}}_{\mathrm{i}\beta} \left[\iota^{\mathrm{es}}_{\alpha\beta} + \chi_{\alpha\beta} \right] \right] - \frac{1}{b} \nabla_{\mathrm{i}} \nu_\alpha \cdot \boldsymbol{s}_\alpha \tag{5.3}$$

and

$$\dot{g}^{\mathrm{s}}_{\mathrm{i}\alpha} = \sum_{\beta} \nu_\alpha \left[g^{\mathrm{s}}_{\mathrm{i}\beta} \left[\iota^{\mathrm{ss}}_{\alpha\beta} + \chi_{\alpha\beta} \right] + g^{\mathrm{e}}_{\mathrm{i}\beta} \left[\iota^{\mathrm{se}}_{\alpha\beta} + \chi_{\alpha\beta} \right] \right] - \frac{1}{b} \nabla_{\mathrm{i}} \nu_\alpha \cdot \boldsymbol{t}_\alpha, \tag{5.4}$$

respectively using the above introduced interaction moduli. The first relation in Eq. (5.3) accounts for the impact of stored edge and screw GND densities (with respect to latent slip systems β) on the evolution of the edge GND density of slip system α whereas the second term measures the geometrically necessary edge dislocation density by means of the plastic slip gradient $\nabla_{\mathrm{i}}\nu_\alpha$. A similar relation is given in Eq. (5.4) for the geometrically necessary screw dislocation density.

For the sake of completeness, we recall the balance of linear momentum (with respect to the intermediate configuration) in the absence of body forces and for quasi-static and isothermal conditions,i.e., $\boldsymbol{0} = \mathrm{Div}_{\mathrm{i}}(\boldsymbol{F}_{\mathrm{E}} \cdot \boldsymbol{S}_{\mathrm{E}})$. At the local level, the viscoplastic flow rule is defined in the form of Perzyna, i.e., $\nu_\alpha = \nu_0 [< \phi_\alpha > / C_0]^m$, cf. Eq. $(4.7)_2$.

5.2.2 Constitutive relations

The free energy density ψ_{i} is additively decomposed as shown in Eq. (3.64). The hyperelastic energy contribution $\psi^{\mathrm{el}}_{\mathrm{i}}$ is postulated in terms of an isotropic Neo-Hookean law, cf. Eq. (3.25). With respect to the local energy contribution ψ^{l}, a Voce-like relation as prescribed in Eq. (3.80) is adopted, see also [134]. This choice is motivated by numerous observations where the stress-strain response of copper single crystal is characterized by a pronounced saturation behavior, cf. [21, 66, 133, 179].

The free energy increases due to storage of GNDs in the material. Adapting the Ashby-like component representation of the GND density, cf. Eq. (3.84), edge and screw dislocation characters associated with distortion and twisting of the crystal lattice respectively, are introduced into the defect energy. Considering the similarity of slip systems in fcc crystals, the defect energy takes the form

$$\psi^{\mathrm{g}}_{\mathrm{i}} = \frac{1}{2} \sum_{\alpha} l^2 b^2 \left[H^{\mathrm{e}}_0 [g^{\mathrm{e}}_{\mathrm{i}\alpha}]^2 + H^{\mathrm{s}}_0 [g^{\mathrm{s}}_{\mathrm{i}\alpha}]^2 \right]. \tag{5.5}$$

With that, the constitutive relation for the backstress-like vector is obtained from the chain rule

$$\boldsymbol{\kappa}_\alpha = \frac{\partial \psi_{\mathrm{i}}}{\partial \nabla_{\mathrm{i}} \gamma_\alpha} = \frac{\partial \psi^{\mathrm{g}}_{\mathrm{i}}}{\partial g^{\mathrm{e}}_{\mathrm{i}\alpha}} \frac{\partial g^{\mathrm{e}}_{\mathrm{i}\alpha}}{\partial \nabla_{\mathrm{i}} \gamma_\alpha} + \frac{\partial \psi^{\mathrm{g}}_{\mathrm{i}}}{\partial g^{\mathrm{s}}_{\mathrm{i}\alpha}} \frac{\partial g^{\mathrm{s}}_{\mathrm{i}\alpha}}{\partial \nabla_{\mathrm{i}} \gamma_\alpha}. \tag{5.6}$$

Due to the dependence of $\dot{g}^{\mathrm{e}}_{\mathrm{i}\alpha}$ and $\dot{g}^{\mathrm{s}}_{\mathrm{i}\alpha}$ on the slip rate ν_α, the scalar-valued microstress κ_α is determined as

$$\kappa_\alpha = \frac{\partial \psi_{\mathrm{i}}}{\partial \gamma_\alpha} = \frac{\partial \psi^{\mathrm{l}}}{\partial \gamma_\alpha} + \left[\frac{\partial \psi^{\mathrm{g}}_{\mathrm{i}}}{\partial g^{\mathrm{e}}_{\mathrm{i}\alpha}} \frac{\partial g^{\mathrm{e}}_{\mathrm{i}\alpha}}{\partial \gamma_\alpha} + \frac{\partial \psi^{\mathrm{g}}_{\mathrm{i}}}{\partial g^{\mathrm{s}}_{\mathrm{i}\alpha}} \frac{\partial g^{\mathrm{s}}_{\mathrm{i}\alpha}}{\partial \gamma_\alpha} \right]. \tag{5.7}$$

The first derivative on the right-hand side of Eq. (5.7) is previously determined, cf. Eq. (3.81). The term in the brackets describes a latent hardening contribution in terms of GND intersection and collision effects which are particularly pronounced upon load reversal. The specific forms are derived below after application of a time discretization scheme.

5.2.3 Boundary conditions

As we study the bending behavior of a single crystal with free surfaces, microfree boundaries are chosen according to Eq. (3.87). With these conditions, dislocation pile-ups are refused at the exterior of the crystal and, hence, all boundaries appear to be transparent to dislocation motion. Indeed, this is an idealized approximation of the surface mechanics which, nevertheless, may be still appropriate at sufficiently large crystal dimensions.

5.3 Numerical implementation

The solution algorithm for the highly coupled and strongly non-linear multi-field problem is based on the dual-mixed finite element method as proposed by Ekh et al. [70]; see also Bargmann et al. [14, 17]. In this, GND densities are introduced as nodal degrees of freedom in addition to the displacement. The basis for implementing the material model into a finite element framework is the variational form of the underlying governing equations. Applying the principle of virtual work to the balance of linear momentum yields

$$0 = \int_{\mathcal{B}_\mathrm{i}} \frac{1}{2}\boldsymbol{S}_\mathrm{E} : \delta\boldsymbol{C}_\mathrm{E}\mathrm{dV_i} - \int_{\partial\mathcal{B}_\mathrm{i}} \delta\boldsymbol{u}\cdot[\boldsymbol{F}_\mathrm{E}\cdot\boldsymbol{S}_\mathrm{E}]\cdot\boldsymbol{N}_\mathrm{i}\mathrm{dA_i}, \tag{5.8}$$

where $\delta\boldsymbol{u}$ is a vector-valued test function and $\delta\boldsymbol{C}_\mathrm{E} = [\boldsymbol{F}_\mathrm{E}^\mathrm{T}\cdot\nabla_\mathrm{i}(\delta\boldsymbol{u}) + \nabla_\mathrm{i}(\delta\boldsymbol{u})^\mathrm{T}\cdot\boldsymbol{F}_\mathrm{E}]$ denotes the variation of the right Cauchy-Green stretch tensor. The corresponding mechanical boundary conditions read

$$\begin{aligned} [\boldsymbol{F}_\mathrm{E}\cdot\boldsymbol{S}_\mathrm{E}]\cdot\boldsymbol{N}_\mathrm{i} = 0 \quad &\text{on} \quad \partial\mathcal{B}_\mathrm{i}^F \\ \boldsymbol{u} = \bar{\boldsymbol{u}} \quad &\text{on} \quad \partial\mathcal{B}_\mathrm{i}^u, \end{aligned} \tag{5.9}$$

where $\partial\mathcal{B}_\mathrm{i} = \partial\mathcal{B}_\mathrm{i}^F \cup \partial\mathcal{B}_\mathrm{i}^u$. In a similar manner, the variational forms of Eqs. (5.3) and (5.4) are obtained. An implicit finite-difference method is chosen for the time discretization of the global field relations such that $\dot{g}^\mathrm{e}_{\mathrm{i}\alpha} = \Delta g^\mathrm{e}_{\mathrm{i}\alpha}/\Delta t$, where Δt measures the current time increment and $\Delta g^\mathrm{e}_{\mathrm{i}\alpha} = g^\mathrm{e}_{\mathrm{i}\alpha(n+1)} - g^\mathrm{e}_{\mathrm{i}\alpha(n)}$. The same holds for the screw component, i.e., $\Delta g^\mathrm{s}_{\mathrm{i}\alpha} = g^\mathrm{s}_{\mathrm{i}\alpha(n+1)} - g^\mathrm{s}_{\mathrm{i}\alpha(n)}$. As an approximation, plastic slip rates are discretized analogically, i.e., $\nu_\alpha = \Delta\gamma_\alpha/\Delta t$, where $\Delta\gamma_\alpha = \gamma_{\alpha(n+1)} - \gamma_{\alpha(n)}$. With this at hand, the variational forms are written as

$$\begin{aligned} 0 = &\int_{\mathcal{B}_\mathrm{i}} \delta g^\mathrm{e}_\alpha \Delta g^\mathrm{e}_{\mathrm{i}\alpha}\mathrm{dV_i} \\ &- \int_{\mathcal{B}_\mathrm{i}} \delta g^\mathrm{e}_\alpha \sum_\beta \Delta\gamma_\alpha \left[g^\mathrm{e}_{\mathrm{i}\beta}\left[\iota^\mathrm{ee}_{\alpha\beta} + \chi_{\alpha\beta}\right] + g^\mathrm{s}_{\mathrm{i}\beta}\left[\iota^\mathrm{es}_{\alpha\beta} + \chi_{\alpha\beta}\right]\right]\mathrm{dV_i} \\ &- \frac{1}{b}\int_{\mathcal{B}_\mathrm{i}} \Delta\gamma_\alpha \mathrm{Div_i}\left(\delta g^\mathrm{e}_\alpha \boldsymbol{s}_\alpha\right)\mathrm{dV_i} \\ &+ \frac{1}{b}\int_{\partial\mathcal{B}_\mathrm{i}} \delta g^\mathrm{e}_\alpha \Delta\gamma_\alpha \boldsymbol{s}_\alpha\cdot\boldsymbol{N}_\mathrm{i}\mathrm{dA_i}, \end{aligned} \tag{5.10}$$

and

$$
\begin{aligned}
0 = & \int_{\mathcal{B}_\mathrm{i}} \delta g^\mathrm{s}_\alpha \Delta g^\mathrm{s}_{\mathrm{i}\alpha} \mathrm{dV_i} \\
& - \int_{\mathcal{B}_\mathrm{i}} \delta g^\mathrm{s}_\alpha \sum_\beta \Delta\gamma_\alpha \left[g^\mathrm{s}_{\mathrm{i}\beta} \left[\iota^\mathrm{ss}_{\alpha\beta} + \chi_{\alpha\beta} \right] + g^\mathrm{e}_{\mathrm{i}\beta} \left[\iota^\mathrm{se}_{\alpha\beta} + \chi_{\alpha\beta} \right] \right] \mathrm{dV_i} \\
& - \frac{1}{b} \int_{\mathcal{B}_\mathrm{i}} \Delta\gamma_\alpha \mathrm{Div_i} \left(\delta g^\mathrm{s}_\alpha \boldsymbol{t}_\alpha \right) \mathrm{dV_i} \\
& + \frac{1}{b} \int_{\partial\mathcal{B}_\mathrm{i}} \delta g^\mathrm{s}_\alpha \Delta\gamma_\alpha \boldsymbol{t}_\alpha \cdot \boldsymbol{N}_\mathrm{i} \mathrm{dA_i},
\end{aligned}
\tag{5.11}
$$

respectively. Here, $\delta g^\mathrm{s}_\alpha$ and $\delta g^\mathrm{e}_\alpha$ are arbitrary test functions. Next, the time-discretized versions of the microstresses are obtained as

$$
\boldsymbol{\kappa}_\alpha = \frac{\partial \psi^\mathrm{g}_{\mathrm{i}(n+1)}}{\partial \nabla_\mathrm{i} \gamma_{\alpha(n+1)}} = -l^2 b H^\mathrm{e}_0 \left[g^\mathrm{e}_{\mathrm{i}\alpha} \boldsymbol{s}_\alpha + [1-\nu] g^\mathrm{s}_{\mathrm{i}\alpha} \boldsymbol{t}_\alpha \right], \tag{5.12}
$$

resp.

$$
\begin{aligned}
\kappa^\mathrm{g}_\alpha = \frac{\partial \psi^\mathrm{g}_{\mathrm{i}(n+1)}}{\partial \gamma_{\alpha(n+1)}} = l^2 b^2 H^\mathrm{e}_0 \Bigg[& g^\mathrm{e}_{\mathrm{i}\alpha} \sum_\beta \left[g^\mathrm{e}_{\mathrm{i}\beta} \left[\iota^\mathrm{ee}_{\alpha\beta} + \chi_{\alpha\beta} \right] + g^\mathrm{s}_{\mathrm{i}\beta} \left[\iota^\mathrm{es}_{\alpha\beta} + \chi_{\alpha\beta} \right] \right] \\
& + [1-\nu] g^\mathrm{s}_{\mathrm{i}\alpha} \sum_\beta \left[g^\mathrm{s}_{\mathrm{i}\beta} \left[\iota^\mathrm{ss}_{\alpha\beta} + \chi_{\alpha\beta} \right] + g^\mathrm{e}_{\mathrm{i}\beta} \left[\iota^\mathrm{se}_{\alpha\beta} + \chi_{\alpha\beta} \right] \right] \Bigg].
\end{aligned}
\tag{5.13}
$$

Both equations are fully implicit. Therefore, it is not explicitly indicated that the time-dependent quantities are associated with the new time increment $t_{(n+1)} = t_{(n)} + \Delta t$.

5.4 Set-up of the numerical example

5.4.1 Finite element model

The presented gradient-based crystal plasticity model is applied to microbending experiments of copper single crystal. Three micron-sized cantilever beams with varying thickness h in the range between 2.5 µm and 5.0 µm are under investigation, see Table 5.1 for exact sample dimensions. In order to prevent additional influences on the size-dependent hardening, the momentum arm l_b as well as the edge length in width direction w are kept constant for all geometries. This allows for a meaningful interpretation of the results for which a strong correlation between the strength of the material and the thickness of the beam is expected (Evans and Hutchinson [76]). Sample geometries and crystallographic orientation were exemplary chosen in accordance to the experimental set-up of Motz et al. [179]. Details regarding sample preparation and fabrication are provided in [127]. In that experimental study, various single crystalline cantilever beam samples were fabricated by the focused-ion beam (FIB) technique and loaded with an indenter tip at the free end.

With regard to the finite element model, quadratic serendipity elements (twenty-node) have been used for geometry approximation whereas displacement and the GND density degrees of freedom have been solved with a different number of nodes, cf. Fig. 5.1. Here, the solution of

the displacement field is based on a fully quadratic FE-approximation combined with a reduced integration scheme ($2 \times 2 \times 2$ Gauss points). This approach is known to be well suitable for bending-dominated problems. In contrast, the GND densities are only evaluated at the corner nodes in terms of a linear FE-approximation using the full integration scheme, see Fig. 5.1b. This mixed-element formulation - henceforth denoted as 20RI8FI - was examined by Kuroda [151] for the two-dimensional case with respect to simple shear and compression problems and was revealed to be well suitable for applications in the context of higher-order gradient crystal plasticity as it exhibits a reliable performance. The finite element meshes of the cantilever beams are illustrated in Fig. 5.2 whereas the corresponding geometry and discretization data is provided in Table 5.1. Fig. 5.2 includes a mesh for which both fields are approximated with trilinear eight-node elements and $2 \times 2 \times 2$ Gauss points (full integration scheme), cf. Fig. 5.1a. In the results section, a comparison in performance between the mixed-element (20RI8FI) and the fully linear formulation (8FI8FI) is carried out for selected cases concerning cantilever beam #1.

Beam	l_b [µm]	w [µm]	h [µm]	Elements
#1 (8FI8FI)	15	2.5	2.5	8790
#1 (20RI8FI)	15	2.5	2.5	3864
#2 (20RI8FI)	15	2.5	3.5	4480
#3 (20RI8FI)	15	2.5	5.0	5712

Table 5.1: Sample dimensions and discretization data for the here investigated cantilever beam geometries.

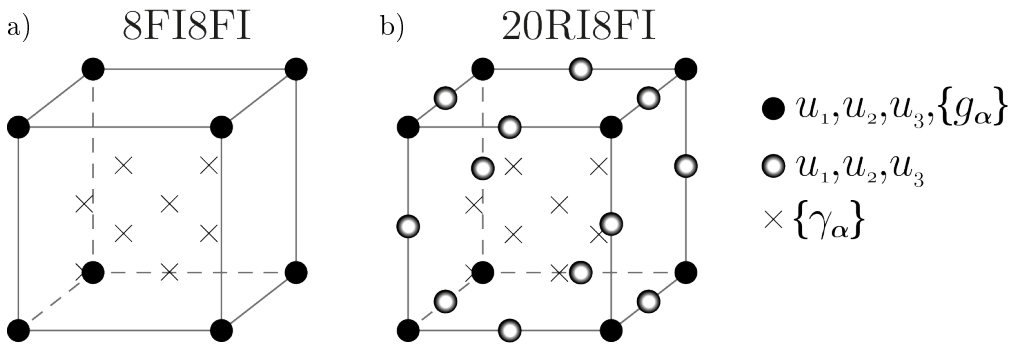

Figure 5.1: Schematic illustration of implemented finite element schemes: a) Eight-node hexahedral element with full integration scheme (8FI8FI) - displacement fields and GND density fields are interpolated by trilinear shape functions; b) Twenty-node hexahedral element with mixed integration scheme (20RI8FI) - displacement fields are interpolated by quadratic serendipity shape functions combined with the reduced integration scheme whereas the GND density fields are interpolated by trilinear shape functions in combination with the full integration scheme).
Reprinted from [109] with permission from MDPI, Copyright 2017

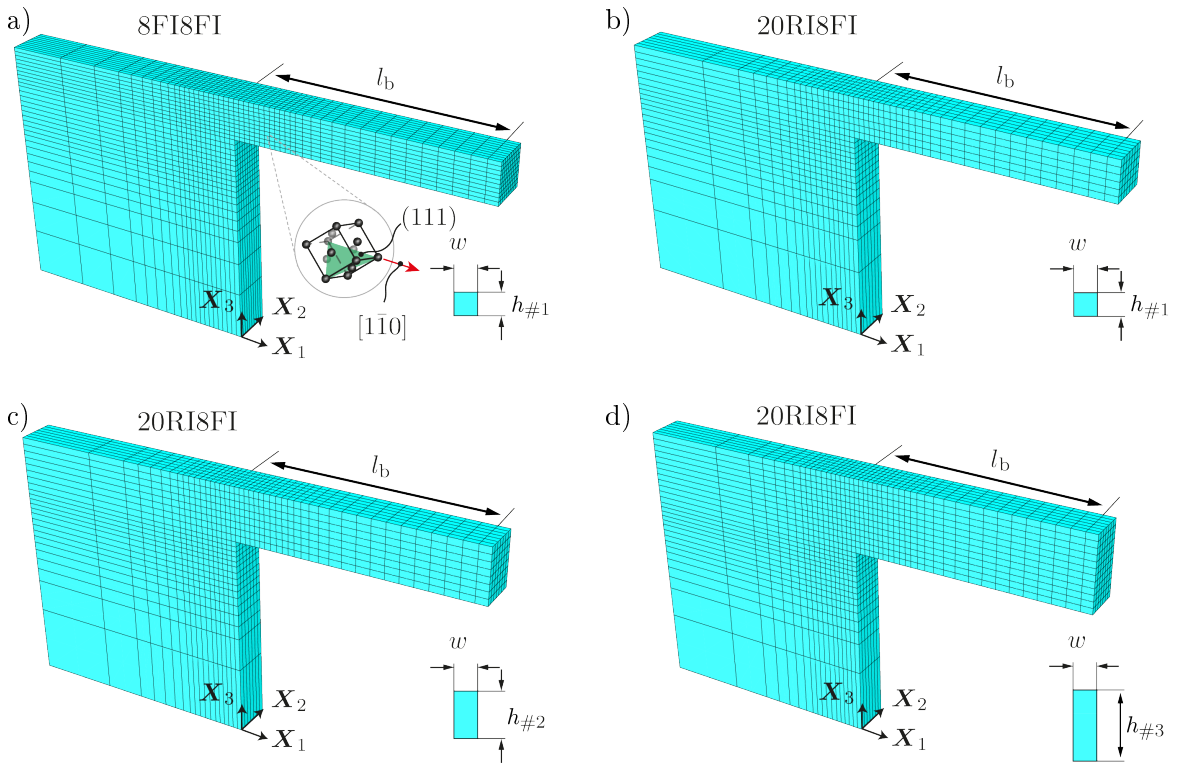

Figure 5.2: Finite-element meshes, crystallographic orientation, and dimensions of investigated cantilever beam geometries: a),b) cantilever beam #1; c) cantilever beam #2; d) cantilever beam #3. Mesh a) is generated by eight-node hexahedral elements whereas meshes b)-d) are generated by twenty-node hexahedral elements, cf. Fig. 5.1. Exact dimensions are summarized in Table 5.1.
Reprinted from [109] with permission from MDPI, Copyright 2017.

5.4.2 Crystallography and material

The crystallographic orientation of the crystals is chosen in accordance to the experiments in [179]: the $[1\bar{1}0]$ direction is aligned parallel to the longitudinal beam axis (parallel to $\boldsymbol{X}_1$) and the (111)-plane is oriented parallel to the $\boldsymbol{X}_1$-$\boldsymbol{X}_2$ plane, cf. Fig. 5.2a. The applied deflection results in the typical tensile and compressive dominated zones which determine the resolved shear stress on the individual slip systems and, thus, dominate their activation (at least for the here relevant bending load regime). There exist four non-zero Schmid factors f_α for the particular crystal orientation as indicated in Table 5.2 together with the slip system designation of the fcc lattice.

In the here considered flow rule, cf. Eq. $(4.7)_2$, each slip direction is associated with a stand-alone slip system. In fcc crystals, there are generally 12 edge and six screw dislocation characters as each screw dislocation line is shared by two slip planes, cf. [147].

The elasticity parameters for copper, i.e., Young's modulus $E = 126.9$ GPa and Poisson's ratio $\nu = 0.35$, are taken from [179], respectively. Further, the initial yield limit is chosen to be $Y_{\alpha 0} = 1.5$ MPa in agreement with experiments of single crystals, see for instance [20, 87]. The magnitude of the Burgers vector is taken as $b = a/\sqrt{2} = 0.2552$ nm, based on a lattice constant of $a = 0.3609$ nm [120]. In order to minimize rate effects, the rate-sensitivity parameter is chosen to be $m = 20$ and the reference slip rate is put on a level with the macroscopic (quasi-

$\sqrt{2}\boldsymbol{s}_\alpha$	$\sqrt{6}\boldsymbol{t}_\alpha$	$\sqrt{3}\boldsymbol{n}_\alpha$	f_α
$[01\bar{1}]$	$[211]$	$[1\bar{1}\bar{1}]$	0.4082
$[101]$	$[\bar{1}\bar{2}1]$	$[1\bar{1}\bar{1}]$	0.4082
$[\bar{1}\bar{1}0]$	$[\bar{1}1\bar{2}]$	$[1\bar{1}\bar{1}]$	0
$[0\bar{1}1]$	$[2\bar{1}\bar{1}]$	$[111]$	0
$[10\bar{1}]$	$[\bar{1}2\bar{1}]$	$[111]$	0
$[\bar{1}10]$	$[\bar{1}\bar{1}2]$	$[111]$	0
$[011]$	$[\bar{2}1\bar{1}]$	$[\bar{1}\bar{1}1]$	0
$[\bar{1}0\bar{1}]$	$[1\bar{2}\bar{1}]$	$[\bar{1}\bar{1}1]$	0
$[1\bar{1}0]$	$[112]$	$[\bar{1}\bar{1}1]$	0
$[0\bar{1}\bar{1}]$	$[\bar{2}\bar{1}1]$	$[\bar{1}1\bar{1}]$	0.4082
$[\bar{1}01]$	$[121]$	$[\bar{1}1\bar{1}]$	0.4082
$[110]$	$[1\bar{1}\bar{2}]$	$[\bar{1}1\bar{1}]$	0

Table 5.2: C.s.s. of copper (fcc): slip direction $\boldsymbol{s}_\alpha$, transversal slip direction $\boldsymbol{t}_\alpha$, slip plane normal $\boldsymbol{n}_\alpha$, and initial Schmid factor f_α. Slip activation is mainly determined by the bending stresses as an accommodation of plastic deformation by slip systems with an initially zero Schmid factor is rather unlikely.

static) load rate, i.e., $\nu_0 = 10^{-3}$ s^{-1}. The drag stress parameter is assumed to be $C_0 = 10$ MPa. Moreover, the same constitutive length-scale parameter is applied to all slip systems in analogy to the Burgers vector magnitude. In [233], l was found to be 4 μm for highly pure Ni. Since a similar magnitude was obtained for torsion tests of copper wires, cf. [80], this value is adopted here. Particular choices for hardening moduli and the saturation rate are discussed in Section 5.5.1. All material parameters are summarized in Table 5.3.

5.5 Numerical results: Microbending of Cu single crystal

5.5.1 Element choice: Eight-node hexahedral element with full integration (8FI8FI) vs. twenty-node hexahedral element with mixed integration (20RI8FI)

As a starting point, the size-independent response is studied, i.e., the bending response in the absence of gradient effects which is obtained when $l/h \approx 0$. By setting $l = 0$, the computations mimic the response of bulk samples independent of the actual sample dimensions. A macroscopic bending test from [179] serves as a reference in order to calibrate the local hardening modulus H_0^{l} as well as the saturation rate c_{sat}. All numerical bending tests were loaded up to 10 % normalized deflection (applied deflection/initial momentum arm). Optimal values are identified as $H_0^{\mathrm{l}} = 77.5$ MPa and $c_{\mathrm{sat}} = 10^3$. The final results are shown in Fig. 5.3. As seen, this choice results in a good saturation behavior with rapid hardening behavior for all three sample sizes associated with the 20RI8FI-formulation. All curves yield the reference

Young's modulus	E	126.9	GPa
Poisson's ratio	ν	0.35	-
Microscopic yield stress	$Y_{\alpha 0}$	1.5	MPa
Local hardening modulus	H_0^{l}	77.5	MPa
Gradient hardening modulus	H_0^{e}	1	GPa
Saturation rate	c_{sat}	10^3	-
Reference slip rate	ν_0	10^{-3}	s^{-1}
Rate sensitivity parameter	m	20.0	-
Drag stress	C_0	10.0	MPa
Length scale	l	4.0	µm
Length of Burgers vector	b	0.2552	nm

Table 5.3: Material parameters of Cu single crystal used for numerical computations.

flow stress of ≈227 MPa, i.e., the bending response is clearly size-independent (independent of the beam thickness). By comparing the bending response of cantilever beam #1 of the two element formulations, it is clearly seen that the 8FI8FI-element formulation overestimates the strength and the bending stiffness. A deviation in the stress-strain curve is already obvious after ≈1% normalized deflection. Further, the saturation level as well as saturation behavior are not captured correctly. This is due to a bending-dominated deformation mode which cannot be properly captured by the linear element formulation due to locking effects.

Next, the size-dependent material behavior is investigated. Exemplarily, cantilever beam #1 is studied as the strongest impact is expected for the beam sample with the smallest thickness. A linear-like hardening behavior is observed (cf. Fig. 5.3) which is associated with a continuously increasing (plastic) strain gradient during bending. The strain gradient scales the higher-order gradient hardening in terms of the back-stress $\mathrm{Div}_{\mathrm{i}}(\boldsymbol{\kappa}_\alpha)$. Hence, the gradient hardening contribution constantly increases which in the end prevents a saturation of the overall hardening response. As in the size-independent case, the 8FI8FI-formulation overestimates the bending response. Yet, the difference at the final deformation state appears to be not that pronounced which indicates that the computational accuracy of the GND field is not affected by the 8FI8FI-element formulation.

In the following, a qualitative comparison with regard to the GND density and the plastic slip is carried out. For that reason, the effective GND density $g_{\mathrm{i}}^{\mathrm{eff}}$ is introduced as a function of the admitted edge and screw GND components

$$g_{\mathrm{i}}^{\mathrm{eff}} = \sqrt{\sum_\alpha \left[g_{\mathrm{i}\alpha}\right]^2} = \sqrt{\sum_\alpha \left[g_{\mathrm{i}\alpha}^{\mathrm{e}}\right]^2 + \left[g_{\mathrm{i}\alpha}^{\mathrm{s}}\right]^2}, \tag{5.14}$$

where $g_{\mathrm{i}\alpha}$ is the net GND density associated with slip system α. In analogy, the effective plastic slip γ^{eff}, computed according to Eq. (3.47), serves as a representative variable in order to compare the distribution of plastic deformation.

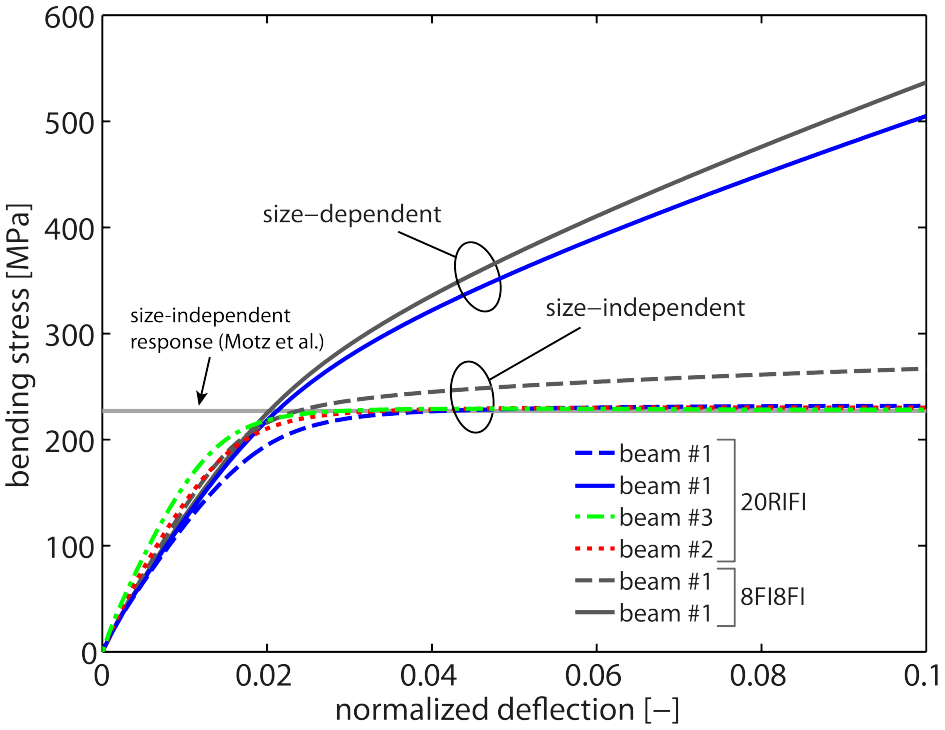

Figure 5.3: Size-independent bending response for $H_0^{\mathrm{l}} = 77.5$ MPa and $c_{\mathrm{sat}} = 10^3$. Simulations of all three sample sizes (20RI8FI) yield the reference data of [179]. The FE-mesh with linear elements (8FI8FI) overestimates the stiffness as well as the strength due to volumetric locking in case of bending-dominated loading for the size-independent as well as the size-dependent case.
Reprinted from [109] with permission from MDPI, Copyright 2017.

Exemplarily, Fig. 5.4 depicts the distribution of the effective GND density $g_{\mathrm{i}}^{\mathrm{eff}}$ along the central middle axis for both element formulations. The results are within the same order of magnitude or even identical, i.e., the GND density field is well captured by both formulations. This holds true for both, the qualitative distribution along the middle central axis as well as the quantitative distribution within the $\boldsymbol{X}_1$-$\boldsymbol{X}_3$-plane. Consequently, the bending response (but not the GND evolution) is affected by volumetric locking in case of the 8FI8FI-element formulation. The contour plot for the case of 20RI8FI-elements is not presented as only marginal differences are present compared to the contour plot in Fig. 5.4. Nevertheless, the contour plot of $g_{\mathrm{i}}^{\mathrm{eff}}$ can be found in Fig. 5.7 where the pile-up characteristic of GNDs is analyzed in more detail.

The distribution of the effective plastic slip γ^{eff} is qualitatively compared along the highest and lowest central path parallel to the beam axis, see Fig. 5.5. In addition, a quantitative comparison is provided on the basis of the effective plastic slip distribution within the central $\boldsymbol{X}_1$-$\boldsymbol{X}_3$-plane. As seen, differences are found near the supporting end, i.e., close to a normalized position of ≈ 0. Here, the 20RI8FI-element formulation resolves a higher magnitude of γ^{eff} which is confirmed by the contour plots. Slightly higher values of γ^{eff} are also computed in regions where both formulations are close to each other. Besides, it can be seen that plastic deformation is only accommodated within the first third/half of the beam sample (referred to the fixed side) whereas the rest of the beam finger remains straight. Such a localized plastic deformation is characteristic for cantilever beam bending.

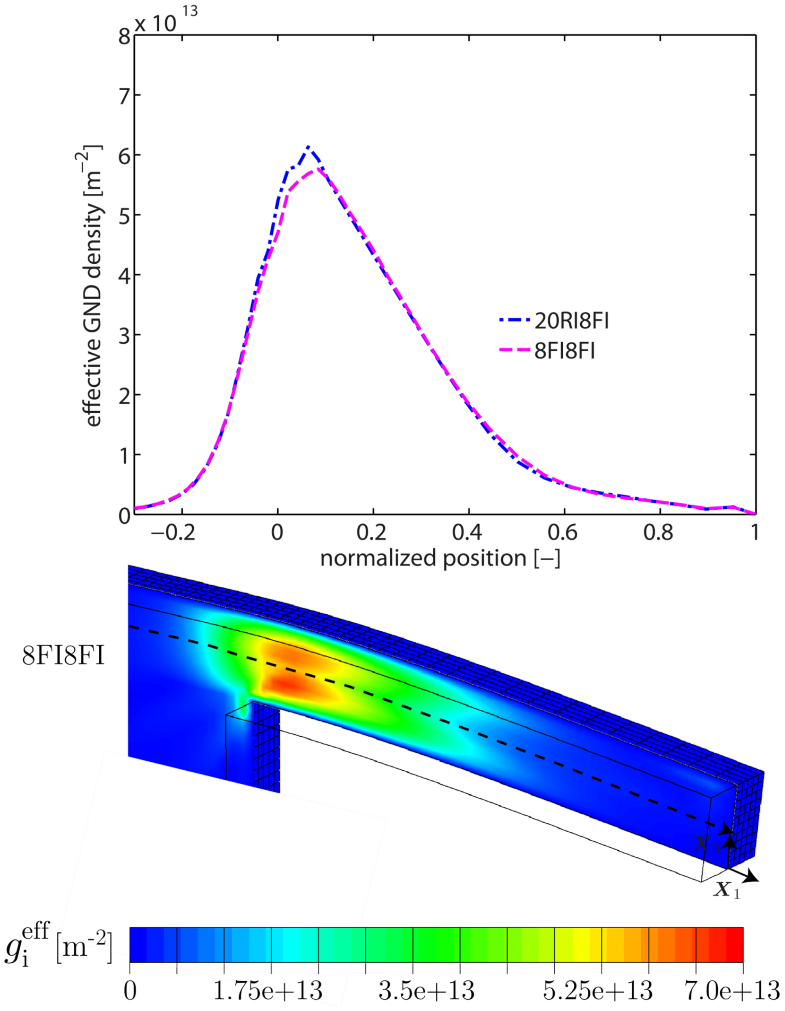

Figure 5.4: Distribution of the effective GND density $g_{\mathrm{i}}^{\mathrm{eff}}$ for the cantilever beam sample #1 along the middle beam axis (from left to right) for the particular case $H_0^{\mathrm{e}} = 1$ GPa. The corresponding contour plot within the central $\boldsymbol{X}_1$-$\boldsymbol{X}_3$-plane is additionally shown for the 8FI8FI-element formulation (cf. Fig. 5.7 for the 20RI8FI-element formulation). Both formulations yield very similar results, indicating that the GND density field is not affected by the choice of element formulation.
Reprinted from [109] with permission from MDPI, Copyright 2017.

5.5.2 Bending size effect: Influence of sample thickness

Experiments show that the bending size effect is strongly correlated to the beam thickness. For that reason, the ability of the model to predict a strengthening effect as a result of thickness reduction is studied. This investigation allows in turn to quantify the role of GNDs within cantilever beam bending experiments. All subsequent computations are based on the 20RI8FI-element formulation. All three sample sizes are loaded up to 10 % normalized deflection using a gradient hardening modulus of $H_0^{\mathrm{e}} = 1$ GPa, which corresponds to $H_0^{\mathrm{s}} = 650$ MPa via Eq. (3.85). The length scale parameter l is involved in all subsequent computations with the value stated in Table 5.3. A relatively high value is chosen in order to obtain a rather strong size effect such that the impact of the characteristic sample dimension is immediately recognizable.

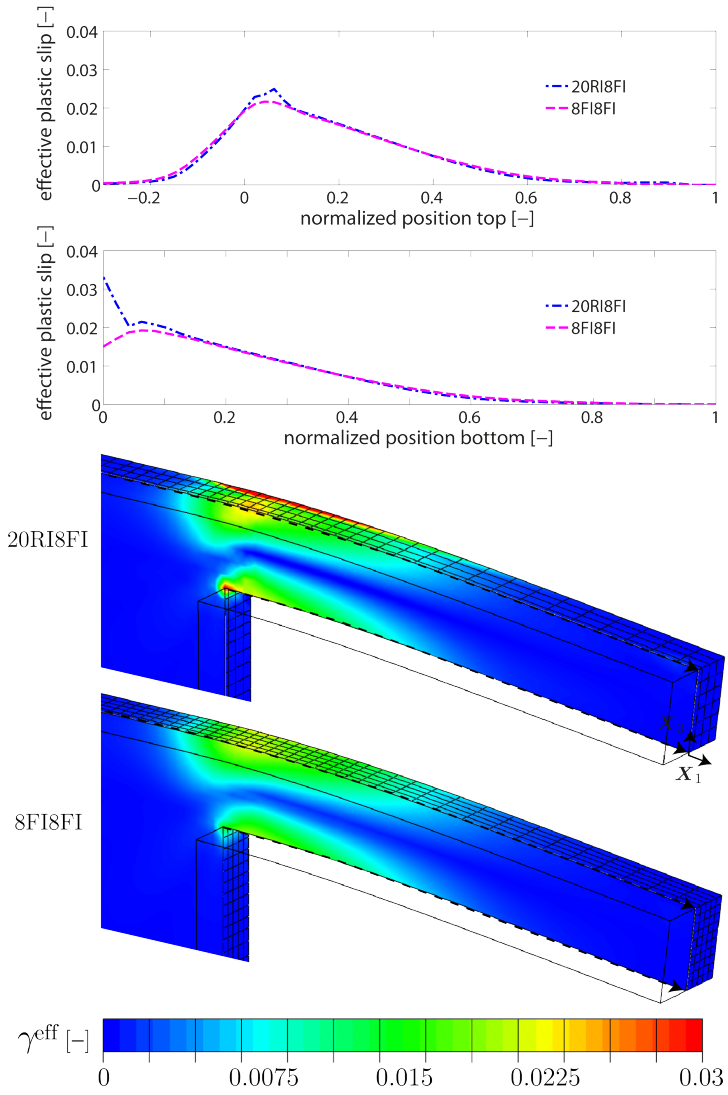

Figure 5.5: Distribution of the effective plastic slip γ^{eff} for the cantilever beam sample #1 along the indicated paths of the central cross section. In addition, the distribution is shown within the central $\boldsymbol{X}_1$-$\boldsymbol{X}_3$-plane. Results show some noticeable differences between both element formulations, in particular, close to the supported end, which refer mainly to the magnitude of γ^{eff}.
Reprinted from [109] with permission from MDPI, Copyright 2017.

The results in terms of stress-strain curves for all three cantilever beam samples are presented in Fig. 5.6. A clearly recognizable increase in strength is obtained for all three beam sizes compared to the reference saturation stress, i.e., the size-independent response measured in [179]. The smallest sample (cantilever beam #1, thickness of $h = 2.5$ µm) exhibits the stiffest response. With increasing beam thickness, the bending response becomes softer. Accordingly, the response of cantilever beam #3 (thickness of $h = 5$ µm) is the softest and for $h = 3.5$ µm (cantilever beam #2), the response is located in between. The obtained size effect is well captured by the non-local crystal plasticity model. The slop in the elasticity-dominated regime shows the exact opposite trend. Here, the slope is determined by the second moment of area and, hence, by the beam thickness h. At a later stage of deformation, the back-stress effect resulting from the storage of GNDs becomes dominant in terms of the work-hardening rate.

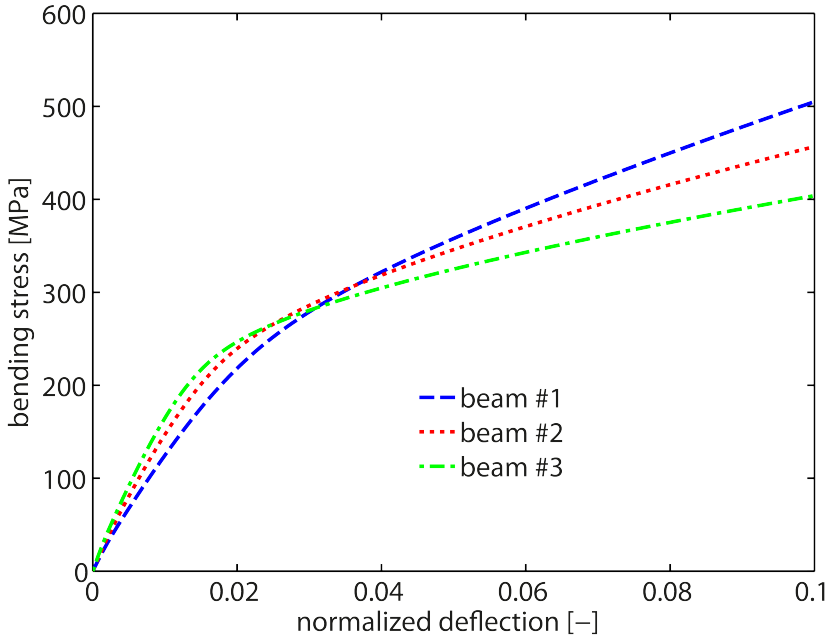

Figure 5.6: Size-dependent bending response of cantilever beams with different thicknesses. The strengthening effect associated with the accumulation of GNDs is the strongest for cantilever beam #1, having the smallest thickness of $h = 2.5$ µm. The softest response is obtained for cantilever beam #3 with $h = 5$ µm. The general trend in terms of smaller is stronger is captured well by the underlying model. All computations refer to the 20RI8FI-element formulation. Reprinted from [109] with permission from MDPI, Copyright 2017.

By considering the distribution of GNDs within the central cross section of the beams, i.e., within the $\boldsymbol{X}_1$-$\boldsymbol{X}_3$-plane as displayed in Fig. 5.7, it is seen that high densities of GNDs are accumulated at the supported end of the beams where the deformation is concentrated. In this region, GNDs pile up along the neutral plane (zero benging stress isoline), which does not necessarily coincide with the middle beam line. In fact, a shift of the stress field towards the bottom is caused to some extent by the supported end of the cantilever beam.

For all three sample sizes, a similar distribution of the effective GND density is found with a maximum value of $g_{\mathrm{i}}^{\mathrm{eff}} \approx 7.0 \times 10^{13}$ m^{-2}, located at the lower half of the clamped side. In other words, the population of GNDs directly scales with the deformation gradient imposed by the normalized deflection as this is the same for all three beam geometries. Nevertheless, the resulting back-stress contributes differently for the samples leading to higher bending stresses σ_{ben} for thinner beam samples. This can be partially explained by the fact that the computed bending stress[1] $\sigma_{\mathrm{ben}} = M_{\mathrm{b}}^{\mathrm{p}}/S^{\mathrm{p}}$ depends on the plastic section modulus $S^{\mathrm{p}} = wh^2/4$ which is a pure geometrical information. Further, $M_{\mathrm{b}}^{\mathrm{p}} = F_{\mathrm{R}} l_{\mathrm{b}}$ denotes the plastic bending moment. Thus, the resulting flow stress scales inversely proportional to the square of the beam thickness h. Accordingly, there must be a scaling effect resulting from the beam width w, even if this effect is expected to be smaller. As w is kept constant in the present study, a pure dependence on the sample thickness is obtained. In the experiments, however, an influence of the beam width w is likely due to dimensional deviations caused by the fabrication process.

[1] It is assumed that plastic deformation dominates which holds true at least in the most relevant strain regime $\varepsilon_{\mathrm{ben}} >\approx 0.35$, i.e., in the regime where the bending stress is saturating (cf. [179]).

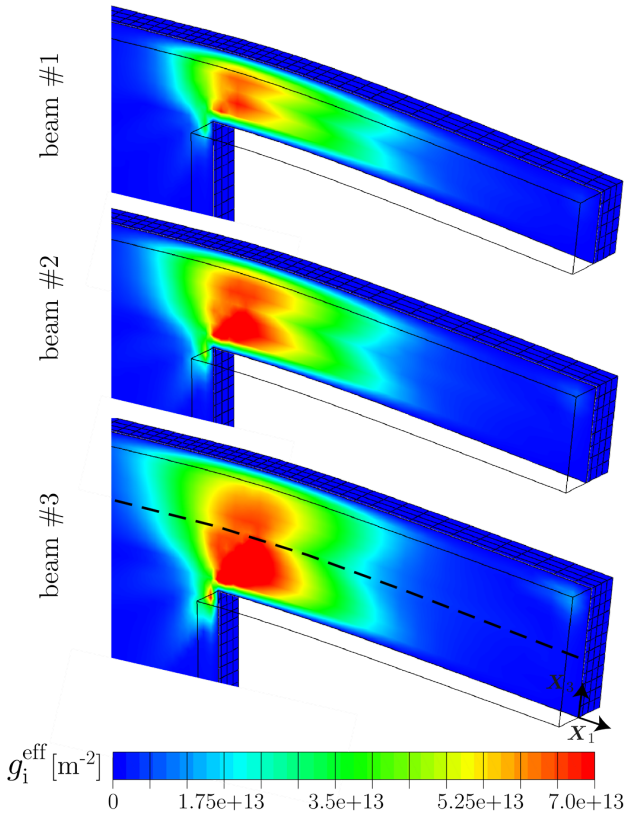

Figure 5.7: Distribution of the effective GND density g_i^{eff} for all three sample sizes within the central cross section ($\boldsymbol{X}_1$-$\boldsymbol{X}_3$-plane) after 10 % normalized deflection. GNDs pile up along the neutral plane indicated by the dashed line. Although the distribution of g_i^{eff} appears to be similar with respect to all three beam sizes, their impact on the bending response is strongly correlated to the beam thickness via the plastic section modulus S^p. In view of the effective SSD density shown in Fig. 5.8, a strong effect on the evolution is found due to the impact of GNDs.
Reprinted from [109] with permission from MDPI, Copyright 2017.

The role of GNDs is further assessed by means of the statistically stored dislocation density. To do so, we introduce the effective SSD density ζ^{eff} as a function of γ^{eff} and the effective free path of moving dislocations L^{eff}

$$\dot{\zeta}^{eff} = \frac{\nu^{eff}}{bL^{eff}}, \tag{5.15}$$

where

$$L^{eff} = \frac{K}{\sqrt{\rho^{eff}}}, \tag{5.16}$$

$\rho^{eff} = \zeta^{eff} + g_i^{eff}$ is the total (effective) dislocation density, and K is a material constant. Eq. (5.15) represents a modified version of the originally proposed relation by Essmann and Mughrabi [75, 240]. Corresponding interaction processes are intrinsically considered via the calculation of γ_α and $g_{i\alpha}$, respectively. $K = 10$ ([78]) and $\zeta_0^{eff} = 2.0 \times 10^{12}$ m^{-2} ([180]) are given in the literature.

In Fig. 5.8, the contour plots illustrate that the density of SSDs is naturally concentrated within highly deformed zones. More interestingly, the magnitude of ζ^{eff} reduces considerably with decreasing thickness of the cantilever beam. This indicates that the impact of GNDs on the evolution of SSDs is increased for smaller samples. In other words, the magnitude of SSDs approaches the magnitude of GNDs with decreasing sample dimensions, leading to a more pronounced influence on the bending response in case of smaller beams coming from accumulated GNDs. This indicates that the location of most prominent dislocation accumulation, for instance in terms of the total dislocation density ρ^{eff}, shifts from the beam surface towards the beam center with decreasing beam thickness.

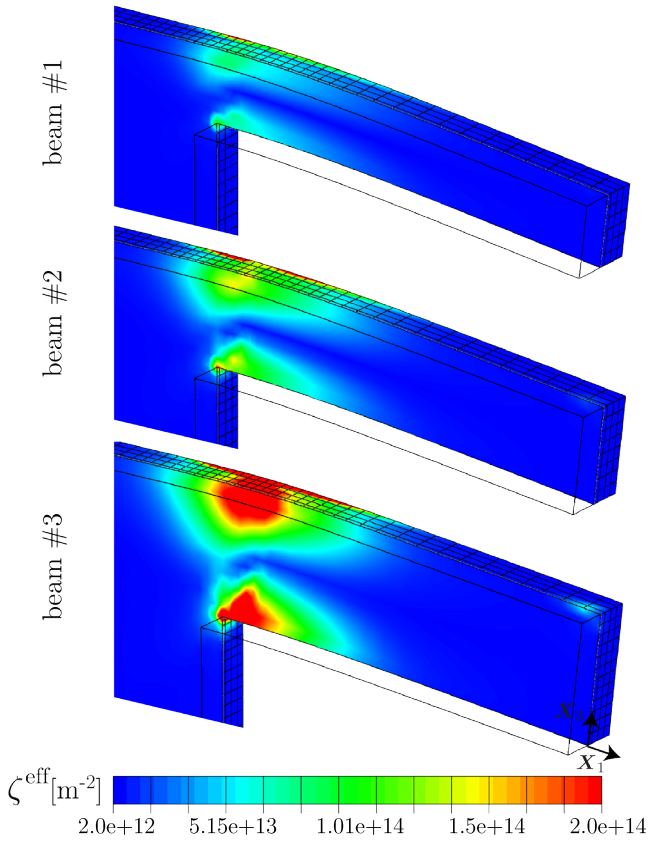

Figure 5.8: Distribution of the effective SSD density ζ^{eff} for all three sample sizes within the central cross section ($\boldsymbol{X}_1$-$\boldsymbol{X}_3$-plane) after 10 % normalized deflection. The density of SSDs approaches the density of GNDs with reducing beam thickness, leading to a more pronounced influence on the mechanical bending response coming from accumulated GNDs.
Reprinted from [109] with permission from MDPI, Copyright 2017.

5.5.3 Bending size effect: Impact of a saturating GND density

The plastic deformation is strongly localized at the supported end of the beam. In this region, the number of GNDs increases with increasing bending load due to compatibility reasons. Accordingly, the hardening contribution from the higher-order gradient $\text{Div}_{\text{i}}(\boldsymbol{\kappa}_\alpha)$ continuously increases which is reflected by the slope in the hardening behavior, cf. for instance Fig. 5.6. However, from a physical point of view, the number of dislocations stored locally cannot be

arbitrary high [105]. For that reason, the impact of a maximum permissible GND density on the bending response is investigated for cantilever beam #1 by setting up two different saturation values which are applied to each slip system independently: $g_{\mathrm{i}\alpha}^{\max} = 1 \times 10^{13}$ m^{-2} and $g_{\mathrm{i}\alpha}^{\max} = 2 \times 10^{13}$ m^{-2}, respectively. Saturated GND densities have been also incorporated, e.g., in [196]. Hence, in consideration of Eqs. (5.4) and (5.4), the evolution equations for edge and screw GND densities are exposed to the following case differentiations

$$\dot{g}_{\mathrm{i}\alpha}^{\mathrm{e}} = \begin{cases} \sum_\beta \nu_\alpha \left[g_{\mathrm{i}\beta}^{\mathrm{e}} \left[\iota_{\alpha\beta}^{\mathrm{ee}} + \chi_{\alpha\beta} \right] + g_{\mathrm{i}\beta}^{\mathrm{s}} \left[\iota_{\alpha\beta}^{\mathrm{es}} + \chi_{\alpha\beta} \right] \right] - \dfrac{1}{b} \nabla_{\mathrm{i}} \nu_\alpha \cdot \boldsymbol{s}_\alpha, & \text{if} \quad g_{\mathrm{i}\alpha(n+1)}^{\mathrm{e}} < g_{\mathrm{i}\alpha}^{\max}; \\ 0, & \text{if} \quad g_{\mathrm{i}\alpha(n+1)}^{\mathrm{e}} \geq g_{\mathrm{i}\alpha}^{\max}, \end{cases} \tag{5.17}$$

and

$$\dot{g}_{\mathrm{i}\alpha}^{\mathrm{s}} = \begin{cases} \sum_\beta \nu_\alpha \left[g_{\mathrm{i}\beta}^{\mathrm{s}} \left[\iota_{\alpha\beta}^{\mathrm{ss}} + \chi_{\alpha\beta} \right] + g_{\mathrm{i}\beta}^{\mathrm{e}} \left[\iota_{\alpha\beta}^{\mathrm{se}} + \chi_{\alpha\beta} \right] \right] - \dfrac{1}{b} \nabla_{\mathrm{i}} \nu_\alpha \cdot \boldsymbol{t}_\alpha, & \text{if} \quad g_{\mathrm{i}\alpha(n+1)}^{\mathrm{s}} < g_{\mathrm{i}\alpha}^{\max}; \\ 0, & \text{if} \quad g_{\mathrm{i}\alpha(n+1)}^{\mathrm{s}} \geq g_{\mathrm{i}\alpha}^{\max}. \end{cases} \tag{5.18}$$

As in the previous cases, all computations are based on the 20RI8FI-element formulation and are performed up to 10 % normalized deflection. The resulting stress-strain curves are presented in Fig. 5.9 together with the size-independent reference and the response of an unrestricted GND density evolution. Those cases represent the lower resp. upper bound of the mechanical bending behavior in terms of strength. The bending response in case of a limited GND evolution shows a saturation-like hardening behavior where the increase in strength relative to the size-independent case is related to the applied GND density limit. Hence, the stress saturation level is steered by the magnitude of $g_{\mathrm{i}\alpha}^{\max}$ in the way that a higher saturation limit causes a delayed deviation from the unrestricted case. In fact, once the saturation limit of $g_{\mathrm{i}\alpha}^{\max}$ is reached, the size-dependent micro-hardening stresses become decoupled from the gradient of plastic slip. Accordingly the size-dependent hardening contribution coming from $\mathrm{Div}_{\mathrm{i}}(\boldsymbol{\kappa}_\alpha)$ is limited. In related experiments, the bending response for a cantilever beam of size $2.5 \times 5.0 \times 16.3$ µm ($h \times w \times l_{\mathrm{b}}$) was found to show a stress saturation already at about 3.5% normalized deflection [179]. Thus, a saturation limit for GNDs around 1×10^{13} m^{-2} appears to be reasonable with respect to the current problem (cf. Fig. 5.9). In comparison to the size-independent case, this yields an increase of about 118 MPa in flow stress which is solely related to the geometrically necessary storage of dislocations. Furthermore, it can be seen from Fig. 5.9 that the bending size effect is conserved when comparing the bending response between the differently sized cantilever beams for the particular case if $g_{\mathrm{i}\alpha}^{\max} = 1 \times 10^{13}$ m^{-2}. The resulting effective back stress $\tau_{\mathrm{b}}^{\mathrm{eff}}$, defined as

$$\tau_{\mathrm{b}}^{\mathrm{eff}} = \sqrt{\sum_\alpha \mathrm{Div}_{\mathrm{i}}(\boldsymbol{\kappa}_\alpha)^2}, \tag{5.19}$$

is compared in Fig. 5.10 for selected magnitudes of $g_{\mathrm{i}\alpha}^{\max}$ and sample thicknesses h. As can be seen, the size-dependent hardening contribution is much higher for the higher GND density limit which is consistent with the determined bending response in Fig. 5.9. At the same time, the impact of the thickness is negligible for a particular $g_{\mathrm{i}\alpha}^{\max}$ value.

5.6 Discussion

The bending size effect is characterized by an increasing strength with decreasing sample thickness. A strong correlation between flow stress and beam thickness was found by Motz

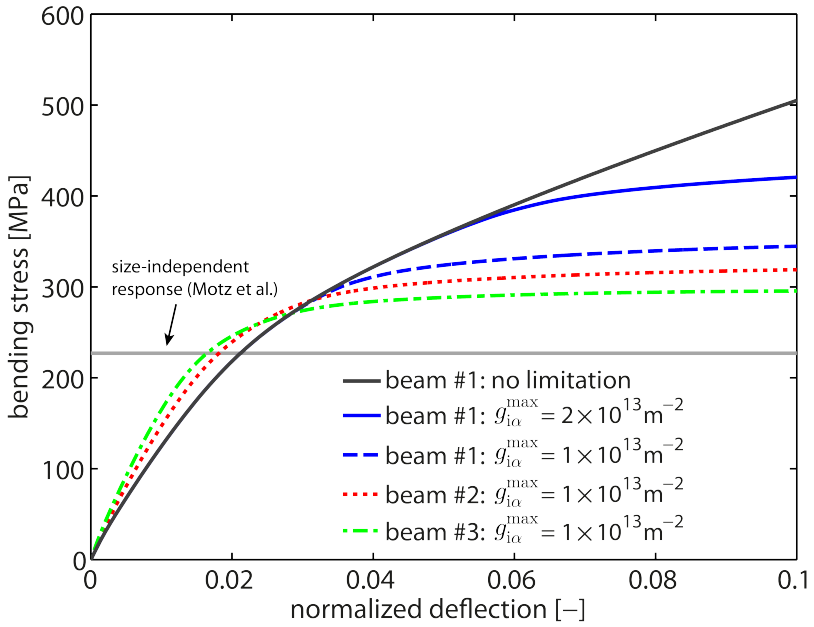

Figure 5.9: Impact of a maximum permissible GND density $g_{i\alpha}^{max}$ on the mechanical bending response of Cu single crystals. As seen for cantilever beam # 1, the resulting saturation level is steered by the magnitude of $g_{i\alpha}^{max}$. Furthermore, the bending size effect is conserved when comparing the response between the differently sized cantilever beams for a GND saturation limit of $g_{i\alpha}^{max} = 1 \times 10^{13}$ m^{-2}. Reprinted from [109] with permission from MDPI, Copyright 2017.

et al. [179] for thicknesses in the range 7.5 μm to 1 μm. A similar trend was found by Demir et al. [66] for alternative single crystal geometries with average thicknesses in the range 4.23 μm to 1.02 μm. In this size regime, the bending size effect is associated with a combination of different mechanism. Besides the geometrically necessary storage of dislocations, dislocation starvation and dislocation source limitation are known to affect the plastic deformation behavior. Dislocation source limitation plays a dominant role for very small beam sizes as the statistical distribution of dislocation sources becomes then more and more crucial, cf. [241]. As a consequence of a limited availability of source density within the localized region of plastic deformation (supported beam end), the yield limit of the material may increase significantly. In this respect, the storage of GNDs imposes an additional resistance to dislocation nucleation, yielding an increasing nucleation strength. Last but not least, plasticity is strongly controlled by the initial dislocation density of the crystal [224]. In the particular case of microbending of single crystals, dislocations are able to leave the crystal through the free surfaces at some point [179]. This process of starving or escaping dislocations finally leads to the extinction of initially available dislocations [88]. Hence, with a sufficiently small number of obstacles in the single crystalline sample, the size-dependent flow stress is additionally governed by the applied deformation rate relative to the dislocation nucleation rate which determines the required stress level for continuing operation of individual dislocation sources, see also Balint et al. [12]. Keeping in mind that an accurate fabrication of micro-cantilever samples is a challenging task, there is currently no sufficient data available allowing for a meaningful interpretation of the impact of each of the sample dimensions - thickness, width, and length - independently. For that reason, strengthening effects mentioned above are neglected in the current numerical study. Instead, the focus is solely on the micromechanical role of GNDs and their impact on the mechanical bending response as a function of the beam thickness h.

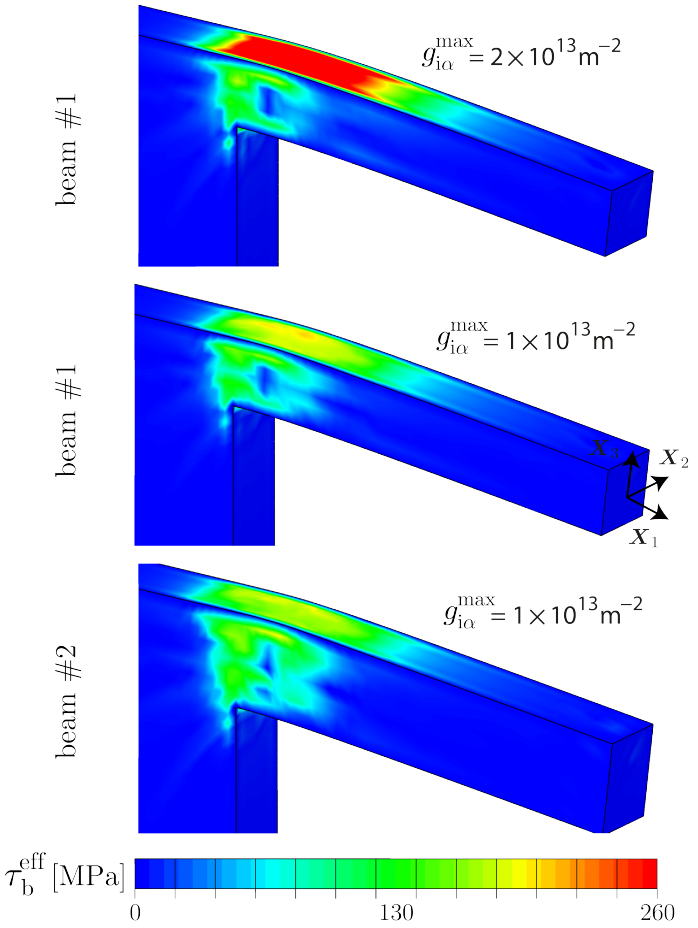

Figure 5.10: Effective back stress τ_b^{eff} for selected $g_{i\alpha}^{max}$ values and cantilever beam sizes. The size-dependent resistance to bending deformation increases with increasing GND density limit. The sample thickness has a negligible impact on the back-stress evolution for a fixed $g_{i\alpha}^{max}$.
Reprinted from [109] with permission from MDPI, Copyright 2017.

The numerical results correctly capture the commonly observed trend 'smaller is stronger'. In fact, the size-dependent strengthening effect due to the back-stress effect induced by the storage of GNDs is predicted very well for two different cases: (i) unrestricted evolution of GND densities and (ii) physically limited GND densities. In case (i), GND densities evolve with increasing plastic slip gradients which, for the particular case of cantilever beam bending, continuously grow within the deformation-localized region. In contrast, the evolution of GND densities is limited in case (ii) and completely vanishes if a certain saturation limit is reached, i.e., if the plastic strain gradient becomes very large. This mimics a more realistic micromechanical behavior as is supported by the characteristics of related experimental force-deflection curves. Moreover, the local number of GNDs to be stored locally cannot be arbitrary high (cf. [105]). The numerically determined flow stresses for the here investigated beam thicknesses and for the particular case of $g_{i\alpha}^{max} = 1 \times 10^{13}$ m^{-2} are illustrated in Fig. 5.11 along with available experimental data from the literature. The simulation data is solely a function of the beam thickness h while experimentally determined data sets might (undesired) be affected by the reduction of the other sample dimensions (l_b and w) or by varying dimension ratios (l_b/h and l_b/w). Apparently, changing sample dimensions and their ratios add substantially to the

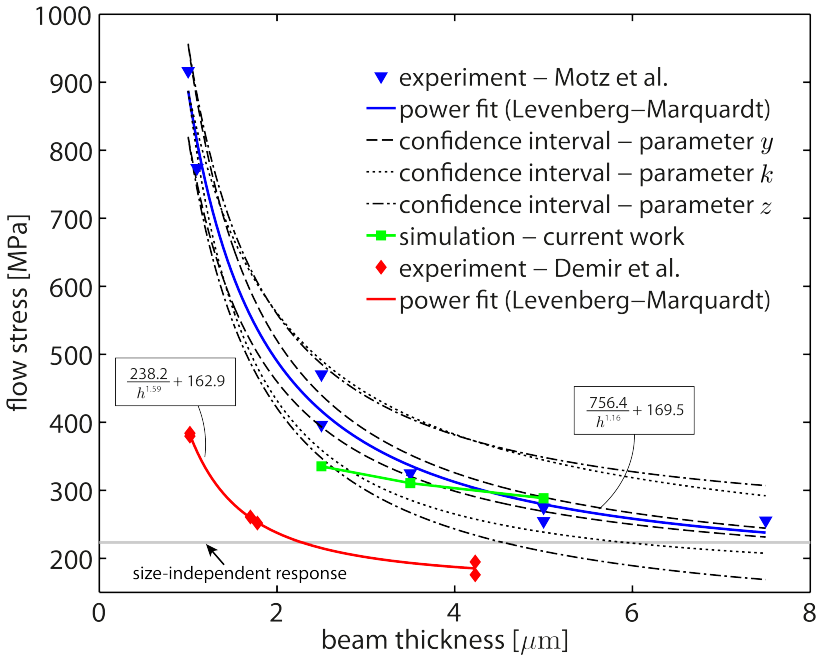

Figure 5.11: Experimentally and numerically determined relation between flow stress σ_{ben} and beam sample thickness h in microbending of Cu single crystals together with associated power fits. The deviations between the two experimental data sets might be explained by the different sample geometries: cantilever beams with rectangular cross section and high l_{b}/h as well as l_{b}/w ratios ([179]); cantilever beams with trapezoidal cross section, high $l_{\mathrm{b}}/h_{\mathrm{avg}}$ ratios, but low l_{b}/w ratios ([66]). The numerically determined flow stress values show a reasonable strengthening effect in the regime where GNDs dominate the micromechanical behavior of the crystal, i.e., in the range $h \gtrsim 3$ µm. For $h \lesssim 3$ µm, the impact of dislocation starvation and source limitation become crucial, leading to an even more pronounced increase in flow stress with decreasing beam thickness h. The data of Demir et al. [66] refers to a flow stress measurement at 0.06 strain.
Reprinted from [109] with permission from MDPI, Copyright 2017.

complexity of the superimposed effect associated with the mechanisms discussed above. This might be one explanation for the deviations between the experimental data sets of [66, 179]. A meaningful discussion regarding the impact of the initially available dislocation density is not possible due to the lack of data.

Both experimental data sets were fitted by a power function of the form $yh^{-k} + z$ using the Levenberg-Marquardt algorithm, see Fig. 5.11. Then, an error analysis is conducted for the data set of Motz et al. [179] in order to draw final conclusions regarding the statistical representativeness of the measurements. The standard deviation is calculated for each fitting parameter y, k, and z. The maximal and minimal standard deviation of each fitting parameter is considered independently to compute upper and lower confidence bounds while the other two parameters are kept constant in each case. The resulting confidence intervals are embedded in Fig. 5.11 and are interpreted independently. The overall fit sensitivity associated with the prefactor y is small due to its narrow confidence interval over the entire beam thickness range. With respect to the exponent k, it is found that the power function is governed by

the exponent k in the regime $h < 2$ μm. As here, one would expect rather large experimental scatter, the power fit appears less sensitive compared to the regime $h > 2$ μm. In fact, the confidence interval associated with the exponent k vanishes if h approaches ≈1 μm. Hence, we conclude that the determined exponent describes the experimentally measured relation between σ_{ben} and h fairly well. The offset parameter z indicates a similar tendency as the exponent, i.e., for $h > 2$ μm the power function becomes more sensitive with respect to z. In comparison to the simulation data which reflects a pure dependence on the beam thickness h, a good agreement is found for $h \gtrsim 3$ μm as the predicted data lies very close to the actual fit. Consequently, it is concluded that the mechanism associated with the geometrically necessary storage of dislocations governs the mechanical bending behavior in this range. For $h \lesssim 3$ μm, the impact of dislocation starvation and source limitation becomes obviously non-negligible. These findings fit also to DDD predictions of Hussein et al. [108] where single crystals with $D_{\mathrm{m}} \leq 1.0$ μm were found to be almost free of dislocations due to the limiting size whereas crystals with $D_{\mathrm{m}} \geq 5.0$ μm show pronounced dislocation activities.

5.7 Conclusions

Based on an extended gradient crystal plasticity model, the role of GNDs in the mechanical bending response of micron-sized, single crystalline Cu was investigated. The underlying model contains non-standard evolution relations for the edge and screw components of the slip system-based dislocation density vector, crystal-specific interaction relations, and higher-order gradient boundary conditions. The cantilever beam geometries considered in the numerical study allowed the examination of the strengthening effect associated with the geometrically necessary storage of dislocations solely as a function of the beam thickness which is a non-trivial task from an experimental point of view. Other size-dependent mechanisms such as dislocation starvation and source limitation were disregarded at the current stage. In particular, the influence of the beam thickness as well as the impact of a maximum permissible GND density was of primary importance. Besides, in relation to the coupled field problem between displacement and GND density degrees of freedom, a quantitative comparison between two different finite element formulations has been carried out. On the basis of our findings, we conclude:

- The bending dominated deformation is captured more accurately by the mixed FE-formulation denoted as 20RI8FI. In contrast, the commonly applied linear FE-formulation (8FI8FI) overestimates the bending response for the size-independent as well as the size-dependent case. The locking phenomenon only influences the predicted bending behavior (and not the predicted GND density) in the case of the 8FI8FI-element formulation.

- The bending size effect is captured by the theory to the extent caused by geometrically necessary storage of dislocations. This size-dependent strengthening effect can be explained as follows: (i) Similar dislocation pile-ups have been found around the neutral plane where dislocations get stuck rapidly and lose the ability to accommodate the beam bending, independent of the beam size. The impact of the resulting back-stress effect on the bending response is nevertheless higher for the smallest beam as the bending stress is inversely proportional to the square of the beam thickness. The same holds for the flow stress computation in related cantilever beam bending experiments. (ii) In contrast to the distribution of the GND density, a much higher population of SSDs was found for the largest cantilever beam sample which indicates that the bending behavior is here mainly

governed by random trapping processes. However, with decreasing beam thickness, these processes become less pronounced. This is supported by the fact that the magnitude of the SSD density becomes comparable to the one of the GND density in the case of the thinnest beam sample. Consequently, the impact of GNDs on the mechanical bending response is most pronounced in the thinnest beam sample. Accordingly, the location of maximum dislocation storage was found to shift from the sample surface towards the beam center when decreasing the beam thickness.

- A physically motivated limitation of the GND density was incorporated into the model by modified evolution equations for the edge and screw GND density components. In the current crystal plasticity framework, this was done at the nodal level as GND densities were treated as additional degrees of freedom. This leads to a bending response with saturation-like hardening behavior - which is in accordance with experimental findings. At the same time, the smaller is stronger trend was conserved in accordance to the unrestricted case. In the end, a saturation limit of $\approx 1 \times 10^{13}$ m^{-2} was found to match well the characteristics in the bending response of related experimental data where a flow stress saturation was obtained at about 3.5 % normalized deflection.
- Numerically determined flow stresses using a saturation limit of $\approx 1 \times 10^{13}$ m^{-2} show a reasonable strengthening effect in the beam thickness range $h \gtrsim 3$ µm. The predicted flow stress of cantilever beam #3 is in great accordance with experimental data. The flow stress associated with cantilever beam #2 still shows an acceptable accuracy as it lies within the confidence interval of the related experimental data. For the thinnest beam sample, a considerable contribution from another size-dependent mechanism occurs. Based on this, it can be argued that GNDs dominate the micromechanical bending response in the thickness range $h \gtrsim 3$ while other mechanisms such as dislocation starvation and source limitation become crucial for $h \lesssim 3$ µm where an even more pronounced increase in flow stress is experimentally measured.

6 Advanced higher-order boundary conditions for dislocation-surface interaction modeling

Extended crystal plasticity theories are well established to study size-dependent hardening of metals. Surface and inner grain boundary conditions play a significant role for crystals at small scales as they affect the dislocation activity and, hence, alter strength and strain hardening behavior. Conventional micro boundary conditions, i.e., microhard and microfree, are unable to capture the underlying physics as they describe ideal and over-simplified surface/interface conditions. In this work, advanced boundary conditions for gradient extended crystal plasticity are introduced to map realistic conditions at external surfaces, interphases, or grain boundaries. They relate the magnitude of plastic slip to surface defect density and slip directions with respect to the surface normal. Characteristic features are highlighted, including the effect of surface yielding and size dependent surface strengthening.

The content of this chapter has been published in [E. Husser and S. Bargmann, *Size affected dislocation activity in crystals: Advanced surface and grain boundary conditions*, Extreme Mechanics Letters, 13, 36-41, 2017] and may include some modifications.

6.1 Introduction

In crystalline solids, perfect crystalline behavior ceases to exist near external surfaces, grain boundaries between two crystals of the same phase and interphase boundaries between two different phases [170, 171]. Since the binding of an atom to its neighbors contributes a negative term to the energy of a crystal, Gibbs free energy at these surfaces is modified due to inhomogeneities at the nanoscale, such as altered bonds. This difference in bonding as compared to the bulk generally causes an extra surface stress [214]. Dislocation dynamics and, thus, macroscopic plastic behavior is also influenced by the presence of a surface to create size effects on yield stress and work hardening. The surface's influence becomes substantial once the number of atoms sitting at the surface relative to those lying within the bulk increases, e.g., in the case of ultra-fine-grained metals, thin films, nanoporous materials [248].

With its nanoscale porosity and high specific surface area, nanoporous gold demonstrates extreme chemo-mechanical activity [220]. Its catalytic activity, electrical conductivity, morphological properties (e.g., high specific surface area), and mechanical properties (e.g., reduced stiffness), make nanoporous gold attractive in numerous applications such as actuation, catalysis, sensors and microfluids [181, 220, 254]. In nanoporous gold the load bearing structure is a network of ligaments (cf. Fig. 6.1) with diameters of 5 nm to several micrometers, depending on the post annealing treatment [101, 123, 219]. Although brittle in tension, nanoporous gold shows considerable malleability, that is, extreme ductility under compressive stress in the vicinity of crack tips with ligaments occasionally strained by as much as 200 % [29, 118]. Microscopic characterization of fracture surfaces indicated that dislocation activity is suppressed in nanoscale ligament structures while dislocation activity is present in heat treated nanoporous gold with average ligament diameter of $\approx 1\,\mu$m [29]. In addition to the effect of suppressed dislocation nucleation [88], emission and reabsorption of dislocations at free surfaces is another source of size dependent hardening [235].

In this work, we study the plastic[1] deformation behavior of nanoporous gold in the context of gradient extended crystal plasticity at finite strains. The focus is on novel higher-order

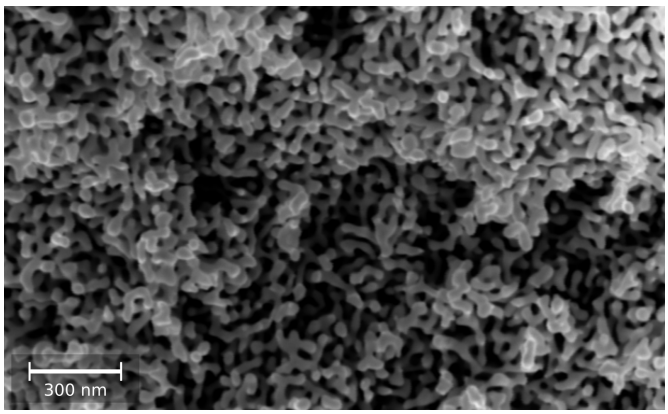

Figure 6.1: Scanning electron micrograph of nanoporous gold with an exceptionally high surface-to-volume ratio. Source: Reprinted from [254]. (Image courtesy of Nadiia Mameka at Helmholtz-Zentrum Geesthacht.)
Reprinted from [112] with permission from Elsevier, Copyright 2017.

[1] The influence of surfaces on the elastic behavior is studied in another work; elastic and plastic Poisson's ratios of nanoporous gold were investigated experimentally and numerically in [161].

boundary conditions reflecting microscopically non-idealized conditions at external surfaces, grain boundaries, or interfaces. In the vast majority of analytical and numerical studies, two types of simple, idealized boundary conditions are adopted, namely microfree and microhard. The former characterizes conditions with vanishing microstresses, i.e., no microscopic force conjugated to geometrically necessary dislocations occurs as a driving force on the body. Dislocations are free to escape at the surface, hence no dislocation pile-ups occur. At the other extreme, i.e., for microhard conditions, plastic slip vanishes at the boundary, preventing any dislocation escape.

Non-idealized boundary conditions are of interest, for instance, if the exterior causes additional resistance to plastic deformation or, in other words, if dislocations are not enabled to move unrestricted through the surface. Related discussions, including size effects on the yield stress and work hardening as well as the impact of surface effects on fracture properties, are found in [91]. Oxidation on nanoporous gold films[2] is higher than on planar gold due to increased catalytic activity of the porous network [258, 266]. Buckley [37] demonstrated that thin films on the surface of single crystal Au increased the surface hardness. This was attributed to increased resistance to plastic deformation by the impeded escape of dislocations by the presence of the oxide film, referred to as the Roscoe effect [212] [3]. Therefore, mechanical properties of small-scaled samples are related (to some extent) to their surfaces.

Although highly relevant, this aspect of dislocation-surface interaction modeling has not been studied in the literature for nanoporous gold. With this work, we attempt to bridge this gap by presenting computational modeling of advanced higher-order boundary conditions for Au single crystals. As a demonstrative example, their impact on the deformation response of a periodic nanoporous Au microstructure is examined. The chosen geometry is characterized by a typical microstructural feature with curved surfaces frequently found in nanoporous metals. This results in many diverse misorientation angles.

Grain boundary conditions, i.e., inner boundaries in polycrystals, which are physically more meaningful than their idealized counterparts have been studied by [23, 69, 84, 98, 195, 247]. Only very few works are devoted to a computational framework for surface effects in single crystals. In these, the formation of surface steps during plastic deformation is taken as an additional source for size-dependent hardening and strengthening [107, 200]. The conditions proposed in this work are more general and capable of modeling a wide range of dislocation-surface interactions.

6.2 Modeling framework

6.2.1 Basic relations

The thermodynamic consistent framework for gradient-enhanced crystal plasticity at large deformations is applied, cf. Chapter 3. In particular, a hyperelastic material behavior according to Eq. (3.25) (isotropic Neo-Hookean law) is postulated. Furthermore, a defect energy of the

[2] At temperatures less than 900°C gold does normally not form a stable oxide in air or oxygen [37, 52]. However, electrochemical techniques allow generation of oxides on gold surface [217].

[3] This scenario is not limited to gold. It is demonstrated in [90] that, on the course of deformation the oxide films in aluminum causes formation of a layer of edge dislocation dipoles trapped beneath the surface and reduction of the amount of surface slip. This reduction is observed to be larger for the increased oxide coating thickness. Hence, the proposed methodologies in this work have a wide range of applications although the current application is concentrated on the nanoporous gold.

form given by Eq. (3.84) is taken into account resulting in a back-stress vector of the following form

$$\boldsymbol{\kappa}_\alpha = -l^2 b \left[H_0^{\mathrm{e}} \boldsymbol{s}_\alpha \int_{t_0}^{t} \dot{g}_{\mathrm{i}\alpha}^{\mathrm{e}} \mathrm{dt} + H_0^{\mathrm{s}} \boldsymbol{t}_\alpha \int_{t_0}^{t} \dot{g}_{\mathrm{i}\alpha}^{\mathrm{s}} \mathrm{dt} \right]. \tag{6.1}$$

Here, $l = l_\alpha$ and $b = b_\alpha$ are taken as constant quantities in regard to the fcc crystal lattice. The mathematical model is formulated in consistency with the second law of thermodynamics. In contrast to the framework outlined in Section 3.3.4, κ_α is not derived from the free energy function. Hence, the reduced dissipation inequality can be formulated as

$$\mathcal{D}_{\mathrm{red}} = \sum_\alpha \left[\int_{\mathcal{B}_{\mathrm{i}}} \nu_\alpha \pi_\alpha \mathrm{dV_i} + \int_{\partial\mathcal{B}_{\mathrm{i}}} \nu_\alpha \boldsymbol{\kappa}_\alpha \cdot \boldsymbol{N}_{\mathrm{i}} \mathrm{dA_i} \right] \geq 0, \tag{6.2}$$

where $\pi_\alpha = \tau_\alpha + \mathrm{Div_i}(\boldsymbol{\kappa}_\alpha)$ denotes the microforce. For similarities between both frameworks, see for instance Ekh [70].

6.2.2 Governing equations

The evolution of edge and screw GND densities is governed by Eqs. $(3.62)_2$ and (3.63), respectively. Both governing equations for GND densities are coupled to the displacement problem via stress measures. For the sake of clarity, recall the balance of linear momentum reads $\boldsymbol{0} = \mathrm{Div_i}(\boldsymbol{F}_{\mathrm{E}} \cdot \boldsymbol{S}_{\mathrm{E}})$ and is coupled to the evolution equations for GND densities. At the local level, the evolution of plastic slip variables is governed the power law relation of the form

$$\nu_\alpha = \nu_0 \left[\frac{\langle \pi_\alpha \rangle}{r_\alpha} \right]^m, \quad \text{with} \quad \langle \bullet \rangle = \frac{1}{2} \left[\bullet + | \bullet | \right]. \tag{6.3}$$

In that

$$r_\alpha = Y_{\alpha 0} + H_0^{\mathrm{l}} \int_{t_0}^{t} \nu_\alpha \mathrm{dt} \tag{6.4}$$

describes the slip system resistance associated with random trapping processes of statistically stored dislocations (SSDs) by means of the local hardening modulus H_0^{l}. SSDs are captured by the resulting slip in the material. Finally, the initial slip system resistance (critical resolved shear stress) is incorporated via $Y_{\alpha 0}$.

6.2.3 Boundary conditions

Standard micro boundary conditions are known as microhard and microfree and are specified on boundary portions $\partial\mathcal{B}_{\mathrm{i}}^{\gamma}$ and $\partial\mathcal{B}_{\mathrm{i}}^{g}$, respectively, cf. Section 3.3.8. These condition mimic idealized conditions at the crystal's surface as illustrated by Fig. 6.2 a) and b). At one extreme, microhard boundaries prevent any transmission of crystallographic slip through the boundary. In this case, the boundary deforms with maximum resistance to plastic deformation such that dislocations are compelled to pile up. This behavior is typically expressed by Eq. (3.88). At the other extreme, microfree boundaries blockade any dislocation pile ups along the exterior. Boundaries are transparent to dislocation motion, leading to zero resistance to plastic deformation. This situation is described by Eq. (3.87). In spirit of Ekh et al. [69], we postulate advanced microflexible boundary conditions for single crystals for which the

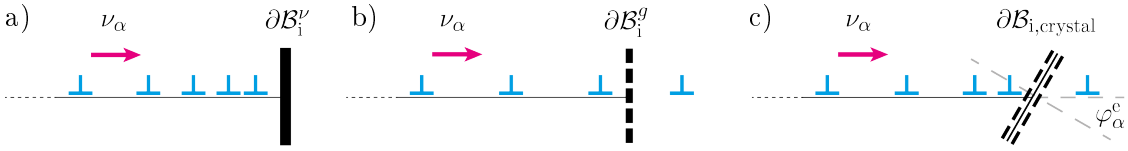

Figure 6.2: Schematic illustration of higher-order boundary conditions: a) microhard; b) microfree; c) (non-idealized) microflexible boundary conditions. While a hard boundary does not permit any slip transmission through the boundary, a free boundary is completely transparent to dislocation motion. The proposed advanced micro flexible boundary conditions relate the boundary slip to the defect density and depend on the misorientation angles $\varphi_\alpha^\mathrm{e}$ and $\varphi_\alpha^\mathrm{s}$. This allows a physically more meaningful modeling.
Reprinted from [112] with permission from Elsevier, Copyright 2017.

magnitude of plastic slip at the boundary is related to the microstress via

$$\nu_\alpha = C_\Gamma l^2 b H_0^\mathrm{e} \left[\boldsymbol{s}_\alpha \cdot \boldsymbol{N}_\mathrm{i} \frac{\dot{g}_{\mathrm{i}\alpha}^\mathrm{e}}{\tan(\varphi_\alpha^\mathrm{e})} + \boldsymbol{t}_\alpha \cdot \boldsymbol{N}_\mathrm{i} \frac{[1-\nu]\dot{g}_{\mathrm{i}\alpha}^\mathrm{s}}{\tan(\varphi_\alpha^\mathrm{s})} \right] \quad \text{on} \quad \partial\mathcal{B}_{\mathrm{i,crystal}}, \tag{6.5}$$

where $C_\Gamma = C_\Gamma(g_\mathrm{i}^\mathrm{eff})$ denotes the boundary coefficient (given in unit area per energy), related to the effective GND density as defined in Eq. (5.14). Moreover,

$$\varphi_\alpha^\mathrm{e} = \arccos(|\boldsymbol{s}_\alpha \cdot \boldsymbol{N}_\mathrm{i}|) \quad \text{and} \quad \varphi_\alpha^\mathrm{s} = \arccos(|\boldsymbol{t}_\alpha \cdot \boldsymbol{N}_\mathrm{i}|) \tag{6.6}$$

are the misorientation angles measured between the boundary normal $\boldsymbol{N}_\mathrm{i}$ and the flow direction of the edge respectively screw dislocation, cf. the illustration in Fig. 6.2 c). Via Eq. (6.5), the slip rate on the boundary is associated with the microstress and the angle[4] at which dislocations escape through the boundary. Microfree and microhard boundary conditions are naturally incorporated for complete alignment and misalignment, respectively [69]. For cases in between these extremes, the proposed boundary conditions result in non-zero boundary dissipation contribution, cf. Eq. (6.2). With respect to $C_\Gamma(g_\mathrm{i}^\mathrm{eff})$, a natural choice might be

$$C_\Gamma = C_0 \exp\left(s_\Gamma \frac{\langle g_\mathrm{i}^\mathrm{eff} - g^\mathrm{c} \rangle}{g^\mathrm{c}} \right), \tag{6.7}$$

in which C_0 is the flexibility boundary coefficient, s_Γ determines the rate of dislocation absorption resp. transmission by the surface, and g^c measures dislocation pile up underneath the surface in terms of critical dislocation density and acts as a threshold for the initiation of dislocation transmission and absorption, leading to changing surface, interface resp. grain boundary conditions. For $g_\mathrm{i}^\mathrm{eff} - g^\mathrm{c} > 0$, C_Γ starts to evolve, resulting in a softening effect due to dislocation escape and absorption. This mechanism represents surface yielding as plastic deformation across the boundary increases. Furthermore, with decreasing length scales, this effect naturally becomes reinforced due to stronger interplay between dislocations and external surfaces as a result of a change in number of atoms exposed to a surface. In contrast to ideally smooth and clean grain boundaries, the proposed concept accounts for inhomogeneities at nanoscale such as surface coatings or passivation layers [116, 121, 267], damage layers induced

[4] For dislocation flow parallel to the surface area, it follows that $1/\tan(\varphi_\alpha^\mathrm{e}) \to 0$ as $\varphi_\alpha^\mathrm{e} \to \pi/2$ and, hence, the corresponding contribution within the boundary term vanishes. For dislocation flow perpendicular to the surface, a threshold is required to ensure numerical treatment of the computation of $1/\tan(\varphi_\alpha^\mathrm{e})$ as $\varphi_\alpha^\mathrm{e} \to 0$. Same holds for $\varphi_\alpha^\mathrm{s}$.

by the FIB milling process [114, 126, 172], oxide layers [83], and may also be extended to interfacial effects in metal polymer (nano-) composites [189].

An important aspect of higher-order boundary conditions is the treatment of the boundary term in the implementation. Due to the similarity of both GND density equations, we limit our attention to the edge component. Then, the variational form of Eqs. $(3.62)_2$ yields

$$0 = b \int_{\mathcal{B}_\mathrm{i}} \delta g^\mathrm{e}_\alpha \dot{g}^\mathrm{e}_{\mathrm{i}\alpha} \mathrm{dV_i} - \int_{\mathcal{B}_\mathrm{i}} \nu_\alpha \mathrm{Div_i} \left(\delta g^\mathrm{e}_\alpha \boldsymbol{s}_\alpha\right) \mathrm{dV_i} + \int_{\partial\mathcal{B}_\mathrm{i}} \delta g^\mathrm{e}_\alpha \nu_\alpha \boldsymbol{N}_\mathrm{i} \cdot \boldsymbol{s}_\alpha \mathrm{dA_i}. \tag{6.8}$$

The boundary condition is then implemented via the surface term. Thus, no additional surface elements are needed.

6.3 Numerical example: nanoporous gold

We demonstrate the performance of the advanced micro boundary conditions by means of compression tests on nanoporous gold. Fig. 6.3 a) depicts a typical structural feature in nanoporous Au which is considered in the here investigated microstructure[5], cf. Fig. 6.3 b). Fig. 6.3 c) shows the corresponding finite element mesh of the periodic unit cell consisting of 25536 linear brick elements. The advanced boundary condition in Eq. (6.5) is applied to the entire surface, i.e., $\partial\mathcal{B}_\mathrm{i} = \partial\mathcal{B}_{\mathrm{i,crystal}}$. Furthermore, periodicity is applied with respect to all displacement and GND density degrees of freedom at unit cell junctions.

Since dealloying conserves the crystal lattice of the parent alloy, the single phase ligament network does not accommodate grain boundaries [118]. Hence, the microstructure is treated as a single crystal. A single slip configuration is adopted with $\boldsymbol{s}_1 = [1\bar{1}\bar{1}]/\sqrt{3}$ and $\boldsymbol{n}_1 = [101]/\sqrt{2}$, resulting in a Schmid factor of 0.4082 for compression along the [001] direction. Edge as

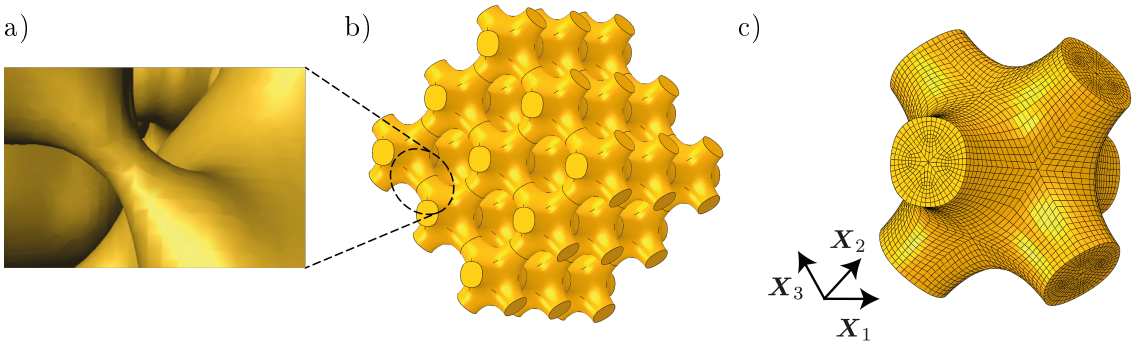

Figure 6.3: a) 3D FIB tomography reconstruction showing a typical structural feature in nanoporous gold with mean ligament diameter of 420 nm (Reprinted from [268]); b) microstructure built up periodically by the indicated unit cell (27.5% gold volume fraction); c) finite element mesh (25536 linear brick elements) of the periodic unit cell.
Reprinted from [112] with permission from Elsevier, Copyright 2017.

[5] For details regarding the microstructure generation see [112]. In summary, the resulting periodic unit cell is characterized by a solid volume fraction of 27.5%. Two mean ligament diameters (measured at the smallest cross-section) are taken into account in this work, namely $D_0 \approx 1000$ nm and $D_0 \approx 250$ nm.

well as screw GND densities are accounted for. The structure is loaded under displacement controlled conditions along the [001] direction up to 5 % compressive strain and at a strain rate of 10^{-3} s^{-1}. The rate of dislocation absorption resp. transmission is set to $s_\Gamma = 100$. All material parameters for Au single crystal are listed in Table 6.1. The empirical approach for the determination of the initial slip resistance is adopted from Bargmann et al. [16].

First, the mechanical response of the microstructure is analyzed for $g_\mathrm{i}^\mathrm{eff} - g^\mathrm{c} \leq 0$ being fulfilled during the entire deformation. The results are shown in Fig. 6.4 for different magnitudes of C_0. The idealized response in terms of microhard and microfree boundary conditions are the upper and lower bound of the crystal's strength. For $C_0 = 0$, the boundary contains the highest density of defects leading to minimum plastic deformation. With increasing C_0, the ability to transmit dislocations through the boundary increases. This, in turn, leads to a softer mechanical response in terms of increasing plastic deformation. A fully transparent boundary, i.e., without any resistance to dislocation motion, is achieved in the limiting case $C_\Gamma \to \infty$. This is illustrated by the contour plot inclusions on the right-hand side of Fig. 6.4 by means of the accumulated plastic slip distribution $\gamma_1 = \int_{t_0}^{t} \nu_1 \mathrm{d}t$. Furthermore, a pronounced effect resulting from a reduction of the characteristic size, here from $D_0 \approx 1000$ nm to $D_0 \approx 250$ nm, is clearly shown for the particular case $C_0 = 1$ µm^2/nJ.

Next, we study the case of an initially impenetrable interface whose resistance to plastic deformation softens after a critical dislocation density is overcome ($g_\mathrm{i}^\mathrm{eff} > g^\mathrm{c}$). A cut-off value $\overline{C}_\Gamma = 100$ µm^2/nJ is introduced in order to ensure numerical stability of the computations during the evolution of the boundary coefficient. The impact on the mechanical response is illustrated in Fig. 6.5 for different threshold values g^c. As shown, dislocation-controlled surface yielding is obtained at different strain levels as a result of spontaneous initiation of plastic slip across the surface. The results clearly demonstrate the ability of the advanced boundary conditions to model surfaces whose properties are influenced by formation of surface films, contamination, fabrication process, coating, etc. which become non-negligible at the submicron scale.

Table 6.1: Material parameters considered in the numerical computations.

Parameter	Symbol	Value
Young's modulus	E	79 GPa
Poisson's ratio	ν	0.44
Burgers vector magnitude	b_α	0.288 nm
Initial slip resistance	$Y_{\alpha 0}$	43.47 MPa
Rate sensitivity parameter	m	20
Reference shear rate	ν_0	10^{-3} s^{-1}
Local hardening modulus	H_0^l	10.2 MPa
Gradient hardening modulus	H_0^e	150.7 MPa
Internal length scale	l	1.5 µm

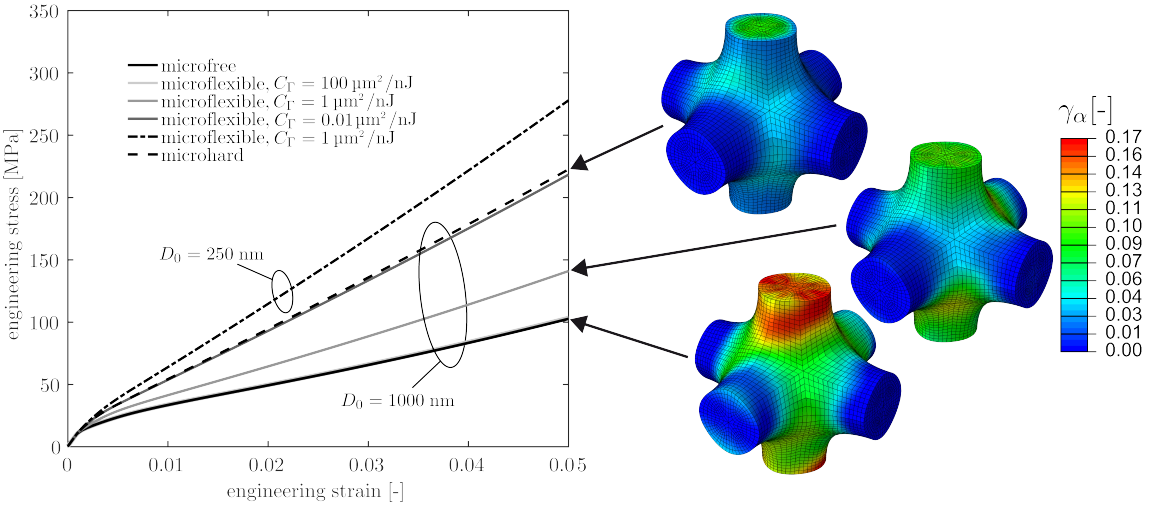

Figure 6.4: Stress-strain response for different surface conditions illustrating the impact of the flexibility boundary coefficient C_0 if $g^c \gg g_i^{eff}$. The contour plots indicate the associated impact on the accumulated plastic slip distribution for both idealized cases as well as for the case of non-idealized boundary conditions. As idealized boundary conditions do not account for the impact of surface effects in a sufficient manner, they underestimate (microhard) resp. overestimate (microfree) the accumulated plastic slip.
Reprinted from [112] with permission from Elsevier, Copyright 2017.

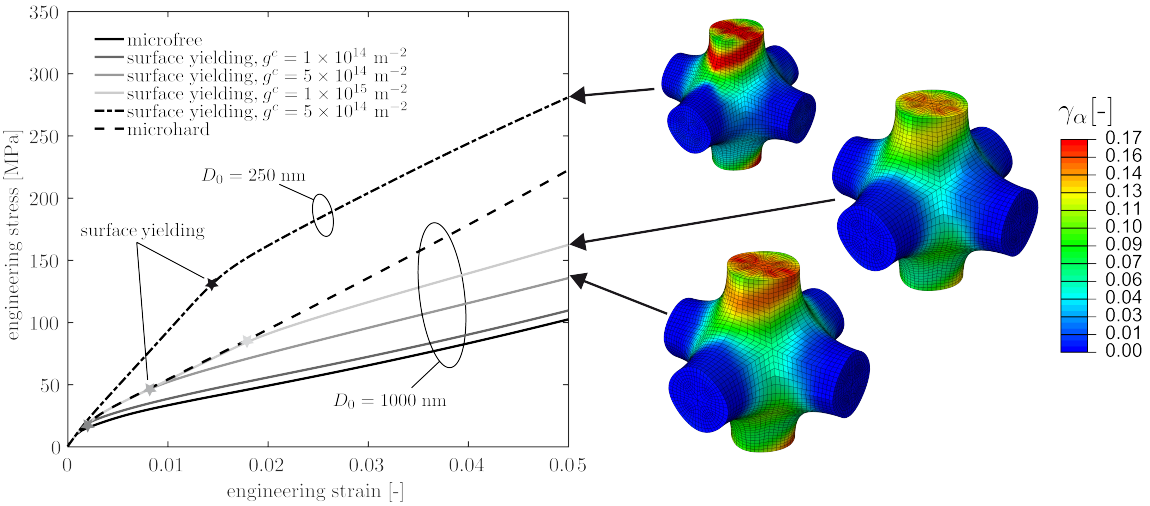

Figure 6.5: Impact of a critical dislocation density g^c if $C_0 = 0.01$ $\mu m^2/nJ$. The star icons indicate the initiation of surface yielding associated with stage II of the boundary conditions, i.e., if $g_i^{eff} > g^c$. Moreover, a clear size effect is predicted for both cases if reducing the characteristic ligament size from $D_0 = 1000$ nm to $D_0 = 250$ nm. One can further observe an increasing surface strength with reducing ligament diameter D_0. The contour plots illustrate the impact on the localized deformation in terms of plastic slip.
Reprinted from [112] with permission from Elsevier, Copyright 2017.

6.4 Conclusions

In extension to the microflexible boundary conditions of Ekh et al. [69] for inner grain boundaries, the advanced micro boundary conditions proposed in this contribution capture physically realistic behavior during plastic deformation compared to conventional boundary conditions. The proposed boundary conditions lead to non-zero boundary dissipation and allow to model a wide range of grain boundary behavior, including the effect of surface yielding and size dependent surface strengthening. Additional surface effects associated with the formation of surface layer, e.g., coating, passivation, oxidation, or damage, can be accounted for within the framework of gradient extended crystal plasticity. An appropriate integration procedure - without the use of additional surface elements - has been applied for a finite element implementation using linear brick elements. By means of a demonstrative problem, the impact of the non-idealized boundary conditions on the mechanical response of nanoporous Au has been illustrated. Furthermore, it has been shown that conventional microhard or microfree conditions are obtained in the limiting cases using the same numerical implementation. An application to polycrystals is straight-forward.

7 Incorporation of deformation twinning - modeling the competitive deformation behavior in crystals at small scales

The deformation behavior of hexagonal close packed materials involves dislocation slip as well as deformation twinning, including a competition between those two. This is due to the limited number of easy to activate slip modes. We present a model that captures dislocation slip, dislocation interaction, size-dependent hardening and deformation twinning. It also accounts for the sudden change of the crystal lattice orientation at the very final stage of the twinning shear process which allows to describe dislocation glide deformation within a twinned region. Along with this, the model further considers the change in the elastic properties associated with the new lattice orientation. Finite element results are presented for the specific example of magnesium and for different characteristic loading conditions in order to mimic local stress distributions as they occur in different regions within a single crystal or grain, e.g., close to a boundary and far off. In addition, the impact of twinning on the mechanical response of Mg single crystal during microcompression is investigated. We show that the suggested model is well capable of predicting the complex microstructural deformation behavior in Mg and compare our numerical results to experimental data.

The content of this chapter has been published in [E. Husser and S. Bargmann, *Modeling twinning-induced lattice reorientation and slip-in-twin deformation*, Journal of the Mechanics and Physics of Solids, 122, 315-339, 2019] and may include some modifications.

7.1 Introduction

Magnesium (Mg) has attracted considerable attention in the early past due to its enormous potential for weight reduction within a wide range of industrial applications. Thus, it is essential to understand its mechanical behavior in order to design products or parts which meet the engineering requirements. As the deformation behavior of such low-symmetric metals is rather complex, micromechanical testing and in-situ microstructural characterization of single crystalline samples of dimensions near the micron range have proven valuable to provide new insights into the local deformation mechanisms. In particular, microcompression testing of small-scale single crystals offers an excellent opportunity to explore the activation of individual deformation modes and their impact on the deformation behavior under comparatively simple loading conditions.

In hexagonal close packed (hcp) metals, the preferred deformation modes depend on the c/a ratio[1] of the crystal lattice, cf. Yoo [259]. In case of Mg, the major deformation modes at room temperature are $(0001)\langle 11\bar{2}0\rangle$ basal slip and $\{10\bar{1}2\}\langle 10\bar{1}1\rangle$ tensile twinning [51, 259]. Basal slip accommodates deformation in two independent directions with $\langle a\rangle$ Burgers vector. Other non-primary slip modes with $\langle a\rangle$ Burgers vector play in general a minor role at room temperature due to their high critical resolved shear stresses (CRSS) compared to the basal slip mode. This includes $\{10\bar{1}0\}\langle 11\bar{2}0\rangle$ prismatic and $\{10\bar{1}1\}\langle 11\bar{2}0\rangle$ first order pyramidal ($\pi 1$) slip. These deformation modes mainly become relevant at elevated temperatures where the critical resolved shear stress is considerably reduced, see, e.g., Miura et al. [178], Chapuis and Driver[46]. The same holds for $\{11\bar{2}2\}\langle 11\bar{2}3\rangle$ second order ($\pi 2$) pyramidal slip with $\langle a+c\rangle$ Burgers vector [46, 132]. Although $\pi 2$ slip accommodates deformation along the crystallographic c-axis, extensive investigations on $\pi 2$ slip have been reported so far mainly for loading-controlled experiments of single crystals where basal slip and twinning are suppressed, see, e.g., Husser et al. [111] and Bočan et al. [33]. For the above reasons, tensile twinning represents an essential mode of deformation in Mg as it significantly affects the ductility.

Tensile twins tend to appear more frequently and by a significantly higher volume fraction in contrast to compression and secondary twins. This is attributed to their low activation energy (Koike [138]) and, therefore, makes them easier to detect [136]. In polycrystals, twins predominately nucleate at grain boundaries. In the case of single crystals, twins nucleate at the surface (exterior) with high imposed stress concentration, e.g., at the contact zone between the indenter and crystal sample, cf. [158, 205, 261]. On the other hand, a nucleation inside the sample is also possible whenever a sufficient stress intensity site is available. For instance, twin nucleation at the particle/matrix interface in Mg single crystals reinforced with Y_2O_3 nanoparticle was observed by Mallmann et al. [166]. Moreover, twin nucleation may also be assisted by grain boundary defects such as lattice distortion and dislocation pile-ups, see [19, 252]. The activation of twinning strongly depends on the amount of prior slip (Barrett et al. [19]), suggesting that the process of twin nucleation in Mg requires dissociations of bulk dislocations. Once a stable twin nucleus is formed, the stress required for lateral twin propagation across the grain/crystal is typically smaller [51]. As a result, the twin propagates relatively fast until it is arrested by an obstacle such as a grain boundary, inclusion, another twin, etc. In contrast, subsequent twin growth in the transverse direction, i.e., twin thickening, generally requires an increasing resolved shear stress along the boundary between twinned and untwinned (parent) matrix of the crystal, cf. Kumar et al. [150]. For example, in the recent work by Liu et al. [158], a CRSS for twin growth has been identified as $\approx$ 30 MPa during

[1] The lattice constant a measures the interatomic distance in any closed-packed $\langle 11\bar{2}0\rangle$-direction while the lattice constant c measures the height of the hcp unit cell normal to the basal plane, i.e., in [0001]-direction.

compression of micron-sized Mg pillars.

Since twinning is a highly discrete process leading to a sharp change in the crystallographic lattice orientation, it is challenging to account for such events in a continuum-based crystal plasticity framework. So far, most attempts to incorporate deformation twinning are based on the idea of treating twin systems as additional so-called pseudo-slip systems as suggested by Van Houtte [249], see also Kalidindi [119]. However, that approach does not account for lattice reorientation and twin band evolution, both having a crucial impact on the mechanical response of hcp metals. Nevertheless, many subsequent crystal plasticity models have adopted that approach and extended the physical basis by characteristic features such as grain boundary accommodation effects [230], tension-compression asymmetry [85], detwinning mechanism [206], slip-twin/twin-twin interaction processes [45, 262], and micro-twin nucleation [47]. However, the majority of the computational studies focuses on polycrystalline microstructures of Mg and/or Mg alloys in which the local evolution of twins is accounted for in terms of a homogenized twin volume fraction. Consequently, the twin morphology and the actual growth behavior are not considered, i.e., neither twin band formation nor lattice reorientation or subsequent slip in twin processes are accounted for by these phenomenological approaches.

Our attention lies on the computational modeling of twin evolution at the microstructural level and the resulting impact on the stress-strain behavior during characteristic deformation stages such as twinning shear evolution, sudden lattice reorientation upon twinning process completion, and subsequent slip activity within the twinned crystal region. So far, only a few publications have addressed the morphological characteristics of individual twins within a continuum framework. Mirkhani and Joshi [177] incorporated twin boundary migration in a crystal plasticity model and studied the growth behavior of pre-existing twin layers in face-centered cubic (fcc) crystals. The migration process is driven by the activity of twin partial slip systems which are modeled via an additional visco-plastic slip law. In the study of Qiao et al. [207], twin propagation was accounted for in addition to twin growth. In fact the twin resistance was modeled in two steps as proposed by Wu et al. [256]. At a low twin volume fraction, stress softening (relaxation) is introduced causing the formation of a strongly localized twin band. After a critical fraction value is reached during subsequent deformation, softening turns into hardening and causes a thickening of the initially narrow twin lamella. Recently, Cheng and Ghosh [48] developed an image-based approach to model the explicit twin formation mechanisms in polycrystalline Mg. A micro-twin nucleation criterion (Cheng and Ghosh [47]) is applied in order to describe the dissociation of a non-planar $\langle a+c \rangle$ dislocation into a twin partial and a stair-rod dislocation. The subsequent process of twin propagation in twinning shear direction and growth in normal plane direction is steered by a corresponding critical stress requirement.

The current study focuses on the incorporation of deformation twinning into a gradient crystal plasticity framework at finite strains — a popular approach to also account for size-dependent hardening, see, e.g., [24, 93, 156, 238]. The twinning-induced reorientation of the crystal lattice is explicitly taken into account. By doing so, the model is able to describe dislocation glide deformation within a twinned region which has not been addressed in the literature so far. Moreover, the change in the elastic properties associated with a new lattice orientation is considered within the constitutive description of anisotropic hyperelasticity. The twinning process is viewed as a competitive deformation mechanism to dislocation slip and is assumed to dominate if deformation is insufficiently accommodated via slip modes. This is a natural outcome of the proposed slip-twin and twin-slip interaction relations defined within the corresponding flow rule which governs the evolution of plastic slip respectively twinning shear. Complex up-scaling of information at the length scale of individual dislocations is avoided by

this approach. The model parameters are identified on the basis of available experimental data for single crystalline Mg. The results demonstrate characteristic features of the model and indicate the inherent complexity of the material.

7.2 Theoretical framework

7.2.1 Kinematics

The classical multiplicative decomposition in Eq. (2.64) is modified in order to account for additional deformation resulting from the twinning process. For that reason, the plastic part $\boldsymbol{F}_{\mathrm{P}}$ is replaced by a more general quantity, the inelastic part $\boldsymbol{F}_{\mathrm{I}} = \boldsymbol{F}_{\mathrm{T}} \cdot \boldsymbol{F}_{\mathrm{P}}$, such that $\boldsymbol{F}_{\mathrm{T}}$ represents deformation associated with twinning and $\boldsymbol{F}_{\mathrm{P}}$ deformation due to dislocation glide. This leads to[2]

$$\boldsymbol{F} = \boldsymbol{F}_{\mathrm{E}} \cdot \boldsymbol{F}_{\mathrm{I}} = \boldsymbol{F}_{\mathrm{E}} \cdot \boldsymbol{F}_{\mathrm{T}} \cdot \boldsymbol{F}_{\mathrm{P}}. \tag{7.1}$$

The inelastic part $\boldsymbol{F}_{\mathrm{I}}$ describes crystallographic gliding of dislocations along active slip planes superimposed by twinning related deformation processes (twin dislocation glide and atomic shuffling) by which the reference configuration undergoes an isochoric deformation. Hence, deformation by twinning preserves the volume similar to deformation by dislocation glide, i.e., $J = \det(\boldsymbol{F}) = \det(\boldsymbol{F}_{\mathrm{E}})$ where $\det(\boldsymbol{F}_{\mathrm{I}}) = 1$. Similar to classical crystal plasticity, a stress free (or relaxed) intermediate configuration is formed due to the decomposition in Eq. (7.1). Subsequent stretch deformation and rotation of the inelastically deformed crystal lattice towards the current deformation is described by the elastic deformation gradient part $\boldsymbol{F}_{\mathrm{E}}$.

The spatial velocity gradient $\boldsymbol{l}$ is introduced by taking the material time derivative of the deformation gradient, i.e., $\dot{\boldsymbol{F}} = \boldsymbol{l} \cdot \boldsymbol{F}$. With the decomposition given by Eq. (7.1), the spatial velocity gradient

$$\boldsymbol{l} = \nabla_{\mathrm{c}}(\dot{\boldsymbol{x}}) = \frac{\partial \dot{\boldsymbol{x}}}{\partial \boldsymbol{x}} = \left[\dot{\boldsymbol{F}}_{\mathrm{E}} \cdot \boldsymbol{F}_{\mathrm{I}} + \boldsymbol{F}_{\mathrm{E}} \cdot \dot{\boldsymbol{F}}_{\mathrm{I}}\right] \cdot \boldsymbol{F}^{-1} = \boldsymbol{l}_{\mathrm{E}} + \boldsymbol{l}_{\mathrm{I}}, \tag{7.2}$$

is split additively into an elastic part $\boldsymbol{l}_{\mathrm{E}} = \dot{\boldsymbol{F}}_{\mathrm{E}} \cdot \boldsymbol{F}_{\mathrm{E}}^{-1}$ and an inelastic part $\boldsymbol{l}_{\mathrm{I}} = \boldsymbol{F}_{\mathrm{E}} \cdot \boldsymbol{L}_{\mathrm{I}} \cdot \boldsymbol{F}_{\mathrm{E}}^{-1}$. The latter represents the push-forward of the intermediate (or lattice) velocity gradient $\boldsymbol{L}_{\mathrm{I}} = \dot{\boldsymbol{F}}_{\mathrm{I}} \cdot \boldsymbol{F}_{\mathrm{I}}^{-1}$ which is the sum of both inelastic velocity gradient parts, i.e.,

$$\boldsymbol{L}_{\mathrm{I}} = \boldsymbol{L}_{\mathrm{T}} + \widetilde{\boldsymbol{L}}_{\mathrm{P}} = \dot{\boldsymbol{F}}_{\mathrm{T}} \cdot \boldsymbol{F}_{\mathrm{T}}^{-1} + \boldsymbol{F}_{\mathrm{T}} \cdot \dot{\boldsymbol{F}}_{\mathrm{P}} \cdot \boldsymbol{F}_{\mathrm{P}}^{-1} \cdot \boldsymbol{F}_{\mathrm{T}}^{-1}. \tag{7.3}$$

Recall the relations in Section 3.1.4, the crystallographic reorientation due to twinning results in two adjacent regions which are separated by a twin plane normal $\boldsymbol{n}_\eta$. The deformation gradient of the twinned lattice differs from the deformation gradient in the parent (untwinned) lattice (at least in the absence of slip deformation) by a superimposed simple shear deformation of the form (see Staroselsky and Anand [230])

$$\boldsymbol{F}_{\mathrm{T}} = \boldsymbol{I} + \eta_0 \boldsymbol{s}_\eta \otimes \boldsymbol{n}_\eta, \tag{7.4}$$

[2] A similar decomposition is used by Idesman et al. [115] in which the contribution by $\boldsymbol{F}_{\mathrm{T}}$ is associated with both, phase transformation and twinning. In contrast to Eq. (7.1), no meaningful distinction of configurations is possible as it would require an imaginary configuration which is stress relaxed and fully untwinned. Such an additional (stand-alone) intermediate configuration is not assignable due to the implicit reorientation effect of twinning-induced plasticity on the reference configuration, cf., e.g., Clayton [54].

where η_0 is the magnitude of twinning shear defined in Eq. (3.14). Due to the lattice reorientation, a distinction of lattice vectors is required, cf. Eq. (3.15). The corresponding transformation matrix describes a reflection in the twin plane.

In analogy to the homogenized twinning shear model proposed by Kalidindi [119], the inelastic velocity gradient tensor is here defined as

$$\boldsymbol{L}_{\mathrm{I}} = \dot{f}_\eta \eta_0 \left[\boldsymbol{s}_\eta \otimes \boldsymbol{n}_\eta\right] + \left[1 - F(f_\eta)\right] \sum_{\alpha}^{n_\alpha} \nu_\alpha \left[\boldsymbol{s}_\alpha \otimes \boldsymbol{n}_\alpha\right] + F(f_\eta) \sum_{\alpha}^{n_\alpha} \widetilde{\nu}_\alpha \left[\widetilde{\boldsymbol{s}}_\alpha \otimes \widetilde{\boldsymbol{n}}_\alpha\right], \tag{7.5}$$

where ν_α and $\widetilde{\nu}_\alpha$ denote n_α number of plastic slip rate variables associated with the parent and twin crystal lattice orientation respectively. $f_\eta \in [0,1]$ is the twin volume fraction restricted to one active twin system[3] and $F(f_\eta) \in \{0,1\}$ represents a step function which identifies the crystallographic lattice orientation as follows:

$$F(f_\eta) = \begin{cases} 0 & \text{if } f_\eta < 1 \text{ (parent lattice)}, \\ 1 & \text{if } f_\eta = 1 \text{ (twin lattice)}. \end{cases} \tag{7.6}$$

If $f_\eta = 0$ and $\dot{f}_\eta = 0$, it follows that $\boldsymbol{F}_{\mathrm{I}} = \boldsymbol{F}_{\mathrm{P}}$ and $\boldsymbol{F}_{\mathrm{T}} = \boldsymbol{I}$, such that $\widetilde{\boldsymbol{L}}_{\mathrm{P}}$ yields the standard definition of the plastic velocity gradient given by Eq. (2.86), i.e., conventional kinematics of crystal plasticity at finite strains associated with the parent orientation are recovered.

7.2.2 Modified evolution of dislocation densities

Both population of dislocation densities (SSDs and GNDs) are incorporated into the current framework of gradient crystal plasticity extended by deformation twinning. Assuming a linear superposition of dislocation densities (Ashby [9]), the definition of the total dislocation density reads

$$\rho_\alpha = \zeta_\alpha + g_{\mathrm{i}\alpha} = \zeta_\alpha + \sqrt{\left[g^{\mathrm{e}}_{\mathrm{i}\alpha}\right]^2 + \left[g^{\mathrm{s}}_{\mathrm{i}\alpha}\right]^2} \tag{7.7}$$

in which $g_{\mathrm{i}\alpha}$ is further split into edge and screw GND density components. In analogy to Eq. (3.62), the slip system-based GND densities are governed by the plastic slip rate gradient of the corresponding lattice configuration, i.e.,

$$\dot{g}^{\mathrm{e}}_{\mathrm{i}\alpha} = -\frac{1}{b_\alpha} \left[\nabla_{\mathrm{i}} \nu_\alpha \cdot \boldsymbol{s}_\alpha + \nabla_{\mathrm{i}} \tilde{\nu}_\alpha \cdot \tilde{\boldsymbol{s}}_\alpha\right] \tag{7.8}$$

and

$$\dot{g}^{\mathrm{s}}_{\mathrm{i}\alpha} = -\frac{1}{b_\alpha} \left[\nabla_{\mathrm{i}} \nu_\alpha \cdot \boldsymbol{t}_\alpha + \nabla_{\mathrm{i}} \tilde{\nu}_\alpha \cdot \tilde{\boldsymbol{t}}_\alpha\right], \tag{7.9}$$

respectively. Stored GND densities remain stored in the material after lattice reorientation as either the right or the left term in the brackets is active at a time (but never both) depending on the actual lattice configuration. At the same time, stored GNDs within the parent lattice increase the twin resistance during twin evolution. The initial conditions are defined as $g^{\mathrm{e}}_{\mathrm{i}\alpha}(t =$

[3] In the current framework, only a single twin system is assignable to a material point while there might in general be different twin variants of a particular twin mode activated throughout the considered domain. Henceforth, the active twin system is indicated by the index 'η' (no summation) without further specification of the actual variant.

$0) = g^{\mathrm{e}}_{\mathrm{i}\alpha 0}$ and $g^{\mathrm{s}}_{\mathrm{i}\alpha}(t = 0) = g^{\mathrm{s}}_{\mathrm{i}\alpha 0}$, with $g^{\mathrm{e}}_{\mathrm{i}\alpha 0}$ and $g^{\mathrm{s}}_{\mathrm{i}\alpha 0}$ being the initial GND densities in the system.

In extension to Eq. (3.46), the evolution of SSD densities ζ_α is described through accumulation and annihilation rates of dislocation densities as (see [5, 75, 77])

$$\dot{\zeta}_\alpha = \frac{1}{b_\alpha}\left[\frac{1}{L_\alpha} - 2y_{\mathrm{c}}\zeta_\alpha\right]\left[|\nu_\alpha| + |\tilde{\nu}_\alpha|\right]. \tag{7.10}$$

Here, y_{c} denotes the dislocation capture radius beneath which two dislocations of opposite sign annihilate each other. Furthermore,

$$L_\alpha = \frac{K}{\sqrt{\sum_\beta^{n_\alpha} k_{\alpha\beta}\rho_\beta}} \tag{7.11}$$

is the mean free path of moving dislocations. Here, K denotes a material constant and $k_{\alpha\beta}$ are the mutual immobilization coefficients. The initial SSD densities are denoted by $\zeta_\alpha(t = 0) = \zeta_{\alpha 0}$. Similar to the modified evolution equations for GND densities, the SSD densities are related to plastic slip rates of the corresponding lattice configuration. Also, stored SSD densities before twinning are assumed to remain stored after lattice reorientation. Hence, the SSD densities with respect to the parent lattice remain an obstacle-like barrier during subsequent dislocation slip in the twinned lattice.

7.2.3 Balance equations

In extension to the well-established gradient crystal plasticity theory, the internal power with respect to the intermediate configuration is expended by the right Cauchy-Green strain rate, two sets of plastic slip rates and their gradients, a set of twinning shear rates and their gradients:

$$\begin{aligned}\rho_{\mathrm{i}}\mathcal{P}^{\mathrm{int}} = &\int_{\mathcal{B}_{\mathrm{i}}} \boldsymbol{S}_{\mathrm{E}} : \dot{\boldsymbol{E}}_{\mathrm{E}}\mathrm{dV_i} + \sum_\alpha^{n_\alpha}\int_{\mathcal{B}_{\mathrm{i}}}\left[\pi_\eta\nu_\alpha + \boldsymbol{\xi}_\alpha\cdot\nabla_{\mathrm{i}}\nu_\alpha + \tilde{\pi}_\alpha\tilde{\nu}_\alpha + \tilde{\boldsymbol{\xi}}_\alpha\cdot\nabla_{\mathrm{i}}\tilde{\nu}_\alpha\right]\mathrm{dV_i}\\ &+ \sum_\eta^{n_\eta}\int_{\mathcal{B}_{\mathrm{i}}}\left[\pi_\eta\dot{f}_\eta\eta_0 + \boldsymbol{\xi}_\eta\cdot\nabla_{\mathrm{i}}\dot{f}_\eta\eta_0\right]\mathrm{dV_i}.\end{aligned} \tag{7.12}$$

Here, π_α and $\boldsymbol{\xi}_\alpha$ are the microforce and the microstress power-conjugate to the slip rate ν_α and the slip rate gradient $\nabla_{\mathrm{i}}\nu_\alpha$ respectively. Both pairs are here related to the initial crystal orientation (parent). Equivalently, ($\tilde{\pi}_\alpha$, $\tilde{\nu}_\alpha$) and ($\tilde{\boldsymbol{\xi}}_\alpha$, $\nabla_{\mathrm{i}}\tilde{\nu}_\alpha$) form power-conjugate pairs with respect to the reoriented crystal lattice (twin). In addition, we introduce an internal microforce π_η power-conjugate to the rate of twin volume fraction $\nu_\eta = \dot{f}_\eta\eta_0$ and a microstress $\boldsymbol{\xi}_\eta$ power-conjugate to the rate of twin volume fraction gradient $\nabla_{\mathrm{i}}\nu_\eta = \nabla_{\mathrm{i}}\dot{f}_\eta\eta_0$. Similar to the generalized framework developed in Gurtin [92], π_η is related to the change of atomic arrangements (shear and shuffling), here as a result of twinning-induced plasticity.

Neglecting macroscopic as well as microscopic body forces, the external power is expressed as

$$\rho_{\mathrm{i}}\mathcal{P}^{\mathrm{ext}} = \int_{\partial\mathcal{B}_{\mathrm{i}}}\left[\boldsymbol{T}_{\mathrm{i}}\cdot\boldsymbol{v} + \Xi_\alpha\nu_\alpha\mathrm{dA_i} + \tilde{\Xi}_\alpha\tilde{\nu}_\alpha\right]\mathrm{dA_i} + \sum_\eta^{n_\eta}\int_{\partial\mathcal{B}_{\mathrm{i}}}\Xi_\eta\dot{f}_\eta\eta_0\mathrm{dA_i}, \tag{7.13}$$

where $\boldsymbol{v} = \dot{\boldsymbol{u}}$ denotes the material time derivative of the displacement field, $\boldsymbol{T}_{\mathrm{i}}$ is the macro-

scopic surface traction and Ξ_α, $\tilde{\Xi}_\alpha$, and Ξ_η are microscopic surface tractions[4].

The principle of virtual power is used to derive macroscopic and microscopic balance relations. Therefore, internal and external power expressions are varied with respect to the following set of kinematic variables

$$\mathcal{V} = \{\boldsymbol{v}, \nu_\alpha, \nabla_{\mathrm{i}}\nu_\alpha, \tilde{\nu}_\alpha, \nabla_{\mathrm{i}}\tilde{\nu}_\alpha, \nu_\eta, \nabla_{\mathrm{i}}\nu_\eta\}. \tag{7.14}$$

Integration by parts and application of the divergence theorem yields the balance of virtual power

$$\begin{aligned}
0 = &\int_{\mathcal{B}_{\mathrm{i}}} \mathrm{Div}_{\mathrm{i}}(\boldsymbol{F}_{\mathrm{E}} \cdot \boldsymbol{S}_{\mathrm{E}}) \cdot \delta\boldsymbol{v} \mathrm{dV_i} + \int_{\partial\mathcal{B}_{\mathrm{i}}} [[\boldsymbol{F}_{\mathrm{E}} \cdot \boldsymbol{S}_{\mathrm{E}}] \cdot \boldsymbol{N}_{\mathrm{i}} - \boldsymbol{T}_{\mathrm{i}}] \, \delta\dot{\boldsymbol{u}} \mathrm{dA_i} \\
&+ \sum_\alpha^{n_\alpha} \int_{\mathcal{B}_{\mathrm{i}}} [\pi_\alpha - \tau_\alpha - \mathrm{Div}_{\mathrm{i}}(\boldsymbol{\xi}_\alpha)] \, \delta\nu_\alpha \mathrm{dV_i} + \sum_\alpha^{n_\alpha} \int_{\partial\mathcal{B}_{\mathrm{i}}} [\boldsymbol{\xi}_\alpha \cdot \boldsymbol{N}_{\mathrm{i}} - \Xi_\alpha] \, \delta\nu_\alpha \mathrm{dA_i} \\
&+ \sum_\alpha^{n_\alpha} \int_{\mathcal{B}_{\mathrm{i}}} \left[\tilde{\pi}_\alpha - \tilde{\tau}_\alpha - \mathrm{Div}_{\mathrm{i}}(\tilde{\boldsymbol{\xi}}_\alpha)\right] \delta\tilde{\nu}_\alpha \mathrm{dV_i} + \sum_\alpha^{n_\alpha} \int_{\partial\mathcal{B}_{\mathrm{i}}} \left[\tilde{\boldsymbol{\xi}}_\alpha \cdot \boldsymbol{N}_{\mathrm{i}} - \tilde{\Xi}_\alpha\right] \delta\tilde{\nu}_\alpha \mathrm{dA_i} \\
&+ \sum_\eta^{n_\eta} \int_{\mathcal{B}_{\mathrm{i}}} \left[\pi_\eta - \tau_\eta - \mathrm{Div}_{\mathrm{i}}(\boldsymbol{\xi}_\eta)\right] \delta\dot{f}_\eta \eta_0 \mathrm{dV_i} + \sum_\eta^{n_\eta} \int_{\partial\mathcal{B}_{\mathrm{i}}} \left[\boldsymbol{\xi}_\eta \cdot \boldsymbol{N}_{\mathrm{i}} - \Xi_\eta\right] \delta\dot{f}_\eta \eta_0 \mathrm{dA_i},
\end{aligned} \tag{7.15}$$

where the resolved shear stresses on corresponding slip and twin systems are determined in terms of the Mandel stress tensor $\boldsymbol{M}_{\mathrm{E}} = \boldsymbol{C}_{\mathrm{E}} \cdot \boldsymbol{S}_{\mathrm{E}}$, as

$$\tau_\alpha = \boldsymbol{M}_{\mathrm{E}} : [\boldsymbol{s}_\alpha \otimes \boldsymbol{n}_\alpha], \quad \widetilde{\tau}_\alpha = \boldsymbol{M}_{\mathrm{E}} : [\widetilde{\boldsymbol{s}}_\alpha \otimes \widetilde{\boldsymbol{n}}_\alpha], \quad \tau_\eta = \boldsymbol{M}_{\mathrm{E}} : [\boldsymbol{s}_\eta \otimes \boldsymbol{n}_\eta]. \tag{7.16}$$

τ_α and τ_η are resolved onto the parent crystal lattice while $\widetilde{\tau}_\alpha$ is associated with the crystal lattice of the active twin variant.

Following standard variational arguments eventually yields the local form of the balance of linear momentum along with the macroscopic traction condition, i.e., $\boldsymbol{0} = \mathrm{Div}_{\mathrm{i}}(\boldsymbol{F}_{\mathrm{E}} \cdot \boldsymbol{S}_{\mathrm{E}})$ in $\mathcal{B}_{\mathrm{i}}$ and $\boldsymbol{T}_{\mathrm{i}} = [\boldsymbol{F}_{\mathrm{E}} \cdot \boldsymbol{S}_{\mathrm{E}}] \cdot \boldsymbol{N}_{\mathrm{i}}$ on $\partial\mathcal{B}_{\mathrm{i}}$.

In addition, a set of microforce balances with associated microtraction conditions is obtained for different subregions of the considered domain:

$$\left.\begin{aligned} 0 &= \pi_\alpha - \tau_\alpha - \mathrm{Div}_{\mathrm{i}}(\boldsymbol{\xi}_\alpha) \\ 0 &= \pi_\eta - \tau_\eta - \mathrm{Div}_{\mathrm{i}}(\boldsymbol{\xi}_\eta) \end{aligned}\right\} \text{ in } \mathcal{B}_{\mathrm{i}}^{\mathrm{p}} \quad \text{with} \quad \left.\begin{aligned} \Xi_\alpha &= \boldsymbol{\xi}_\alpha \cdot \boldsymbol{N}_{\mathrm{i}} \\ \Xi_\eta &= \boldsymbol{\xi}_\eta \cdot \boldsymbol{N}_{\mathrm{i}} \end{aligned}\right\} \text{ on } \partial\mathcal{B}_{\mathrm{i}}^{\mathrm{p}}, \tag{7.17}$$

and

$$0 = \tilde{\pi}_\alpha - \tilde{\tau}_\alpha - \mathrm{Div}_{\mathrm{i}}(\tilde{\boldsymbol{\xi}}_\alpha) \text{ in } \mathcal{B}_{\mathrm{i}}^{\mathrm{tw}} \qquad \text{with} \quad \tilde{\Xi}_\alpha = \tilde{\boldsymbol{\xi}}_\alpha \cdot \boldsymbol{N}_{\mathrm{i}} \qquad \text{on } \partial\mathcal{B}_{\mathrm{i}}^{\mathrm{tw}}. \tag{7.18}$$

Obviously, the considered subregion determines the relevant microforce balance. Hence, the considered domain $\mathcal{B}_{\mathrm{i}} = \mathcal{B}_{\mathrm{i}}^{\mathrm{p}} \cup \mathcal{B}_{\mathrm{i}}^{\mathrm{tw}}$ may be composed of a subregion associated with the initial (parent) lattice configuration $\mathcal{B}_{\mathrm{i}}^{\mathrm{p}}$ and a subregion associated with the reoriented (twin) lattice configuration $\mathcal{B}_{\mathrm{i}}^{\mathrm{tw}}$. An analogous decomposition holds for the boundary, i.e., $\partial\mathcal{B}_{\mathrm{i}} = \partial\mathcal{B}_{\mathrm{i}}^{\mathrm{p}} \cup \partial\mathcal{B}_{\mathrm{i}}^{\mathrm{tw}}$.

[4] The summation terms in Eq. (7.12) and Eq. (7.13) associated with η do not violate the assumption made above because there might be n_η number of twin variants of a particular twin mode in the considered domain in general.

7.2.4 Dissipation inequality

The Helmholtz free energy per unit intermediate volume is assumed to take the following form

$$\psi_\mathrm{i} = \psi_\mathrm{i}(\boldsymbol{C}_\mathrm{E}, \boldsymbol{A}_\mathrm{i}, f_\eta, \nabla_\mathrm{i} f_\eta, \{g^\mathrm{e}_{\mathrm{i}\alpha}\}, \{g^\mathrm{s}_{\mathrm{i}\alpha}\}), \tag{7.19}$$

where $\boldsymbol{A}_\mathrm{i}$ characterizes a preferred or characteristic crystallographic direction (axis of transverse isotropy) in hcp crystals. With this functional relation and with the internal stress power given in Eq. (7.12), the dissipation inequality for the case of isothermal and quasi-static conditions may be written as

$$\begin{aligned}
0 \geq & \int_{\mathcal{B}_\mathrm{i}} \left[\boldsymbol{S}_\mathrm{E} - \frac{\partial \psi}{\partial \boldsymbol{C}_\mathrm{E}} : \frac{\partial \boldsymbol{C}_\mathrm{E}}{\partial \boldsymbol{E}_\mathrm{E}} \right] : \dot{\boldsymbol{E}}_\mathrm{E} \mathrm{dV_i} \\
& + \sum_\alpha^{n_\alpha} \int_{\mathcal{B}_\mathrm{i}} \pi_\alpha \nu_\alpha \mathrm{dV_i} + \sum_\alpha^{n_\alpha} \int_{\mathcal{B}_\mathrm{i}} \left[\boldsymbol{\xi}_\alpha - \left[\frac{\partial \psi_\mathrm{i}}{\partial g^\mathrm{e}_{\mathrm{i}\alpha}} \frac{\partial g^\mathrm{e}_{\mathrm{i}\alpha}}{\partial \nabla_\mathrm{i} \nu_\alpha} + \frac{\partial \psi_\mathrm{i}}{\partial g^\mathrm{s}_{\mathrm{i}\alpha}} \frac{\partial g^\mathrm{s}_{\mathrm{i}\alpha}}{\partial \nabla_\mathrm{i} \nu_\alpha} \right] \right] \cdot \nabla_\mathrm{i} \nu_\alpha \mathrm{dV_i} \\
& + \sum_\alpha^{n_\alpha} \int_{\mathcal{B}_\mathrm{i}} \tilde{\pi}_\alpha \tilde{\nu}_\alpha \mathrm{dV_i} + \sum_\alpha^{n_\alpha} \int_{\mathcal{B}_\mathrm{i}} \left[\tilde{\boldsymbol{\xi}}_\alpha - \left[\frac{\partial \psi_\mathrm{i}}{\partial g^\mathrm{e}_{\mathrm{i}\alpha}} \frac{\partial g^\mathrm{e}_{\mathrm{i}\alpha}}{\partial \nabla_\mathrm{i} \tilde{\nu}_\alpha} + \frac{\partial \psi_\mathrm{i}}{\partial g^\mathrm{s}_{\mathrm{i}\alpha}} \frac{\partial g^\mathrm{s}_{\mathrm{i}\alpha}}{\partial \nabla_\mathrm{i} \tilde{\nu}_\alpha} \right] \right] \cdot \nabla_\mathrm{i} \tilde{\nu}_\alpha \mathrm{dV_i} \\
& + \sum_\eta^{n_\eta} \int_{\mathcal{B}_\mathrm{i}} \left[\pi_\eta - \frac{\partial \psi_\mathrm{i}}{\partial f_\eta} \right] \dot{f}_\eta \eta_0 \mathrm{dV_i} + \sum_\eta^{n_\eta} \int_{\mathcal{B}_\mathrm{i}} \left[\boldsymbol{\xi}_\eta - \frac{\partial \psi_\mathrm{i}}{\partial \nabla_\mathrm{i} f_\eta} \right] \cdot \nabla_\mathrm{i} \dot{f}_\eta \mathrm{dV_i}.
\end{aligned} \tag{7.20}$$

In view of modeling twinning, a reasonable classification of dissipative and energetic contributions within the inequality given in Eq. (7.20) is required. Because detwinning[5] ($\dot{f}_\eta < 0$) is not considered at this stage, it appears reasonable to consider the coupled process of atomic shear and shuffling as a pure dissipative and therefore non-reversible process. Hence, π_η is treated as pure dissipative. On the other hand, the condition defining the presence of a twin boundary appears only temporary. For that reason, $\boldsymbol{\xi}_\eta$ is taken as a pure energetic quantity.

Although the internal microforces π_α and $\tilde{\pi}_\alpha$ may involve an energetic portion as discussed in [93], the resulting effect accounting for the reversible motion of characteristic defects upon load removal and therefore for the temporal change in the defect energy is usually neglected in crystal plasticity theories. Accordingly, both microforces are taken as pure dissipative in nature. Regarding the microstress vectors $\boldsymbol{\xi}_\alpha$ and $\tilde{\boldsymbol{\xi}}_\alpha$, an additive decomposition into energetic and dissipative contributions was proposed, e.g., by Gurtin and Anand [97]. The results of Bargmann et al. [15] suggest that the impact of a dissipative microstress contribution is more relevant after sufficient load reversal. Since no cyclic loading is studied in this work, both microstress vectors are taken as energetic quantities.

With the above assumptions, one can determine the following constitutive relations, namely

$$\left.\begin{aligned}
\boldsymbol{\xi}_\eta &= \frac{\partial \psi_\mathrm{i}}{\partial \nabla_\mathrm{i} f_\eta} \\
\boldsymbol{\xi}_\alpha &= -\frac{1}{b_\alpha} \left[\frac{\partial \psi_\mathrm{i}}{\partial g^\mathrm{e}_{\mathrm{i}\alpha}} \boldsymbol{s}_\alpha + \frac{\partial \psi_\mathrm{i}}{\partial g^\mathrm{s}_{\mathrm{i}\alpha}} \boldsymbol{t}_\alpha \right]
\end{aligned}\right\} \text{ in } \mathcal{B}^\mathrm{p}_\mathrm{i}, \tag{7.21}$$

and

$$\tilde{\boldsymbol{\xi}}_\alpha = -\frac{1}{b_\alpha} \left[\frac{\partial \psi_\mathrm{i}}{\partial g^\mathrm{e}_{\mathrm{i}\alpha}} \tilde{\boldsymbol{s}}_\alpha + \frac{\partial \psi_\mathrm{i}}{\partial g^\mathrm{s}_{\mathrm{i}\alpha}} \tilde{\boldsymbol{t}}_\alpha \right] \text{ in } \mathcal{B}^\mathrm{tw}_\mathrm{i}. \tag{7.22}$$

[5] Detwinning describes the removal of twins upon load removal/reversal. Experimental evidence for detwinning is for instance given by Oliver et al. [192].

For the sake of clarity, the second Piola-Kirchhoff stress tensor satisfies $\boldsymbol{S}_{\mathrm{E}} = 2\partial\psi/\partial\boldsymbol{C}_{\mathrm{E}}$ in $\mathcal{B}_{\mathrm{i}}$ and $\partial\boldsymbol{C}_{\mathrm{E}}/\partial\boldsymbol{E}_{\mathrm{E}} : \dot{\boldsymbol{E}}_{\mathrm{E}} = 2\dot{\boldsymbol{E}}_{\mathrm{E}}$. The reduced dissipation inequality then becomes

$$\sum_{\alpha}^{n_\alpha} \int_{\mathcal{B}_{\mathrm{i}}} \left[\pi_\alpha \nu_\alpha + \tilde{\pi}_\alpha \tilde{\nu}_\alpha\right] \mathrm{dV_i} + \sum_{\eta}^{n_\eta} \int_{\mathcal{B}_{\mathrm{i}}} \pi_\eta \dot{f}_\eta \eta_0 \mathrm{dV_i} \geq 0. \tag{7.23}$$

7.3 Constitutive Modeling

The free energy density is split into

$$\begin{aligned}\psi_{\mathrm{i}}(\boldsymbol{C}_{\mathrm{E}}, \boldsymbol{A}_{\mathrm{i}}, f_\eta, \nabla_{\mathrm{i}} f_\eta, \{g^{\mathrm{e}}_{\mathrm{i}\alpha}\}, \{g^{\mathrm{s}}_{\mathrm{i}\alpha}\}) =& \hat{\psi}^{\mathrm{el}}_{\mathrm{i}}(\boldsymbol{C}_{\mathrm{E}}, \boldsymbol{A}_{\mathrm{i}}, f_\eta) + \psi^{\mathrm{tb}}_{\mathrm{i}}(\nabla_{\mathrm{i}} f_\eta) \\ &+ \psi^{\mathrm{g}}_{\mathrm{i}}(\{g^{\mathrm{e}}_{\mathrm{i}\alpha}\}, \{g^{\mathrm{s}}_{\mathrm{i}\alpha}\}),\end{aligned} \tag{7.24}$$

i.e., an elastic $\hat{\psi}^{\mathrm{el}}_{\mathrm{i}}$ contribution, a contribution related to the appearance of a twin boundary $\psi^{\mathrm{tb}}_{\mathrm{i}}$, and a defect energy contribution $\psi^{\mathrm{g}}_{\mathrm{i}}$. Furthermore, due to twinning-induced lattice reorientation, the elastic free energy is assumed to experience a similar change during lattice change as the inelastic velocity gradient, cf. Eq. (7.5),

$$\hat{\psi}^{\mathrm{el}}_{\mathrm{i}} = \left[1 - F(f_\eta)\right] \psi^{\mathrm{el}}_{\mathrm{i}}(\boldsymbol{C}_{\mathrm{E}}, \boldsymbol{A}_{\mathrm{i}}) + F(f_\eta) \tilde{\psi}^{\mathrm{el}}_{\mathrm{i}}(\boldsymbol{C}_{\mathrm{E}}, \widetilde{\boldsymbol{A}}_{\mathrm{i}}). \tag{7.25}$$

$\boldsymbol{A}_{\mathrm{i}}$ transforms analogously to normal vectors, i.e., $\widetilde{\boldsymbol{A}}_{\mathrm{i}} = \boldsymbol{A}_{\mathrm{i}} \cdot \boldsymbol{Q}^{\mathrm{T}}_\eta$, cf. Eq. (3.15). $\psi^{\mathrm{el}}_{\mathrm{i}}$ and $\tilde{\psi}^{\mathrm{el}}_{\mathrm{i}}$ have the same structure but make use of a different characteristic lattice direction. For the sake of brevity, attention is restricted to $\psi^{\mathrm{el}}_{\mathrm{i}}$ in the following.

7.3.1 Elastic energy $\psi^{\mathrm{el}}_{\mathrm{i}}$

The directional dependence of elastic properties is described in terms of transverse isotropy, cf. Section 3.2.2. In summary, the elastic free energy reads

$$\begin{aligned}\psi^{\mathrm{el}}_{\mathrm{i}}(\boldsymbol{C}_{\mathrm{E}}) = & \frac{1}{2}\mu^{\perp} \left[I_1 - 3 - 2\ln(J_{\mathrm{E}})\right] + \frac{1}{2}\lambda^{\perp} \ln(J_{\mathrm{E}})^2 \\ &+ \alpha \left[I_4 - 1\right] \ln(J_{\mathrm{E}}) + 2\beta \left[I_5 - 2I_4 + 1\right] + \frac{1}{2}\delta \left[I_4 - 1\right]^2.\end{aligned} \tag{7.26}$$

The relation between elastic constants and elastic model parameters is described in Eq. (3.42). From this, the second Piola-Kirchhoff yields

$$\begin{aligned}\boldsymbol{S}_{\mathrm{E}} = & \mu^{\perp} \left[\boldsymbol{I} - \boldsymbol{C}^{-1}_{\mathrm{E}}\right] + \lambda^{\perp} \ln(J_{\mathrm{E}}) \boldsymbol{C}^{-1}_{\mathrm{E}} \\ &+ \alpha \left[2\ln(J_{\mathrm{E}}) \boldsymbol{A}_{\mathrm{i}} \otimes \boldsymbol{A}_{\mathrm{i}} + \left[I_4 - 1\right] \boldsymbol{C}^{-1}_{\mathrm{E}}\right] \\ &+ 4\beta \left[\boldsymbol{A}_{\mathrm{i}} \otimes \boldsymbol{C}_{\mathrm{E}} \cdot \boldsymbol{A}_{\mathrm{i}} + \boldsymbol{C}_{\mathrm{E}} \cdot \boldsymbol{A}_{\mathrm{i}} \otimes \boldsymbol{A}_{\mathrm{i}} - 2\boldsymbol{A}_{\mathrm{i}} \otimes \boldsymbol{A}_{\mathrm{i}}\right] \\ &+ 2\delta \left[I_4 - 1\right] \boldsymbol{A}_{\mathrm{i}} \otimes \boldsymbol{A}_{\mathrm{i}}.\end{aligned} \tag{7.27}$$

The direction of $\widetilde{\boldsymbol{A}}_{\mathrm{i}}$ is directly known from the reoriented lattice vector $\widetilde{\boldsymbol{n}}_{\mathrm{basal}}$. Consequently, no additional rotation operations are required compared to the classical approach in which coordinate transformation is applied to the forth order elastic tensor, cf. [119]. Alternative approaches to consider non-linear elastic anisotropy include the usage of third-order elastic constants [53] and the identification of elastic modulus tensor parameters for a specific polyconvex strain energy density [45, 218].

7.3.2 Defect energy $\psi_{\mathrm{i}}^{\mathrm{g}}$

The defect energy considers coupling between GND densities and is given in the form

$$\psi_{\mathrm{i}}^{\mathrm{g}} = \frac{1}{2}\sum_{\alpha,\beta} l_\alpha l_\beta b_\alpha b_\beta \left[H^{\mathrm{e}}_{\alpha\beta} g^{\mathrm{e}}_{\mathrm{i}\alpha} g^{\mathrm{e}}_{\mathrm{i}\beta} + H^{\mathrm{s}}_{\alpha\beta} g^{\mathrm{s}}_{\mathrm{i}\alpha} g^{\mathrm{s}}_{\mathrm{i}\beta}\right], \tag{7.28}$$

see also, e.g., [24]. The coupling between GND densities is taken into account via edge and screw energetic hardening coefficients, $H^{\mathrm{e}}_{\alpha\beta} = q^{\xi}_{\alpha\beta} H^{\mathrm{e}}_0$ resp. $H^{\mathrm{s}}_{\alpha\beta} = q^{\xi}_{\alpha\beta} H^{\mathrm{s}}_0$. Taking

$$H^{\mathrm{e}}_0 = \frac{\mu^{\perp}}{8\left[1-\nu^{\perp}\right]} \quad \text{and} \quad H^{\mathrm{s}}_0 = 2H^{\mathrm{e}}_0\left[1-\nu^{\perp}\right] \tag{7.29}$$

in accordance with the stress prefactors[6] derived in Bayley [24], the energetic micro-stress vector yields

$$\boldsymbol{\xi}_\alpha = \sum_\beta l_\alpha l_\beta b_\alpha b_\beta q^{\xi}_{\alpha\beta}\left[H^{\mathrm{e}}_0 \frac{\partial g^{\mathrm{e}}_{\mathrm{i}\alpha}}{\partial \nabla_{\mathrm{i}}\gamma_\alpha} g^{\mathrm{e}}_{\mathrm{i}\beta} + H^{\mathrm{s}}_0 \frac{\partial g^{\mathrm{s}}_{\mathrm{i}\alpha}}{\partial \nabla_{\mathrm{i}}\gamma_\alpha} g^{\mathrm{s}}_{\mathrm{i}\beta}\right]. \tag{7.30}$$

Analogically, the micro-stress vector with respect to the twinned lattice orientation reads

$$\tilde{\boldsymbol{\xi}}_\alpha = \sum_\beta l_\alpha l_\beta b_\alpha b_\beta q^{\xi}_{\alpha\beta}\left[H^{\mathrm{e}}_0 \frac{\partial g^{\mathrm{e}}_{\mathrm{i}\alpha}}{\partial \nabla_{\mathrm{i}}\tilde{\gamma}_\alpha} g^{\mathrm{e}}_{\mathrm{i}\beta} + H^{\mathrm{s}}_0 \frac{\partial g^{\mathrm{s}}_{\mathrm{i}\alpha}}{\partial \nabla_{\mathrm{i}}\tilde{\gamma}_\alpha} g^{\mathrm{s}}_{\mathrm{i}\beta}\right]. \tag{7.31}$$

7.3.3 Twin boundary energy $\psi_{\mathrm{i}}^{\mathrm{tb}}$

In line with the definition of the defect energy, the twin boundary energy is defined as

$$\psi_{\mathrm{i}}^{\mathrm{tb}} = \frac{b_\eta^2}{2} \nabla_{\mathrm{i}} f_\eta \cdot \boldsymbol{H}^{\mathrm{tb}} \cdot \nabla_{\mathrm{i}} f_\eta, \tag{7.32}$$

where $\boldsymbol{H}^{\mathrm{tb}}$ represents the interfacial hardening matrix, here defined in an anisotropic fashion to promote propagation in longitudinal twinning direction as observed in experiments (e.g. [158, 166]), i.e.,

$$\boldsymbol{H}^{\mathrm{tb}} = \frac{\Gamma}{l_\eta} \boldsymbol{s}_\eta \otimes \boldsymbol{s}_\eta. \tag{7.33}$$

Here, Γ denotes the twin boundary energy parameter and l_η the twin boundary thickness. With this, the microstress relation in Eq. $(7.21)_1$ yields

$$\boldsymbol{\xi}_\eta = \frac{\Gamma b_\eta^2}{l_\eta}\left[\nabla_{\mathrm{i}} f_\eta \cdot \boldsymbol{s}_\eta\right] \boldsymbol{s}_\eta. \tag{7.34}$$

A similar energy format is also used in recent phase field models of deformation twinning, e.g., [56] and [103].

[6] Here defined in terms of in-plane elastic parameters with the in-plane Poisson's ratio $\nu^{\perp} = \lambda^{\perp}/2\left[\lambda^{\perp}+\mu^{\perp}\right]$.

7.3.4 Plastic flow rule

The dissipative microforce $\pi_{\mathrm{i}\alpha}$ is assumed to follow a visco-plastic power-law of the form

$$\pi_\alpha = r_\alpha \left[\frac{\nu_\alpha}{\nu_0}\right]^{\frac{1}{m}} \mathrm{sgn}(\nu_\alpha), \tag{7.35}$$

where m is the rate sensitivity exponent, ν_0 is the reference slip rate, and r_α denotes the slip system resistance. With $\pi_\alpha = \tau_\alpha + \mathrm{Div}_{\mathrm{i}}(\boldsymbol{\xi}_\alpha)$ (cf. Eq. $(7.17)_1$), the above power-law relation serves as the evolution equation for the plastic slip rate:

$$\nu_\alpha = \nu_0 \left[\frac{|\tau_\alpha + \mathrm{Div}_{\mathrm{i}}(\boldsymbol{\xi}_\alpha)|}{r_\alpha}\right]^m \mathrm{sgn}(\tau_\alpha + \mathrm{Div}_{\mathrm{i}}(\boldsymbol{\xi}_\alpha)). \tag{7.36}$$

With respect to the parent lattice orientation, the total slip system resistance r_α is assumed to be decomposed in the following way

$$r_\alpha = \tau_\alpha^{\mathrm{y}} + \tau_\alpha^{\mathrm{h}} + \tau_\alpha^{\mathrm{tw}\to\mathrm{sl}}. \tag{7.37}$$

τ_α^{y} represents the size-dependent initial yield strength. In the context of dislocation-mediated plasticity, τ_α^{y} describes effectively the strength of the weakest dislocation source in a confined crystal volume as is described in more detail below, see also [71]. Furthermore, $\tau_\alpha^{\mathrm{h}} = \hat{\tau}_\alpha^{\mathrm{h}}(\nu_\alpha)$ denotes the evolving slip system hardening governed by random trapping of dislocations in the crystal. As is illustrated in a subsequent section, the relations for τ_α^{h} may differ for different slip modes in hcp crystals due to their characteristic behaviors. Finally, the last term in Eq. (7.37) accounts for the additional resistance to slip resulting from the interaction of dislocations with an evolving energetic barrier associated with the twinning process.

The evolution of the slip rate with respect to the twin lattice orientation $\tilde{\nu}_\alpha$ follows a relation equivalent to Eq. (7.36). In this case, the microforce is replaced by $\tilde{\pi}_\alpha = \tilde{\tau}_\alpha + \mathrm{Div}_{\mathrm{i}}(\tilde{\boldsymbol{\xi}}_\alpha)$, cf. Eq. (7.18), and the total slip system resistance becomes

$$\tilde{r}_\alpha = \tau_\alpha^{\mathrm{y}} + \tilde{\tau}_\alpha^{\mathrm{h}}. \tag{7.38}$$

While τ_α^{y} is unaltered, the hardening contribution coming from random trapping of dislocations takes the evolution of slip in both lattice configurations into account, i.e., $\tilde{\tau}_\alpha^{\mathrm{h}} = \hat{\tilde{\tau}}_\alpha^{\mathrm{h}}(\nu_\alpha, \tilde{\nu}_\alpha)$. The interaction term does not apply for the reoriented/twinned lattice.

7.3.5 Size-dependent yield strength

The yield strength of confined crystals or grains is known to increase with decreasing characteristic crystal size or volume (e.g. [157] in the context of Mg) and strongly depends on the initially available dislocation density[7]. In this study, we capture the size-dependent initial yield strength by the generalized Taylor-strengthening law established in [71]

$$\tau_\alpha^{\mathrm{y}} = \mu^\perp \left[k_1 \frac{\rho_{\alpha 0}^{-0.5}}{D_0} + k_2 \frac{b_\alpha}{\rho_{\alpha 0}^{-0.5}}\right], \tag{7.39}$$

[7] The initial dislocation density affects the strength of micron-sized crystals. Experiments indicate that the strengthening effect can be compensated - at least to some extent - if the initial dislocation density is increased, cf. [71].

with k_1 and k_2 being dimensionless constants to be determined for the particular material under consideration. The first term relates the intrinsic (or microstructural) length scale $\rho_{\alpha 0}^{-0.5}$ associated with the initial dislocation substructure to the extrinsic length scale of the sample (or grain) D_0 which imposes a confinement on the plastic process zone. This ratio is expected to be directly proportional to the yield strength as was previously discussed, e.g., in [111]. Therefore, this term mimics effectively the strength of the weakest dislocation source [71] which scales inversely with D_0[8].

The second term in Eq. (7.39) accounts for forest strengthening based on the magnitude of the slip system Burgers vector, normalized by the intrinsic length scale. Hence, if $D_0 \gg \rho_{\alpha}^{-0.5}$, Eq. (7.39) reduces to

$$\tau_{\alpha}^{\mathrm{y}} \approx \mu^{\perp} k_2 \frac{b_{\alpha}}{\rho_{\alpha 0}^{-0.5}} = Y_{\alpha 0}, \tag{7.40}$$

i.e., the yield strength of bulk single crystal denoted by $Y_{\alpha 0}$ is recovered if the considered crystal size (or volume) is sufficiently large compared to the intrinsic length scale.

7.3.6 Slip resistance and twin-slip interaction

In practice, basal and non-basal hardening are known to behave quite differently [85]. While basal slip is a very soft slip mode, prismatic and in particular pyramidal slip show much higher slip resistance. Following Graff et al. [85], linear hardening for basal slip and Voce-like hardening for non-basal slip is assumed. With respect to the parent lattice orientation, the hardening relation for all systems $\alpha \in \{\text{basal}\}$ reads

$$\tau_{\alpha,\mathrm{basal}}^{\mathrm{h}} = H_{\alpha 0}^{\mathrm{l}} \sum_{\beta} q_{\alpha\beta} \int \nu_{\beta} \mathrm{d}t, \tag{7.41}$$

with $H_{\alpha 0}^{\mathrm{l}}$ being the local hardening modulus and $q_{\alpha\beta}$ are the associated latent hardening coefficients[9]. For all systems $\alpha \in \{\text{prismatic, pyramidal}\}$, $\tau_{\alpha}^{\mathrm{h}}$ is defined as

$$\tau_{\alpha,\mathrm{pris}/\pi 2}^{\mathrm{h}} = [h_{\alpha}^{\infty} - \tau_{\alpha}^{\mathrm{y}}] \left[1 - \exp\left(-c_{\alpha,\mathrm{sat}} \int \nu_{\alpha} \mathrm{d}t\right)\right] + H_{\alpha 0}^{\mathrm{l}} \sum_{\beta \neq \alpha} q_{\alpha\beta} \int \nu_{\beta} \mathrm{d}t, \tag{7.42}$$

where h_{α}^{∞} denotes the ultimate stress of each slip system, $c_{\alpha,\mathrm{sat}}$ defines the corresponding hardening rate. Moreover, self-hardening for non-basal slip is governed by a Voce-like relation while a linear relation is assumed for the latent hardening contribution.

In consistency with the kinematics of dislocation densities, the total accumulated slip $\int \nu_{\alpha} \mathrm{d}t + \int \tilde{\nu}_{\alpha} \mathrm{d}t$ is considered for the hardening relations for $\tilde{\tau}_{\alpha,\mathrm{basal}}^{\mathrm{h}}$ and $\tilde{\tau}_{\alpha,\mathrm{pris}/\pi 2}^{\mathrm{h}}$, i.e., within the twinned crystal lattice.

An additional contribution to the slip resistance arises from twin-slip interaction processes and is denoted as $\tau_{\alpha}^{\mathrm{tw}\to\mathrm{sl}}$ in Eq. (7.37). This contribution to the slip resistance is assumed to increase with increasing twin volume fraction f_{η}. Furthermore, the arising barrier is measured

[8] If the sample size reduces to the sub-micron range, double-pinned dislocation sources become single-ended sources due to interaction with the free surface, cf. [197]. Such truncated single arms are harder to operate resulting in an increasing CRSS.

[9] Other recent contributions that deal with self- and latent hardening include the works [13, 17, 59, 77, 156].

in terms of the material-specific twin boundary energy Γ yielding

$$\tau_{\alpha}^{\mathrm{tw}\to\mathrm{sl}} = f_{\eta}\eta_0 b_{\alpha}^{-1}\Gamma. \tag{7.43}$$

By this relation, $\tau_{\mathrm{tw}\to\mathrm{sl}}$ vanishes if $f_{\eta} = 0$, i.e. twinning is not active or fully suppressed due to extensive slip activation. In contrast, $\tau_{\mathrm{tw}\to\mathrm{sl}} = \eta_0 b_{\alpha}^{-1}\Gamma$ if $f_{\eta} = 1$, i.e. the barrier reaches its maximum if the twinning shear reaches the threshold magnitude η_0 of the corresponding twinning mode. In turn, the contribution of $\tau_{\mathrm{tw}\to\mathrm{sl}}$ to the slip system resistance affects the evolution of SSD densities as a result of an aggravated slip system activity.

7.3.7 Twinning flow rule

The evolution of twinning shear is assumed to follow a power-law relation similar to the plastic flow rule. Such an approach is commonly used for continuum-based models in order to describe the shear associated with the motion of twin partials [48, 177, 207]. In this respect, the microforce π_{η} is defined as

$$\pi_{\eta} = r_{\eta}\left[\frac{\langle \dot{f}_{\eta}\eta_0\rangle}{\nu_0}\right]^{\frac{1}{m}}, \tag{7.44}$$

where the unidirectional nature of twinning is considered via $\langle\bullet\rangle = \max(0,\bullet)$ and r_{η} defines the resistance against twinning shear. The visco-plastic parameters are taken to be the same as for the plastic slip relations. With $\pi_{\eta} = \tau_{\eta} + \mathrm{Div}_{\mathrm{i}}(\boldsymbol{\xi}_{\eta})$ from Eq. $(7.17)_2$, the evolution of twinning shear rate (here in terms of the twin volume fraction) becomes

$$\dot{f}_{\eta} = \frac{\nu_0}{\eta_0}\left[\frac{\langle \tau_{\eta} + \mathrm{Div}_{\mathrm{i}}(\boldsymbol{\xi}_{\eta})\rangle}{r_{\eta}}\right]^{m}. \tag{7.45}$$

The twinning shear resistance is decomposed into three contributions:

$$r_{\eta} = \tau_{\eta}^{\mathrm{y}} + \tau_{\eta}^{\mathrm{int}} + \tau_{\eta}^{\mathrm{sl}\to\mathrm{tw}}. \tag{7.46}$$

In this relation, τ_{η}^{y} describes the friction stress for twinning which can be size-dependent. However, in view of single crystals, τ_{η}^{y} is assumed to be size-independent[10]. $\tau_{\eta}^{\mathrm{int}}$ denotes the friction stress required to overcome the energetic barrier during the twin nucleation process. Finally, $\tau_{\eta}^{\mathrm{sl}\to\mathrm{tw}}$ denotes the stress associated with interaction processes with obstacles such as stored dislocations.

7.3.8 Twinning resistance and slip-twin interaction

The second term in Eq. (7.46) refers to the interfacial energetic barrier arising from an evolving twin nucleus. Although the twin nucleation process is not explicitly modeled, it is assumed that a relatively high stress $\tau_{\eta}^{\mathrm{int}}(f_{\eta} = 0)$ must be overcome initially, i.e., the maximum twinning resistance is obtained if $f_{\eta} = 0$. With evolving twin volume fraction, this barrier shrinks and eventually vanishes once the twinning shear reaches its maximum value η_0 or equivalently if $f_{\eta} = 1$. This continuum approximation of the twinning process resembles a softening or

[10] The activation stress for twin boundary migration was found to exhibit a negligible size effect during microcompression of Mg single crystals with diameters in the range between 3 µm and 10 µm, cf. Liu et al. [158].

relaxation behavior in the flow relation for the twin evolution[11]. In the current framework, τ_η^{int} is defined as

$$\tau_\eta^{\text{int}} = [1 - f_\eta] \frac{\Gamma}{d_{\text{tw}}}, \tag{7.47}$$

where d_{tw} is the twin thickness at the final stage of the twin evolution and Γ denotes the twin boundary energy. The twin thickness is taken as $d_{\text{tw}} = 6d_{\{10\bar{1}2\}}$ with $d_{\{10\bar{1}2\}} = \sqrt{3a^2 + c^2}$ being the distance between $\{10\bar{1}2\}$-planes. A twin boundary energy of $\Gamma = 117$ mJm$^-2$ is obtained for Mg from density function theory computations in [253]. τ_η^{int} solely has a local effect on the twinning evolution process while $\boldsymbol{\xi}_\eta$ generally has a non-local effect, i.e., it governs the growth behavior.

An additional resistance to twinning shear arises from interaction processes with stored dislocation populations. Stored dislocations act as obstacles to the motion of twin partials. This phenomena is addressed via a Taylor-like relation, i.e.,

$$\tau_\eta^{\text{sl}\to\text{tw}} = 0.5\mu^{\perp} b_\eta \sqrt{\sum_\alpha \rho_\alpha}, \tag{7.48}$$

where the Burgers vector amplitude of twinning dislocations is defined as a fraction of the perfect direction vector along which twinning shear takes place, i.e., $b_\eta = n\Lambda[10\bar{1}1]$ with n being the number of twin layers and

$$\Lambda = \frac{\text{abs}(c^2 - 3a^2)}{c^2 + 3a^2}, \tag{7.49}$$

defines the shear magnitude on each layer, cf. Yoo [259]. According to Wang et al. [253], the required number of twin layers must be at least six in order to obtain a stable twin nucleus. We focus on the particular case $n = 6$. In view of Eqs. (7.43) and 7.48, the competitive characteristic between both deformation mechanisms (slip and twinning) is fully described within the current framework.

7.4 Validation - anisotropic elastic and plastic deformation of Mg single crystal

7.4.1 Directional-dependent elastic response

The anisotropic elastic behavior of Mg single crystal is modeled via transverse isotropic hyperelasticity as described in Section 3.2.2. The model parameters are obtained from five independent elastic constants listed in Table 7.1. Using the angular relations given in Tromans [243], the elastic anisotropy in terms of the Young's modulus is visualized in a polar plot in Fig. 7.1 a). The magnitude of the Young's modulus in a particular loading direction is determined by the distance between the indicated origin and the intersection between plotted surface and considered loading direction. The angular dependence of the Young's modulus E^ϕ for loading between [0001]-direction and any direction within the plane of isotropy, e.g., the $[2\bar{1}\bar{1}0]$-direction, is highlighted in Fig. 7.1 b).

[11] Stress relaxation associated with the twinning process has also been addressed by, e.g., Wu et al. [256] and Qiao et al. [207].

Table 7.1: Adiabatic elastic constants for pure Mg. The values are experimentally determined by [160]. All values are given in GPa.

C_{11}	C_{33}	C_{44}	C_{12}	C_{13}
59.70	61.70	16.40	26.20	21.70

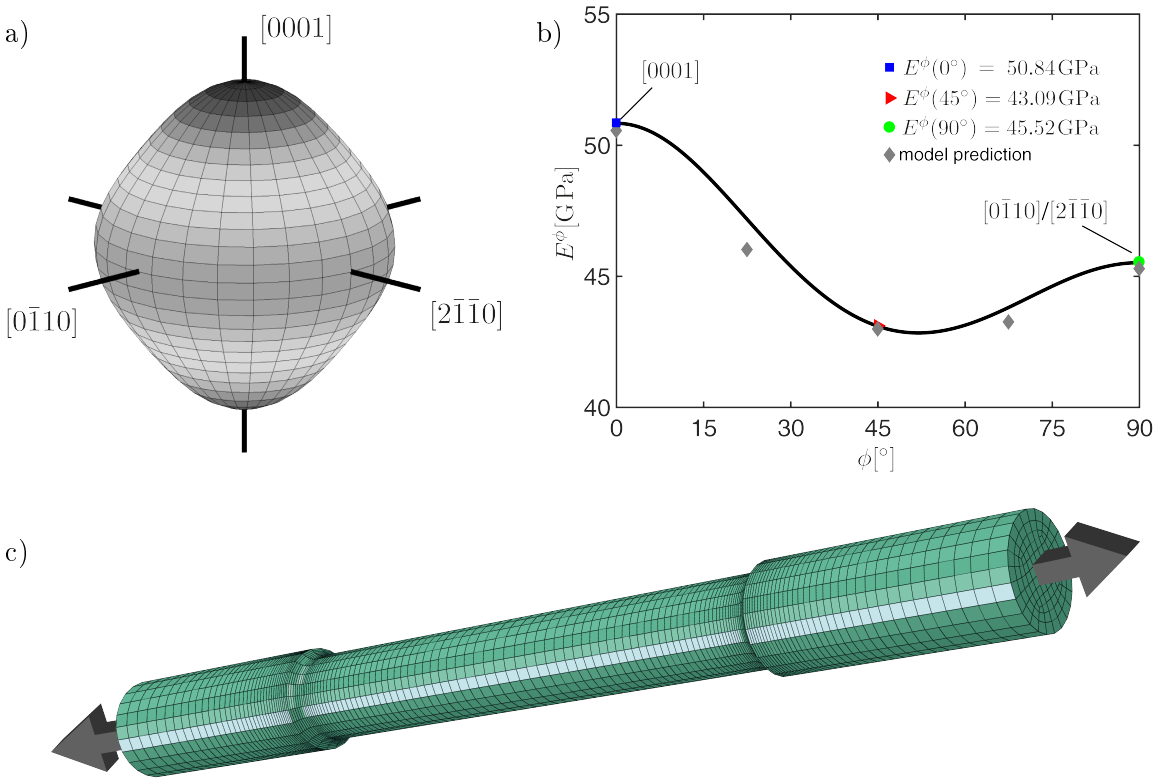

Figure 7.1: Directional dependence of Young's modulus E^ϕ in pure Mg: a) Polar plot of elastic anisotropy in terms of Young's modulus. The distance between the origin and any point on the surface represents the magnitude of E^ϕ in this loading direction. b) Angular dependence of the Young's modulus E^ϕ for loading between [0001]-direction and any direction within the plane of isotropy. Data points indicate theoretical values using elastic constants from Table 7.1 while predicted values are obtained from the transversely isotropic Neo-Hookean model (see Table 7.2 for a qualitative comparison). c) Tensile probe used in numerical computations.
Reprinted from [110] with permission from Elsevier, Copyright 2019.

Uniaxial tension simulations have been carried out for five loading directions in intervals of 22.5°. The tensile probe is illustrated in Fig. 7.1 c). As can seen be seen from the graph, the numerical prediction of E^ϕ is in great accordance with the analytical results. Theoretically calculated and numerically predicted Young's moduli are also given in Table 7.2 along with corresponding errors.

Table 7.2: Theoretical and computed Young's moduli for different loading directions. The error differs between 0.3 % and 2.5 %. Both data sets are based on the elastic constants provided in Table 7.1.

ϕ	E^{ϕ}_{theo} [GPa]	E^{ϕ}_{comp} [GPa]	error [-]
0°	50.84	50.54	0.0059
22.5°	47.19	46.00	0.0252
45°	43.10	42.97	0.003
67.5°	43.81	43.24	0.013
90°	45.52	45.27	0.0055

7.4.2 Bulk hardening behavior

Critical resolved shear stresses and bulk hardening parameters are determined using experimental test data of Kelley and Hosford [122]. In these tests, a channel-die set-up is used to study the stress-strain response of single crystalline Mg compressed for different crystallographic orientations. As is illustrated in Fig. 7.2 a), the numerical set-up is comprised by a deformable bulk single crystal of size 6.35 mm × 9.525 mm × 12.7 mm (height × length × width) and the rigid tools (punch and channel-die). The impact of higher-order gradients is neglected due to the considered sample size in the millimeter regime. Experimental tests with original labels A, B, C, D, and G are considered here. Because twinning is not relevant for these experiments, the corresponding data sets allow identification of the CRSS and other hardening parameters for basal, prismatic, and pyramidal ($\pi 2$) slip modes.

All computations are performed using a rate-sensitivity exponent of $m = 20$ and a reference shear rate of $\nu_0 = 10^{-3}$ s^{-1}, cf. Table 7.3 for the set of generally applied parameters for plastic computations. The imposed compression rate $[\dot{\boldsymbol{\epsilon}}]_{33} = 10^{-3}$ s^{-1} is chosen in accordance to ν_0. As suggested in [122], a correction factor of 0.89 is used to convert the friction effected compressive stress. With $[\boldsymbol{\epsilon}]_{33}$ being the applied compressive true strain, the true compressive stress component becomes

$$[\boldsymbol{\sigma}]_{33} = 0.89 \frac{F_{\text{R}}}{A_0} \exp([\boldsymbol{\epsilon}]_{33}), \tag{7.50}$$

where F is the computed force in the $\boldsymbol{X}_3$-direction and A_0 is the initial cross section with respect to the $\boldsymbol{X}_1$-$\boldsymbol{X}_2$ plane.

The numerical results are presented in Fig. 7.2 b) along with experimental data sets provided by Kelley and Hosford [122]. The inclusions indicate the dominant slip modes for the individual experiments on the basis of their relative fraction of activation. While experiment G results in massive basal slip due to the perfect Schmid factor of $f_{\text{basal}} = 0.5$, the deformation behavior in experiment C and D is mainly dominated by prismatic slip with small basal and pyramidal slip contributions. In contrast, activation of basal, prismatic, and pyramidal slip is in strong competition for crystal orientations associated with experiment A and B while the pyramidal slip mode is the most dominant for these cases. The identified parameters in terms of critical resolved shear stresses of the individual slip modes and bulk hardening parameters are summarized in Table 7.4 for the here considered slip modes. The following latent hardening

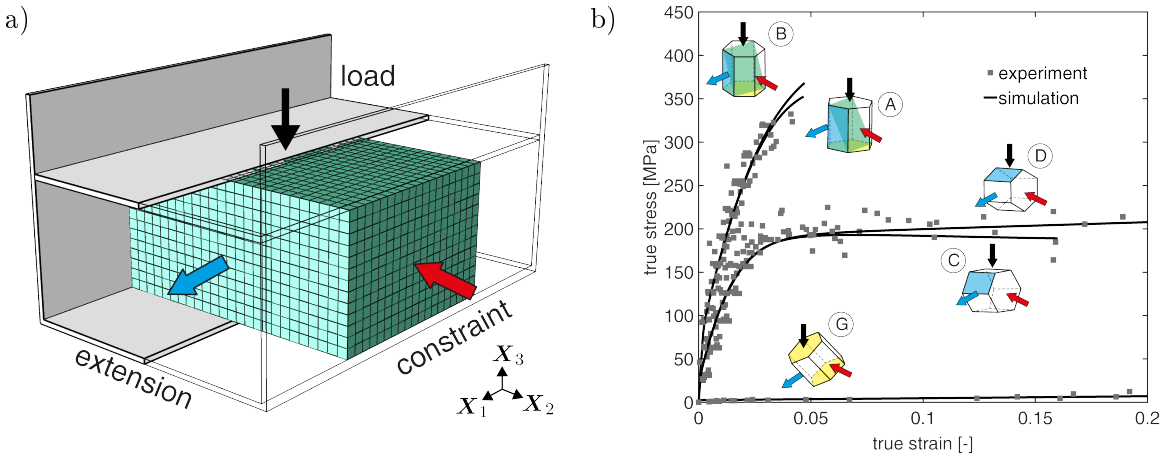

Figure 7.2: Hardening behavior of Mg single crystal: a) Channel-die finite element set-up with illustration of plane strain conditions. b) Quantitative comparison between experimental data from Kelley and Hosford [122] and numerical computations for different crystallographic orientations. The dominant slip modes are highlighted as follows: yellow for basal slip, blue for prismatic slip, and green for pyramidal slip.
Reprinted from [110] with permission from Elsevier, Copyright 2019.

Table 7.3: Crystal plasticity parameters applying to all computations involving plastic deformation.

m [-]	ν_0 [-]	y_c [nm]	K [-]	$g^{e}_{i\alpha 0}$ [mm^{-2}]	$g^{s}_{i\alpha 0}$ [mm^{-2}]	$\zeta_{\alpha 0}$ [mm^{-2}]
20	10^{-3}	1.6	10	0	0	10^{12}

Table 7.4: Identified critical resolved shear stresses and hardening parameters of individual slip modes in bulk-sized Mg single crystal. Latent hardening moduli for non-basal slip are taken as $H^{l}_{\alpha 0} = h^{\infty}_{\alpha}$.

slip mode	$Y_{\alpha 0}$ [MPa]	$H^{l}_{\alpha 0}$ [MPa]	h^{∞}_{α} [MPa]	c_{sat} [-]
basal	1.375	5	-	-
prismatic	15	89	89	84
pyramidal	40	172	172	129

coefficients are used

$$q_{\alpha\beta} = \begin{cases} 0.2 & \text{if } \alpha \in \{\text{prismatic, pyramidal}\} \text{ and } \beta \in \{\text{basal}\}, \\ 0.5 & \text{if } \alpha \in \{\text{basal ,pyramidal}\} \text{ and } \beta \in \{\text{prismatic}\}, \\ 0.75 & \text{if } \alpha \in \{\text{basal, prismatic}\} \text{ and } \beta \in \{\text{pyramidal}\}. \end{cases} \tag{7.51}$$

Furthermore, interaction between slip systems of the same mode is quantified by $q_{\alpha\beta} = 0.2$ and self-hardening of basal slip systems is given by $q_{\alpha\beta} = 1$.

7.4.3 Size-dependent basal deformation

A reliable approach to investigate size effects associated with individual slip modes in single crystals is based on testing micron-sized and typically pillar-shaped samples with varying diameters under uniaxial compression. However, due to a lack of available data in the literature, a characterization of the size-dependent slip deformation of all relevant slip modes is not possible at the current stage. In particular, the easy activation of basal slip in contrast to non-basal slip makes it very challenging to experimentally investigate individual non-basal slip modes independently, i.e., without activation of basal slip. For that reason, we restrict ourselves to the basal slip mode for which sufficient experimental data is available.

The yield strength of crystals is governed, inter alia, by the degree of confinement of the plastic process zone (source-truncation hardening) and the available dislocation density (source-limitation) within. These mechanisms are accounted for via the generalized Taylor-strengthening law given by Eq. (7.39). Considering first the case of a sufficiently large crystal for which a large number of dislocation sources is available, i.e., the case when the intrinsic length scale of the material becomes unaffected by the actual crystal dimensions. Then, parameter k_2 can be determined via Eq. (7.40) in which the yield strength of bulk single crystal $Y_{\alpha 0}$ is known from conventional (macroscopic) testing methods. For the here identified critical resolved shear stress for basal slip (cf. Table 7.4) we obtain $k_2 = 0.2565$. In contrast, parameter k_1 is determined by means of the least square method for a given set of size-dependent yield strength data, here taken from [122] for millimeter-sized probes, [158] for the range $D_0 = \{3, 5, 10\}$ µm, and [261] for the range $D_0 \in [0.4, 1.6]$ µm. Fig. 7.3 a) shows the predicted yield strength for a resulting value of $k_1 = 0.0025$ and an initial dislocation density of $\rho_{\alpha 0} = 10^{12}$ m^{-2} (neither well-annealed nor strongly cold-rolled material). For comparison reasons, we included an additional approximation of the yield strength data using the conventional Hall-Petch relation

$$\tau_\alpha^{\mathrm{y}} = Y_{\alpha 0} + k_{\mathrm{HP}} D_0^{-0.5}, \tag{7.52}$$

with the Hall-Petch parameter $k_{\mathrm{HP}} = 49$ MPa m$^{0.5}$ (least square method). Although Eq. (7.52) is successfully used to predict grain-boundary strengthening, it results in a poor approximation of the size-dependent yield strength of micron-sized Mg single crystal.

Besides an increasing yield stress with decreasing micropillar diameter, the microcompression data of [158] indicates that there is also an increase in the work hardening slope for micropillars favored for basal slip deformation. For that reason, the higher-order gradient crystal plasticity model is validated against the data for diameters between 3 µm and 10 µm. The crystals are loaded in normal direction to the $\{2\bar{1}\bar{1}4\}$-plane resulting in a maximum Schmid factor of 0.489 and a secondary Schmid factor of 0.245 for basal slip. As a result, a strong localization associated with the dominant slip system follows which is very common in microcompression testing. In the numerical computations, the non-local hardening moduli were computed by Eq. (7.29), giving $H_0^{\mathrm{e}} = 3.013$ GPa resp. $H_0^{\mathrm{s}} = 4.188$ GPa. The lattice constants a and c were adopted from [111]. Moreover, the characteristic length scale is taken as $l_\alpha = 1$ µm, a magnitude which reasonably applies to micromechanical testing of Mg single crystals for a moderate range of deformation, cf. the work of [111], in particular, the detailed comparison of local lattice rotation measured by EBSD and numerically computed GND density distributions associated with the chosen length scale. The higher-order boundary conditions are modeled as explained in detail in [111]: microhard conditions are adopted at the contact interface and microfree conditions at the lateral surface of the pillar. A friction coefficient of 0.03 is considered as suggested by [265]. Parameters related to size-dependent yielding and hardening are summarized in Table 7.5. All other parameters are taken as previously determined or

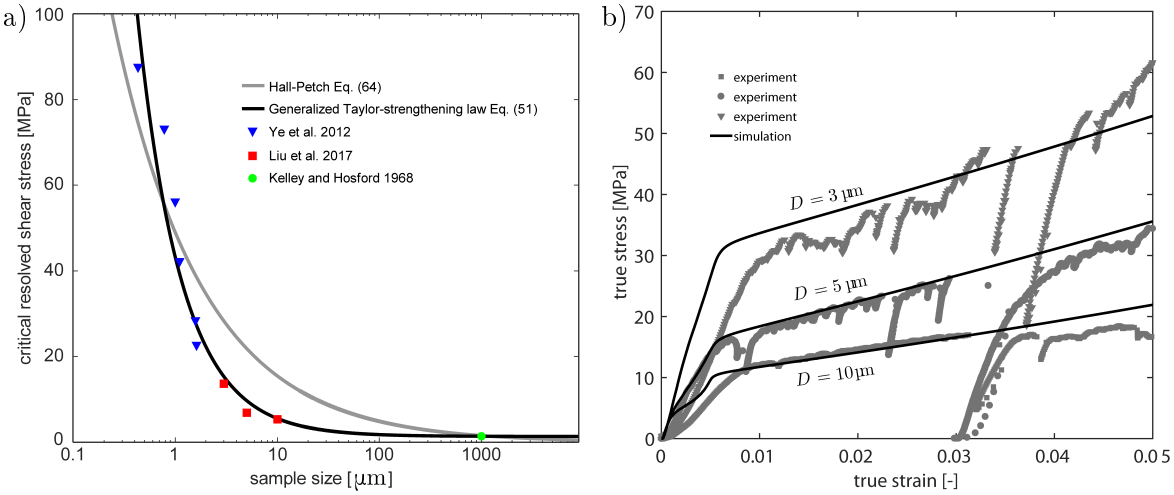

Figure 7.3: Size-dependent basal deformation of Mg single crystal: a) Critical resolved shear stress as a function of the microcrystal size (diameter) for $\rho_{\alpha 0} = 10^{12}$ m^{-2}. The generalized Taylor-strengthening law given by Eq. (7.39) with $k_1 = 0.0025$ and $k_2 = 0.2565$ yields the experimental data very well. In contrast, the Hall-Petch relation given by Eq. (7.52) results in a poor approximation of the size-dependent yield strength. b) Comparison of the stress-strain response between numerical results and experimental data of [158] for three different micropillar sizes.
Reprinted from [110] with permission from Elsevier, Copyright 2019.

defined.

Table 7.5: Parameters associated with size-dependent yielding and hardening. Energetic hardening stresses H_0^{e} and H_0^{s} are taken in accordance to [24], i.e., are natural outcomes of the here considered anisotropic elastic constants. The characteristic length scale l_α is adopted from our previous work on non-local deformation behavior of Mg single crystal [111] which is supported by EBSD measurements.

$\rho_{\alpha 0}$ [m^{-2}]	k_1 [-]	k_2 [-]	H_0^{e} [GPa]	H_0^{s} [GPa]	l_α [μm]	a [nm]	c [nm]
10^{12}	0.0025	0.2565	3.013	4.188	1	0.32	0.52

The numerical results are presented in Fig. 7.3 b) along with experimental data of [158]. As can be seen, the size-dependent work-hardening behavior as well as the yielding points are captured very well by the simulations. The corresponding finite element set-up as well as an exemplary plastic slip distribution of a deformed micropillar are shown in Fig. 7.4 a) and b) respectively.

From previous microcompression studies, it is known that the mechanical response is strongly affected by diverse factors associated with the sample geometry and the experimental set-up, see [265] and [49]. For instance, the aspect ratio between height and diameter as well as the taper angle[12] are known to affect the elastic and plastic behavior. In agreement with [158] (ra-

[12] A pillar geometry usually differs from an ideal cylindrical form if the sample is fabricated by FIB. This

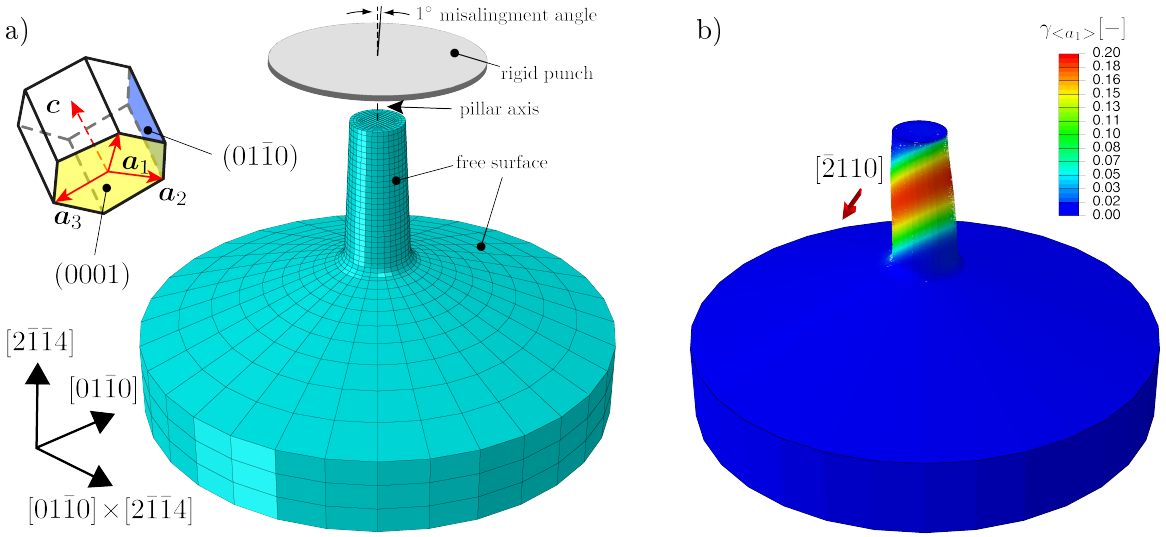

Figure 7.4: Numerical set-up for microcompression simulations favored oriented for basal slip deformation: a) crystal orientation and undeformed finite element mesh. Loading is applied in the $[\bar{2}11\bar{4}]$-direction yielding in a maximum Schmid factor of 0.489 for basal slip. b) Deformed finite element mesh for $D = 10$ µm. Deformation localizes with respect to the dominant slip mode, i.e., in the $[\bar{2}110]$-direction.
Reprinted from [110] with permission from Elsevier, Copyright 2019.

tio between 1 and 2.5), aspect ratios of 2 resp. 2.5 are used. Although the taper angle varies in [158] between 2° and 5°, a constant angle of 2.5° is adopted for all micropillars. In summary, the overall size-dependent response is very well captured by the computations. The initial elastic regime is strongly controlled by the misalignment between the axis of compression and the pillar axis, see, for instance [49]. Such an initially compliant response is often observed during microcompression testing of Mg single crystals and can be explained by microplasticity combined with evolving contact conditions between the sample and indenter [157]. In order to account for the initially compliant response, all computations have been performed using a misalignment angle of 1°. From Fig. 7.3 b), it is seen that this results in a good agreement for the particular sample size with $D = 5$ µm. It appears that the misalignment angle might be different from test to test and, additionally, the direction of tilting may also vary. This can significantly affect slip system activation and elastic response in case of strong anisotropic crystals. However, an extensive investigation of tilt angle and tilting direction for each of the considered Mg crystal compression tests exceeds the scope of this work. Instead, we focus on a qualitative assessment of the work-hardening behavior. Besides for the micropillar with $D = 3$ µm for which the response is strongly affected by intermediate strain bursts, the work-hardening behavior is captured very well. This can be attributed to the operation and shutdown of single-arm dislocation sources as discussed by [61]. Although the impact of truncated single arm dislocations on the CRSS is considered here, the appearance of intermediate strain bursts is not accounted for at this stage.

deviation is characterized by the taper angle which is defined as the angle between the pillar axis and the vertical tangent along the lateral surface.

7.5 Results

In the following, selected problems are studied to demonstrate the major features of the higher-order gradient crystal plasticity model coupled to deformation twinning. Of particular interest is the impact of twinning on the plastic deformation of Mg single crystal. This includes the explicit effect of twinning-induced lattice reorientation and slip-in-twin deformation. Details regarding the numerical implementation are presented in Appendix A.

7.5.1 Local deformation behavior

The competitive deformation behavior for Mg single crystals under compression along the $[2\bar{1}\bar{1}0]$-direction is analyzed in the absence of gradient effects. Under this loading condition, the c-axis of the crystal experiences a tensile stress which leads to the activation of a $\{10\bar{1}2\}$-twin variant. Only a single twin variant, namely $(10\bar{1}2)[\bar{1}011]$, is considered as illustrated by Fig. 7.5 a) and Fig. 7.6 a) for low and respectively high constraint boundary conditions. By these two set-ups for the mechanical boundary conditions, different local deformation behavior is studied as found, e.g., near a constraint region such as grain boundary or contact boundary and at a far distance from such constraint regions. Moreover, the considered problems allow a much easier understanding of underlying features of the proposed model including the impact of twin-slip and slip-twin interactions, lattice reorientation after full twinning, and subsequent slip deformation within twinned regions. Besides the perfect orientation shown for instance in Fig. 7.5 a), the mechanical response is studied for different rotation angles φ relative to the perfect orientation of the crystal lattice. The angle defines a clock-wise rotation around the $\{01\bar{1}0\}$-axis which leads to a gradual increase of the initial Schmid factor f_{basal} for basal slip modes. Initial Schmid factors f_α for different rotation angles φ and for all considered deformation modes are summarized in Table 7.6. The loading is applied under quasi-static conditions with a nominal strain rate of 10^{-3} s^{-1} similar to typical experimental conditions. Material parameters related to the tensile twinning mode in Mg are listed in Table 7.7.

Considering the case of low constraint boundary conditions, the relative activation of slip and twinning modes[13] indicates a strong initial competition between prismatic slip and tensile twinning for $\varphi = 0°$, cf. Fig. 7.5 c). Pyramidal slip activation is only marginal while basal slip is completely suppressed due to its zero Schmid factor, cf. Table 7.6. At ca. 1 % strain, tensile twinning dampens prismatic slip activity and changes the characteristic of the stress-strain curve from hardening towards softening, cf. Fig. 7.5 b). Once the sample is fully twinned, the crystal lattice reorients. Basal slip within the twin immediately initiates and causes an additional stress drop due to its very low critical resolved shear stress combined with a Schmid factor as high as $\tilde{f}_{\text{basal}} = 0.432$. A small variance of the rotation angle φ drastically changes the mechanical response. While the behavior is the same for $\varphi = 1°$ (marginal basal slip activation - not shown in the figure), tensile twinning becomes fully suppressed at a rotation angle of $\varphi = 1.5°$ as shown in Fig. 7.5 d). Instead, prismatic and basal slip activations are observed at the initial strain stage of deformation. Due to slip system interactions in combination with the low basal yield stress, basal slip takes over very fast. This behavior is directly reflected by the corresponding stress-strain response. It is remarkable that basal slip governs the mechanical response after such a small rotation as the Schmid factor is still quite low ($f_{\text{basal}} = 0.026$).

[13] The relative slip/twinning mode activity is defined as $\sum_{ip} V^{ip} \int \varpi^{ip}_{\text{mode}} \text{dt} / \sum_{\text{mode}} \sum_{ip} V^{\text{ip}} \int \varpi^{ip}_{\text{mode}} \text{dt}$ where mode denotes the active twinning or slip mode and V^{ip} is the volume portion related to integration point ip. $\varpi^{ip}_{\text{mode}}$ represents the local twinning shear rate if mode refers to the active twin system; else $\varpi^{ip}_{\text{mode}}$ represents the local plastic shear rate of a particular slip system in the parent or in the twin lattice.

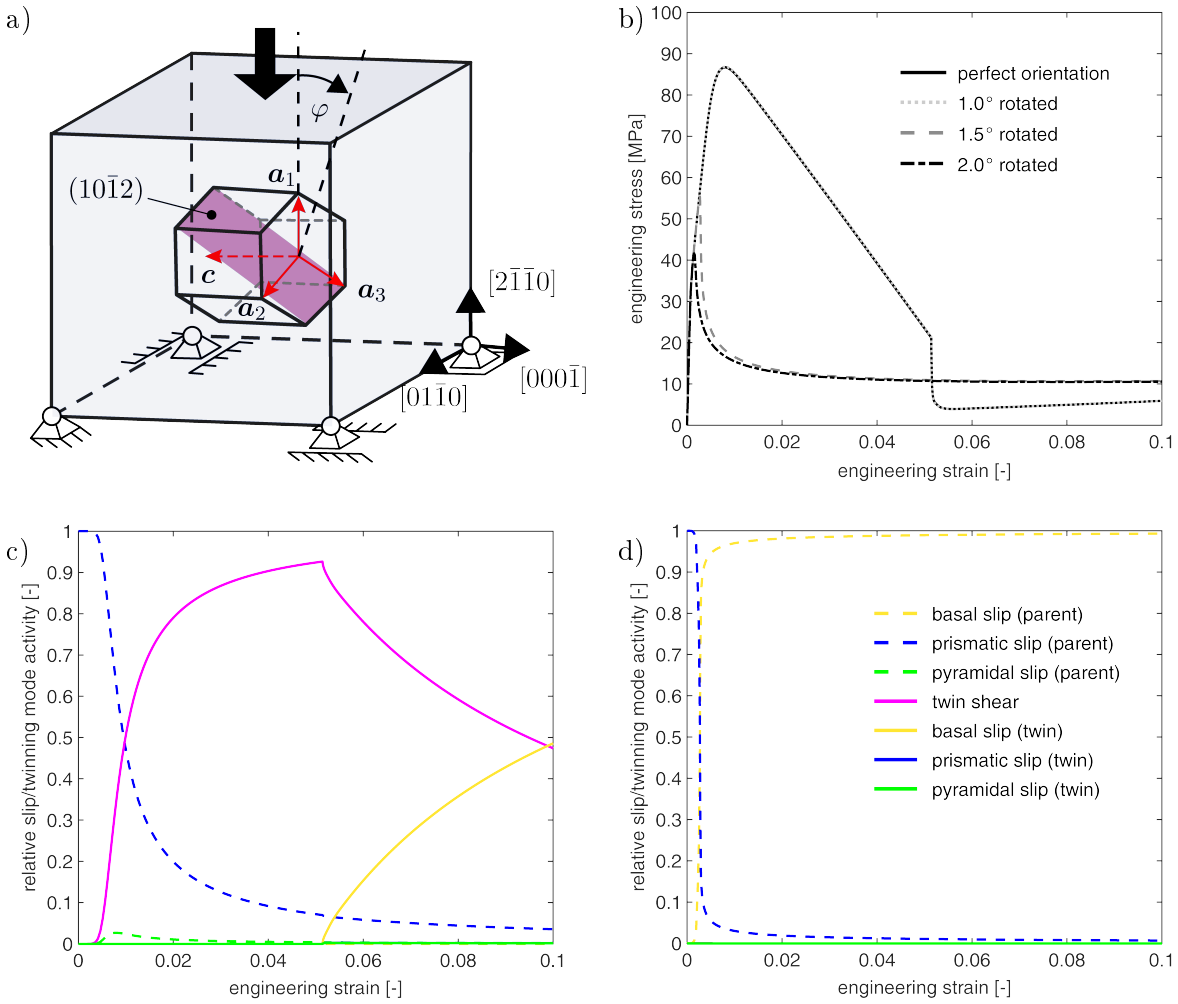

Figure 7.5: Competition between slip and twinning deformation in Mg single crystal during compression in the $[2\bar{1}\bar{1}0]$-direction and for different rotation angles φ: a) Problem illustration for low constraint boundary conditions including crystallographic orientation. b) Stress-strain response for different rotation angles φ. c) Relative activation of slip and twinning modes for $\varphi = 0°$ (perfect orientation). d) Relative activation of slip and twinning modes for $\varphi = 1.5°$. The low constraint to plastic deformation leads to a fast transition from twinning dominated deformation towards basal slip dominated deformation, i.e., already at a very low rotation angle.
Reprinted from [110] with permission from Elsevier, Copyright 2019.

With further increasing rotation angle φ, the stress-strain response approaches the behavior of bulk single crystal, similar to case G in Fig. 7.2. If the constraint level for mechanical boundary conditions is increased as in the set-up sketched in Fig. 7.6 a), basal slip is less easy to activate at low rotation angles. The response for $\varphi = 0°$ is very similar to the low constraint case in terms of slip and twinning mode activation as well as stress-strain response. However, with increasing rotation angle, the negative slop prior lattice reorientation decreases, cf. Fig. 7.6 b). This is due to intensified interactions between basal slip, prismatic slip and tensile twinning as indicated for $\varphi = 5°$ in Fig. 7.6 c). By comparing the stress-strain curves for $\varphi = 5°$ and $\varphi = 10°$ in Fig. 7.6 b), it can be seen that the softening behavior eventually changes towards a hardening-like response before the onset of lattice reorientation. At the same time,

Table 7.6: Max. Schmid factors f_α for selected rotation angles φ.

$\varphi[^\circ]$	f_{basal}	f_{pris}	$f_{\pi 2}$	$f_{\text{t-tw}}$
0	0	0.433	0.447	0.374
1.5	0.026	0.433	0.458	0.375
2.0	0.035	0.433	0.461	0.375
5.0	0.087	0.43	0.479	0.372
10.0	0.171	0.42	0.497	0.357
15.0	0.25	0.404	0.5	0.33
20.0	0.383	0.356	0.459	0.24

Table 7.7: Parameters related to the tensile twinning mode in Mg.

Symbol	Magnitude	Source
Γ	117 mJ/m^2	[253]
l_η	1 nm	[56]
η_0	0.1295	Eq. (3.14),[259]
n	6	[253]
Λ	0.0646	Eq. (7.49)

the critical strain at which lattice reorientation takes place increases or, in other words, the twinning process delays due to pronounced interaction processes between active slip modes and the tensile twinning mode. For $\varphi = 15^\circ$, activation of tensile twinning is even more damped due to enhanced slip deformation. As is illustrated by Fig. 7.6 d), high basal and prismatic slip activity combined with low pyramidal slip activity is obtained for this case. Although the reorientation angle is relatively large, the maximum twinning shear is still reached at around 9 % strain causing lattice reorientation. In contrast to this, lattice reorientation does not occur if the rotation angle is further increased, e.g., for $\varphi = 25^\circ$. In that case, the relative activation (not plotted) at the final deformation stage comprises approximately 65 % basal slip, 19 % prismatic slip, 8 % pyramidal slip, and 8 % twinning shear. Similarly to the low constraint problem, basal slip activation maximizes at $\varphi = 45^\circ$ as the maximum basal Schmid factor is obtained for this angle, yielding in a strongly basal-dominated deformation response. Finally, it should be pointed out that the hardening slope after lattice reorientation is steeper if slip activity in the parent lattice is more pronounced, cf. the different stress-strain curves in Fig. 7.6 b) for the three rotation angles $\varphi = 5^\circ$, $\varphi = 10^\circ$, and $\varphi = 15^\circ$. This is associated with the fact that stored dislocations are assumed to remain stored after lattice reorientation.

7.5.2 Application to microcompression testing

As a further problem, the non-local twinning effect is studied for a micropillar sample with edge length of $D_0 = 10$ µm, cf. Fig. 7.7. The pillar is loaded up to 5 % engineering strain although

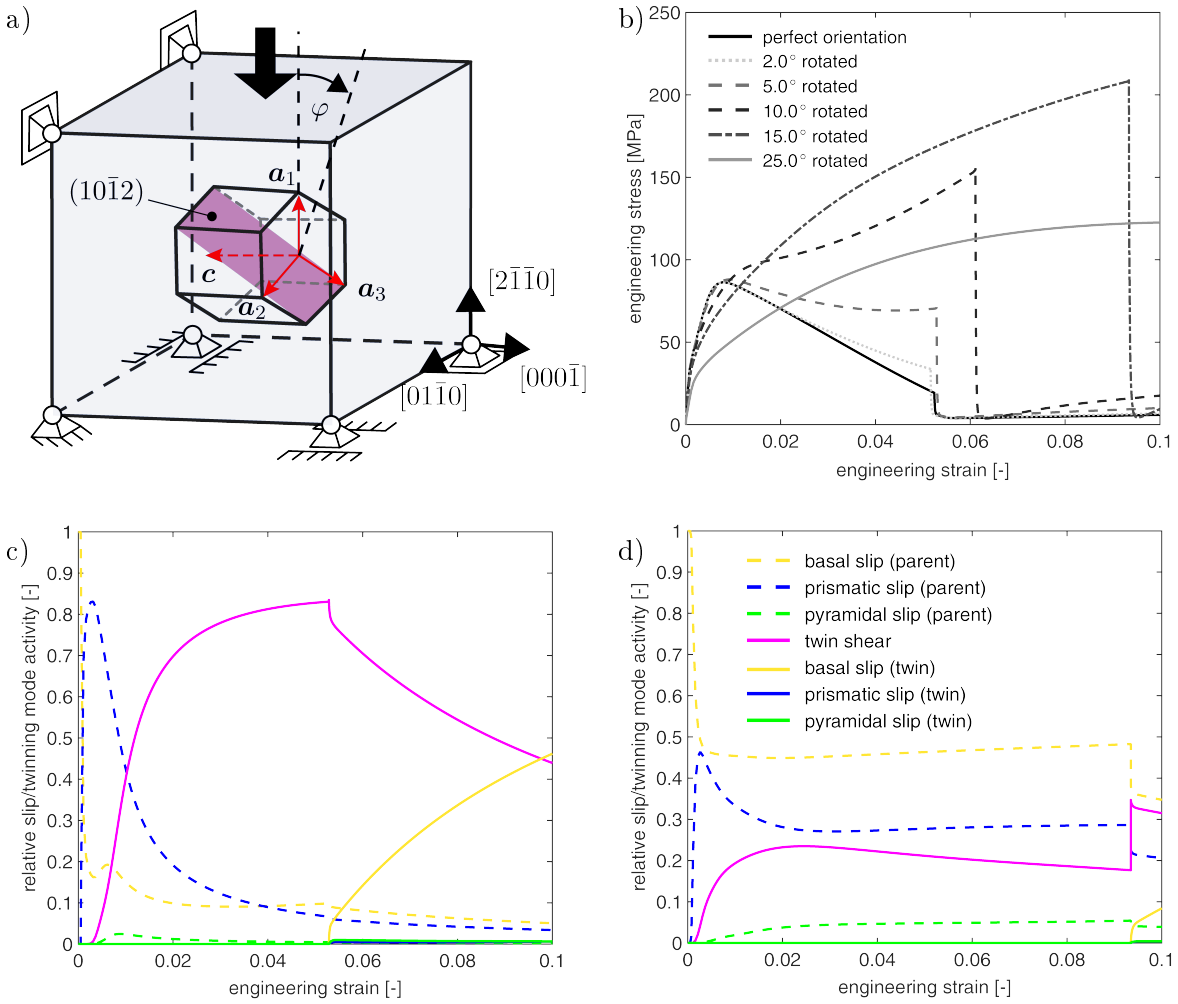

Figure 7.6: Competition between slip and twinning deformation in Mg single crystal during compression in the $[2\bar{1}\bar{1}0]$-direction and for different rotation angles φ: a) Problem illustration for high constraint boundary conditions including crystallographic orientation. b) Stress-strain response for different rotation angles φ. c) Relative activation of slip and twinning modes for $\varphi = 5°$. d) Relative activation of slip and twinning modes for $\varphi = 15°$. Due to the higher constraint to plastic deformation (in particular to basal slip), the transition from twinning dominated deformation towards slip dominated deformation is delayed. Furthermore, the twinning process is completed at a higher strain level, for instance, if comparing the case $\varphi = 15°$ with the case $\varphi = 5°$.
Reprinted from [110] with permission from Elsevier, Copyright 2019.

the true strain measure is used for the result illustration. The considered crystal orientation with respect to the loading direction is chosen in accordance to, e.g., [158]; a set-up typically used to study twinning. Again, a single twin variant is considered for simplicity. All material parameters remain the same as previously discussed or determined. The stress-strain response is illustrated in Fig. 7.7 for two considered simulation cases. First, the artificial case when slip deformation is fully excluded from the numerical computation is considered. By doing so, the strain solely accommodated by twin deformation can be easily analyzed. Second, the full modeling framework without slip gradient contributions is considered in order to keep the

total degrees of freedom on a reasonable level. By comparing both cases with each other, the impact of dislocation slip on the initiation and completion of the twinning process can be assayed. The contour plots embedded in Fig. 7.7 illustrate the twinning process in case of the full modeling framework. There are no obvious differences between the two considered cases because the twinning mode is most favorable due to the considered crystal orientation; initial Schmid factor for tensile twinning is 0.499 while basal slip has initially no contribution at all. As can be seen, the twin propagates in a continuum manner through the entire pillar. With increasing compressive strain, the twin shear reaches its maximum value within a relatively thin layer which corresponds to the active twin plane. The twin band thickness increases during further loading and, eventually, an almost fully twinned crystal is left behind. The longitudinal strain accommodated by the twinning shear can be estimated as

$$\epsilon = f_\eta^{\mathrm{tot}} f_{\text{t-tw}} \eta_0. \tag{7.53}$$

For the here considered case, $f_{\text{t-tw}} = 0.499$ and the total twin volume fraction is determined as $f_\eta^{\mathrm{tot}} \approx 0.72$ at final strain stage. Interestingly, there is almost no difference in the total twin volume fraction between the two considered cases, i.e., the strain accommodation by twinning is approximately 0.042 whether or not slip deformation is admitted. This is a considerable amount of strain accommodated only by the formation and growth of a single twin. In comparison, a longitudinal strain accommodation of approx 80 % was determined in [129] in case of a similar set-up for microcompression of Mg single crystal. Also, an almost entirely twinned crystal was found in the recent work of [166]. With respect to the case in which dislocation plasticity is disabled, the twinning process imposes a temporal flattening of the slope as can be seen from the corresponding stress strain curve, cf. Fig. 7.7. As expected, the response approaches the elastic behavior of the twinned lattice orientation as the twin volume fraction saturates. In contrast, if slip deformation is permitted, the stress-strain curve passes a plateau stage during which twinning propagates and a thin layer develops. Additional deformation is mainly accommodated by pyramidal and prismatic slip associated with the parent lattice orientation and in regions outside of the twinning dominated region. After a sufficient twin volume fraction is formed, slip deformation initiates within the twinned region. This process is reflected by a hardening slope which directly follows after the stress plateau. The extent to which slip contributes to the inelastic deformation is quantified via effective accumulated plastic slip quantities defined as

$$\gamma_{\text{eff}} = \sqrt{\sum_\alpha \left[\int \nu_\alpha \mathrm{d}t\right]^2}, \quad \widetilde{\gamma}_{\text{eff}} = \sqrt{\sum_\alpha \left[\int \widetilde{\nu}_\alpha \mathrm{d}t\right]^2}. \tag{7.54}$$

Fig. 7.8 indicates the relative activity of deformation modes in terms of effective plastic slip within the parent and twin as well as twinning shear. As can be seen, slip within the parent is accumulated in regions where boundary effects impose complex stress distributions leading to the activation of the hard slip modes, i.e., prismatic and pyramidal slip. The relative twinning mode activity governs the deformation but saturates as soon as almost the entire crystal volume has twinned. Within the twinned zone, plastic slip is solely accommodated in terms of pyramidal slip which has the highest maximum Schmid factor of 0.47. In contrast, basal slip (Schmid factor ≈ 0.06) and prismatic slip (Schmid factor ≈ 0.002) are not likely to contribute to the deformation due to latent hardening effects combined with the very low orientation factors. This simulation outcome is in accordance with the work of [166] in which similar stages of deformation have been recently observed. Besides the initial stage of deformation which is governed by microplasticity and evolving contact conditions at a finite alignment

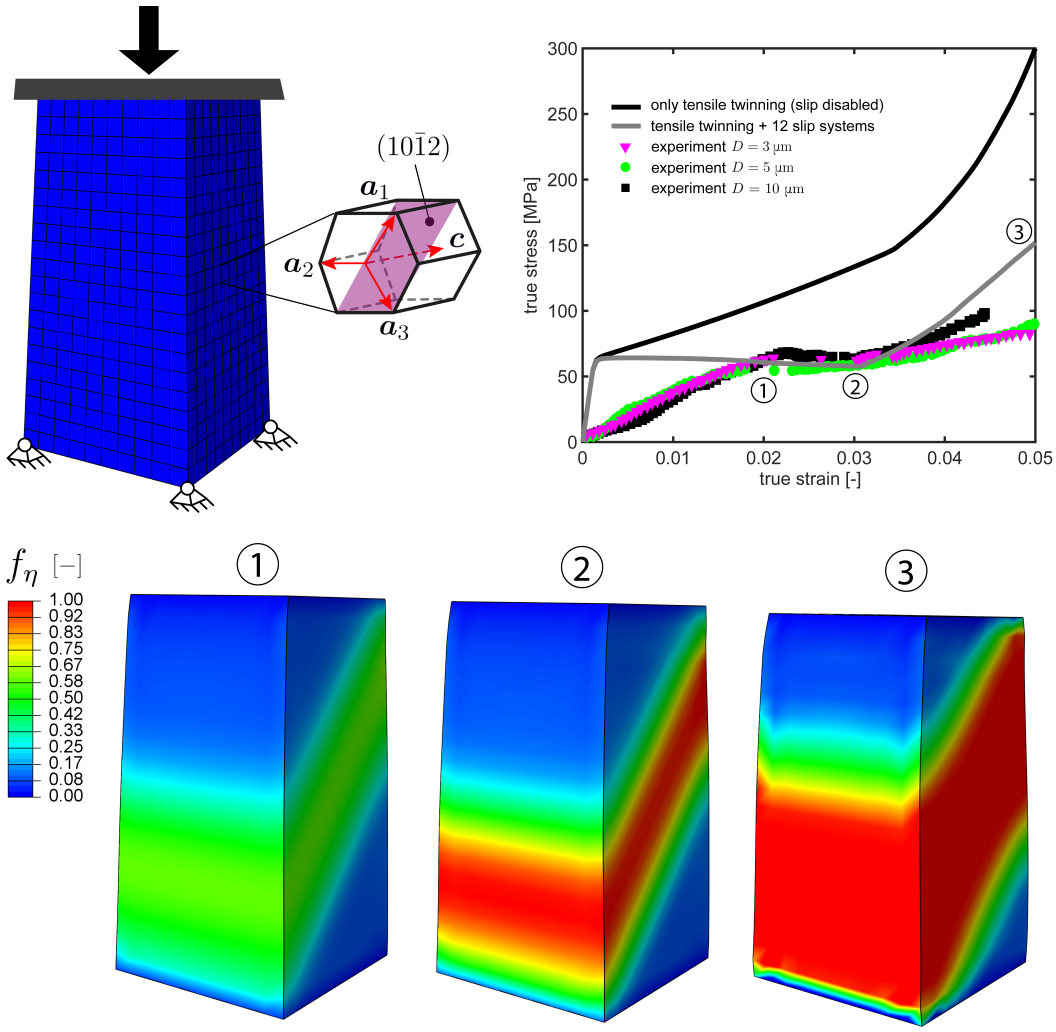

Figure 7.7: Micropillar set-up favorable for tensile twinning activation. The experimental data is taken from [158]. Besides the initial deformation regime which is governed by microplasticity and evolving contact conditions between the sample and indenter punch, the computed response mimics the mechanical behavior during twinning-dominated deformation very well. In particular, the stress plateau and the subsequent hardening slope associated with slip-in-twin deformation is well captured by the model.
Reprinted from [110] with permission from Elsevier, Copyright 2019.

mismatch between pillar axis and loading axis, the overall behavior matches qualitatively very well with the experimental data of [158]. This includes in particular the stress plateau and the subsequent hardening slope associated with slip-in-twin deformation.

7.6 Conclusions

The proposed model incorporates the mechanics of deformation-induced twinning in an extended crystal plasticity framework. In contrast to other pseudo-slip twinning models, the model accounts for the sudden change of the crystal lattice orientation at the very final stage

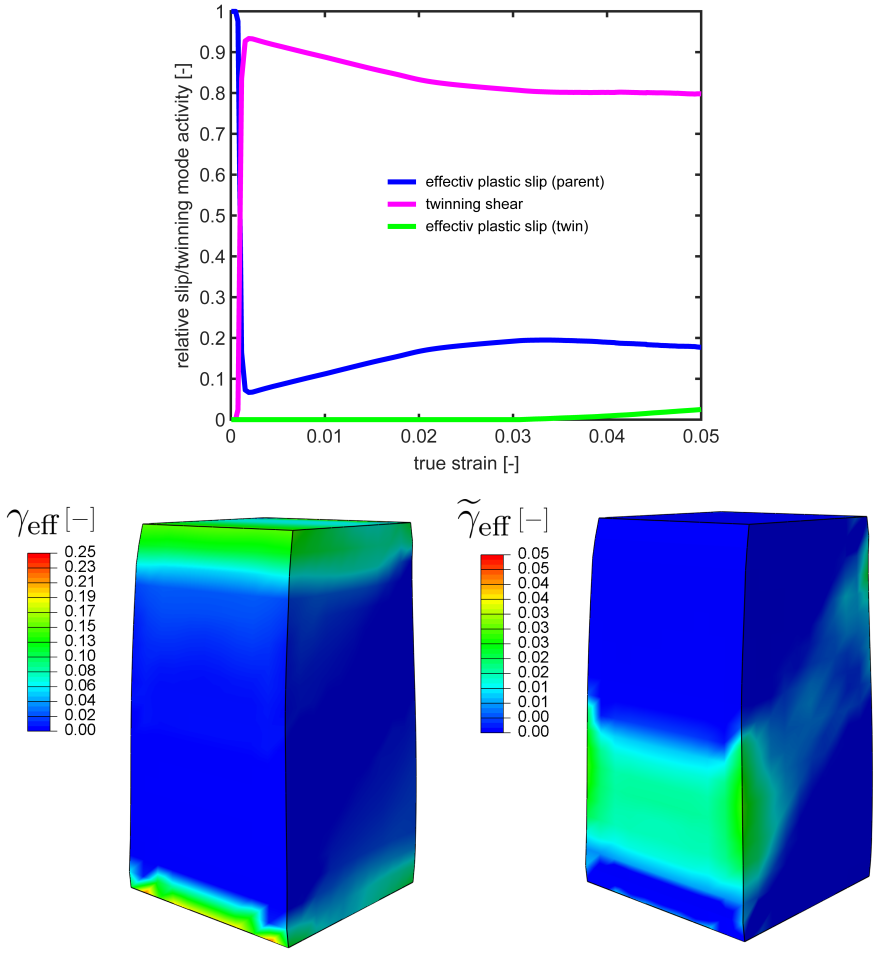

Figure 7.8: Relative activity of deformation modes during micro-compression testing. Inelastic deformation within the parent crystal is governed by twinning shear superimposed by secondary plastic slip within regions which are affected by boundary effects. Within the reoriented crystal lattice, plastic slip initiates in terms of pyramidal slip modes which have the highest orientation factor.
Reprinted from [110] with permission from Elsevier, Copyright 2019.

of the twinning shear process. With focus on the most relevant twinning mode in Mg (tensile/extension twinning), the crystallographic $< c >$ axis rotates by $\approx 86.3°$. This affects the direction-dependent elastic response as well as the subsequent deformation in terms of dislocation glide within the twinned volume as experimentally observed, e.g., in [166]. As demonstrated by our results, the critical strain at which lattice reorientation takes place is strongly influenced by the intensity of preceding slip deformation. In this respect, the completion of the twinning process may be delayed due to extensive slip-slip, twin-slip, and slip-twin interactions or even be completely suppressed in case of slip dominated deformation. Furthermore, the reorientation process has an impact on the hardening behavior for subsequent slip deformation within the twinned region. In contrast to mobile dislocations which may undergo a dissociation process during lattice reorientation, stored dislocation are assumed to remain unaltered as it is unknown what happens to them at this stage. Another phenomenon often correlated with extensive appearance of twinning is stress relaxation during the nucleation process. Besides the fact that twin nucleation requires a higher stress state than subsequent

twin growth [158], a second relaxation effect results from the local stress drop associated with an improved orientation factor for easy slip modes within the twinned volume. This stress drop is found to increase with extensive slip activity before lattice reorientation and is naturally cut-off if slip becomes the dominant deformation mechanism under a suitable crystal orientation and constraint level.

Although there might be a large number of relevant twin modes in Mg as was recently found and discussed by [234], the current work deals with tensile twinning only since it represents the most relevant and widely observed twin mode in Mg. The results show that a very low Schmid factor for basal slip leads to slip dominated deformation if the constraint level is rather small. For a higher constraint level, activation of twinning is favored for a large range of crystal orientations for which the twinning Schmid factor is comparable to that of basal slip. Furthermore, the extent of slip activation before completion of the twinning shear process affects the critical strain at which sudden lattice reorientation takes place, the associated stress relaxation, and the hardening behavior with respect to the new crystal orientation. Based on these findings, the interplay between slip modes and twinning appears to be more complex than what is commonly considered in crystal plasticity models.

An illustrative microcompression scenario reveals the impact of the non-local twinning effect on the mechanical response of Mg single crystal. The obtained results are qualitatively comparable to experimental data which are obtained for a similar set-up. Here, it was found that a single twin can accommodate a substantiation amount of compressive strain. The simulation results indicate further that the typically observed stress plateau during such experiments can be attributed to the extension and growth of a single twin variant and the interplay with secondary slip deformation. Last but not least, the explicitly modeled crystal reorientation mechanism is essential in naturally predicting the hardening slope associated with slip-in-twin deformation mechanisms. In view of future application of the presented model, the obtained results appear promising for possible modeling of twinning deformation in polycrystals at the microscale level.

8 Summary

The focus of the present thesis was on the computational modeling of crystal plasticity and deformation twinning in micron-sized crystalline materials. Micromechanical problems including microcompression and microbending testing have been investigated on a numerical basis. The computational approach is based on a finite-deformation, continuum mechanics framework of gradient crystal plasticity. A physically motivated measure of lattice incompatibility is introduced through densities of geometrically necessary dislocations in order to account for non-local effects at the micron scale. As a result, higher-order gradients are considered which manifest itself as size-dependent hardening in terms of an internal backstress contribution. The model is implemented in a three-dimensional finite element software via a user subroutine interface. The implementation is based on a dual-mixed finite element algorithm which implies that GND densities are handled as nodal degrees of freedom while their dual variables - the plastic slip variables - are assigned at the integration point level.

The application to microcompression testing of single crystals illustrates the importance of the gradient crystal plasticity theory, allowing to capture a realistic material behavior. This comprises a localized plastic deformation behavior as well as a size-affected stress-strain response, both not accessible by conventional crystal plasticity models. A physical agreement between experiments and simulations is emphasized qualitatively by EBSD measurements of the local lattice rotation which correlates greatly with computed densities of accumulated dislocations. While the gradient effect during microcompression testing has many similarities to the well known Hall-Patch effect associated with fine-grained polycrystals, the role of GNDs during microbending is somewhat different. An externally imposed strain gradient forces dislocations to accommodate the lattice curvature which is known to occur in terms of dislocation pile-ups along the neutral plane. The numerical results suggest that their exists a size limit upon which the related back stress effect can be considered as the reason for the bending size effect. Sample sizes below that limit indicate generally an even more enhanced strengthening effect which can be attributed to dislocation starvation and source limitation phenomena. The transition from the back stress dominated size range towards the size range of enhanced strengthening may depend, however, on the overall crystal volume, the initial microstructure, and the state of the free surfaces. As the role of free surfaces becomes different for sample sizes with high surface-to-volume ratio, dislocation-surface interactions deserve much more attention in order to map realistic surface or boundary conditions. For that reason, advanced higher-order boundary conditions have been proposed which are able to take surface yielding and size dependent surface strengthening into account. A nanoporous metallic structure exposed to compression loading served as an illustrative example. In contrast to standard boundary conditions, the proposed boundary conditions allow a more general and flexible treatment of the surface behavior.

With particular focus on hcp crystals, the kinematics of the theoretical framework are further extended in order to account for the mechanics associated with twinning-induced plasticity. In particular, tensile twinning is known as an important mode of deformation in low-symmetric hexagonal close-packed crystal structures such as magnesium. To this end, the twinning process is incorporated into the gradient crystal plasticity framework in terms of a shear

deformation due to motion of twin partials. Furthermore, the completion of the process is assumed to trigger lattice reorientation which in turn blazes the trail for subsequent slip-in-twin deformation. Such twinning-related phenomena are observed in many recent experimental studies but are still neglected or over-simplified in crystal plasticity models. The developed theory is set up in such a way that activation of slip and twinning modes is governed by interaction processes between both deformation mechanisms. The results demonstrate the strong competitive nature between these mechanisms for different loading conditions and a variety of crystal orientations. Based on the described modeling approach, it was possible to predict the complex strain-stress response of a micropillar-shaped Mg single crystal favorable oriented for tensile twinning under compression. In particular, the stress plateau associated with the extension and thickening of a twin band as well as the subsequent hardening slope associated with the activation of slip within the twin band is captured by the non-local twinning model.

The nonlocal crystal plasticity formulation coupled with the nonlocal description of deformation twinning allows to consider a high level of physical detail. In view of future work, it is conceivable to integrate the present model into an algorithm suitable to deal with the computation of material systems with polycrystalline microstructure such as textured alloys or nanoporous metals. With the advanced modeling basis provided by the model, it would be possible to investigate, e.g., the role of growing twins during deformation and their interaction with each other or with grain boundaries.

A Algorithmic procedure of the twinning model

The implementation is based on a dual-mixed formulation, i.e., gradient-related quantities $g^{\mathrm{e}}_{\mathrm{i}\alpha}(\nabla_{\mathrm{i}}\gamma_\alpha), g^{\mathrm{s}}_{\mathrm{i}\alpha}(\nabla_{\mathrm{i}}\gamma_\alpha), \nabla_{\mathrm{i}} f_\eta$ are considered as primary fields. Due to the extended degrees of freedom compared to a conventional 8-node hexahedral element with only displacement degrees of freedom, an user-defined finite element with trilinear interpolation was implemented in Abaqus via the user interface UEL. The coupling between governing equations at the nodal level and evolution equation at the integration point level results in a strongly non-linear problem which is faced by a two-level Newton-Raphson iteration scheme.

The deformation state is assumed to be known for a given time history at $t = t_{(n)}$. Hence, the aim of the local iteration procedure is to find $\{\nu_{\alpha(n+1)}\}, \{\widetilde{\nu}_{\alpha(n+1)}\}$, and $\dot{f}_{\eta(n+1)}$ which, in turn, allow to determine $\boldsymbol{F}_{\mathrm{E}(n+1)}$ and $\boldsymbol{F}_{\mathrm{I}(n+1)}$ for a given deformation $\boldsymbol{F}_{(n+1)}$. The inelastic velocity gradient part $\boldsymbol{L}_{\mathrm{I}} = \dot{\boldsymbol{F}}_{\mathrm{I}} \cdot \boldsymbol{F}_{\mathrm{I}}^{-1}$ is discretized in time using the fully implicit time integration scheme (Euler-backward). Due to the impact of twinning on the lattice configuration, this results in the following incremental relation

$$\boldsymbol{F}_{\mathrm{I}(n+1)} = \begin{cases} \mathrm{uni}\left(\boldsymbol{I} + \Delta t \eta_0 \dot{f}_{\eta(n+1)} \left[\boldsymbol{s}_\eta \otimes \boldsymbol{n}_\eta\right] + \Delta t \sum_\alpha \nu_{\alpha(n+1)} \left[\boldsymbol{s}_\alpha \otimes \boldsymbol{n}_\alpha\right]\right) \cdot \boldsymbol{F}_{\mathrm{I}(n)} & \text{for } f_{\eta(n+1)} < 1, \\ \mathrm{uni}\left(\boldsymbol{I} + \Delta t \sum_\alpha \widetilde{\nu}_{\alpha(n+1)} \left[\widetilde{\boldsymbol{s}}_\alpha \otimes \widetilde{\boldsymbol{n}}_\alpha\right]\right) \cdot \boldsymbol{F}_{\mathrm{I}(n)} & \text{for } f_{\eta(n+1)} = 1, \end{cases} \tag{A.1}$$

with the time increment $\Delta t = t_{(n+1)} - t_{(n)}$ defining the time interval $[t_{(n+1)}, t_{(n)}]$ of consideration. Here, $\dot{f}_{\eta(n+1)}$ and $\nu_{\alpha(n+1)}$ or respectively $\widetilde{\nu}_{\alpha(n+1)}$ are the converged quantities from the local iteration procedure sketched in Table A.1, respectively Table A.2, depending on the actual lattice configuration. In either case, the iteration procedure requires the computation of the elastic trial $\boldsymbol{F}^{\mathrm{tr}}_{\mathrm{E}(n+1)} = \boldsymbol{F}_{(n+1)} \cdot \boldsymbol{F}^{-1}_{\mathrm{I}(n)}$. The converged values are eventually used to compute the local balance of momentum, the governing equations for the edge and screw GND density, and the governing equation for the twin volume fraction gradient. Further implementation details with respect to higher-order gradient crystal plasticity is presented in 5.3.

Table A.1: Algorithmic procedure of the coupled slip/twinning problem.

if $f_{\eta(n)} < 1$ **then**

1. Initialize

$\nu_{\alpha(k+1)} = \nu_{\alpha(n)}$, $\dot{f}_{\eta(k+1)} = \dot{f}_{\eta(n)}$

2. Find ν_α and f_η

while $|\boldsymbol{R}_{\alpha\eta}| < tol$ **do**

2.1. Compute stress tensor

$\boldsymbol{F}_{\mathrm{I}(k+1)} = \mathrm{uni}\left(\boldsymbol{I} + \Delta t \eta_0 \dot{f}_{\eta(k+1)} [\boldsymbol{s}_\eta \otimes \boldsymbol{n}_\eta] + \Delta t \sum_\alpha \nu_{\alpha(k+1)} [\boldsymbol{s}_\alpha \otimes \boldsymbol{n}_\alpha]\right) \cdot \boldsymbol{F}_{\mathrm{I}(n)}$

$\boldsymbol{F}_{\mathrm{E}(k+1)} = \boldsymbol{F}_{\mathrm{E}}^{\mathrm{tr}} \cdot \boldsymbol{F}_{\mathrm{I}(n)} \cdot \boldsymbol{F}_{\mathrm{I}(k+1)}^{-1}$, $\boldsymbol{C}_{\mathrm{E}(k+1)} = \boldsymbol{F}_{\mathrm{E}(k+1)}^{\mathrm{T}} \cdot \boldsymbol{F}_{\mathrm{E}(k+1)}$

$\boldsymbol{S}_{\mathrm{E}(k+1)} = \partial \hat{\psi}_{(k+1)}(\boldsymbol{C}_{\mathrm{E}}, \boldsymbol{A}_{\mathrm{i}}) / \partial \boldsymbol{C}_{\mathrm{E}(k+1)}$

2.2. Compute slip residuum vector

for $\alpha \in n_\alpha$ **do**

$\pi_{\alpha(k+1)} = \left[\boldsymbol{C}_{\mathrm{E}(k+1)} \cdot \boldsymbol{S}_{\mathrm{E}(k+1)}\right] : [\boldsymbol{s}_\alpha \otimes \boldsymbol{n}_\alpha] + \mathrm{Div_i}(\boldsymbol{\xi}_{\alpha(n+1)})$

$R_\alpha = \nu_{\alpha(k+1)} - \nu_0 \left[\dfrac{|\pi_{\alpha(k+1)}|}{\tau_\alpha^{\mathrm{y}} + \tau_{\alpha(k+1)}^{\mathrm{h}} + \tau_{\alpha(k+1)}^{\mathrm{tw}\to\mathrm{sl}}}\right]^m \mathrm{sgn}\left(\pi_{\alpha(k+1)}\right)$

end

2.3 Compute twin residuum vector

$\pi_{\eta(k+1)} = \left[\boldsymbol{C}_{\mathrm{E}(k+1)} \cdot \boldsymbol{S}_{\mathrm{E}(k+1)}\right] : [\boldsymbol{s}_\eta \otimes \boldsymbol{n}_\eta] + \mathrm{Div_i}(\boldsymbol{\xi}_{\eta(n+1)})$

$R_\eta = \dot{f}_{\eta(k+1)} - \dfrac{\nu_0}{\eta_0} \left[\dfrac{\langle \pi_{\alpha(k+1)} \rangle}{\tau_\eta^{\mathrm{y}} + \tau_{\eta(k+1)}^{\mathrm{int}} + \tau_{\alpha(k+1)}^{\mathrm{sl}\to\mathrm{tw}}}\right]^m$

2.4 Compute tangent contributions

$K_{\alpha\beta} = \dfrac{\partial R_\alpha}{\partial \nu_\beta}$, $K_{\alpha\eta} = \dfrac{\partial R_\alpha}{\partial \dot{f}_\eta}$, $K_{\eta\beta} = \dfrac{\partial R_\eta}{\partial \nu_\beta}$, $K_{\eta\eta} = \dfrac{\partial R_\eta}{\partial \dot{f}_\eta}$

2.5 Assembly

$\boldsymbol{R}_{\alpha\eta} = \begin{bmatrix} \boldsymbol{R}_\alpha \\ R_\eta \end{bmatrix}$, $\boldsymbol{K}_{\alpha\eta} = \begin{bmatrix} \boldsymbol{K}_{\alpha\beta} & \boldsymbol{K}_{\alpha\eta} \\ \boldsymbol{K}_{\eta\beta} & \boldsymbol{K}_{\eta\eta} \end{bmatrix}$

2.6 Update

$\nu_{\alpha(k+1)} \to \nu_{\alpha(k)}$, $\dot{f}_{\eta(k+1)} \to \dot{f}_{\eta(k)}$

$\begin{bmatrix} \boldsymbol{\nu}_{(k+1)} \\ \dot{f}_{\eta(k+1)} \end{bmatrix} = \begin{bmatrix} \boldsymbol{\nu}_{(k)} \\ \dot{f}_{\eta(k)} \end{bmatrix} - \boldsymbol{K}_{\alpha\eta}^{-1} \cdot \boldsymbol{R}_{\alpha\eta}$

end

3. Check for completion of the twinning process

if $f_{\eta(k+1)} > 1$ **then**

3.1 Apply constraint for twinning shear magnitude

$f_{\eta(k+1)} = 1$, $\dot{f}_{\eta(k+1)} = \dfrac{1 - f_{\eta(n)}}{\Delta t}$

3.2 Recompute $\boldsymbol{F}_{\mathrm{I}(k+1)}$

end

4. Transfer to global level

$\nu_{\alpha(k+1)} \to \nu_{\alpha(n+1)}$, $\dot{f}_{\eta(k+1)} \to \dot{f}_{\eta(n+1)}$, $\boldsymbol{F}_{\mathrm{I}(k+1)} \to \boldsymbol{F}_{\mathrm{I}(n+1)}$

end

Table A.2: Algorithmic procedure after lattice reorientation due to twinning.

if $f_{\eta(n)} = 1$ **then**

1. Initialize

$\widetilde{\nu}_{\alpha(k+1)} = \widetilde{\nu}_{\alpha(n)}$

2. Find $\widetilde{\nu}_{\alpha}$

while $|\boldsymbol{R}_{\alpha\eta}| < tol$ **do**

2.1. Compute stress tensor

$\boldsymbol{F}_{\mathrm{I}(n+1)} = \mathrm{uni}\left(\boldsymbol{I} + \Delta t \sum_{\alpha} \widetilde{\nu}_{\alpha(n+1)} \left[\widetilde{\boldsymbol{s}}_{\alpha} \otimes \widetilde{\boldsymbol{n}}_{\alpha}\right]\right) \cdot \boldsymbol{F}_{\mathrm{I}(n)}$

$\boldsymbol{F}_{\mathrm{E}(k+1)} = \boldsymbol{F}_{\mathrm{E}}^{\mathrm{tr}} \cdot \boldsymbol{F}_{\mathrm{I}(n)} \cdot \boldsymbol{F}_{\mathrm{I}(k+1)}^{-1}$, $\boldsymbol{C}_{\mathrm{E}(k+1)} = \boldsymbol{F}_{\mathrm{E}(k+1)}^{\mathrm{T}} \cdot \boldsymbol{F}_{\mathrm{E}(k+1)}$

$\boldsymbol{S}_{\mathrm{E}(n+1)}^{\mathrm{tr}} = \partial \hat{\psi}_{(n+1)}(\boldsymbol{C}_{\mathrm{E}}, \widetilde{\boldsymbol{A}}_{\mathrm{i}}) / \partial \boldsymbol{C}_{\mathrm{E}(n+1)}^{\mathrm{tr}}$

2.2 Compute slip residuum vector

for $\alpha \in n_{\alpha}$ **do**

$\widetilde{\pi}_{\alpha(k+1)} = \left[\boldsymbol{C}_{\mathrm{E}(k+1)} \cdot \boldsymbol{S}_{\mathrm{E}(k+1)}\right] : \left[\widetilde{\boldsymbol{s}}_{\alpha} \otimes \widetilde{\boldsymbol{n}}_{\alpha}\right] + \mathrm{Div}_{\mathrm{i}}(\widetilde{\boldsymbol{\xi}}_{\alpha(n+1)})$

$R_{\alpha} = \widetilde{\nu}_{\alpha(k+1)} - \nu_0 \left[\frac{|\widetilde{\pi}_{\alpha(k+1)}|}{\tau_{\alpha}^{\mathrm{y}} + \widetilde{\tau}_{\alpha(k+1)}^{\mathrm{h}}}\right]^{m} \mathrm{sgn}\left(\widetilde{\pi}_{\alpha(k+1)}\right)$

end

2.3 Compute tangent contributions

$K_{\alpha\beta} = \dfrac{\partial R_{\alpha}}{\partial \widetilde{\nu}_{\beta}}$

3.4 Update

$\widetilde{\nu}_{\alpha(k+1)} \to \widetilde{\nu}_{\alpha(k)}$

$\widetilde{\boldsymbol{\nu}}_{(k+1)} = \widetilde{\boldsymbol{\nu}}_{(k)} - \boldsymbol{K}_{\alpha\eta}^{-1} \cdot \boldsymbol{R}_{\alpha\eta}$

end

3. Transfer to global level

$\widetilde{\nu}_{\alpha(k+1)} \to \widetilde{\nu}_{\alpha(n+1)}$, $\dot{f}_{\eta(n+1)} = 0$, $\boldsymbol{F}_{\mathrm{I}(k+1)} \to \boldsymbol{F}_{\mathrm{I}(n+1)}$

end

Bibliography

[1] Acharya, A. Bassani, J. L. (2000). Lattice incompatibility and a gradient theory of crystal plasticity. *Philosophical Magazine*, 48(8):1565–1595.

[2] Akhtar, A. and Teghtsoonian, E. (1969). Solid solution strengthening of magnesium single crystals - I alloying behaviour in basal slip. *Acta Metallurgica*, 17(11):1339–1349.

[3] Altenbach, H., Matsuda, T., and Okumura, D. (2015). *Creep Damage Mechanics to Homogenization Methods: A Liber Amicorum to Celebrate the Birthday of Nobutada Ohno*, chapter - Strain Gradient Plasticity: A Variety of Treatments and Related Fundamental Issues, Kuroda, M., pages 199–218. Springer.

[4] Arsenlis, A. and Parks, D. M. (1999). Crystallographic aspects of geometrically-necessary and statistically-stored dislocation density. *Acta Materialia*, 47(5):1597–1611.

[5] Arsenlis, A. and Parks, D. M. (2002). Modeling the evolution of crystallographic dislocation density in crystal plasticity. *Journal of the Mechanics and Physics of Solids*, 50(9):1979–2009.

[6] Arzt, E. (1998). Size effects in materials due to microstructural and dimensional constraints: a comparative review. *Acta Materialia*, 46(16):5611–5626.

[7] Asaro, R. J. (1983a). Crystal plasticity. *Journal of Applied Mechanics*, 50(4b):921–934.

[8] Asaro, R. J. (1983b). Micromechanics of crystals and polycrystals. *Advances in Applied Mechanics*, 23:1–115.

[9] Ashby, M. F. (1970). The deformation of plastically non-homogeneous materials. *Philosophical Magazine*, 21(170):399–424.

[10] Atkinson, M. (1995). Further analysis of the size effect in indentation hardness tests of some metals. *Journal of Materials Research*, 10(11):2908–2915.

[11] Avedesian, M. M. and Baker, H. (1999). *ASM specialty handbook: magnesium and magnesium alloys*. ASM international.

[12] Balint, D., Deshpande, V. S., Needleman, A., and van der Giessen, E. (2006). Size effects in uniaxial deformation of single and polycrystals: A discrete dislocation plasticity analysis. *Modelling and Simulation in Materials Science and Engineering*, 14(3):409.

[13] Bardella, L., Segurado, J., Panteghini, A., and Llorca, J. (2013). Latent hardening size effect in small-scale plasticity. *Modelling and Simulation in Materials Science and Engineering*, 21(5):055009.

[14] Bargmann, S., Ekh, M., Runesson, K., and Svendsen, B. (2010). Modeling of polycrystals with gradient crystal plasticity: A comparison of strategies. *Philosophical Magazine*, 90(10):1263–1288.

[15] Bargmann, S., Reddy, D., and Klusemann, B. (2014). A computational study of a model of single-crystal strain-gradient viscoplasticity with an interactive hardening relation. *International Journal of Solids and Structures*, 51(15):2754–2764.

[16] Bargmann, S., Soyarslan, C., Husser, E., and Konchakova, N. (2016). Materials based design of structures: Computational modeling of the mechanical behavior of gold-polymer nanocomposites. *Mechanics of Materials*, 94:53–65.

[17] Bargmann, S., Svendsen, B., and Ekh, M. (2011). An extended crystal plasticity model for latent hardening in polycrystals. *Computational Mechanics*, 48(6):631–645.

[18] Barnett, M. R. (2007). Twinning and the ductility of magnesium alloys: Part I. "Tension" twins. *Materials Science and Engineering: A*, 464(1):1–7.

[19] Barrett, C. D., El Kadiri, H., and Tschopp, M. A. (2012). Breakdown of the Schmid law in homogeneous and heterogeneous nucleation events of slip and twinning in magnesium. *Journal of the Mechanics and Physics of Solids*, 60(12):2084–2099.

[20] Basinski, Z. S. and Basinski, S. (1964). Dislocation distributions in deformed copper single crystals. *Philosophical Magazine*, 9(97):51–80.

[21] Basinski, Z. S., Korbel, A. S., and Basinski, S. J. (1980). The temperature dependence of the saturation stress and dislocation substructure in fatigued copper single crystals. *Acta Metallurgica*, 28(2):191–207.

[22] Bayerschen, E. and Böhlke, T. (2016). Power-law defect energy in a single-crystal gradient plasticity framework: a computational study. *Computational Mechanics*, 58:13–27.

[23] Bayerschen, E., McBride, A., Reddy, B., and Böhlke, T. (2016). Review on slip transmission criteria in experiments and crystal plasticity models. *Journal of Materials Science*, 51(5):2243–2258.

[24] Bayley, C. J., Brekelmans, W. A. M., and Geers, M. G. D. (2006). A comparison of dislocation induced back stress formulations in strain gradient crystal plasticity. *International Journal of Solids and Structures*, 43(24):7268–7286.

[25] Bayley, C. J., Brekelmans, W. A. M., and Geers, M. G. D. (2007). A three-dimensional dislocation field crystal plasticity approach applied to miniaturized structures. *Philosophical Magazine*, 87(8-9):1361–1378.

[26] Begley, M. R. and Hutchinson, J. W. (1998). The mechanics of size-dependent indentation. *Journal of the Mechanics and Physics of Solids*, 46(10):2049–2068.

[27] Bei, H., Shim, S., Pharr, G. M., and George, E. P. (2008). Effects of pre-strain on the compressive stress-strain response of Mo-alloy single-crystal micropillars. *Acta Materialia*, 56(17):4762–4770.

[28] Bertram, A. (2005). *Elasticity and plasticity of large deformations*. Springer-Verlag.

[29] Biener, J., Hodge, A. M., and Hamza, A. V. (2005). Microscopic failure behavior of nanoporous gold. *Applied Physics Letters*, 87(12):121908.

[30] Bilby, B. A. and Crocker, A. G. (1965). The theory of the crystallography of deformation twinning. *Proceedings of the Royal Society of London A: Mathematical, Physical and Engineering Sciences*, 288(1413):240–255.

[31] Bilby, B. A., Gardner, L. R. T., and Smith, E. (1958). The relation between dislocation density and stress. *Acta Metallurgica*, 6(1):29–33.

[32] Bilby, B. A., Gardner, L. R. T., and Stroh, A. N. (1957). Continuous distributions of dislocations and the theory of plasticity. In *Proceedings of the Ninth International Congress of Applied Mechanics*, volume 8, pages 35–44.

[33] Bočan, J., Tsurekawa, S., and Jäger, A. (2017). Fabrication and in situ compression testing of Mg micropillars with a nontrivial cross section: Influence of micropillar geometry on mechanical properties. *Materials Science and Engineering A*, 58(19):6230–6242.

[34] Bravais, A. (1850). Mémoire sur les systèmes formés par des points distribués régulièrement sur un plan ou dans l'espace. *Journal de l'Ecole Polytechnique*, 19:1–128.

[35] Brinckmann, S., Siegmund, T., and Huang, Y. (2006). A dislocation density based strain gradient model. *International Journal of Plasticity*, 22(9):1784–1797.

[36] Brown, S. B., Kim, K. H., and Anand, L. (1989). An internal variable constitutive model for hot working of metals. *International Journal of Plasticity*, 5(2):95–130.

[37] Buckley, D. (1968). Influence of surface films on friction and deformation of single-crystal and polycrystalline gold. Technical report, NASA technical note NASA TN D-4875, Lewis Research Center Cleveland, Ohio.

[38] Budiman, A. S. (2015). *Probing Crystal Plasticity at the Nanoscales*. Springer, Singapore.

[39] Burgers, J. M. (1995). Physics.- Some considerations on the fields of stress connected with dislocations in a regular crystal lattice. I. In *Selected Papers of JM Burgers*, pages 335–389. Springer, Dordrecht.

[40] Byer, C. M., Li, B., Caoa, B., and Ramesha, K. T. (2010). Microcompression of single-crystal magnesium. *Scripta Materialia*, 62(8):536–539.

[41] Byer, C. M. and Ramesha, K. T. (2013). Effects of the initial dislocation density on size effects in single-crystal magnesium. *Acta Materialia*, 61(10):3808–3818.

[42] Cermelli, P. and Gurtin, M. E. (2001). On the characterization of geometrically necessary dislocations in finite plasticity. *Journal of the Mechanics and Physics of Solids*, 49(7):1539–1568.

[43] Chaboche, J. L. (2008). A review of some plasticity and viscoplasticity constitutive theories. *International Journal of Plasticity*, 24(10):1642–1693.

[44] Chadwick, P. (2012). *Continuum mechanics: concise theory and problems*. Courier Corporation.

[45] Chang, Y. and Kochmann, D. M. (2015). A variational constitutive model for slip-twinning interactions in hcp metals: Application to single-and polycrystalline magnesium. *International Journal of Plasticity*, 73:39–61.

[46] Chapuis, A. and Driver, J. H. (2011). Temperature dependency of slip and twinning in plane strain compressed magnesium single crystals. *Acta Materialia*, 59(5):1986–1994.

[47] Cheng, J. and Ghosh, S. (2015). A crystal plasticity FE model for deformation with twin nucleation in magnesium alloys. *International Journal of Plasticity*, 67:148–170.

[48] Cheng, J. and Ghosh, S. (2017). Crystal plasticity finite element modeling of discrete twin evolution in polycrystalline magnesium. *Journal of the Mechanics and Physics of Solids*, 99:512–538.

[49] Choi, I. S., Uchic, M. D., Parthasarathy, T. A., and Dimiduk, D. M. (2007). Numerical study on microcompression tests of anisotropic single crystals. *Scripta Materialia*, 57(9):849–852.

[50] Christian, J. W. (1983). Some surprising features of the plastic deformation of body-centered cubic metals and alloys. *Metallurgical Transactions A*, 14(7):1237–1256.

[51] Christian, J. W. and Mahajan, S. (1995). Deformation twinning. *Progress in Materials Science*, 39(1):1–157.

[52] Clark, D., Dickinson, T., and Mair, W. N. (1961). On the oxidation of gold. *The Journal of Physical Chemistry*, 65(8):1470.

[53] Clayton, J. D. (2009). A continuum description of nonlinear elasticity, slip and twinning, with application to sapphire. *In Proceedings of the Royal Society of London A: Mathematical, Physical and Engineering Sciences*, 465(2101):307–334.

[54] Clayton, J. D. (2015). *Differential geometry and kinematics of continua*. World Scientific.

[55] Clayton, J. D., Bammann, D. J., and McDowell, D. L. (2004a). Anholonomic configuration spaces and metric tensors in finite elastoplasticity. *International Journal of Non-Linear Mechanics*, 39(6):1039–1049.

[56] Clayton, J. D. and Knap, J. (2011). A phase field model of deformation twinning: nonlinear theory and numerical simulations. *Physica D: Nonlinear Phenomena*, 240(9):841–858.

[57] Clayton, J. D., McDowell, D. L., and Bammann, D. J. (2004b). A multiscale gradient theory for single crystalline elastoviscoplasticity. *International Journal of Engineering Science*, 42(5):427–457.

[58] Cleveringa, H. H. M., Van der Giessen, E., and Needleman, A. (1999). A discrete dislocation analysis of bending. *International Journal of Plasticity*, 15(8):837–868.

[59] Conti, S. and Ortiz, M. (2005). Dislocation microstructures and the effective behavior of single crystals. *Archive for Rational Mechanics and Analysis*, 176(1):103–147.

[60] Csikor, F. F., Motz, C., Weygand, D., Zaiser, M., and Zapperi, S. (2007). Dislocation avalanches, strain bursts, and the problem of plastic forming at the micrometer scale. *Science*, 318(5848):251–254.

[61] Cui, Y. N., Lin, P., Liu, Z. L., and Zhuang, Z. (2014). Theoretical and numerical investigations of single arm dislocation source controlled plastic flow in FCC micropillars. *International Journal of Plasticity*, 55:279–292.

[62] Cuitino, A. M. and Ortiz, M. (1993). Computational modelling of single crystals. *Modelling and Simulation in Materials Science and Engineering*, 1(3):225.

[63] De Graef, M. (2003). *Introduction to conventional transmission electron microscopy*. Cambridge University Press.

[64] De Graef, M. and McHenry, M. E. (2007). *Structure of materials: an introduction to crystallography, diffraction and symmetry*. Cambridge University Press.

[65] Demir, E. and Raabe, D. (2010). Mechanical and microstructural single-crystal bauschinger effects: Observation of reversible plasticity in copper during bending. *Acta Materialia*, 58(18):6055–6063.

[66] Demir, E., Raabe, D., and Roters, F. (2010). The mechanical size effect as a mean-field breakdown phenomenon: Example of microscale single crystal beam bending. *Acta Materialia*, 58(5):1876–1886.

[67] Dimiduk, D. M., Uchic, M. D., and Parthasarathy, T. A. (2005). Size-affected single-slip behavior of pure nickel microcrystals. *Acta Materialia*, 15(53):4065–4077.

[68] Dorfmann, L. and Ogden, R., editors (2015). *Nonlinear mechanics of soft fibrous materials*. Springer.

[69] Ekh, M., Bargmann, S., and Grymer, M. (2011). Influence of grain boundary conditions on modeling of size-dependence in polycrystals. *Acta Mechanica*, 218(1-2):103–113.

[70] Ekh, M., Grymer, M., Runesson, K., and Svedberg, T. (2007). Gradient crystal plasticity as part of the computational modelling of polycrystals. *International Journal for Numerical Methods in Engineering*, 72(2):197–220.

[71] El-Awady, J. A. (2015). Unravelling the physics of size-dependent dislocation-mediated plasticity. *Nature Communications*, 6.

[72] El-Awady, J. A., Uchic, M. D., Shade, P. A., Kim, S. L., Rao, S. I., Dimiduk, D. M., and Woodward, C. (2013). Pre-straining effects on the power-law scaling of size-dependent strengthening in Ni single crystals. *Scripta Materialia*, 68(3):207–210.

[73] Epstein, M. (2010). *The Geometrical Language of Continuum Mechanics*. Cambridge University Press, New York.

[74] Ertürk, I., Van Dommelen, J. A. W., and Geers, M. G. D. (2002). Energetic dislocation interactions and thermodynamical aspects of strain gradient crystal plasticity theories. *Journal of the Mechanics and Physics of Solids*, 57(11):1801–1814.

[75] Essmann, U. and Mughrabi, H. (1979). Annihilation of dislocations during tensile and cyclic deformation and limits of dislocation densities. *Philosophical Magazine A*, 40(6):731–756.

[76] Evans, A. G. and Hutchinson, J. W. (2009). A critical assessment of theories of strain gradient plasticity. *Acta Materialia*, 57(5):1675–1688.

[77] Evers, L. P., Brekelmans, W. A. M., and Geers, M. G. D. (2004a). Non-local crystal plasticity model with intrinsic SSD and GND effects. *Journal of the Mechanics and Physics of Solids*, 52(10):2379–2401.

[78] Evers, L. P., Brekelmans, W. A. M., and Geers, M. G. D. (2004b). Scale dependent crystal plasticity framework with dislocation density and grain boundary effects. *International Journal of Solids and Structures*, 41(18):5209–5230.

[79] Fleck, N. A. and Hutchinson, J. W. (1997). Strain gradient plasticity. *Advances in Applied Mechanics*, 33:296–361.

[80] Fleck, N. A., Muller, G. M., Ashby, M. F., and Hutchinson, J. W. (1994). Strain gradient plasticity: theory and experiment. *Acta Metallurgica et Materialia*, 42(2):475–487.

[81] Florando, J. N. and Nix, W. D. (2005). A microbeam bending method for studying stress-strain relations for metal thin films on silicon substrates. *Journal of the Mechanics and Physics of Solids*, 53(3):619–638.

[82] Gao, H., Huang, Y., Nix, W. D., and Hutchinson, J. W. (1999). Mechanism-based strain gradient plasticity - I. Theory. *Journal of the Mechanics and Physics of Solids*, 47(6):1239–1263.

[83] Gilman, J. J. (2004). Oxide surface films on metal crystals. *Science*, 306(5699):1134–1135.

[84] Gottschalk, D., McBride, A., Reddy, B. D., Javili, A., and Wriggers, P. (2016). Computational and theoretical aspects of a grain-boundary model that accounts for grain misorientation and grain-boundary orientation. *Computational Materials Science*, 111:443–459.

[85] Graff, S., Brocks, W., and Steglich, D. (2007). Yielding of magnesium: from single crystal to polycrystalline aggregates. *International Journal of Plasticity*, 23(12):1957–1978.

[86] Green, A. E. and Zerna, W. (1968). *Theoretical Elasticity*. Oxford University Press, Oxford.

[87] Greenfield, I. G. and Wilsdorf, H. G. F. (1961). Effect of neutron irradiation on the plastic deformation of copper single crystals. *Journal of Applied Physics*, 32(5):827–839.

[88] Greer, J. R. and De Hosson, J. T. M. (2011). Plasticity in small-sized metallic systems: Intrinsic versus extrinsic size effect. *Progress in Materials Science*, 56(6):654–724.

[89] Greer, J. R., Oliver, W. C., and Nix, W. D. (2005). Size dependence of mechanical properties of gold at the micron scale in the absence of strain gradients. *Acta Materialia*, 53(6):1821–1830.

[90] Grosskreutz, J. C. (1967). The effect of oxide films on dislocation-surface interactions in aluminum. *Surface Science*, 8:173–190.

[91] Grosskreutz, J. C. and Benson, D. K. (1968). *The Effects of the Surface on the Mechanical Properties of Metals*, pages 61–94. Springer US, Boston, MA.

[92] Gurtin, M. E. (1996). Generalized Ginzburg-Landau and Cahn-Hilliard equations based on a microforce balance. *Physica D: Nonlinear Phenomena*, 92(3-4):178–192.

[93] Gurtin, M. E. (2000). On the plasticity of single crystals: free energy, microforces, plastic-strain gradients. *Journal of the Mechanics and Physics of Solids*, 48(5):989–1036.

[94] Gurtin, M. E. (2002). A gradient theory of single-crystal viscoplasticity that accounts for geometrically necessary dislocations. *Journal of the Mechanics and Physics of Solids*, 50(1):5–32.

[95] Gurtin, M. E. (2008). A finite-deformation, gradient theory of single-crystal plasticity with free energy dependent on densities of geometrically necessary dislocations. *International Journal of Plasticity*, 24(4):702–725.

[96] Gurtin, M. E. and Anand, L. (2005). A theory of strain-gradient plasticity for isotropic, plastically irrotational materials. Part II: Finite deformations. *International Journal of Plasticity*, 21(12):2297–2318.

[97] Gurtin, M. E. and Anand, L. (2006). A gradient theory for single-crystal plasticity. *Modelling and Simulation in Materials Science and Engineering*, 15(1):263.

[98] Gurtin, M. E. and Needleman, A. (2005). Boundary conditions in small-deformation, single-crystal plasticity that account for the Burgers vector. *Journal of the Mechanics and Physics of Solids*, 53(1):1–31.

[99] Gurtin, M. E. and Reddy, B. D. (2014). Gradient single-crystal plasticity within a Mises-Hill framework based on a new formulation of self-and latent-hardening. *Journal of the Mechanics and Physics of Solids*, 68:134–160.

[100] Hahn, T. (1996). *International Tables for Crystallography: Volume A - Space Group Symmetry*. International Union Of Crystallography, Kluwer Academic Publishers, Dordrecht.

[101] Hakamada, M. and Mabuchi, M. (2007). Mechanical strength of nanoporous gold fabricated by dealloying. *Scripta Materialia*, 56(11):1003–1006.

[102] Hall, E. Q. (1951). The deformation and aging of mild steel: III discussion of results. *Proceedings of the Physical Society of London*, 64(Section B):747–753.

[103] Hildebrand, F. and Miehe, C. (2013). A phase field model for the formation and evolution of martensitic laminate microstructure at finite strains. *Philosophical Magazine*, 92(34):4250–4290.

[104] Holzapfel, G. A. (2008). *Nonlinear Solid Mechanics*. John Wiley & Sons, Chichester.

[105] Huang, Y., Zhang, F., Hwang, K. C., Nix, W. D., Pharr, G. M., and Feng, G. (2006). A model of size effects in nano-indentation. *Journal of the Mechanics and Physics of Solids*, 54(8):1668–1686.

[106] Hull, D. and Bacon, D. J. (2001). *Introduction to dislocations*. Butterworth-Heinemann.

[107] Hurtado, D. E. and Ortiz, M. (2012). Surface effects and the size-dependent hardening and strengthening of nickel micropillars. *Journal of the Mechanics and Physics of Solids*, 60(8):1432–1446.

[108] Hussein, A. M., Rao, S. I., Uchic, M. D., Dimiduk, D. M., and El-Awady, J. A. (2015). Microstructurally based cross-slip mechanisms and their effects on dislocation microstructure evolution in fcc crystals. *Acta Materialia*, 85:180–190.

[109] Husser, E. and Bargmann, S. (2017). The role of geometrically necessary dislocations in cantilever beam bending experiments of single crystals. *Materials*, 10(3):289.

[110] Husser, E. and Bargmann, S. (2019). Modeling twinning-induced lattice reorientation and slip-in-twin deformation. *Journal of the Mechanics and Physics of Solids*, 122:315–339.

[111] Husser, E., Lilleodden, E., and Bargmann, S. (2014). Computational modeling of intrinsically induced strain gradients during compression of c-axis-oriented magnesium single crystal. *Acta Materialia*, 71:206–219.

[112] Husser, E., Soyarslan, C., and Bargmann, S. (2017). Size affected dislocation activity in crystals: Advanced surface and grain boundary conditions. *Extreme Mechanics Letters*, 13:36–41.

[113] Hutchinson, J. W. (1976). Bounds and self-consistent estimates for creep of polycrystalline materials. *Proceedings of the Royal Society of London A: Mathematical, Physical and Engineering Sciences*, 348(1652):101–127.

[114] Hütsch, J. and Lilleodden, E. T. (2014). The influence of focused-ion beam preparation technique on microcompression investigations: Lathe vs. annular milling. *Scripta Materialia*, 77:49–51.

[115] Idesman, A. V., Levitas, V. I., and Stein, E. (1999). Elastoplastic materials with martensitic phase transition and twinning at finite strains: numerical solution with the finite element method. *Computer Methods in Applied Mechanics and Engineering*, 173(1):71–98.

[116] Jennings, A. T., Gross, C., Greer, F., Aitken, Z. H., Lee, S. W., Weinberger, C. R., and Greer, J. R. (2012). Higher compressive strengths and the Bauschinger effect in conformally passivated copper nanopillars. *Acta Materialia*, 60(8):3444–3455.

[117] Jette, E. R. and Foote, F. (1935). Precision determination of lattice constants. *The Journal of Chemical Physics*, 3(10):605–616.

[118] Jin, H.-J., Kurmanaeva, L., Schmauch, J., Rösner, R., Ivanisenko, Y., and Weissmüller, J. (2009). Deforming nanoporous metal: Role of lattice coherency. *Acta Materialia*, 57(9):2665 – 2672.

[119] Kalidindi, S. R. (1998). Incorporation of deformation twinning in crystal plasticity models. *Journal of the Mechanics and Physics of Solids*, 46(2):267–290.

[120] Karlsson, N. (1951). An x-ray study of the phases in the copper-titanium system. *Journal of the Institute of Metals*, 79:391–405.

[121] Keller, R. M., Baker, S. P., and Arzt, E. (1998). Effects of film thickness, grain size, and passivation. *Journal of Materials Research*, 13(5):1307–1317.

[122] Kelley, E. W. and Hosford, W. (1968). Plane-strain compression of magnesium and magnesium alloy crystals. *Transactions of the Metallurgical Society*, 242(1):5–13.

[123] Kertis, F., Snyder, J., Govada, L., Khurshid, S., Chayen, N., and Erlebacher, J. (2010). Structure/processing relationships in the fabrication of nanoporous gold. *The Journal of The Minerals*, 62(6):50–56.

[124] Kiener, D., Motz, C., and Dehm, G. (2008). Dislocation-induced crystal rotations in micro-compressed single crystal copper columns. *Journal of Materials Science*, 43(7):2503–2506.

[125] Kiener, D., Motz, C., Grosinger, W., Weygand, D., and Pippan, R. (2010). Cyclic response of copper single crystal micro-beams. *Scripta Materialia*, 63(5):500–503.

[126] Kiener, D., Motz, C., Rester, M., Jenko, M., and Dehm, G. (2007). FIB damage of Cu and possible consequences for miniaturized mechanical tests. *Materials Science and Engineering: A*, 459(1):262–272.

[127] Kiener, D., Motz, C., Schöberl, T., Jenko, M., and Dehm, G. (2006a). Determination of mechanical properties of copper at the micron scale. *Advanced Engineering Materials*, 11(8):1119–1125.

[128] Kiener, D., Pippan, R., Motz, C., and Kreuzer, H. (2006b). Microstructural evolution of the deformed volume beneath microindents in tungsten and copper. *Acta Materialia*, 54(10):2801–2811.

[129] Kim, G. S., Yi, S., Huang, Y., and Lilleodden, E. (2009). Twining and slip activity in magnesium <11-20> single crystal. *MRS Proceedings*, 1224:1224–FF05.

[130] Kirchlechner, C., Grosinger, W., Kapp, M. W., Imrich, P. J., Micha, J. S., Ulrich, O., Keckes, J., Dehm, G., and Motz, C. (2012). Investigation of reversible plasticity in a micron-sized, single crystalline copper bending beam by X-ray μLaue diffraction. *Philosophical Magazine A*, 92(25-27):3231–3242.

[131] Kirchlechner, C., Keckes, J., Motz, C., Grosinger, W., Kapp, M. W., Micha, J. S., Ulrich, O., and Dehm, G. (2011). Impact of instrumental constraints and imperfections on the dislocation structure in micron-sized Cu compression pillars. *Acta Materialia*, 59(14):5618–5626.

[132] Kitahara, T., Ando, S., Tsushida, M., Kitahara, H., and Tonda, H. (2007). Deformation behavior of magnesium single crystals in c-axis compression. *Key Engineering Materials*, 345:129–132.

[133] Kleemola, H. J. and Nieminen, M. A. (1974). On the strain-hardening parameters of metals. *Metallurgical Transactions*, 5(8):1863–1866.

[134] Klusemann, B., Fischer, G., Böhlke, T., and Svendsen, B. (2015). Thermomechanical characterization of Portevin-Le Chatelier bands in AlMg3 (AA5754) and modeling based on a modified Estrin-McCormick approach. *International Journal of Plasticity*, 67:192–216.

[135] Klusemann, B., Svendsen, B., and Bargmann, S. (2013). Analysis and comparison of two finite element algorithms for dislocation density based crystal plasticity. *GAMM-Mitteilungen*, 36(2):219–238.

[136] Knezevic, M., Levinson, A., Harris, R., Mishra, R. K., Doherty, R. D., and Kalidindi, S. R. (2010). Deformation twinning in AZ31: influence on strain hardening and texture evolution. *Acta Materialia*, 58(19):6230–6242.

[137] Kocks, U. F. (1970). The relation between polycrystal deformation and single-crystal deformation. *Metallurgical and Materials Transactions*, 1(5):1121–1143.

[138] Koike, J. (2005). Enhanced deformation mechanisms by anisotropic plasticity in polycrystalline Mg alloys at room temperature. *Metallurgical and Materials Transactions A*, 36(7):1689–1696.

[139] Kondo, K. (1964). On the analytical and physical foundations of the theory of dislocations and yielding by the differential geometry of continua. *International Journal of Engineering Science*, 2(3):219–251.

[140] Kouzeli, M. and Mortensen, A. (2002). Size dependent strengthening in particle reinforced aluminium. *Acta Materialia*, 50(1):39–51.

[141] Kraft, O., Gruber, P. A., Mönig, R., and Weygand, D. (2010). Plasticity in confined dimensions. *Annual Review of Materials Research*, 40:293–317.

[142] Kröner, E. (1960). Allgemeine Kontinuumstheorie der Versetzungen und Eigenspannungen. *Archive for Rational Mechanics and Analysis*, 4(1):273–334.

[143] Kröner, E. (1962). Dislocations and continuum mechanics. *Applied Mechanics Review*, 15(8):599–606.

[144] Kröner, E. (1963). On the physical reality of torque stresses in continuum mechanics. *International Journal of Engineering Science*, 1(2):261–278.

[145] Kröner, E. and Seeger, A. (1959). Nicht-lineare Elastizitatstheorie der Versetzungen und Eigenspannungen. *Applied Mechanics Review*, 3(2):97–119.

[146] Kubin, L. (2013). *Dislocations, mesoscale simulations and plastic flow*. Oxford University Press.

[147] Kubin, L. P., Canova, G., Condat, M., Devincre, B., Pontikis, V., and Bréchet, Y. (1992). Dislocation microstructures and plastic flow: a 3D simulation. *Solid State Phenomena*, 23-24:455–472.

[148] Kuhlmann-Wilsdorf, D. (1989). Theory of plastic deformation: properties of low energy dislocation structures. *Materials Science and Engineering: A*, 113:1–41.

[149] Kuhlmann-Wilsdorf, D. (1999). The theory of dislocation-based crystal plasticity. *Philosophical Magazine A*, 79(4):955–1008.

[150] Kumar, M. A., Kanjarla, A. K., Niezgoda, S. R., Lebensohn, R. A., and Tomé, C. N. (2015). Numerical study of the stress state of a deformation twin in magnesium. *Acta Materialia*, 84:349–358.

[151] Kuroda, M. (2011). On large-strain finite element solutions of higher-order gradient crystal plasticity. *International Journal of Solids and Structures*, 48(24):3382–3394.

[152] Kuroda, M. (2013). Higher-order gradient effects in micropillar compression. *Acta Materialia*, 61(7):2283–2297.

[153] Kuroda, M. and Tvergaard (2008). On the formulations of higher-order strain gradient crystal plasticity models. *Journal of the Mechanics and Physics of Solids*, 56(8):1591–1608.

[154] Lee, E. H. (1969). Elastic-plastic deformation at finite strains. *Journal of Applied Mechanics*, 36(1):1–6.

[155] Lee, E. H. and Liu, D. T. (1967). Finite-strain elastic-plastic theory with application to plane-wave analysis. *Journal of Applied Physics*, 38(1):19–27.

[156] Levkovitch, V. and Svendsen, B. (2006). On the large-deformation- and continuum-based formulation of models for extended crystal plasticity. *International Journal of Solids and Structures*, 43(24):7246–7267.

[157] Lilleodden, E. (2010). Microcompression study of Mg (0 0 0 1) single crystal. *Scripta Materialia*, 62(8):532–535.

[158] Liu, Y., Li, N., Kumar, M. A., Pathak, S., Wang, J., McCabe, R. J., Mara, N., and Tomé, C. N. (2017). Experimentally quantifying critical stresses associated with basal slip and twinning in magnesium using micropillars. *Acta Materialia*, 135:411–421.

[159] Lloyd, D. J. (1994). Particle reinforced aluminium and magnesium matrix composites. *International Materials Reviews*, 39(1):1–23.

[160] Long, T. R. and Smith, C. S. (1957). Single-crystal elastic constants of magnesium and magnesium alloys. *Acta Metallurgica*, 5(4):200–207.

[161] Lührs, L., Soyarslan, C., Markmann, J., Bargmann, S., and Weissmüller, J. (2016). Elastic and plastic Poisson's ratios of nanoporous gold. *Scripta Materialia*, 110:65–69.

[162] Ma, A. and Roters, F. (2004). A constitutive model for fcc single crystals based on dislocation densities and its application to uniaxial compression of aluminium single crystals. *Acta Materialia*, 52(12):3603–3612.

[163] Ma, Q. and Clarke, D. R. (1995). Size dependent hardness of silver single crystals. *Journal of Materials Research*, 10(4):853–863.

[164] Maaß, R., Van Petegem, S., Grolimund, D., Van Swygenhoven, H., Kiener, D., and Dehm, G. (2008). Crystal rotation in Cu single crystal micropillars: in situ Laue and electron backscatter diffraction. *Applied Physics Letters*, 92(7):071905.

[165] Maaß, R., Van Petegem, S., Van Swygenhoven, H., Derlet, P. M., Volkert, C. A., and Grolimund, D. (2007). Time-resolved Laue diffraction of deforming micropillars. *Physical Review Letters*, 99(14):145505.

[166] Mallmann, C., Simar, A., Ferrié, E., Fivel, M., and Lilleodden, E. T. (2017). Influence of Y2O3 nanoparticles on the twinning of single crystalline magnesium. *Scripta Materialia*, 138:79–82.

[167] Mandel, J. (1972). *Plasticité classique et viscoplasticité*. Course held at the Department of Mechanics of Solids, Sept.-Oct. 1971. Springer.

[168] Mandel, J. (1973). Equations constitutives et directeurs dans les milieux plastiques et viscoplastiques. *International Journal of Solids and Structures*, 9(6):725–740.

[169] Mandel, J. (1974). *Foundations of continuum thermodynamics*, chapter Thermodynamics and plasticity, pages 283–304. Macmillan Education UK.

[170] Marder, M. P. (2010). *Condensed Matter Physics*. Wiley, Chichester, New York.

[171] Martin, J., Doherty, R., and Cantor, B. (1997). *Stability of Microstructure in Metallic Systems*. Cambridge Solid State Science Series, Cambridge University Press.

[172] Mayer, J., Giannuzzi, L. A., Kamino, T., and Michael, J. (2007). TEM sample preparation and FIB-induced damage. *Mrs Bulletin*, 32(5):400–407.

[173] McBride, A. T., Gottschalk, D., Reddy, B. D., Wriggers, P., and Javili, A. (2016). Computational and theoretical aspects of a grain-boundary model at finite deformations. *Technische Mechanik*, 36(1-2):92–109.

[174] McElhaney, K. W., Vlassak, J. J., and Nix, W. D. (1998). Determination of indenter tip geometry and indentation contact area for depth-sensing indentation experiments. *Journal of Materials Research*, 13(05):1300–1306.

[175] Miehe, C. and Schröder, J. (2001). A comparative study of stress update algorithms for rate-independent and rate-dependent crystal plasticity. *International Journal for Numerical Methods in Engineering*, 50(2):273–298.

[176] Miller, W. H. (1839). *A Treatise on Crystallography*. Cambridge, Deighton.

[177] Mirkhani, H. and Joshi, S. P. (2014). Mechanism-based crystal plasticity modeling of twin boundary migration in nanotwinned face-centered-cubic metals. *Journal of the Mechanics and Physics of Solids*, 85(30):3553–3565.

[178] Miura, H., Yang, X., Sakai, T., Nogawa, H., Miura, S., Watanabe, Y., and Jonas, J. J. (2005). High temperature deformation and extended plasticity in Mg single crystals. *Philosophical Magazine*, 85(30):3553–3565.

[179] Motz, C., Schöberl, T., and Pippan, R. (2005). Mechanical properties of micro-sized copper bending beams machined by the focused ion beam technique. *Acta Materialia*, 53(15):4269–4279.

[180] Motz, C., Weygand, D., Senger, J., and Gumbsch, P. (2008). Micro-bending tests: A comparison between three-dimensional discrete dislocation dynamics simulations and experiments. *Acta Materialia*, 56(9):1942–1955.

[181] Ngô, B.-N. D., Stukowski, A., Mameka, N., Markmann, J., Albe, K., and Weissmüller, J. (2015). Anomalous compliance and early yielding of nanoporous gold. *Acta Materialia*, 93:144 – 155.

[182] Niordson, C. F. and Kysar, J. W. (2014). Computational strain gradient crystal plasticity. *Journal of the Mechanics and Physics of Solids*, 62:31–47.

[183] Nix, W. D. and Gao, H. (1998). Indentation size effects in crystalline materials: a law for strain gradient plasticity. *Journal of the Mechanics and Physics of Solids*, 46(3):411–425.

[184] Nix, W. D., Greer, J. R., Feng, G., and Lilleodden, E. T. (2007). Deformation at the nanometer and micrometer length scales: Effects of strain gradients and dislocation starvation. *Thin Solid Films*, 515(6):3152–3157.

[185] Noll, W. (1972). A new mathematical theory of simple materials. *Rational Mechanics and Analysis*, 48(1):1–50.

[186] Nye, J. F. (1953). Some geometrical relations in dislocated crystals. *Acta Metallurgica*, 1(2):153–162.

[187] Obara, T., Yoshinga, H., and Morozumi, S. (1973). $\{11\bar{2}2\}\langle 11\bar{2}3\rangle$ Slip system in magnesium. *Acta Metallurgica*, 21(7):845–853.

[188] Ogden, R. W. (1997). *Non-Linear Elastic Deformations*. Dover Publications, New York.

[189] Oh, S. H., Rentenberger, C., Im, J., Motz, C., Kiener, D., Karnthaler, H. P., and Dehm, G. (2011). Dislocation plasticity of Al film on polyimide investigated by cross-sectional in situ transmission electron microscopy straining. *Scripta Materialia*, 65(5):456–459.

[190] Ohashi, T. (1994). Numerical modelling of plastic multislip in metal crystals of fcc type. *Philosophical Magazine A*, 70(5):793–803.

[191] Okamoto, P. R. and Thomas, G. (1968). On the four-axis hexagonal reciprocal lattice and its use in the indexing of transmission electron diffraction patterns. *Physica Status Solidi (b)*, 25(1):81–91.

[192] Oliver, E. C., Daymond, M. R., and Withers, P. J. (2005). Neutron diffraction study of extruded magnesium during cyclic and elevated temperature loading. *Materials Science Forum. Trans Tech Publications*, 490:257–262.

[193] Orowan, E. (1934). Zur Kristallplastizität. III. *Zeitschrift für Physik*, 89(9-10):634–659.

[194] Ortiz, M., Repetto, E. A., and Stainier, L. (2000). A theory of subgrain dislocation structures. *Journal of the Mechanics and Physics of Solids*, 48(10):2077–2114.

[195] Özdemir, I. and Yalçinkaya (2014). Modeling of dislocation-grain boundary interactions in a strain gradient crystal plasticity framework. *Computational Mechanics*, 54(2):255–268.

[196] Öztop, M. S., Niordson, C. F., and Kysar, J. W. (2013). Length-scale effect due to periodic variation of geometrically necessary dislocation densities. *International Journal of Plasticity*, 41:189–201.

[197] Parthasarathy, T. A., Rao, S. I., Dimiduk, D. M., Uchic, M. D., and Trinkle, D. R. (2007). Contribution to size effect of yield strength from the stochastics of dislocation source lengths in finite samples. *Scripta Materialia*, 56(4):313–316.

[198] Peirce, D., Asaro, R. J., and Needleman, A. (1982). An analysis of nonuniform and localized deformation in ductile single crystals. *Acta Metallurgica*, 30(6):1087–1119.

[199] Peirce, D., Asaro, R. J., and Needleman, A. (1983). Material rate dependence and localized deformation in crystalline solids. *Acta Metallurgica*, 31(12):1951–1976.

[200] Peng, X. L. and Huang, G. Y. (2015). Modeling dislocation absorption by surfaces within the framework of strain gradient crystal plasticity. *International Journal of Solids and Structures*, 72:98–107.

[201] Peng, X. L., Husser, E., Huang, G. Y., and Bargmann, S. (2018). Modeling of surface effects in crystalline materials within the framework of gradient crystal plasticity. *Journal of the Mechanics and Physics of Solids*, 72:98–107.

[202] Perzyna, P. (1971). Thermodynamic theory of viscoplasticity. *Advances in applied mechanics*, 11:313–354.

[203] Petch, N. J. (1953). The cleavage strength of polycrystals. *Journal of the Iron and Steel Institute*, 174:25–28.

[204] Pharr, G. M., Herbert, E. G., and Gao, Y. (2010). The indentation size effect: A critical examination of experimental observations and mechanistic interpretations. *Annual Review of Materials Research*, 40:271–292.

[205] Prasad, K. E., Rajesh, K., and Ramamurty, U. (2014). Micropillar and macropillar compression responses of magnesium single crystals oriented for single slip or extension twinning. *Acta Materialia*, 65:316–325.

[206] Proust, G., Tomé, C. N., Jain, A., and Agnew, S. R. (2009). Modeling the effect of twinning and detwinning during strain-path changes of magnesium alloy AZ31. *International Journal of Plasticity*, 25(5):861–880.

[207] Qiao, H., Barnett, M. R., and Wu, P. D. (2016). Modeling of twin formation, propagation and growth in a Mg single crystal based on crystal plasticity finite element method. *International Journal of Plasticity*, 86:70–92.

[208] Raabe, D., Ma, D., and Roters, F. (2007). Effects of initial orientation, sample geometry and friction on anisotropy and crystallographic orientation changes in single crystal microcompression deformation: A crystal plasticity finite element study. *Acta Materialia*, 55(13):4567–4583.

[209] Reddy, B. D. (2011). The role of dissipation and defect energy in variational formulations of problems in strain-gradient plasticity. Part 2: single-crystal plasticity. *Continuum Mechanics and Thermodynamics*, 23(6):551–572.

[210] Reed-Hill, R. E. and Robertson, W. D. (1957). Deformation of magnesium single crystals by nonbasal slip. *Journal of Metals-Transactions AIME*, 220:496–502.

[211] Rice, J. R. (1971). Inelastic constitutive relations for solids: an internal variable theory and its application to metal plasticity. *Journal of the Mechanics and Physics of Solids*, 19(6):433–455.

[212] Roscoe, R. (1936). The plastic deformation of cadmium single-crystals. *Philosophical Magazine and Journal of Science*, 21:399–406.

[213] Rösler, J., Harders, H., and Bäker, M. (2007). *Mechanical behaviour of engineering materials: metals, ceramics, polymers, and composites*. Springer Science & Business Media, Berlin Heidelberg.

[214] Sander, L. (2009). *Advanced Condensed Matter Physics*. Cambridge University Press.

[215] Schmid, E. (1924). Yield point of crystals, critical shear stress law. In *Proceedings of the First International Congress for Applied Mechanics*, Delft.

[216] Schmid, E. and Boas, W. (1950). *Plasticity of crystals*. Hughes, London.

[217] Schmid, G. M. and Hackerman, N. (1963). Electrical double layer capacities and adsorption of alcohols on gold. *Journal of the Electrochemical Society*, 110(5):440–444.

[218] Schröder, J., Neff, P., and Ebbing, V. (2008). Anisotropic polyconvex energies on the basis of crystallographic motivated structural tensors. *Journal of the Mechanics and Physics of Solids*, 56(12):3486–3506.

[219] Seker, E., Gaskins, J. T., Bart-Smith, H., Zhu, J., Reed, M. L., Zangari, G., Kelly, R., and Begley, M. R. (2007). The effects of post-fabrication annealing on the mechanical properties of freestanding nanoporous gold structures. *Acta Materialia*, 55(14):4593–4602.

[220] Seker, E., Reed, M. L., and Begley, M. R. (2009). Nanoporous gold: Fabrication, characterization, and applications. *Materials*, 2(4):2188.

[221] Sevillano, J. G. (2000). Intrinsic and extrinsic size effects in plasticity by dislocation glide. *MRS Proceedings*, 653:Z8.5.1–Z8.5.12.

[222] Sevillano, J. G., Arizcorreta, I. O., and Kubin, L. P. (2001). Intrinsic size effects in plasticity by dislocation glide. *Materials Science and Engineering: A*, 309:393–405.

[223] Shade, P. A., Wheeler, R., Choi, Y. S., Uchic, M. D., Dimiduk, D. M., and Fraser, H. L. (2009). A combined experimental and simulation study to examine lateral constraint effects on microcompression of single-slip oriented single crystals. *Acta Materialia*, 57(15):4580–4587.

[224] Shan, Z. W., Mishra, R. K., Asif, S. S., Warren, O. L., and Minor, A. M. (2008). Mechanical annealing and source-limited deformation in submicrometre-diameter Ni crystals. *Nature Materials*, 7(2):115–119.

[225] Shizawa, K. and Zbib, H. H. (1999). A thermodynamical theory of gradient elastoplasticity with dislocation density tensor. I: Fundamentals. *Philosophical Magazine*, 15(9):899–938.

[226] Silhavy, M. (1997). *The mechanics and thermodynamics of continuous media*. Springer Verlag.

[227] Soyarslan, C., Husser, E., and Bargmann, S. (2017). Effect of surface elasticity on the elastic response of nanoporous gold. *Journal of Nanomechanics and Micromechanics*, 7(4):04017013.

[228] Spencer, A. J. M. (1982). Mechanical behavior of anisotropic solids/comportment méchanique des solides anisotropes. In *The formulation of constitutive equation for anisotropic solids*, pages 3–26. Springer Netherlands.

[229] Spencer, A. J. M. (1984). Constitutive theory for strongly anisotropic solids. In *Continuum theory of the mechanics of fibre-reinforced composites*, pages 1–32. Springer New York.

[230] Staroselsky, A. and Anand, L. (2003). A constitutive model for hcp materials deforming by slip and twinning: application to magnesium alloy AZ31B. *International Journal of Plasticity*, 19(10):1843–1864.

[231] Stelmashenko, N. A., Walls, M. G., Brown, L. M., and Milman, Y. V. (1993). Microindentations on W and Mo oriented single crystals: an STM study. *Acta Metallurgica et Materialia*, 41(10):2855–2865.

[232] Stohr, J. F. and Poirier, J. P. (1973). Etude en microscopie electronique du glissement pyramidal {1122} <1123> dans le magnesium. *Philosophical Magazine*, 25(6):1313–1329.

[233] Stölken, J. S. and Evans, A. G. (1998). A microbend test method for measuring the plasticity length scale. *Acta Materialia*, 46(14):5109–5115.

[234] Sun, D., Ponga, M., Bhattacharya, K., and Ortiz, M. (2018). Proliferation of twinning in HCP metals: Application to magnesium. *Journal of the Mechanics and Physics of Solids*, 112:368–384.

[235] Sun, X. Y., Xu, G. K., Li, X. Feng, X. Q., and Gao, H. (2013). Mechanical properties and scaling laws of nanoporous gold. *Journal of Applied Physics*, 113(2):023505.

[236] Svedberg, T. and Runesson, K. (1998). An algorithm for gradient-regularized plasticity coupled to damage based on a dual mixed FE-formulation. *Computer Methods in Applied Mechanics and Engineering*, 161(1):49–65.

[237] Svendsen, B. (2002). Continuum thermodynamic models for crystal plasticity including the effects of geometrically-necessary dislocations. *Journal of the Mechanics and Physics of Solids*, 50(6):1297–1329.

[238] Svendsen, B. and Bargmann, S. (2010). On the continuum thermodynamic rate variational formulation of models for extended crystal plasticity at large deformation. *Journal of the Mechanics and Physics of Solids*, 58(9):1253–1271.

[239] Swadener, J. G., George, E. P., and Pharr, G. M. (2002). The correlation of the indentation size effect measured with indenters of various shapes. *Journal of the Mechanics and Physics of Solids*, 50(4):681–694.

[240] Tabourot, L., Fivel, M., and Rauch, E. (1997). Generalised constitutive laws for fcc single crystals. *Materials Science and Engineering: A*, 234:639–642.

[241] Tarleton, E., Balint, D. S., Gong, J., and Wilkinson, A. J. (2015). A discrete dislocation plasticity study of the micro-cantilever size effect. *Acta Materialia*, 88:271–282.

[242] Taylor, G. I. (1938). Plastic strain in metals. *Journal of the Institute of Metals*, 62:307–324.

[243] Tromans, D. (2011). Elastic anisotropy of hcp metal crystals and polycrystals. *International Journal of Research and Reviews in Applied Sciences*, 6(4):462–483.

[244] Truesdell, C. (1968). *Essays in the History of Mechanics*. Springer-Verlag, New York.

[245] Uchic, M. D., Dimiduk, D. M., Florando, J. N., and Nix, W. D. (2004). Sample dimensions influence strength and crystal plasticity. *Science*, 305(5686):986–989.

[246] Uchic, M. D., Shade, P. A., and Dimiduk, D. M. (2009). Plasticity of micrometer-scale single crystals in compression. *Annual Review of Materials Research*, 39:361–386.

[247] van Beers, P. (2015). Multiscale modelling of grain boundary plasticity. *Ph.D. thesis, TU Eindhoven, Netherlands*.

[248] van Beers, P., McShane, G., Kouznetsova, V., and Geers, M. (2013). Grain boundary interface mechanics in strain gradient crystal plasticity. *Journal of the Mechanics and Physics of Solids*, 61(12):2659–2679.

[249] Van Houtte, P. (1978). Simulation of the rolling and shear texture of brass by the Taylor theory adapted for mechanical twinning. *Acta Metallurgica*, 26(4):591–604.

[250] Voce, E. (1955). A practical strain-hardening function. *Metallurgia*, 51(307):219–226.

[251] Volkert, C. A. and Lilleodden, E. T. (2006). Size effects in the deformation of sub-micron Au columns. *Philosophical Magazine*, 86(33-35):5567–5579.

[252] Wang, J., Beyerlein, I. J., and Tomé, C. N. (2010). An atomic and probabilistic perspective on twin nucleation in Mg. *Scripta Materialia*, 63(7):741–746.

[253] Wang, J., Hirth, J. P., and Tomé, C. N. (2009). $(\bar{1}012)$ Twinning nucleation mechanisms in hexagonal-close-packed crystals. *Acta Materialia*, 18(57):5521–5530.

[254] Wilmers, J., McBride, A., and Bargmann, S. (2017). Interface elasticity effects in polymer-filled nanoporous metals. *Journal of the Mechanics and Physics of Solids*, 99:163–177.

[255] Wonsiewicz, B. C. and Backofen, W. A. (1967). Plasticity of magnesium crystals. *Transaction of Metallurgical Society of AIME*, 239(9):1422–1431.

[256] Wu, P. D., Guo, X. Q., Qiao, H., and Lloyd, D. J. (2015). A constitutive model of twin nucleation, propagation and growth in magnesium crystals. *Materials Science and Engineering: A*, 625:140–145.

[257] Wu, T. Y., Bassani, J. L., and Laird, C. (1991). Latent hardening in single crystals I. theory and experiments. *Proceedings of the Royal Society of London A: Mathematical, Physical and Engineering Sciences*, 435(1893):1–19.

[258] Xu, C., Su, J., Xu, X., Liu, P., Zhao, H., Tian, F., and Ding, Y. (2007). Low temperature CO oxidation over unsupported nanoporous gold. *Journal of the American Chemical Society*, 129:42–43.

[259] Yoo, M. H. (1981). Slip, twinning, and fracture in hexagonal close-packed metals. *Metallurgical Transactions A*, 12(3):409–418.

[260] Yoshinaga, H. and Horiuchi, R. (1964). On the nonbasal slip in magnesium crystals. *Transactions of the Japan Institute of Metals*, 5(1):14–21.

[261] Yu, Q., Qi, L., Chen, K., Mishra, R. K., Li, J., and Minor, A. M. (2012). The nanostructured origin of deformation twinning. *Nano letters*, 12(2):887–892.

[262] Yu, Q., Wang, J., Jiang, Y., McCabe, R. J., Li, N., and Tomé, C. N. (2014). Twin-twin interactions in magnesium. *Acta Materialia*, 77:28–42.

[263] Zaafarani, N., Raabe, D., Singh, R. N., Roters, F., and Zaefferer, S. (2006). Three-dimensional investigation of the texture and microstructure below a nanoindent in a Cu single crystal using 3D EBSD and crystal plasticity finite element simulations. *Acta Materialia*, 54(7):1863–1876.

[264] Zaiser, M. and Aifantis, E. C. (2006). Randomness and slip avalanches in gradient plasticity. *International Journal of Plasticity*, 22(8):1432–1455.

[265] Zhang, H., Schuster, B. E., Wei, Q., and Ramesh, K. T. (2006). The design of accurate micro-compression experiments. *Scripta Materialia*, 54(2):181–186.

[266] Zhang, J., Liu, P., Ma, H., and Ding, Y. (2007). Nanostructured porous gold for methanol electro-oxidation. *The Journal of Physical Chemistry C*, 111:10382–10388.

[267] Zhou, C., Biner, S., and LeSar, R. (2010). Simulations of the effect of surface coatings on plasticity at small scales. *Acta Materialia*, 63(11):1096–1099.

[268] Ziehmer, M., Hu, K., Wang, K., and Lilleodden, E. T. (2016). A principle curvatures analysis of the isothermal evolution of nanoporous gold: Quantifying the characteristic length-scales. *Acta Materialia*, 120:24–31.